SYNTHESIS, CHARACTERIZATION AND PROPERTIES OF NEW LOW-VALENT PALLADIUM AND PLATINUM CLUSTERS OF DIARSINE AND DIISOCYANIDE LIGANDS

by

Tianle Zhang

A thesis presented to the Département de chimie
in fulfillment of the requirements for
the degree of Philosophiae Doctor (Ph.D.)

FACULTÉ DES SCIENCES
UNIVERSITÉ DE SHERBROOKE

Sherbrooke, Canada, August 1998

Le 98/09/25 , le jury suivant a accepté cette thèse dans sa version finale.
date

Président-rapporteur:	M. Jean Lessard Département de chimie	_____
Membre:	M. Hugues Ménard Département de chimie	_____
Membre:	M. Pierre D. Harvey Département de chimie	_____
Membre externe:	M. André Beauchamp Université deMontréal	_____

SUMMARY

The low-valent palladium and platinum clusters have been the topic of long standing interest because of their intriguing bonding and excellent catalytic properties. In this project, diarsine (dpam=bis(diphenylarsino)methane) and diisocyanide (dmb=1,8-diisocyano-*p*-menthane) ligands have been used to build the low-valent palladium and platinum clusters, based upon the different purposes. Two kinds of clusters (polyhedral and linear chain clusters) have been successfully synthesized and fully characterized.

Direct reduction of $Pd(CH_3COO)_2$ in acetone by CO in the presence of a mixture of dpam, CF_3COOH and water, gave a trinuclear cluster, $[Pd_3(dpam)_3(\mu_3\text{-}CO)]^{2+}$. The crystal structure determined by X-ray crystallography, is isomorphous with that of the dppm analogue, but the size of the cavity formed by six phenyl groups adopting axial configuration, is large, where one PF_6^- anion is located inside. The binding constants of this modified host system were measured by UV-vis spectroscopy, and compared with those of the dppm analogue. Interestingly the binding constant values for the larger hosts are always larger for the same substrate-solvent system, which clearly shows a direct consequence of the increase in the cavity size induced by long Pd-As (~2.42 Å) bond length (Pd-P:~2.32 Å). The large PF_6^- anion, also binds weakly to $[Pd_3(dpam)_3(\mu_3\text{-}CO)]^{2+}$, which does not bind to the dppm analogue. Further this cluster reacts with I^- to give the expected cluster adduct, $[Pd_3(dpam)_3(\mu_3\text{-}CO)(\mu_3\text{-}I)]^+$, where a trigonal bipyramid structure is observed. But in the presence of O_2, an unexpected oxidation-fragmentation reaction occurs and leads to the breakdown to a dinuclear complex, $[Pd_2(dpam)_2I_4]$, as identified from X-ray crystallography. In this case, dpam ligands coordinate the Pd(II) centers in a bridging fashion, not in a chelating mode as commonly encountered for dppm in mononuclear complex, $[Pd(dppm)X_2]$ (X = Cl, Br, Cl). The long distance of Pd···Pd (3.3896(9) Å) indicates that there is no weak interaction between two Pd atoms.

The reduction of $Pt(dpam)(CF_3COO)_2$ by CO in a mixture of methanol and water leads to the preparation of a 58-electron "butterfly" cluster, $[Pt_4(dpam)_3(\mu_2\text{-}CO)_3(\eta^1\text{-}dpam)]^{2+}$, as a CF_3COO^- salt. The PF_6^- salt is easily prepared by metathesis of the anions. The crystal structure was determined by X-ray crystallography, in which two edge sharing Pt_3 triangles are found (a large and a small triangle). In the small one, the average Pt-Pt distance is 2.626 Å; in the large one, the distance increases to 2.69 Å. In solution, the fluxionality occurs, which was confirmed by variable-temperature measurements of ^1H NMR spectra. At low temperature ($T< 193$ K), the spectra become complex, indicating the loss of 3-fold symmetry. The spectra also confirmed that there are two isomers in solution. It was proposed that the +2 charge is located on the small triangle based upon the comparisons with the crystal data of a series of related clusters in literature. This cluster is luminescent at 77K, but not at room temperature. The luminescence is a phosphorescence, and the emission lifetime (τ_e) is 3.2 ± 0.2 μs. The electronic spectroscopic properties have been rationalized by EHMO computations.

The preparation of a tetranuclear platinum complex containing linear metal-metal chain has been achieved by the direct reaction between $Pt_2(dba)_3{\cdot}CHCl_3$ and an excess of dmb. The air-stable complex, $[Pt_4(dmb)_4(PPh_3)_2]Cl_2$ was isolated as a red-orange crystalline solid. The crystal structure was determined by X-ray crystallography, where four Pt atoms are connected through short metal-metal bonds (2.654, 2.641 and 2.666 Å) and form a linear chain ($\angle PtPtPt = 175.3^\circ$). A catenate structure was observed where the two $Pt_2(dmb)_2$ units (20-member ring) interlock each other to form this unique structure. The Pd analogue was synthesized in the same way. $Pd_2(dba)_3{\cdot}CHCl_3$ was used instead of $Pt_2(dba)_3{\cdot}CHCl_3$, where the bond distance of Pd-Pd is about 2.53 Å. Both clusters are isostructural. This chemistry has been expanded to the polymers containing $[M_4(dmb)_4]$ units (M = Pd, Pt). The organometallic polymers, $\{[Pt_4(dmb)_4]\text{-diphosphine}\}_n$ ($Ph_2P\text{-}(CH_2)_x\text{-}PPh_2$, x = 4, 5, 6; dppb, dppp, dpph, respectively) complexes, have been synthesized, where the $[Pt_4(dmb)_4]$ units are connected by diphosphine ligands, $\{[Pt_4(dmb)_4]\text{–P-}(CH_2)_x\text{-P–}\}_n$. Their polymeric features have been

addressed by X-ray powder diffraction, T_1 (^{13}C NMR spin-lattice relaxation time) and viscosity measurements. In one case, $\{[Pd_4(dmb)_5]^{2+}\}_n$ has been characterized from X-ray crystallography. In this structure, the $[Pd_4(dmb)_4]$ units are linked by dmb ligand adopting Z-shaped conformation to form one-dimensional chain. In the unit, the catenade structure remains. The distances of the Pd-Pd bonds are longer than those in $[Pd_4(dmb)_4(PPh_3)_2]^{2+}$ (2.608, 2.597 and 2.623 Å). The absorption spectra of these complexes are characterized by strong narrow peaks located at ~ 400 nm for Pt_4, and ~ 510 - 540 nm for Pd_4 species. These absorption bands arise from $d\sigma^* \rightarrow d\sigma^*$ transitions, which are consistent with the EHMO calculations. For $[Pd_4(dmb)_4(PPh_3)_2]^{2+}$ complex, the above assignment was confirmed by the first (ν_{max} vs T) and second moment ($fwhm^2$ vs T) analysis of the absorption band. The emissions of all the these complexes are phosphorescence, and also arise from $d\sigma^* \rightarrow d\sigma^*$ transitions.

The linear complexes, $\{[M_4(dmb)_m]Cl_2\}_n$ (M = Pd, Pt), prepared from the reaction between $M_2(dba)_3 \cdot CHCl_3$ and dmb, are reactive. The palladium species, $\{[Pd_4(dmb)_m]Cl_2\}_n$ reacts with neutral TCNQ to give an oxidized dinuclear complex, $[Pd_2(dmb)_4(\mu_2\text{-}Cl)](TCNQ)_4$, where the Cl^- is encapsulated by two Pd(II) atoms. This result confirmed the composition of the intermediate species, $\{[Pd_4(dmb)_m]Cl_2\}_n$, and suggested that chlorocarbons are involved in the reactions between $M_2(dba)_3 \cdot CHCl_3$ and dmb, which leads to the oxidized complexes, $[M_4(dmb)_4(PPh_3)_2]Cl_2$ in the presence of PPh_3. The reaction between $\{[Pt_4(dmb)_m]Cl_2\}_n$ and $Au(PPh_3)_2^+$ led to the preparation of a heterometallic cluster, $[Pt_2Au_2(dmb)_2(PPh_3)_4]^{2+}$, with a rhombic geometry. In this molecule, long Pt-Au (~2.82 Å) and short Au-Au (~2.598 Å) bond lengths were observed. The properties of this complex have also been studied.

SOMMAIRE

Les agrégats métalliques de palladium et de platine de basse valence ont été le sujet d'intérêts depuis longtemps à cause de leurs propriétés catalytiques et de la présence de liaisons métal-métal intrigantes. Dans ce projet deux ligands assembleurs ont été utilisés pour construire ces agrégats, soit le dpam (bis(diphénylarsino)méthane) et le dmb (1,8-diisocyano-*p*-menthane). En effet, deux sortes d'agrégats (polyèdre et chaîne linéaire) ont été préparés avec succès, et ont été pleinement caractérisés.

La réduction directe du $Pd(CH_3COO)_2$ dans l'acétone en présence d'un mélange de dpam, CF_3COOH et de l'eau, par le CO produit l'agrégat $[Pd_3(dpam)_3(\mu_3\text{-}CO)]^{2+}$. La structure du cation a été déterminée par la technique de diffraction des rayons-X, et est isostructurale au dérivé dppm correspondant. Dans ce cas, la dimension de la cavité formée par les six groupes phényles adoptant la configuration axiale est grande, où le contre anion PF_6^- se retrouve. Les constantes d'association de cette molécule hôte modifiée ont été obtenues par spectroscopie UV-visible, et ont été comparées avec celles du dérivé dppm correspondant connu. Comme prévu, ces constantes d'association sont plus élevées pour la grande cavité (dpam) pour un même système substrat-hôte, ceci montre clairement la conséquence directe de l'augmentation de la dimension de la cavité via l'augmentation de la liaison M-L (Pd-As ~2,42 Å, Pd-P ~2,32 Å). Durant ces expériences, on s'aperçoit que l'anion PF_6^- se lie faiblement au $[Pd_3(dpam)_3(\mu_3\text{-}CO)]^{2+}$, alors que cela ne survient pas pour l'analogue au dppm. Cet agrégat métallique réagit avec I^- pour former le composé attendu $[Pd_3(dpam)_3(\mu_3\text{-}CO)(\mu_3\text{-}I)]^+$, où une structure bipyramide trigonale est observée. Subséquemment, la présence de O_2 conduit à une réaction de fragmentation oxydante et le complexe $Pd_2(dpam)_2I_4$ a été isolé, et identifié par cristallographie. Dans ce cas les ligands dpam pontent les deux centres Pd (II), et ils ne chélatent pas le métal tel qu'observé pour les complexes mononucléaires $Pd(dppm)X_2$ (X = Cl, Br, I). La longue distance Pd···Pd (3,3896(9) Å) indique l'absence d'interaction Pd···Pd.

La réduction du $Pt(dpam)(O_2CCF_3)_2$ par le CO dans un mélange méthanol/eau, conduit à la préparation d'un agrégat de géométrie papillon à 58 électrons de valence, $[Pt_4(dpam)_3(\mu_2\text{-}CO)(\eta^1\text{-}dpam)]^{2+}$ sous forme de sel de $CF_3CO_2^-$. Le sel de PF_6^- correspondant peut être obtenu par métathèse de l'anion. La structure a été déterminée par méthode cristallographique, dans laquelle on retrouve deux triangles Pt_3 (un petit et un grand) partageant un même côté. Dans le petit triangle, la distance Pt-Pt moyenne est 2,626 Å, alors que dans le plus grand, cette distance est de 2,690 Å. En solution un processus fluxionnel survient, lequel a été confirmé par des mesures de spectre RMN ^1H en fonction de la température. À basse température ($T<193$ K) les spectres deviennent très complexes indiquant une perte de la symétrie C_3. Les spectres ont également montré la présence de deux isomères en solution, associés probablement à la coordination ou non du groupe CF_3COO^-. Il a aussi été proposé que la charge 2+ soit localisée sur le fragment Pt_3 (petit) sur une base comparative avec des données cristallographiques trouvées dans la littérature pour des agrégats appartenant à la même famille. De plus, cet agrégat est luminescent à 77 K, mais pas à la température de la pièce. Cette émission est une phosphorescence avec une durée de vie (τ_e) de $3,2 \pm 0,2$ µs. Ces propriétés ont été discutées à l'aide de calculs EHMO.

La préparation d'un nouveau complexe linéaire Pt_4 contenant des liaisons Pt-Pt a été réussie via la réaction directe entre le $Pt_2(dba)_3{\cdot}CHCl_3$ et un excès de dmb. Ce complexe stable à l'air, $[Pt_4(dmb)_4(PPh_3)_2]Cl_2$, a été isolé sous forme de cristaux rouge-orange. La structure a été déterminée à l'aide de la technique de diffraction des rayons-X. Pour cette molécule, les quatre atomes de Pt sont reliés entre eux par des liaisons courtes (2,654, 2,641 et 2,666 Å), et forment une chaîne linéaire ($\angle PtPtPt=175,3°$). Une structure caténate a été également observée où deux unités de $Pt_2(dmb)_2$ (anneaux à 20 membres) s'enchaînent l'un dans l'autre pour former cette géométrie spéciale. Le dérivé au palladium a été synthétisé de la même manière, en utilisant le $Pd_2(dba)_3{\cdot}CHCl_3$ à la place du $Pt_2(dba)_3{\cdot}CHCl_3$. Dans ce cas, la distance Pd-Pd est d'environ 2,53 Å, et une structure similaire est observée. Cette chimie a été appliquée pour la préparation de polymères organométalliques contenant les fragments

$[M_4(dmb)_4]$ (M = Pd, Pt). Les polymères organométalliques, du type $[Pt_4(dmb)_4]$-diphosphine (Ph_2P-$(CH_2)_x$-PPh_2, x = 4, 5, 6; dppb, dppp, dpph, respectivement), ont été synthétisés où les unités de $[Pt_4(dmb)_4]$ sont reliées ensemble par des ligands diphosphinés, $\{[Pt_4(dmb)_4]$–P-$(CH_2)_x$-P–$\}_n$. Pour le dérivé du palladium, le polymère, $\{[Pd_4(dmb)_5]^{2+}\}_n$ a été caractérisé par cristallographie, où les unités $Pd_4(dmb)_4^{2+}$ sont reliés par un autre dmb adoptant une conformation-Z (au lieu de -U) pour former une chaîne unidimensionnelle. La structure caténade est toujours présente dans les unités Pd_4 dans ce polymère. Les distances Pd-Pd sont plus longues que dans le $[Pd_4(dmb)_4(PPh_3)_2]^{2+}$ (2,608, 2,597 et 2,623 Å). Les spectres d'absorption de ces complexes sont caractérisés par des bandes minces et intenses autour de ~400 nm pour le Pt_4^{2+} et ~510-540 nm pour les espèces Pd_4. Ces bandes d'absorption proviennent de transitions électroniques du type $d\sigma^* \rightarrow d\sigma^*$, en accord avec les prédictions obtenues par les calculs EHMO. Pour le complexe $[Pd_4(dmb)_4(PPh_3)_2]^{2+}$, cette attribution a été confirmée en utilisant des analyses du premier (ν_{max} vs T) et second moment ($fwhm^2$ vs T) de la bande d'absorption. Les émissions de tous ces complexes sont des phosphorescences, et proviennent également des transitions électroniques du type $d\sigma^* \rightarrow d\sigma^*$.

Ces complexes linéaires $\{[M_4(dmb)_m]Cl_2\}_n$ (M = Pd, Pt) qui ont été préparés à partir des dimères $M_2(dba)_3 \cdot CHCl_3$ et dmb sont réactifs. Les composés de palladium $\{[Pd_4(dmb)_m]Cl_2\}_n$ réagissent avec le TCNQ neutre pour former le complexe dinucléaire oxydé $[Pd_2(dmb)_4(\mu_2$-$Cl)](TCNQ)_4$ où un des Cl^- est maintenant encapsulé entre deux atomes de Pd(II). Ce résultat indique que la composition de l'intermédiaire est $\{[M_4(dmb)_m]Cl_2\}_n$ dans la réaction entre le $M_2(dba)_3 \cdot CHCl_3$ et dmb et le PPh_3 conduisant au produit $[Pd_4(dmb)_4(PPh_3)_2]Cl_2$. La réaction entre le $\{[Pt_4(dmb)_m]Cl_2\}_n$ et $Au(PPh_3)_2^+$ conduit à la préparation de l'agrégat hétéronucléaire $[Pt_2Au_2(dmb)_2(PPh_3)_4]^{2+}$. Dans cette molécule, des liaisons très longues Pt-Au (~2,82 Å) et une très courte Au-Au (~2,598 Å) ont été observées. Certaines propriétés de ce complexe ont également été étudiées.

ACKNOWLEDGEMENTS

This project has been carried out in Prof. P. D. Harvey's laboratory. I thank Professor P. D. Harvey for his giving me the chance to study and do the research in this interesting field, and his supervision and support in study and living.

During my study in Sherbrooke, I have got support from my colleagues, R. Provencher, D. Fortin, J. Gagnon, M. Turcotte and M. Vézina. I particularly express my gratitude to M. Drouin for his measurements of the X-ray structures of all the complexes in this project.

I am very grateful to my family. Their support made this work possible.

The NSERC (Natural Sciences and Engineering Research Council) and the FCAR (Fonds Concertés pour l'Avancement de la Recherche) are thanked for their financial support.

TABLE OF CONTENTS

SUMMARY ii

ACKNOWLEDGEMENTS viii

TABLE OF CONTENTS ix

LIST OF ABBREVIATIONS xiv

LIST OF TABLES xvi

LIST OF FIGURES xx

LIST OF SCHEMES xxv

INTRODUCTION 1

CHAPTER 1 - THEORY 5

1.1 Binding constants and UV-vis spectrophotometry 5

1.1.1 The equilibrium constant 5

1.1.2 Model 6

1.1.3 The binding isotherm 8

1.2 X-ray diffraction 16

1.2.1 Single crystal X-ray diffraction 16

1.2.2 X-ray powder diffraction 20

1.3 Nuclear magnetic resonance 20

1.3.1 Nuclei energies in magnetic field 20

1.3.2 Spin-lattice relaxation 21

1.3.2.1 Spin-lattice relaxation time (T_1) 21

1.3.2.2 The measurement of T_1 by Fourier Transform Spectroscopy ... 25

1.3.3 The relation between T_1 and molecular dimension 26

1.4 Photophysical concepts 26

1.4.1 Jablonski diagram 26
1.4.2 The Franck-Condon principle 28
1.4.3 Internal conversion and intersystem crossing 29
1.4.4 Fluorescence and phosphorescence 31
1.4.5 Transition probability 31
1.4.6 Lifetime 36
1.5 Polymers 37
1.5.1 Definition 37
1.5.2 Determination of molecular weight by viscosity measurements 38

CHAPTER 2 - PALLADIUM AND PLATINUM CLUSTERS OF DIARSINE 40
2.1 The tuning of binding properties via the change in cavity size of the unsaturated palladium clusters 40
2.1.1 Synthesis and crystal structure of $[Pd_3(dpam)_3CO](PF_6)_2$ 41
2.1.2 Host-guest chemistry 44
2.1.3 Reaction with iodide salt 48
2.2 Properties of a new 58-electron butterfly $[Pt_4(dpam)_3(\mu_2\text{-}CO)(\eta^1\text{-}dpam)](PF_6)_2$ cluster 53
2.2.1 Synthesis and crystal structure of $[Pt_4(dpam)_3(\mu_2\text{-}CO)(\eta^1\text{-}dpam)](PF_6)_2$. 55
2.2.2 FT-Raman spectrum 60
2.2.3 ^1H NMR spectra and fluxionality 62
2.2.4 EHMO computations 67
2.2.5 UV-vis and emission spectra 70

CHAPTER 3 - PALLADIUM AND PLATINUM COMPLEXES OF DIISOCYANIDE . 72
3.1 The linear tetranuclear platinum complex $[Pt_4(dmb)_4(PPh_3)_2]^{2+}$ and its diphosphine polymers 72
3.1.1 Synthesis of $[Pt_4(dmb)_4(PPh_3)_2]Cl_2$ 73

3.1.2 Characterization 76
3.1.2.1 NMR spectra 76
3.1.2.2 Crystal structure 80
3.1.3 Isomers (head-to-tail dmb chemistry) 84
3.1.4 Raman spectrum 87
3.1.5 Preparation and characterization of polymers containing $[Pt_4(dmb)_4]$ units 89
3.1.6 X-ray powder diffraction 89
3.1.7 Viscosity and T_1 measurements 91
3.1.8 EHMO computations 94
3.1.9 Electronic spectra 98
3.2 Preparation, spectroscopic and structural characterization of $[Pd_4(dmb)_4(PPh_3)_2]^{2+}$ and its organometallic polymer $\{[Pd_4(dmb)_5](CH_3COO)_2\}_n$. The first 58-electron tetranuclear linear chain Pd clusters 103
3.2.1 Preparation and characterization of $[Pd_4(dmb)_4(PPh_3)_2]Cl_2$ 103
3.2.2 Reactivity 104
3.2.3 Preparation and structure of polymer $\{[Pd_4(dmb)_5](CH_3COO)_2\}_n$ 108
3.2.4 Raman spectra 114
3.2.5 EHMO computations 116
3.2.6 UV-vis spectra and moment band analysis 118
3.2.7 Luminescence properties 127
3.3 Reactivity of low-valent platinum-diisocyanide complex. Synthesis, crystal structure and properties of $[Pt_2Au_2(dmb)_2(PPh_3)_4](PF_6)_2$ 128
3.3.1 Synthesis and characterization 129
3.3.2 Crystal structure of $[Pt_2Au_2(dmb)_2(PPh_3)_2](PF_6)_2$ 131
3.3.3 ^{31}P NMR spectrum 137
3.3.4 FT-Raman spectrum of $[Pt_2Au_2(dmb)_2(PPh_3)_2](PF_6)_2$ 139
3.3.5 Electronic spectra 140

CONCLUSION 144

EXPERIMENTAL SECTION 147

1 Materials 147

1.1 Clusters $[Pd_3(dpam)_3CO]Y_2$(Y=CF_3COO^-, PF_6^-, $[B(C_6H_5)_4]^-$) and $[Pt_4(dpam)_4 \cdot(CO)_3]Y_2$ (Y= CF_3COO^-, PF_6^-) 147

1.2 Linear clusters, $[M_4(dmb)_4(PPh_3)_2]^{2+}$ (M = Pd, Pt) and polymers 147

2 Instruments 147

3 X-ray crystallography 148

4 Synthesis 153

4.1 Synthesis of $[Pd_3(dpam)_3CO](CF_3COO)_2$ 153

4.2 Preparation of $[Pd_3(dpam)_3CO](PF_6)_2$ 153

4.3 Preparation of $[Pd_3(dpam)_3CO][B(C_6H_5)_4]_2$ 154

4.4 Synthesis of $[Pd_3(dpam)_3(CO)(I)](CF_3COO)$ 154

4.5 Synthesis of $[Pd_2(dpam)_2I_4]$ 154

4.6 Synthesis of $[Pt_4(dpam)_4(CO)_3](CF_3COO)_2$ 155

4.6.1 Preparation of $Pt(dpam)Cl_2$ 155

4.6.2 Preparation of $Pt(dpam)(CF_3COO)_2$ 155

4.6.3 Preparation of $[Pt_4(dpam)_4(CO)_3](CF_3COO)_2$ 155

4.7 Preparation of $[Pt_4(dpam)_4(CO)_3](PF_6)_2$ 156

4.8 Synthesis of $[Pt_4(dmb)_4(PPh_3)_2]Cl_2$ 156

4.9 Synthesis of $\{[Pt_4(dmb)_4(dppb)]Cl_2\}_n$ 157

4.10 Synthesis of $\{[Pt_4(dmb)_4(dppp)]Cl_2\}_n$ 158

4.11 Synthesis of $\{[Pt_4(dmb)_4(dpph)]Cl_2\}_n$ 158

4.12 Synthesis of $[Pd_4(dmb)_4(PPh_3)_2]Cl_2$ 159

4.13 Synthesis of $[Pd_2(dmb)_4(\mu_2\text{-}Cl)](TCNQ)_4$ 159

4.14 Synthesis of polymer $\{[Pd_4(dmb)_5](CH_3COO)_2\}_n$ 160

4.15 Synthesis of $[Pt_2Au_2(dmb)_2(PPh_3)_4](PF_6)_2$ 160

4.16 Synthesis of $Pt_2(dmb)_2Cl_2$ 162
4.16.1 Synthesis of $Pt_2(dmb)_2Cl_4$ 162
4.16.2 Synthesis of $Pt_2(dmb)_2Cl_2$ 162

BIBLIOGRAPHY 164

LIST OF ABBREVIATIONS

A: absorbance.

ε: molar absorption coefficient.

CVE: cluster valence electron count.

dba: dibenzylideneacetone

dmb: 1,8-diisocyano-*p*-menthane.

dpam: bis(diphenylarsino)methane.

dppb: bis(diphenylphosphino)butane.

dpph: bis(diphenylphosphino)hexane.

dppp: bis(diphenylphosphino)pentane.

EHMO: Extended Hückel Molecular Orbital.

FAB: fast atomic bombardment.

fwhm: full width at half-maximum.

HOMO: highest occupied molecular orbital.

HOMO-n: orbital lying below HOMO.

LUMO: lowest unoccupied molecular orbital.

LUMO+n: orbital lying above LUMO.

MLCT: metal to ligand charge transfer.

TCNQ: 7, 7', 8, 8'-tetracyanoquinodimethane.

LIST OF TABLES

1. Crystallographic data for $[Pd_3(dpam)_3(CO)](PF_6)_2$ 41

2. Selected bond distances (Å) and angles (°) for $[Pd_3(dpam)_3CO](PF_6)_2$ 43

3. Comparison of the binding constants for $[Pd_3(dppm)_3CO]^{2+}$ and $[Pd_3(dpam)_3CO]^{2+}$ . . 47

4. Crystal data for $[Pd_3(dpam)_3(CO)(I)](CF_3COO)$ and $[Pd_2(dpam)_2I_4]$ 49

5. Selected bond distances (Å) and angles (°) for $[Pd_3(dpam)_3(CO)(I)](CF_3CO_2)$ 51

6. Selected bond lengths (Å) and angles (°) for $[Pd_2(dpam)_2I_4]$ 51

7. Crystal data for $[Pt_4(dpam)_3(\mu_2\text{-}CO)(\eta^1\text{-}dpam)](PF_6)_2$ (4b) 56

8. Selected bond distances (Å) and angles (°) for $[Pt_4(dpam)_3(\mu_2\text{-}CO)(\eta^1\text{-}dpam)](PF_6)_2$ (4b) 58

9. Comparison of Pt-Pt distances (Å) in butterfly clusters 59

10. Comparison of the ν(Pt-Pt) data for cyclic Pt clusters 61

11. Selected mass FAB data for solid $[Pt_4(dmb)_4(PPh_3)_2]Cl_2$ 75

12. Isotopomer distribution for $[Pt_4(dmb)_4(PPh_3)_2]^{2+}$ 77

13. Comparison of the NMR data (^{31}P, ^{195}Pt) for selected polynuclear Pt complexes . . . 79

14. Crystallographic data for $[Pt_4(dmb)_4(PPh_3)_2]Cl_2$ 80

15. Selected bond distances (Å) and angles (°) for $[Pt_4(dmb)_4(PPh_3)_2]Cl_2$ 82

16. Comparison of the Pt-Pt distances for various Pt_4 Species 83

17. Comparison of the spectroscopic and structural data for linear Pt_3 and Pt_4 complexes . 88

18. Spectroscopic data for $[Pt_4(dmb)_4(PPh_3)_2]Cl_2$ and related polymers 90

19. The values of T_1 and intrinsic viscosities of the polymers 92

20. EHMO atomic contributions for $[Pt_4(CNMe)_8(PH_3)_2]^{2+}$ 97

21. Spectroscopic data for $[Pt_4(dmb)_4(PPh_3)_2]Cl_2$ 100

22. Comparison of the electronic spectroscopic data for tetramer and polymers 101

23. Spectroscopic comparison for various low-valent M_n-isocyanide complexes exhibiting either M-centered or MLCT emissions 102

24. Selected mass FAB data for solid $[Pd_4(dmb)_4(PPh_3)_2]Cl_2$ 105

25. Crystallographic data for $[Pd_2(dmb)_4(\mu\text{-}Cl)](TCNQ)_4$ 106

26. Selected bond lengths (Å) and angles (°) for $[Pd_2(dmb)_4(\mu\text{-}Cl)](TCNQ)_4$ 108

27. Crystal data for $\{[Pd_4(dmb)_5](CH_3COO)_2(H_2O)_4\}_n$ 109

28. Selected bond lengths (Å) and angles (°) for $\{[Pd_4(dmb)_5](CH_3COO)_2(H_2O)_4\}_n$ . . . 112

29. Comparison of the dmb bite distances (> 4.9 Å) 113

30. Comparison of the spectroscopic and structural data for linear and cyclic Pd_n clusters .115

31. EHMO atomic contributions for $[Pd_4(CNMe)_8(PH_3)_2]^{2+}$ 117

32. Comparison of the first and second moment band analysis for various Pd_n^{2+} species . . 125

33. Selected ΔQ values vs $\hbar\omega_{e1}$ for the excited states of $[Pd_4(dmb)_4(PPh_3)_2]^{2+}$ 126

34. Electronic spectroscopic data for $[Pd_4(dmb)_4(PPh_3)_2]Cl_2$ and polymer $\{[Pd_4(dmb)_5]\bullet (CH_3COO)_2(H_2O)_4\}_n$ 128

35. Assignment of the fragments for $[Pt_4(dmb)_4(PPh_3)_2](PF_6)_2$ 130

36. Assignment of the fragments for $[Pt_2Au_2(dmb)_2(PPh_3)_4](PF_6)_2$ 131

37. Crystal data for $[Pt_2Au_2(dmb)_2(PPh_3)_4](PF_6)_2$ 133

38. Selected bond lengths (Å) and angles (°) for $[Pt_2Au_2(dmb)_2(PPh_3)_4](PF_6)_2$ 135

39. IR active ν(CN) data for various Pt-CNR (alkyl) complexes 136

40. Coupling constants for $[Pt_2Au_2(dmb)_2(PPh_3)_4](PF_6)_2$ 139

41. UV-vis spectroscopic data ($[Pt_2Au_2(dmb)_2(PPh_3)_4](PF_6)_2$) 141

LIST OF FIGURES

1. Crystal structure of $[Pd_3(CNCH_3)_6(PPh_3)_2]^{2+}$ 3

2. Direct binding curve plot 9

3. Double-reciprocal plot 9

4. y-Reciprocal plot 10

5. x-Reciprocal plot 10

6. Typic absorption spectrum of a 1:1 complexing system 12

7. The conventional derivation of the Bragg law treats each plane as reflecting the incident radiation 17

8. An electron-density map of a benzoic acid molecule determined from the X-ray diffraction pattern of a benzoic acid crystal 19

9. The nuclear spin energy levels of a spin-1/2 nucleus in a magnetic field 21

10. Orientation of the dipolar interaction relative to the magnetic field 23

11. Determination of T_1 by the inversion-recovery method 25

12. Jablonski diagram 27

13. Diatomic potential energy curves and Franck-Condon transition 25

14. Diatomic potential energy curves and intersystem crossing 30

15. Franck-Condon potential curves of the ground and excited states of a diatomic molecule and typic absorption spectra 33

16. Scheme for the absorption and emission (fluorescence) spectra (a); an example of absorption and fluorescence spectra (b) 34

17. The concentration dependence of the viscosity number for polystyrene in toluene at 30°C 39

18. Crystal structure of $[Pd_3(dpam)_3(\mu_3\text{-}CO)](PF_6)_2\cdot CH_2Cl_2$ 42

19. Absorption spectra of $[Pd_3(dpam)_3(\mu_3\text{-}CO)](PF_6)_2$: acetonitrile system in acetone . . . 45

20. Typical binding constant (K_{11}) measurement experiment (linear plots): Benesi-Hildebrand, Scott, and Scatchard's associated with Figure 19 46

21. Crystal structure of $[Pd_3(dpam)_3(\mu_3\text{-}CO)(\mu_3\text{-}I)](CF_3COO)$ 50

22. Crystal structure of $[Pd_2(dpam)_2I_4]$ 52

23. Crystal structure of $[Pt_4(\mu_2\text{-dpam})_3(\mu_2\text{-}CO)_3(\eta^1\text{-dpam})](PF_6)_2$ (4b) 57

24. FT-Raman spectrum for $Pt_4(dpam)_4(CO)_3](CF_3COO)_2$ (4a) 61

25. ^{1}H NMR spectrum of $Pt_4(dpam)_4(CO)_3](CF_3COO)_2$ (4b) in acetone-d_6 62

26. ^{1}H NMR spectra of $[Pt_4(\mu_2\text{-dpam})_3(\mu_2\text{-CO})_3(\eta^1\text{-dpam})](CF_3COO)_2$ (4a) in DMSO-d_6 in the 5.6-6.2 ppm region (H_b and H_b') as a function of selected temperatures 64

27. Ball-and-stick drawing based upon the X-ray structure of 4b showing H_a and H_b (conformer 2) with respect to $Pt(\mu_2\text{-CO})_2(\eta^1\text{-dpam})$ fragment and CO group under the Pt_3As_6 plane 65

28. ^{1}H NMR spectra of $[Pt_4(\mu_2\text{-dpam})_3(\mu_2\text{-CO})_3(\eta^1\text{-dpam})](CF_3COO)_2$ (4a) in the 5.4-6.1 ppm region 66

29. Interaction diagram for $Pt_4(\mu_2\text{-CO})_3(AsH_3)_7^{2+}$ 69

30. Absorption (left) and emission spectra (right) of $[Pt_4(\mu_2\text{-dpam})_3(\mu_2\text{-CO})_3(\eta^1\text{-dpam})]\cdot(PF_6)_2$ (4b) in ethanol at 77 K 71

31. Low-resolution mass FAB spectrum of $[Pt_4(dmb)_4(PPh_3)_2]Cl_2$ 74

32. ^{195}Pt NMR spectrum of $[Pt_4(dmb)_4(PPh_3)_2]Cl_2$ in CD_3CN 76

33. ^{31}P NMR spectra (experimental and simulated) of $[Pt_4(dmb)_4(PPh_3)_2]Cl_2$ in CD_3CN . 78

34. Crystal structure of $[Pt_4(dmb)_4(PPh_3)_2]Cl_2$ 81

35. Schematic drawings of 5 geometric and 2 optical isomers for $[M_4(dmb)_4(PPh_3)_2]^{2+}$. . 85

36. ^{13}C NMR spectrum for $[Pt_4(dmb)_4(PPh_3)_2]Cl_2$ in CD_3CN 86

37. FT-Raman spectrum for solid $[Pt_4(dmb)_4(PPh_3)_2]Cl_2$ 87

38. X-ray powder diffraction patterns for $[Pt_4(dmb)_4(PPh_3)_2]Cl_2$ and its polymer 91

39. The concentration dependence of the viscosity number at low concentrations 93

40. MO correlation diagram between the $[\bullet Pt_2(CNR)_4(PH_3)]^+$ and $[\bullet Pt(CNR)_2(PH_3)]^+$ fragments 96

41. Plot of the total EHMO energy vs the twist angle for $[Pt_4(CNCH_3)_8(PH_3)_2]^{2+}$ 98

42. Absorption spectrum of $[Pt_4(dmb)_4(PPh_3)_2]Cl_2$ in ethanol at 77 K 99

43. Emission spectrum of $[Pt_4(dmb)_4(PPh_3)_2]Cl_2$ in ethanol at 77 K 101

44. Crystal structure of $[Pd_2(dmb)_4(\mu_2\text{-}Cl)](TCNQ)_4$ 107

45. Crystal structure of polymer $\{[Pd_4(dmb)_5](CH_3COO)_2\}_n$ 111

46. FT-Raman spectrum for $[Pd_4(dmb)_4(PPh_3)_2]Cl_2$ 115

47. UV-vis spectra of $[Pd_4(dmb)_4(PPh_3)_2]^{2+}$ and polymer $\{[Pd_4(dmb)_5]^{2+}\}_n$ in butyronitrile at 77 K 118

48. UV-vis spectra of $[Pd_4(dmb)_4(PPh_3)_2]Cl_2$ in butyronitrile vs temperature. 121

49. Variation of ν_{max} of the lowest energy band vs temperature 122

50. The second moment plot of the lowest energy band for $[Pd_4(dmb)_4(PPh_3)_2]Cl_2$ in butyronitrile 124

51. The emission spectrum of $[Pd_4(dmb)_4(PPh_3)_2]Cl_2$ in ethanol at 77 K 128

52. Mass FAB spectrum of $[Pt_2Au_2(dmb)_2(PPh_3)_4](PF_6)_2$ 132

53. Crystal structure of $[Pt_2Au_2(dmb)_2(PPh_3)_4](PF_6)_2$ 134

54. ^{31}P NMR spectra of $[Pt_2Au_2(dmb)_2(PPh_3)_4](PF_6)_2$ in CD_2Cl_2 138

55. FT-Raman spectrum of $[Pt_2Au_2(dmb)_2(PPh_3)_4](PF_6)_2$ 139

56. Absorption spectra of $[Pt_2Au_2(dmb)_2(PPh_3)_4](PF_6)_2$ in butyronitrile at 298 and 77 K . 141

57. The excitation and emission spectra of $[Pt_2Au_2(dmb)_2(PPh_3)_4](PF_6)_2$ 142

LIST OF SCHEMES

I. Molecular structures of the 58-CVE clusters 54

II. C_3-rotation fluxional process 62

III. Proton labelling for ^1H NMR analysis 63

IV. Conformers 1 (H_a', H_b') and 2 (H_a, H_b) 63

V. Interactions between $Pt(AsH_3)_2^{2+}$ and the $Pt_3(\mu_2\text{-}CO)_3(AsH_3)_5$ center 68

VI. Qualitative scheme for the interacting MO's for fragment A and B 68

VII. Synthetic route to $[Pt_4(dmb)_4(PPh_3)_2]Cl_2$ 73

VIII. Side by side interaction between two square planar $\bullet ML_3$ fragments 94

IX. A frontier orbital (a_1 symmetry) of the $\bullet Pt(CNR)_2(PH_3)^+$ fragment 95

X. Synthetic route to $[Pd_4(dmb)_4(PPh_3)_2]Cl_2$ 104

XI. U- and Z-shaped conformations of dmb 110

INTRODUCTION

Clusters can be considered as a group metal core encompassed by ligands or small pieces of metal with chemisorbed species on the periphery. This kind of complexes represent an intermediate state between simple complex containing only one metal atom and bulk metal, where a group of metal atoms are separated by distances that approximate to those found in the bulk metals. The related chemistry has developed rapidly over the past several decades due to the following reasons (1, 2, 3): a) The clusters adopt a bewildering variety of structures. Up to now, a very large number of clusters have been prepared, and the crystal structures of many clusters have been measured. The structures of clusters can be very complicated. The interesting features are, what factors control the structures, and what size the clusters can achieve; b) The physical properties of clusters are very different from those of bulk metals, even supramolecular clusters containing very high nuclearity of metal atoms. For example, most clusters are "fragile". Is it possible that, if the size of cluster is large, the clusters can behave as bulk metals, having the metallic properties? c) Clusters have important catalytic properties, and this chemistry may provide valuable insight into chemisorption and catalysis on metal surfaces (4). Although cluster structures may be very complex, the most recurrent structural feature in clusters is the triangular unit M_3. The complex clusters can be thought as the assemblies of this "building block". This simple unit, trinuclear complexes M_3, can react with many kinds of substrates as Lewis acids or bases to give rich chemistry (5).

For platinum and palladium, there is a long standing interest in their clusters due to their intriguing metal-metal bonding and excellent catalytic properties (2, 4, 5, 6). The simple mimic of metal surface, which has been intensively studied in the past two decades, is platinum(I) and palladium(I) dimer, in which two metal atoms are locked together to form a strong metal-metal bond by two dppm ligands (bis(diphenylphosphino)methane), $[M_2(dppm)_2X_2]$ (M = Pt, Pd; X = Cl, Br, I). The most standard reaction is that small molecules, such as CO, SO_2, S, CH_2 or CS_2, RC≡CR, can insert to metal-metal bond to form "A-Frame" complexes and be

activated (6, 7, 8). Later, the interest shifted to trinuclear clusters M_3, which would be a better model of metal surface. Puddepphatt and coworkers synthesized the "open-face" unsaturated dppm-bridged triangular platinum and palladium clusters, $[M_3(dppm)_3(CO)]^{2+}$ (9, 10, 11). They found that many kinds of substrates, including anions, neutral molecules (Cl^-, S^{2-}, CS_2, RC≡CR, etc.), and even metal atoms with d^{10} electronic configuration (Ag^+, Au^+, Hg, Pt, etc.), can be added to the triangular face formed by three metal atoms (9). The crystallographic studies revealed that three metal atoms are encircled by a cylindrical array of six phenyl groups. Therefore these systems can also be considered as bifunctional recognition hosts because of the different properties of M_3 center and phenyl groups. P. D. Harvey's group systematically studied the guest-host chemistry of this novel bowl-shaped host system both in ground and excited states (12, 13), measuring the competitive binding constants with different kinds of substrates, including salts and neutral molecules. This chemistry is related to the charge, ligand behavior, the size and the hydrophobic properties of the substrates. This knowledge is essential to understanding the catalytic processes on the surface of bulk metals.

In cluster chemistry, most of clusters adopt triangular and polyhedral structures. Recently, there are considerable interests in polynuclear clusters containing metal-metal chain for both chemists and material scientists, because of the metal-metal bonding in linear metal chain, the potential application as molecular wires and unusual properties of low-dimensional materials (14, 15, 16). It is well known that, in mixed oxidation states, rhodium atoms have a strong tendency to aggregate to form oligomeric complexes containing metal-metal chain, even infinite chain (16, 17). In the platinum and palladium chemistry, the most famous examples are the inorganic conducting polymers called the Krogmann's salts, in which the square-planar d^8 platinum atoms form infinite linear metal-metal chain across the crystal through overlapping of p_z or d_{z2} orbitals (18, 19). In the low oxidation states, there is also a strong tendency to form metal-metal bonds, but these linear complexes are generally constructed with the help of bridging or polydentate ligands (20, 21). However in some cases, such as in $[Pd_2(CNCH_3)_6]^{2+}$, there is an unsupported Pd-Pd bond (22). Later this metal-metal bond was extended by a

direct reaction of $[Pd_2(CNCH_3)_6]^{2+}$ with $Pd(CNCH_3)_x$ in the presence of an excess of isocyanide ligand, to give a linear trinuclear complex, $[Pd_3(CNCH_3)_8]^{2+}$, in which two unsupported metal-metal bonds occur. This trinuclear complex is more reactive than the dimer (Figure 1) (23). Recently $[Pd_3(PPh_3)_4]^{2+}$ was reported, which also contains trinuclear linear chain (24). The platinum analogue, $[Pt_3(CNCH_3)_8]^{2+}$, was synthesized by electrochemical reduction of the corresponding monomer, $[Pt(CNCH_3)_4]^{2+}$ (25). The remarkable features of these complexes are the short metal-metal bonds, 2.5921 (5) Å for Pd-Pd bond and 2.6389 (7) Å for Pt-Pt bond, respectively, indicating the strong interaction between metal atoms. The extensive investigations have been performed in order to prepare longer Pt and Pd chain complexes in the low oxidation states, but no progress has been made so far.

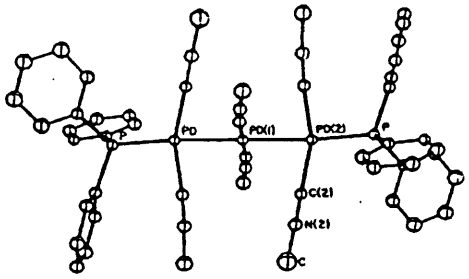

Figure 1. Crystal structure of $[Pd_3(CNCH_3)_6(PPh_3)_2]^{2+}$(taken from reference 23).

It is well known that, isocyanide ligands are good reagents to stablize the Pt and Pd atoms in the low oxidation states, and play an important role in the formation of linear chain complexes (22, 23, 24). Diisocyanide ligands, e.g. dmb, were also explored in order to prepare dinuclear or polymeric complexes (16, 20, 26, 27, 28, 29). The most interesting features are: 1) a wide range of the bite distances is known; 2) dmb ligand also has the ability to encapsulate metal atoms to form linear trinuclear metal atom chain (30). This gives us an expectation that, it is possible to build longer chain complexes for Pt and Pd, if dmb is used as a ligand based upon its encapsulating ability, also considering the fact that Pt(0) can insert to Pt(I)-Pt(I) bond to form triplatinum "A-Frame" complexes (25).

In our laboratory, there are strong interests in Pt and Pd complexes, especially diphosphine and diisocyanide complexes of these metals, because of their interesting metal-metal bonding and potential applications in catalysis (12, 13, 20, 28, 31). In this project, two kinds of ligands are continued to be used to design and synthesize a series of new Pt and Pd complexes based on different purposes:

1. It is reported that the "open-face" unsaturated triangular Pt or Pd clusters can be considered as novel host systems, for examples, $[M_3(dppm)_3CO]^{2+}$ clusters (12, 13). But the effect of host system on this chemistry remains to be explored. To design modified host system, diarsine ligand, dpam (instead of dppm) will be used as a ligand to synthesize new clusters. It is expected that, compared to the dppm analogue, the size of the cavity will be large, because the distance of M-As bond is longer than that of M-P bond. How does the size of the cavity have an influence upon host-guest chemistry? Secondly, for the ^1H NMR analysis of the dpam species, since As atoms will not couple with the H atoms because of its high quadrupolar moment, their ^1H NMR signals will be much simpler than that of the dppm systems. This will be beneficial to study the behaviors or structures of clusters in solutions.

2. Construction of linear chain complexes will be explored because of their interesting polynuclear metal-metal bonding, and their applications as molecular wires and low dimensional materials. The design and preparation of new and longer metal-metal chain complexes are anticipated, and based upon that, the development of new low-dimensional materials are aimed. In this section, the diisocyanide ligand, dmb, will be used as a bridging ligand to prepare linear chain complexes. Because Pt and Pd complexes in the low oxidation states are very reactive (32, 33, 34), the chemistry of Pt or Pd and dmb complexes in low oxidation states will be investigated.

CHAPTER 1
THEORY

1.1 Binding constants and UV-vis spectrophotometry

1.1.1 The equilibrium constant

Considering the three simplest complex stoichiometries: SL, SL_2, and S_2L, it is chemically reasonable to assume that every complex is formed in a bimolecular process, so these complexes are related by the following equilibria:

$$S + L = SL$$
$$SL + L = SL_2$$
$$SL + S = S_2L$$

The stepwise binding constants are defined as:

$$K_{11} = \frac{[SL]}{[S]\,[L]} \qquad [1.1]$$

$$K_{12} = \frac{[SL_2]}{[SL]\,[L]} \qquad [1.2]$$

$$K_{13} = \frac{[S_2L]}{[S]\,[SL]} \qquad [1.3]$$

Any complex of the type S_mL_n can be constructed in this manner. The formation reaction of higher complexes directly from the substrate and ligand can be written as:

$$mS + nL = S_mL_n$$

and the expression for the overall binding constant is defined as:

$$K_{11} = \frac{[S_mL_n]}{[S]^m[L]^n} \qquad [1.4]$$

1.1.2 Model

A potential model for this chemistry is built upon a hypothesis. Let m be the maximum number of binding sites on ligand L, with h the number of occupied sites; thus h = 1, 2, 3, ···, m; similarly, n is the maximum number of binding sites on substrates S, with i = 0, 1, 2, ···, n being the corresponding running index. Then the basic statement of a stoichiometric model involves the values of m and n.

The mass balance expressions of S and L can be defined, where S_t and [S] represent total and free substrate concentrations, respectively, and similarly for ligand, all concentrations being on the molarity scale:

$$S_t = [S] + \sum_{\substack{h=1 \\ i=1}}^{m,\,n} h[S_hL_i] \qquad [1.5]$$

$$L_t = [L] + \sum_{\substack{h=1 \\ i=1}}^{m,\,n} i[S_hL_i] \qquad [1.6]$$

Equations (1.5) and (1.6) are not completely general, because they do not include provision for dimers, trimers, and so on, of S and L, but these can be added as necessary.

As one measure of extent of binding, $\bar{i}$ is defined as the average number of ligand molecules bound per molecule of substrate, or

$$\bar{i} = \frac{\Sigma(\text{bound to S})}{\Sigma\,(\text{all S})} = \frac{L_t - [L]}{S_t} \qquad [1.7]$$

In the form of species S_hL_i, the fraction of substrate f_{hi} is defined as:

$$f_{hi} = \frac{h[S_hL_i]}{S_t} \qquad [1.8]$$

so that

$$\sum_{\substack{h=1 \\ i=1}}^{m,\,n} f_{hi} = 1 \qquad [1.9]$$

and $f_{10} = [S]/S_t$, the fraction of free substrate. Choosing the important special case m = 1, the following expression is given by:

$$\bar{i} = \sum_{i=1}^{n} i f_{1i} \qquad [1.10]$$

The development of a model into a useful and testable form involves converting this basic model into a functional relationship called the *binding isotherm*.

1.1.3 The binding isotherm

The simplest of these models, namely, 1:1 complex formation will be treated. This is the most important isotherm, first because it is often applicable to real systems (it will be used to measure the binding constants in this research project.), and second because many other systems can be viewed as extensions of, or deviations from, this simple case.

In its simplest form the isotherm for 1:1 binding is given by:

$$f_{11} = \frac{K_{11}[\mathrm{L}]}{1 + K_{11}[\mathrm{L}]} \qquad [1.11]$$

For generality, the function can be written as Eq. 1.12:

$$\mathrm{y} = \frac{d\mathrm{x}}{f + e\mathrm{x}} \qquad [1.12]$$

where y is the dependent variable, x is the independent variable, and d, e, f are constants or parameters (Figure 2).

There are three nonlogarithmic linear plotting forms of the rectangular hyperbola. From Eq. 1.12, the following equation can be obtained:

$$\frac{1}{\mathrm{y}} = \frac{f}{d} \times \frac{1}{\mathrm{x}} + \frac{e}{d} \qquad [1.13]$$

A plot of 1/y against 1/x is linear (double-reciprocal plot) (Figure 3).

Equation 1.12 also yields:

$$\frac{x}{y} = \frac{e}{d} \times x + \frac{f}{d} \qquad [1.14]$$

This equation is called the y-reciprocal plot (Figure 4).

The third linear form is called the x-reciprocal plot (Figure 5):

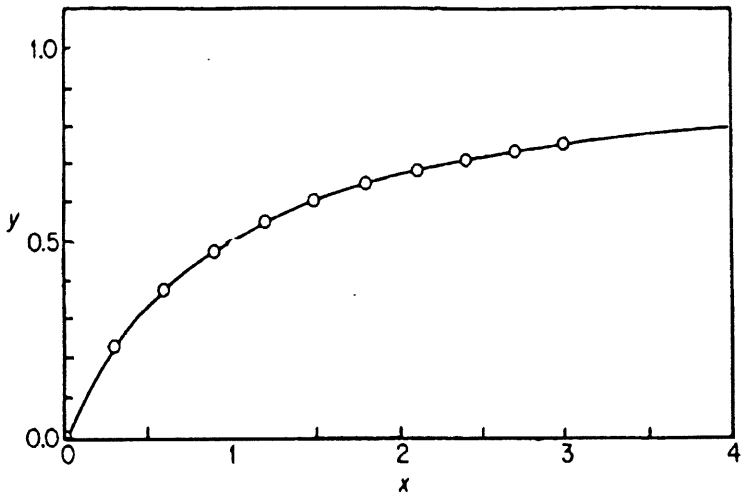

Figure 2. Direct binding curve plot (Eq. 1.12) (taken from reference 35).

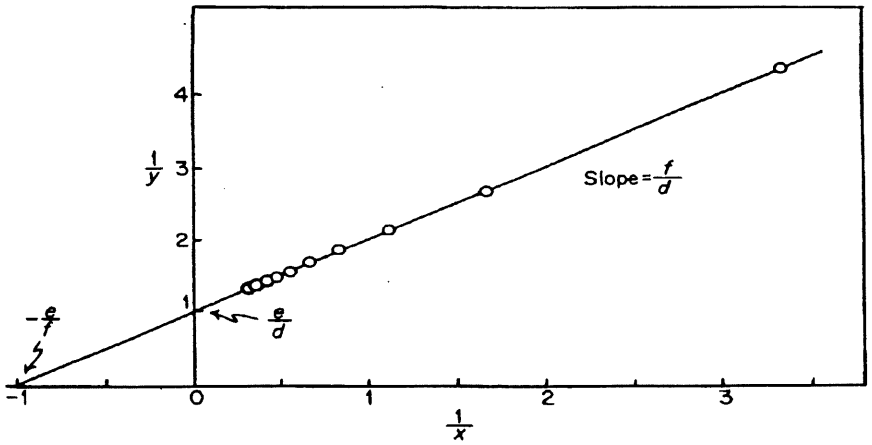

Figure 3. Double-reciprocal plot (Eq. 1.13) (taken from reference 35).

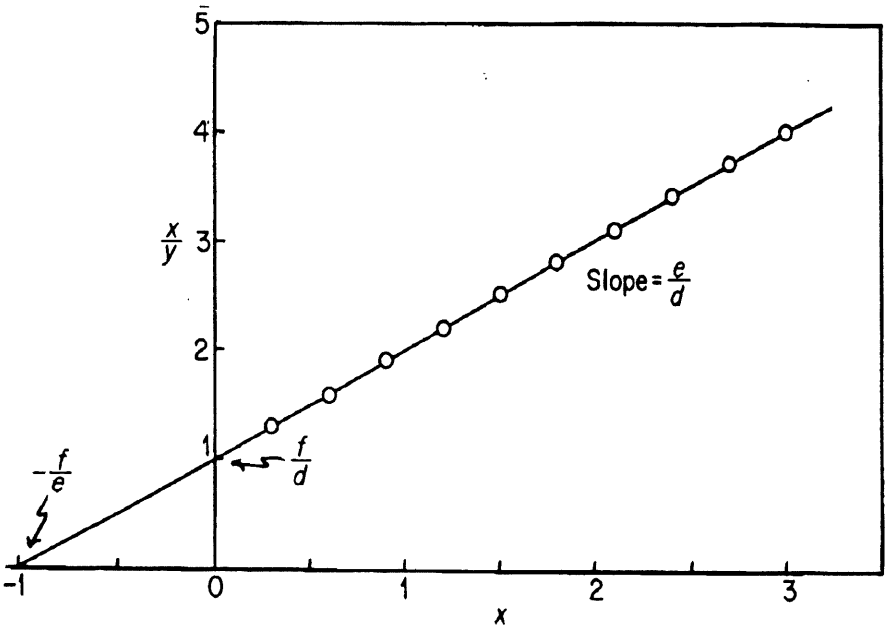

Figure 4. y-Reciprocal plot (Eq. 1.14) (taken from reference 35).

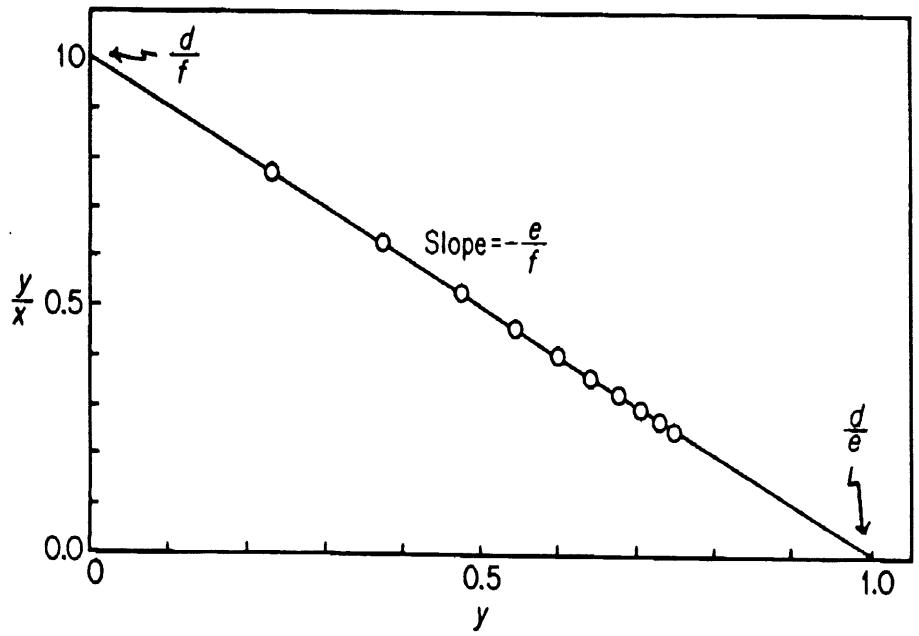

Figure 5. x-Reciprocal plot (Eq. 1.15) (taken from reference 35).

$$\frac{y}{x} = \frac{e}{f} \times y + \frac{d}{f} \qquad [1.15]$$

These three linear plotting forms are not equivalent in an experimental sense, and there is continuing controversy about their advantages and limitations. The salient features are as follows: When the values of the independent variable x are chosen to be equally spaced, the linearization transformation can change this relationship. The double-reciprocal plot is notorious for this effect (Figure 3). It is shown that the points at low x are widely spaced, with those at high x being closely bunched. The results is that the placement of the line is extremely sensitive to the y value of the point having the smallest x. The double-reciprocal plot has the advantage that the variables x and y remain separated on the abscissa and ordinate; in the other plotting forms the variables become mixed. This is important because the uncertainty in the dependent variable y is usually much greater than that in the independent variable. Equations 1.13 and 1.14 have the advantage that the dependent variable appears only on the ordinate, so the uncertainty of the abscissa values is negligible, and this simplifies the statistical analysis. In the y-reciprocal plot, the equal spacing of x values is retained (Figure 4). The x-reciprocal plot (Figure 5), has the dependent variable on both axes, but it has an advantage in that it provides a closed scale representation of y on the abscissa, unlike the other two plots, which are open-ended (35).

Consider a two-state system whose two states have different absorption spectra. If the spectra, expressed on a molar basis, are superimposed, and if they intersect, then evidently the spectrum of any mixture of the two states, also expressed on a molar basis, will pass through the point of intersection. This point of common absorption intensity is called an isosbestic point. Figure 6 shows an isosbestic point of a typical two-state system. It is possible for a two-state system to exhibit more than one isosbestic point, or even no such point if the spectra nowhere intersect. But if there is an intersection of any two members of such a family of

spectra, and if the system possesses just two states, all possible members must pass through the isosbestic point.

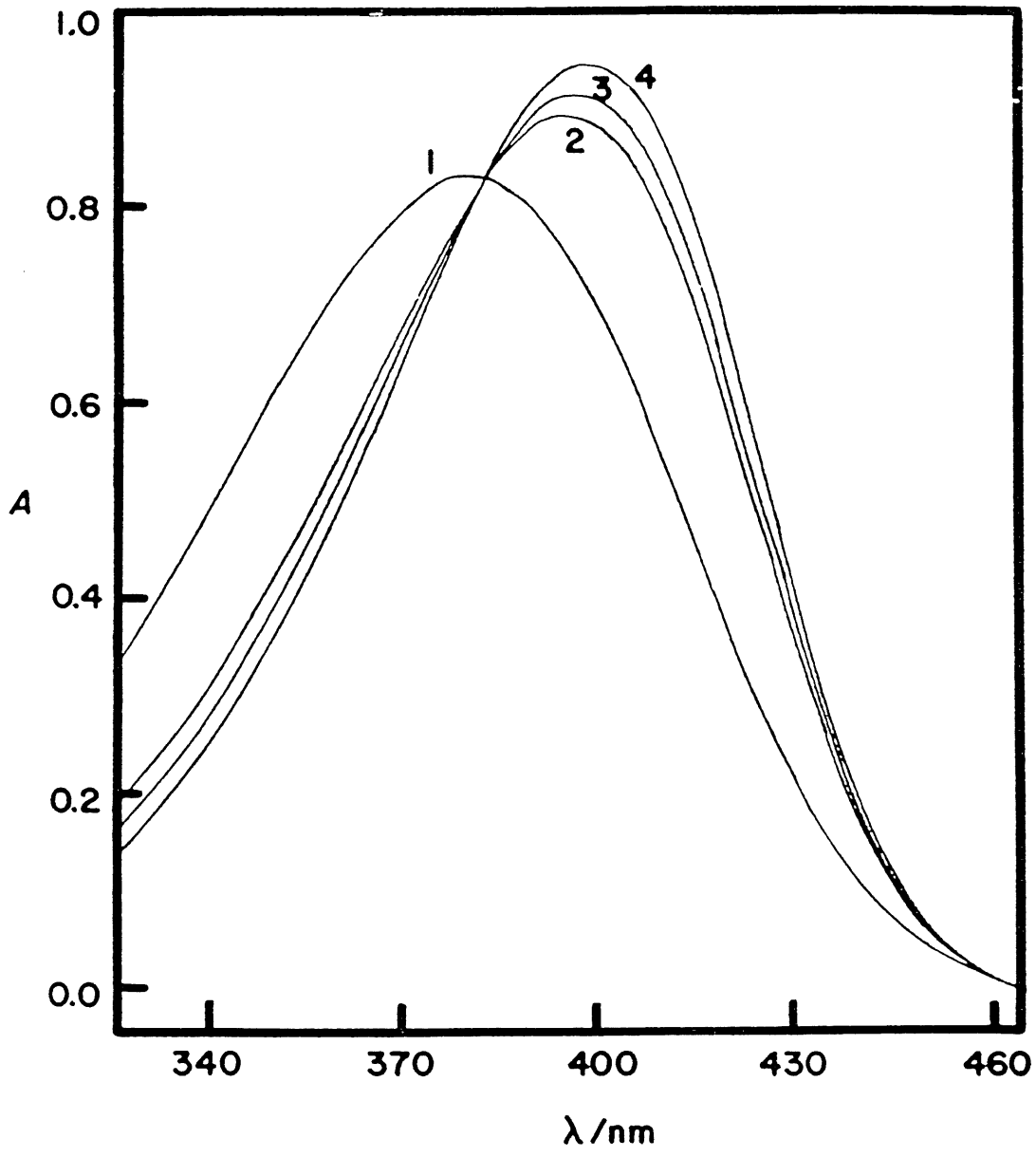

Figure 6. Typical absorption spectrum of a 1:1 complexing system (taken from reference 35).

In making use of this spectral property, it is noted that, if an isosbestic point is observed over a wide range of composition, it can be concluded that the system has just two states; in other words, only one complex is formed. The corollary is that if two spectra of a family intersect, but not all of the spectra pass through a common point, the system must possess more than two states, that is, more than one complex stoichiometry. These conclusions are based upon the assumption that the observed spectral shifts are ascribable entirely to the changes in concentrations of the absorbing species as the ligand concentration is changed; that is, it is assumed that the spectral characteristics of the absorbing species are constant, unaffected by the inevitable changes in solution composition. However it is possible that, a system possesses only two states, but fail to exhibit a sharp isosbestic point if a spectral solvent dependence were operative, or even though the system possesses more than two states, the effects may combine to generate an isosbestic point. Isosbestic point observations constitute only one piece of evidence in the study of a complexing system.

In a system, a single 1:1 complex SL is formed, with the complex and the free substrates S having significantly different absorption spectra. It is assumed that Beer-Lambert law is followed by all species. A wavelength is selected at which the molar absorptivities ε_s and ε_{11} are different. At total concentration S_t of substrate, in the absence of ligand, the solution absorbance is given by the Beer-Lambert law:

$$A_o = \varepsilon_s l S_t$$

In the presence of ligand at total concentration L_t, the absorbance of a solution containing the same total substrate concentration is now:

$$A_L = \varepsilon_s l[S] + \varepsilon_L l[L] + \varepsilon_{11} l[SL]$$

which combined with the mass balances on S and L, gives:

$$A_L = \varepsilon_s l S_t + \varepsilon_L l L_t + \Delta\varepsilon_{11} l [SL]$$

where $\Delta\varepsilon_{11} = \varepsilon_{11} - \varepsilon_s - \varepsilon_L$. By measuring the solution absorbance against a reference containing ligands at the same total concentration L_t, the measured absorbance becomes:

$$A = \varepsilon_s l S_t + \Delta\varepsilon_{11} l [SL] \qquad [1.16]$$

Combining Eq. 1.16 with the stability constant definition, $K_{11} = [SL]/[S][L]$, gives

$$\Delta A = K_{11} \Delta\varepsilon_{11} l [S][L] \qquad [1.17]$$

where $\Delta A = A - A_o$. From the mass balance expression $S_t = [S] + [SL]$ or $[S] = S_t/(1+K_{11}[L])$, Eq. 1.18 can be obtained as the relationship between the observed absorbance change per centimeter, and the system variables and parameters.

$$\frac{\Delta A}{l} = \frac{S_t K_{11} \Delta\varepsilon_{11} l [L]}{1 + K_{11}[L]} \qquad [1.18]$$

This equation is the binding isotherm, which shows the hyperbolic dependence on free ligand concentration. It must be noted that the reference solution contains the same total ligand concentration L_t as the sample solution.

Eq. 1.18 can be used to describe the spectral data for a 1:1 complexing system. The double-reciprocal form of plotting the rectangular hyperbola (Eq. 1.13) is based on the linearization of Eq. 1.18 according to Eq. 1.19.

$$\frac{l}{\Delta A} = \frac{1}{S_t K_{11} \Delta\varepsilon_{11} [L]} + \frac{1}{S_t \Delta\varepsilon_{11}} \qquad [1.19]$$

Equation 1.19 is called the Benesi-Hildebrand equation. The plot of $1/\Delta A$ against $1/[L]$ is linear. The parameters are evaluated from this plot according to the following equations.

$$K_{11} = \frac{\text{(y-intercept)}}{\text{(slope)}} \qquad [1.20]$$

$$\Delta\varepsilon_{11} = \frac{1}{S_t(\text{y-intercept})} \qquad [1.21]$$

The y-reciprocal form is Eq. 1.22, called the Scott equation.

$$\frac{l\,[L]}{\Delta A} = \frac{[L]}{S_t\Delta\varepsilon_{11}} + \frac{1}{S_tK_{11}\Delta\varepsilon_{11}} \qquad [1.22]$$

The parameters are given by:

$$K_{11} = \frac{\text{(slope)}}{\text{(y-intercept)}} \qquad [1.23]$$

$$\Delta\varepsilon_{11} = \frac{1}{S_t(\text{slope})} \qquad [1.24]$$

The x-reciprocal form is written as:

$$\frac{\Delta A}{l[L]} = -\frac{K_{11}\Delta A}{l} + S_tK_{11}\Delta\varepsilon_{11} \qquad [1.25]$$

It is called a Scatchard plot. The parameters are evaluated with Eqs. 1.26 and 1.27.

$$K_{11} = -\,(\text{slope}) \qquad [1.26]$$

$$\Delta\varepsilon_{11} = \frac{(\text{x-intercept})}{S_t} \qquad [1.27]$$

In the experiment for the 1:1 case, the fixed wavelength is usually chosen so as to give the largest possible values of ΔA, and the range of L_t should be as large as is permitted by the experimental situation. It must be noted that, linear plotting of spectral data yields estimates of the product $K_{11}\Delta\varepsilon_{11}$ that are more reliable than are the separate parameters K_{11} and $\Delta\varepsilon_{11}$, especially for weak complexes. In the double-reciprocal plot, the product is obtained from the slope, whereas the intercept gives $\Delta\varepsilon_{11}$, and K_{11} is obtained by a combination of these results. In the other linear forms, the product $K_{11}\Delta\varepsilon_{11}$ is obtained from an intercept. In linear plotting, a slope is usually estimated more reliable than is an intercept, because an intercept requires extrapolation, often over long distances; moreover, an intercept close to the origin may have a high relative error. It is helpful to make use of more than one of the linear plots, seeking estimates of K_{11} and $\Delta\varepsilon_{11}$ that are consistent with all of the plots and placing emphasis on the graphical features that are most reliably estimated.

1.2 X-ray diffraction

1.2.1 Single crystal X-ray diffraction

X-rays are electromagnetic radiations with wavelengths of about 10 Å. When the rays pass through a crystal, the diffraction will happen because their wavelengths are comparable to the separation of lattice planes.

In Figure 7, it is shown that the path-length difference of the two rays can be given by:

$$AB + BC = l = 2d \sin\theta$$

d — separation of lattice planes; θ — glancing angle

When l is not an integral number of wavelengths, the waves interfere destructively; when l is an integral number of wavelengths, $l = n\lambda$, the reflected waves are in phase and interfere constructively, and the Bragg Law is satisfied:

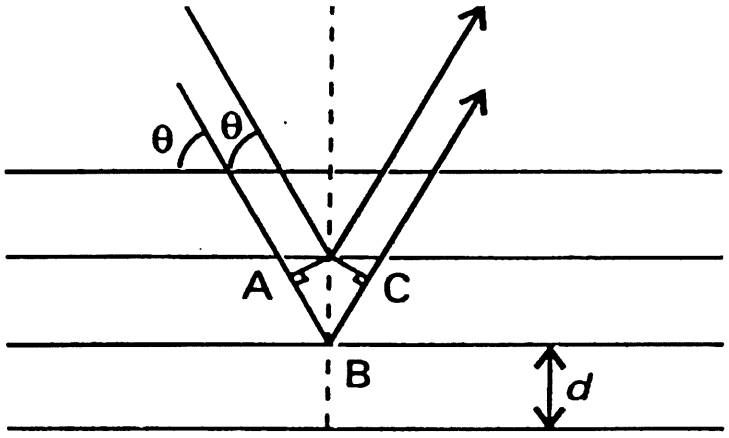

Figure 7. The conventional derivation of the Bragg law treats each plane as reflecting the incident radiation (taken from reference 36)

$$\lambda = 2d \sin\theta \qquad [1.28]$$

Here, d is the separation of the (n*h*, n*k*, n*l*) planes, and relates with

$$\frac{1}{d^2_{hkl}} = \frac{h^2}{a^2} + \frac{k^2}{b^2} + \frac{l^2}{c^2} \qquad [1.29]$$

where a, b, c are the lengths of the three sides of the unit cell, and *h k l* are the Miller indices of the diffracting planes.

Computing techniques are applied to this area, which lead to automated indexing and to the automated determination of the shape, symmetry, and size of the unit cell. Four-circle diffractometer is the most common instrument to determine the structure of single crystals. The computer determines the settings of the diffractometer's four angles (ϕ, χ, ω, 2θ), which are used to adjust the orientation of the crystal and counter so as to bring any desired plane into a reflecting position and detect this reflection. The diffraction intensity is measured to each setting and background intensities are assessed by making measurements at slightly different settings.

X-ray are scattered by the electrons in crystals. Because both the number of electrons and the size of the atomic orbitals vary from atom to atom, different atoms have different scattering efficiencies. The scattering factor of an atom, f, is defined by:

$$f = 4\pi \int \rho(r) \frac{\sin kr}{kr} r^2 \, dr \qquad [1.30]$$

where $\rho(r)$ is the spherically symmetric electron density (number of electrons per unit volume) of the atom and $k = (4\pi/\lambda)\sin\theta$, where θ is the scattering angle and λ is the wavelength of the X-radiation.

It is known that the intensity of a diffraction spot from a crystal is proportional to the square of the magnititude of the structure factor,

$$I \propto |F(hkl)|^2$$

For a unit cell that contains atoms of type *i* located at points x_i, y_i, and z_i, structure factor is defined by:

$$F(hkl) = \sum_i f_i e^{2\pi i(hx_i/a + ky_i/b + lz_i/c)} \qquad [1.31]$$

where f_i is the scattering factor of an atom of type *i*.

The details of electron distribution inside a unit cell are contained in the structure factors. The electron density in the unit cell is constructed by using the relation:

$$\rho(r) = \frac{1}{V} \sum_{hkl} F_{hkl} e^{-2\pi i(hx_i/a + ky_i/b + lz_i/c)} \qquad [1.32]$$

where V is the volume of the unit cell.

Experimental diffraction patterns gives I_{hkl}. So $|F(hkl)|^2$ can be obtained. The problem is in fact that F_{hkl} is not determined, hence $\rho(r)$ is also not determined as well. This is called the phase

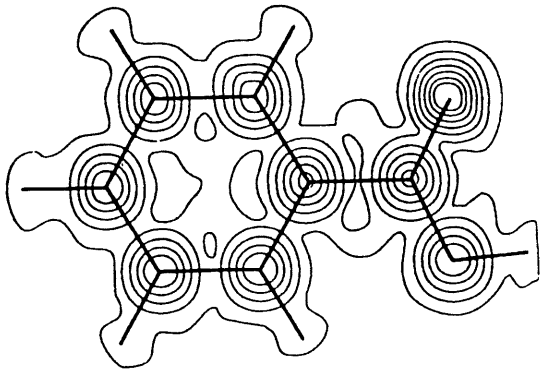

Figure 8. An electron-density map of a benzoic acid molecule determined from the X-ray diffraction pattern of a benzoic acid crystal. Each contour line corresponds to constant value of the electron density (taken from reference 37).

problem. If this problem is solved, then the electron density can be calculated (Figure 8). The positions of the nuclei are readily deduced from the electron density map, from which bond length and bond angle information can be determined (36, 37).

1.2.2 X-ray powder diffraction

Consider that the powder is just a collection of many small crystals. At least some of the crystallites will be orientated so as to satisfy the Bragg condition for each set of plane (*hkl*). The major use of X-ray powder diffraction is for the identification of samples, especially those compounds which have similar structures, by comparison (38).

This method is very useful in determination of the crystallinity of the polymer sample since polymers exhibit structures covering the entire range from amorphous to crystalline states (39).

1.3 Nuclear magnetic resonance

1.3.1 Energies of nuclei in magnetic field

For a nucleus with non-zero spin, the z component, μ_z, of a magnetic moment depends upon the orientation of the spin,

$$\mu_z = \gamma \hbar m_I \qquad [1.33]$$

where γ is the magnetogyric ratio of the nucleus. The magnetic moment is also expressed in terms of the nuclear g-factor g_I and the nuclear magneton μ_N:

$$\gamma \hbar = g_I \mu_N$$

In Eq. 1.33, each value of m_I corresponds to a different orientation of the nuclear magnetic moment. In a magnetic field B, the $2I + 1$ orientations of the nucleus have different energies given by:

$$E_{mI} = -\mu_z B = -\gamma \hbar B m_I \qquad [1.34]$$

or in terms of the Larmor frequency ω ($\omega = -\gamma B$),

$$E_{mI} = -m_I \hbar \omega$$

The energy separation of the two states of spin-1/2 nuclei is

$$\Delta E = E_\beta - E_\alpha = \gamma \hbar B \qquad [1.35]$$

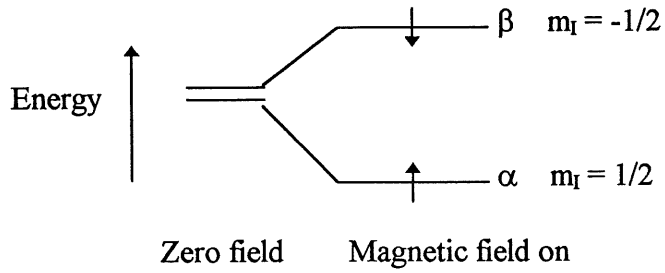

Figure 9. The nuclear spin energy levels of a spin-1/2 nucleus in a magnetic field.

The β state lies above the α state, so there are more α spins than β spins. If the sample is put in radiation of frequency ν, the energy separations come into resonance with the radiation when the frequency satisfies the resonance condition:

$$h\nu = \gamma \hbar B \qquad [1.36]$$

1.3.2 Spin-lattice relaxation

1.3.2.1 Spin-lattice relaxation time (T_1)

The z component of magnetization, M(z), can be perturbed with the radio frequency pulse. In order for the spin system to return to equilibrium, there must be an interaction between the spins and the surroundings, or lattices, leading to a loss of the excess energy. At thermal equilibrium the spins have a Boltzmann distribution, with more α spins than β spins; after a 90° pulse, a magnetization vector in the xy plane immediately has equal number of α and β spins. The populations revert to their thermal equilibrium values exponentially

$$M_z(t) - M_z \propto e^{-t/T_1} \qquad [1.37]$$

The T_1, time constant, serves as a measure of the rate with which the spin system comes into equilibrium with its environment, called the spin-lattice relaxation time, since this relaxation process involves giving up energy to the surroundings (40, 41, 42, 43).

There are a number of mechanisms which can contribute to spin-lattice relaxation in a molecule. The most common of these along with their associated relaxation time are:

dipole-dipole	T_{1DD}
spin-rotation	T_{1SR}
quadrupolar	T_{1Q}
scalar	T_{1SC}
chemical shift anisotropy	T_{1CSA}

An overall spin-lattice relaxation time T_1 is given by:

$$\frac{1}{T_1} = \frac{1}{T_{1DD}} + \frac{1}{T_{1SR}} + \frac{1}{T_{1Q}} + \frac{1}{T_{1SC}} + \frac{1}{T_{1CSA}} \qquad [1.38]$$

1. Dipolar relaxation Any magnetic nucleus in a molecule supplies an instantaneous magnetic dipole field, which is proportinal to the magnetic moment of the nucleus. When the nucleus undergoing relaxation is directly bonded to a second nucleus possessing a magnetic spin, the

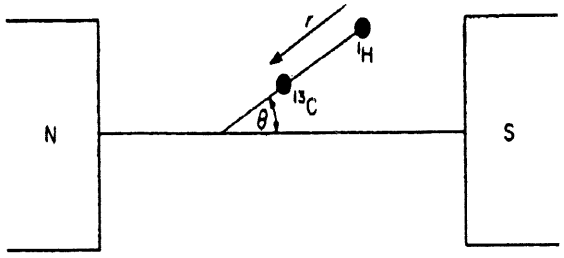

Figure 10. Orientation of the dipolar interaction relative to the magnetic field.

possibility of an efficient relaxation mechanism exists. Taking into account the specific case of a ^{13}C nucleus which is directly bonded to a proton, the two spins can each be considered as small dipoles located at the centre of the ^{13}C and ^{1}H atoms. Therefore the ^{13}C nucleus will experience a small field due to the dipolar interaction with the proton.

The magnetic field H_{DD} created at the ^{13}C nucleus is given by:

$$H_{DD} = \frac{\gamma_H h}{4\pi r^3}(3\cos^2\theta - 1) \qquad [1.39]$$

As the molecule tumbles in solution, the variation in θ will cause fluctuations in H_{DD}. Relaxation can be induced by any oscillating electric or magnetic field which has a component at, or close to, the Lamor frequency of the nucleus concerned. Consequently, the oscillations in H_{DD} constitute a possible relaxation mechanism. For most non-viscous solutions, the contribution made by this mechanism can be expressed as:

$$\frac{1}{T_{1DD}} = \frac{N\hbar^2\gamma_C^2\gamma_H^2}{10\,(r_{CH})^6}\left\{\frac{\tau_c}{1+(\omega_C-\omega_H)\tau_c^2} + \frac{3\tau_c}{1+\omega_C^2\tau_c^2} + \frac{6\tau_c}{1+(\omega_C+\omega_H)^2\tau_c^2}\right\} \qquad [1.40]$$

N is the number of hydrogens directly bonded to ^{13}C, ω is the Lamor frequency, and τ_c is the correlation time.

In large molecules with slow tumbling and long correlation times, short T_1 values are found, and dipole-dipole relaxation appears to predominate as long as no internal motion of molecular segments takes place. For ^{13}C nuclei which have no directly bonded protons, the dipolar relaxation for these carbons is less effective, leading to longer relaxation times.

2. Spin-rotation relaxation This arises due to fluctuating magnetic fields generated by the movement of atoms within the molecule and is normally only important for small highly symmetrical groups. For example, in the ^{13}C NMR spectrum of toluene, because of this relaxation, the methyl signal at high field is appreciably smaller than that of the other protonated carbons.

3. Quadrupolar relaxation This mechanism is important for nuclei with spin > 1/2. Such nuclei possess a quadrupole moment which gives rise to an electric field gradient at the nucleus, providing a highly efficient relaxation mechanism, both for themselves and for any neighbouring ^{13}C nuclei.

4. Chemical shift anisotropy relaxation The magnetic field at the nucleus is given by:

$$H = (1 - \sigma) H_0 \qquad [1.41]$$

where σ is the shielding factor. It is found that an anisotropy in σ may result in pronounced effects on chemical shifts, and may also furnish a mechanism for relaxation since as the molecule tumbles in solution, the field at the nucleus is continually changing in magnitude. The components of random tumbling motion at the Larmor frequency can then lead to spin-lattice relaxation.

If σ is axially symmetric, theory predicts that in the extreme narrowing limits usually found for small molecules, T_{1CSA} is given by:

$$R_1 = 1/T_{1CSA} = (2/15)\gamma^2 H_0^2 (\sigma^{//} - \sigma^{\perp})^2 \tau_c \qquad [1.42]$$

where $\sigma^{//}$ and $\sigma^{\perp}$ refer to the components of the shielding tensor parallel and perpendicular to the axis of symmetry. R_1 increases quadratically with increasing magnetic field. For ^{13}C, usually other relaxation mechanisms dominate.

5. Scalar relaxation Any process that gives rise to a fluctuating magnetic field at a nucleus might cause relaxation. When two nuclei *I* and *S* are spin-coupled, the value of J, the scalar spin-spin coupling constant, measures the magnitude of the magnetic field at nucleus *I* arising from the spin orientation of nucleus *S*. As *S* relaxes, *I* experiences a magnetic field fluctuation; Likewise if J changes, because of bond breaking in chemical exchange process, *I* experiences a similar fluctuation.

1.3.2.2 The measurement of T_1 by Fourier Transform Spectroscopy

The most common means of measuring T_1 is the inversion-recovery, or 180°-τ-90°, method. A 180° pulse first inverts magnetization from its equilibrium value of M_0 to $-M_0$. If the pulse is

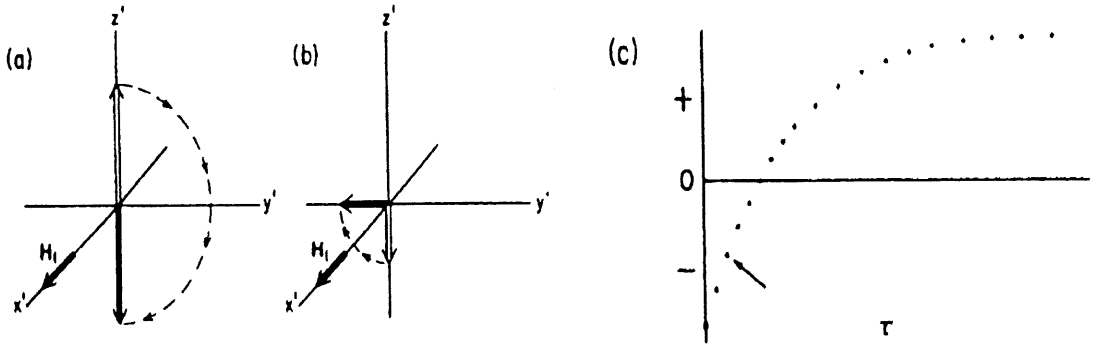

Figure 11. Determination of T_1 by the inversion-recovery method. (a) M is inverted by 180° pulse at time 0. (b) After a time interval τ, a 90° pulse rotates the remaining M to the xy plane. (c) The initial amplitude of the FID or the height of a given line in the Fourier transformed spectrum is plotted as a function of τ (taken from reference 39).

perfect, there is no xy magnetization and hence no singal will be detected. The magnetization will return from $-M_0$ to the equilibrium value of M_0 at the spin-lattice relaxation rate (R_1). If at a time τ after the 180° pulse, a 90° pulse is applied, magnetization will be forced to appear in the xy plane so that the relaxation of this magnetization can be monitored. A free induction decay results, the initial height of which is proportional to the magnitude of M (magnetization), hence to the value of M_z, at the time t. If the system is allowed to return to equilibrium by waiting at least five times T_1 and the 180°-τ-90° sequence repeated for a different value of τ, the decay rate of M_Z can be established (Figure 11).

1.3.3 The relation between T_1 and molecular dimension

In equation 1.40, τ_c is the correlation time, which is related to the molecular dimensions. For the spherical model, the equation is the following (Stoke-Debye-Einstein):

$$\tau_c = 4\pi a^3 \eta / 3kT \qquad [1.43]$$

where a is the radii of the molecule, k is the Boltzmann constant, η is the viscosity of the medium, and T is the temperature.

If in the compounds, T_1 is dominated by dipole-dipole interactions, according to Eq. 1.40, τ_c can be calculated. By replacing $4\pi a^3/3$ by $\pi a^2 l$ where l is the length of a cylindrical molecule, the length of molecule, l, can be estimated approximately by the following equation (26, 36):

$$\tau_c = \pi a^2 l \eta / kT \qquad [1.44]$$

1.4 Photophysical concepts

1.4.1 Jablonski diagram

Absorption of a photon (quantum) of light can significantly excite a particular bond or group in a given molecule. The various intramolecular processes initiated by light absorption are illustrated schematically in Figure 12 (44). In this diagram, the electronic states are represented by heavy horizontal lines; the symbols S_0, S_1 and S_2 represent the ground state, first and second excited singlet states, respectively, and T_1 and T_2 represent the triplet states.

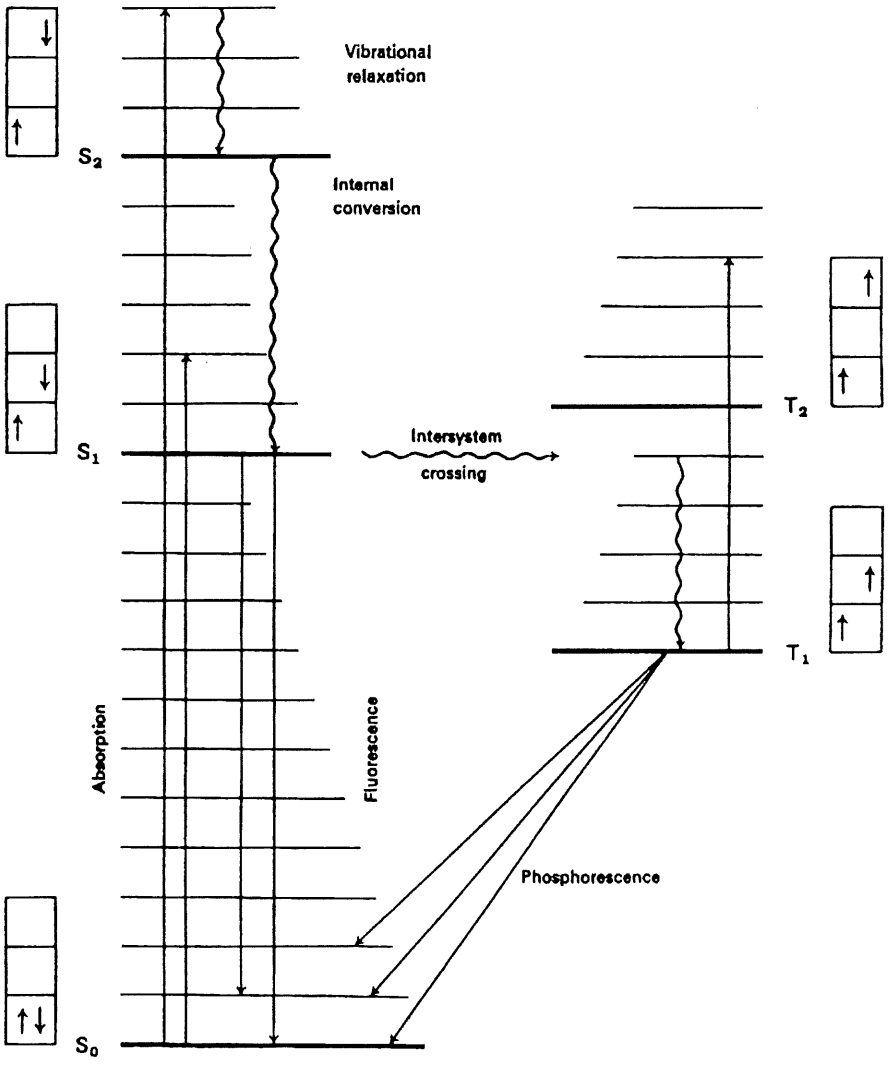

Figure 12. Jablonski diagram (taken from reference 44).

1.4.2 The Franck-Condon principle

The relative intensities of the vibrational parts of an electronic absorption or emission are rationalized by the Franck-Condon principle: electronic transitions are so fast (10^{-15} sec) in comparison with nuclear motion (10^{-12} sec) that immediately after the transition, the nuclei have nearly the same relative position and velocities as they did just before the transition. This implies that the initially formed excited state must have the same geometry as the ground state (Figure 13). For all the points along the curve the nuclei of the molecule are motionless. The horizontal lines in the wells of these potential curves represent the vibrational levels of the states. At room temperature (25 C°), most but not all of the molecules of interest will be in their lowest vibrational level; therefore excitation will occur from this level. Since the geometry can not change during excitation, the molecule must find itself with the same internuclear distances after light absorption as it had before (Franck-Condon principle). This corresponds to the vertical arrow in Figure 13 and is termed a vertical or Franck-Condon transition.

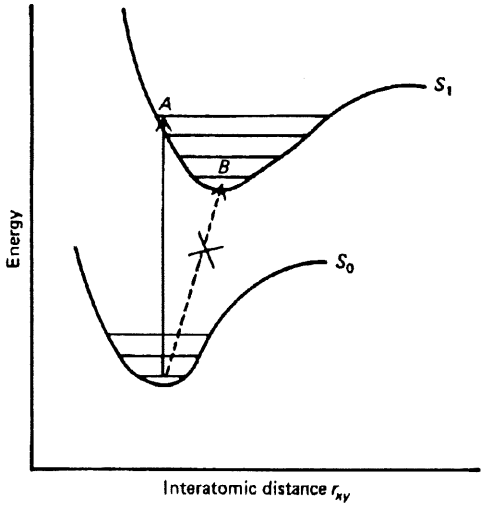

Figure 13. Diatomic potential energy curves and Franck-Condon transition (taken from reference 44).

1.4.3 Internal conversion and intersystem crossing

After excitation has occurred, the excitation energy, may be dissipated by any one of the three general processes:

$$A^*(\text{excited}) \xrightarrow{\text{emission}} A_0 + h\nu$$

$$A^*(\text{excited}) \xrightarrow[\text{conversion}]{\text{radiationless}} A_0 + \text{heat}$$

$$A^*(\text{excited}) \xrightarrow[\text{reaction}]{\text{chemical}} \text{products}$$

In Figure 12, the important processes involving electronically excited states are illustrated. In the excited state, the molecule is in highly vibrational levels above its minimum energy. The excess vibrational energy can be dissipated via bimolecular collisions with solvent molecules. This process is called vibrational relaxation.

Internal conversion This process is a nonradiative transition between states of like multiplicity.

$$S_2 \longrightarrow S_1$$

$$S_1 \longrightarrow S_0$$

The conversion from S_i to S_j is an isoenergetic process that is followed by vibrational relaxation of the new vibrationally hot state.

Intersystem crossing This is related with a nonradiative transition between states of different multiplicity:

$$S_2 \longrightarrow T_1$$

$$T_1 \longrightarrow S_0$$

The crossing from the singlet to the triplet state has a maximum probability at point A (Figure 14), where the energy and geometry of the two states are equal.

The rate of these nonradiative processes are influenced by the following factors:

1. Energy separation: the larger the energy gap (difference between the lowest vibrational levels of the two states), the slower the rate:

$$k\,(S_2 \longrightarrow S_1) > k\,(S_1 \longrightarrow S_0)$$

2. Conservation of spin: transitions between states of different multiplity are forbidden. This would be strictly true if the spin and orbital motions of the electrons were independent. In fact, these transitions can often compete favorably with allowed processes because of spin-orbital coupling:

$$k\,(S_2 \longrightarrow S_1) > k\,(S_1 \longrightarrow T_1)$$

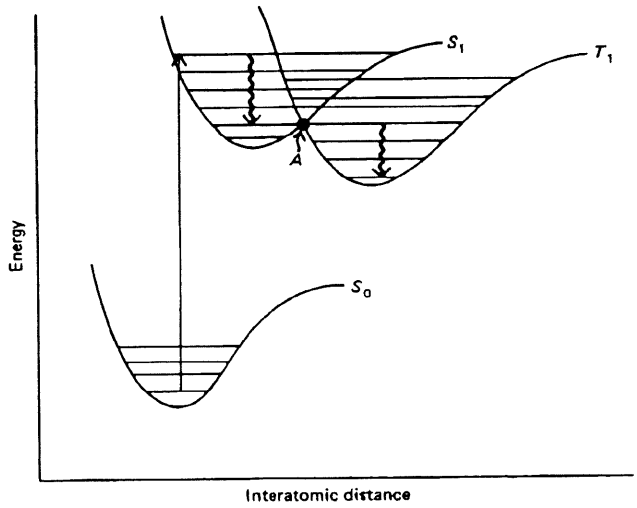

Figure 14. Diatomic potential energy curves and intersystem crossing (taken from reference 44).

1.4.4 Fluorescence and Phosphorescence

These are radiative processes. Kasha's rule states that the light-emitting level of a given multiplicity is the lowest excited level of that multiplicity because of the large ratio constants for the nonradiative processes.

1. Fluorescence The radiative transitions between states of like multiplicity are called fluorescence, the reverse of normal singlet-singlet absorption process. Generally this occurs at high frequency and relatively short-lived.

2. Phosphorescence These radiative transitions occur between the states of unlike multiplicity (triplet-singlet), the reverse of the strongly forbidden singlet-triplet absorption process. The life-time is long compared to fluorescent process.

1.4.5 Transition probability

It is known that Franck-Condon principle is one of factors to control the absorption and emission spectra. In fact, a light wave can be described in terms of electric and magnetic fields with electric and magnetic vectors corresponding to these fields mutually perpendicular to each other and to the direction of propagation of the wave. If light interacts with the electrons of an absorbing molecule, the electric field component of the light wave interacts with electron and excites it from the initial state ψ_i to a final state ψ_j. Since this constitutes a relocation of charge, there must be a change in dipole moment during the transition. The probability for the transition is proportional to the square of the integral of the product of the wave function for the ground state ψ_i multiplied by an operator M that changes the position of the charge, multiplied by the wave function for the final state ψ_j:

$$Pr \propto R_{ij}^2 = (\int \psi_i M \psi_j d\tau)^2 = \langle \psi_i | M | \psi_j \rangle^2 \qquad [1.45]$$

Pr is the probability for the transition and R_{ij} is the transition dipole moment integral.

The wave function can be written in terms of electronic, vibronic, and spin wave functions:

$$\psi_i = \psi_{ei}\,\psi_{vi}\,\psi_{si}$$

Therefore, the transition moment integral can be rewritten as

$$R_{ij}^2 = \langle\psi_{ei}|M|\psi_{ej}\rangle^2\langle\psi_{vi}|\psi_{vj}\rangle^2\langle\psi_{si}|\psi_{sj}\rangle^2 \qquad [1.46]$$

1. Electronic integral Since the operator has the form, $M = \sum_i \mathbf{er}_i$ ($\mathbf{r}_i$ is the vector distance of the *i*th electron from the origin of a fixed coordinate system for the molecule), so it is an odd function. If $R_e^2 = \langle\psi_{e1}|M|\psi_{e2}\rangle^2$ is nonzero, ψ_{e1} and ψ_{e2} must have different symmetries. Generally for simplicity, one just needs to consider the highest occupied one-electron molecular orbitals (HOMO) and the lowest unoccupied molecular orbitals (LUMO). Filled molecular orbitals must be even functions.

$$\langle odd|\,odd|\,odd\rangle^2 = (\int odd)^2 = 0$$

$$\langle even|\,odd|\,odd\rangle^2 = (\int even)^2 \neq 0$$

2. Vibronic integral (Franck-Condon factors) The intensity of a vibronic transition depends upon the square of the overlap integral of the vibrational wave functions,

$$I \propto \langle\psi_{vi}|\psi_{vj}\rangle^2 \qquad [1.47]$$

In Figure 15, a diatomic molecule with the energy curves is considered. In Figure 15a, the ground and excited states have the same equilibrium internuclear distance r_a. The overlap integral $\int\psi_{v1}^0\psi_{v2}^j\,dr$ will be a maximum for j = 0 for the case in Figure 15a. When there is little

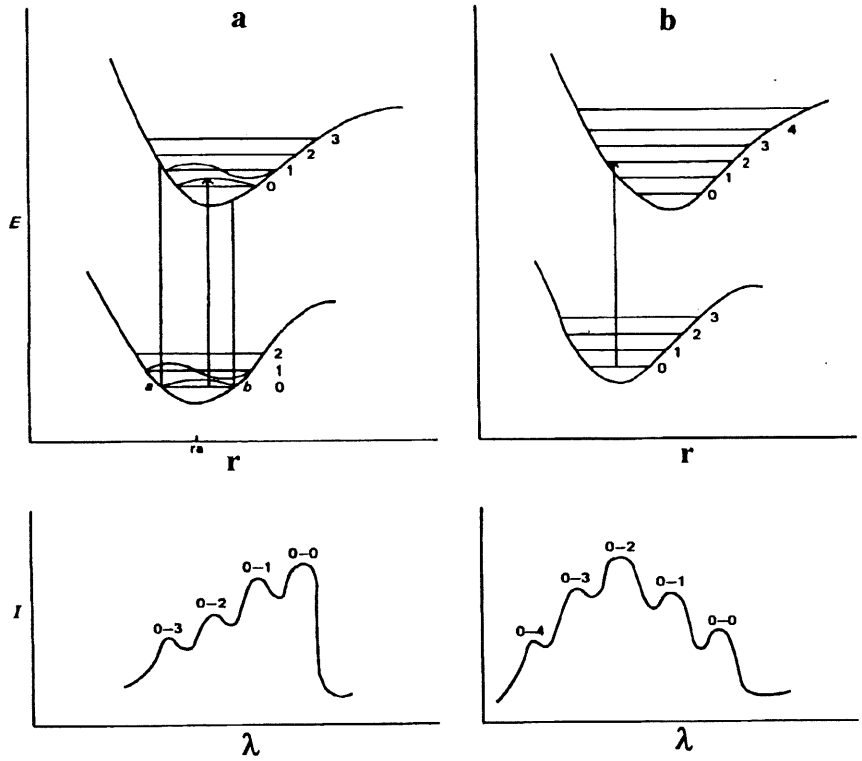

Figure 15. Franck-Condon potential curves of the ground and excited states of a diatomic molecule and typic absorption spectra. The internuclear distances are same in (a); are different in (b) (taken from reference 44).

change in the geometry of the excited state relative to the ground state, it is expected that the 0→0 transition will be always be the most intense. But when there is a large change in the equilibrium geometry of the two electronic states (Figure 15b), the most intense transition may not be the 0→0 transition.

From absorption and emission spectra, one can also get some structural information. When the ground and excited states have similar geometries, the absorption and fluorescence spectra have mirror image symmetry (Figure 16). However, if the difference in geometries is large, the mirror image symmetry is lost in some cases.

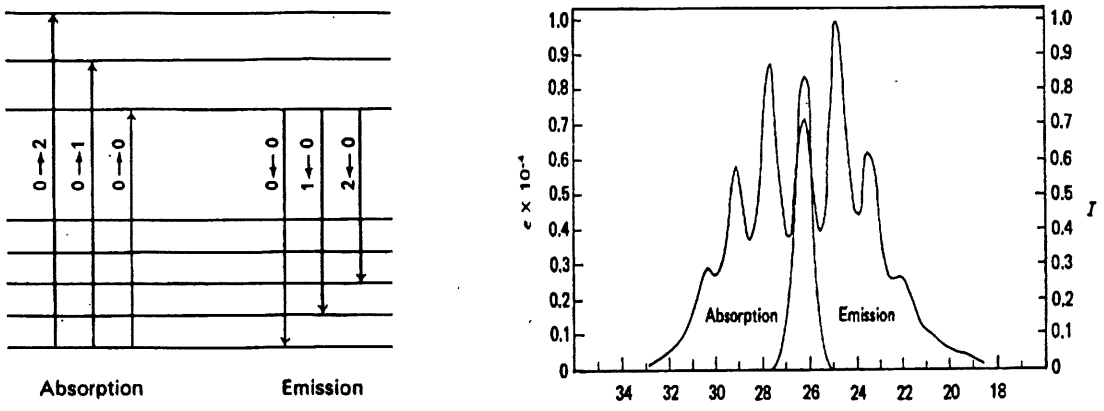

a b

Figure 16. a) Scheme for the absorption and emission (fluorescence) spectra (similar geometries in ground and excited states); b) An example of absorption and fluorescence spectra (mirror image symmetry)(taken from reference 44).

3. Spin restriction The portion of the transition probability determined by the spin wave functions is:

$$Pr \propto \langle \psi_{s1} | \psi_{s2} \rangle^2 \qquad [1.48]$$

For S $\rightarrow$S and T$\rightarrow$T transitions, the spin integral is unity, while for S $\rightarrow$T or T$\rightarrow$S transitions, the value of the integral is zero. This implies that only the transitions between same multiplicity could occur, otherwise, the transitions were forbidden.

4. Spin-orbital coupling According to Eq. 1.48, electronic dipole transition between pure singlet and pure triplet states are rigorously forbidden because of the orthogonality of the spin wave functions. A perturbation, external or internal, is required to "mix" pure singlet and pure triplet states, permitting transitions between the "impure" singlet and "impure" triplet. The form of the Hamiltonian which mixes these states is of interest for the understanding of the processes involving intercombinational transitions.

The classical operator which corresponds to this perturbation is the spin-orbital operator. Spin-orbital coupling arises from magnetic interactions between the orbital motion of an electron and the electron's spin magnetic moment. The magnetic moment S of the electron is parallel to its axis of the spin, and the energy of the spinning electron depends on the relative magnitude of the electron's orbital motion L and the direction of the spin. The net result is that the energy of a molecule depends on the relative orientation of the spin axis and the orbital angular-momentun axis of the electrons. The classical spin-orbital operator for single electron in a central potential field has the form (45) :

$$\mathbf{H}_{SO} = k\zeta(\mathbf{L} \cdot \mathbf{S}) \qquad [1.49]$$

where ζ is a term which depends on the field of the nucleus, **L** is the electron orbital angular-momentum operator, **S** is the spin angular-momentum operator and k is a constant which depends on the given molecule.

Taking into account spin-orbital coupling, a typical wave function can be written in the form:

$$\Psi_{SO} = \Psi_T^0 + \lambda\Psi_S^0 \qquad [1.50]$$

where Ψ_T^0 is the pure unperturbed triplet, Ψ_S^0 represents an appropriate singlet state which may "mix" with the triplet under spin-orbital interaction, and λ is a measure of the extent of mixing.

$$\lambda = \frac{\int \Psi_S^0 \mathbf{H}_{SO} \Psi_T^0 \, d\tau}{E_T - E_S} \qquad [1.51]$$

where E_T is the energy of the triplet Ψ_T^0, and E_S is the energy of the singlet Ψ_S^0. Therefore, under spin-orbital coupling the transition moment R is given by:

$$R_{SO} = \int \Psi_{SO}^{0} \mathbf{R} \Psi_1 \, d\tau$$

$$= \int \Psi_T^{0} \mathbf{R} \Psi_1 d\tau + \lambda \int \Psi_S^{0} \mathbf{R} \Psi_1 d\tau \qquad [1.52]$$

where Ψ_1 is the molecular wave function of the ground state. The first term of Eq. 1.52 is equal to zero because a transition occurs between a pure singlet and triplet. The second term is a transition moment for singlet-singlet transitions.

It is found that the part of Ψ_{SO} which contributes to the singlet-triplet transition may be written as:

$$\Psi_{SO} \propto \frac{\zeta \int \Psi_S^{0} (\mathbf{L} \cdot \mathbf{S}) \Psi_T^{0} \, d\tau}{| E_T - E_S |} \Psi_S^{0} \qquad [1.53]$$

It is instructive to note that important contributions to the degree of mixing result from the size of ζ which is related to the potential field of the nucleus, thus, spin-orbital coupling is more pronounced when the electron is in an orbital which has a high probability of being close to the nucleus, especially in an orbital which is close to a nucleus of high atomic number, and $| E_T - E_S |$ which means that the magnitude of spin-orbital coupling depends inversely on the energetic separation of the triplet and the mixing singlet.

1.4.6 Lifetime

Suppose a radiationless process and emission are the sole processes available for the deactivation of an excited state A*.

$$A^* \xrightarrow{k_1} A_0 + h\nu \qquad [1.54]$$

$$A^* \xrightarrow{k_2} A_0 + \text{heat} \qquad [1.55]$$

Therefore

$$-\frac{d[A^*]}{dt} = (k_1 + k_2)[A^*] \qquad [1.56]$$

where [A*] is the concentration of the excited state at time t. The relative concentration of A* are given by:

$$\ln \frac{[A^*]_t}{[A^*]_{t=0}} = -(k_1 + k_2)\, t \qquad [1.57]$$

so that the mean lifetime τ of [A*] is:

$$\tau = 1/(k_1 + k_2) \qquad [1.58]$$

which simply states that the measured unimolecular radiative lifetime is the reciprocal of the sum of the unimolecular rate constants for the deactivation processes. In general, the equation is given by:

$$\tau = 1/\sum_i k_i \qquad [1.59]$$

where τ is the measured radiative lifetime, and the rate constants k_i represent unimolecular or pseudo-unimolecular processes which deactivate A*(45).

1.5 Polymers

1.5.1 Definition

Polymers are high molecular weight compounds composed repetitively by simple units. This work deals with low-dimensional organometallic polymers, in which the repetitive are inorganic units containing metal-metal bonds:

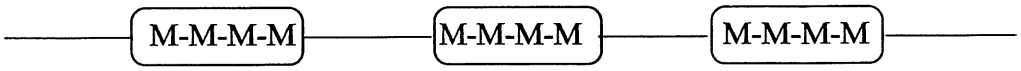

——— = bridging ligands M-M-M-M = $[M_4(dmb)_4]$

dmb = 1, 8-diisocyano-*p*-menthane

Because synthetic polymers generally contain molecules with a wide range of molecular weights, the average value is defined:

number average molecular weight $\overline{M}_n$: $\overline{M}_n = (\sum N_i M_i)/ \sum N_i$ [1.60]

weight average molecular weight $\overline{M}_w$: $\overline{M}_w = (\sum w_i M_i)/ \sum w_i$ [1.61]

1.5.2 Determination of molecular weight by viscosity measurements

A particularly noticeable feature of polymer solutions is their increased viscosity compared with the pure solvent. This increase is obvious for most polymers even at weight concentrations as low as 0.5-1% (46). At low concentrations the viscosity of the solution η is related to the viscosity of the pure solvent η^* by

$$\eta/\eta^* = 1 + [\eta]c + kc^2 + \cdots\cdots \quad [1.62]$$

where $[\eta]$ is called intrinsic viscosity, and c is the weight concentration of polymer.

In the Ubbelohde viscometer (46), the ratio of the viscosities of the solution and the pure solvent is proportional to the drainage time t and t*:

$$\frac{\eta}{\eta^*} = \frac{t}{t^*} \times \frac{\rho}{\rho^*} \qquad [1.63]$$

If the concentrations of polymer are very low, from Eq. 1.62 the following can be obtained:

$$\frac{(\eta-\eta^*)}{\eta^* c} = [\eta] + kc \qquad [1.64]$$

A plot of the quantity of the left-hand side against c is a straight line of slope k and intercept at c = 0 of [η]. [η] is related to molecular weight of polymer by:

$$[\eta] = K M^a \qquad [1.65]$$

where K and a are constants that depend on the solvent and type of polymers. At 30°C, the plot of $(\eta-\eta^*)/\eta^* c$ vs c for a sample of polystyrene in toluene is shown in Figure 17, and yields $[\eta]=129.2\ cm^3g^{-1}$. For this system, the K and a are $1.05 \times 10^{-2}\ cm^3g^{-1}$ and 0.73, respectively. According to Eq. 1.65, this value of [η] corresponds to a molecular weight of 440,000.

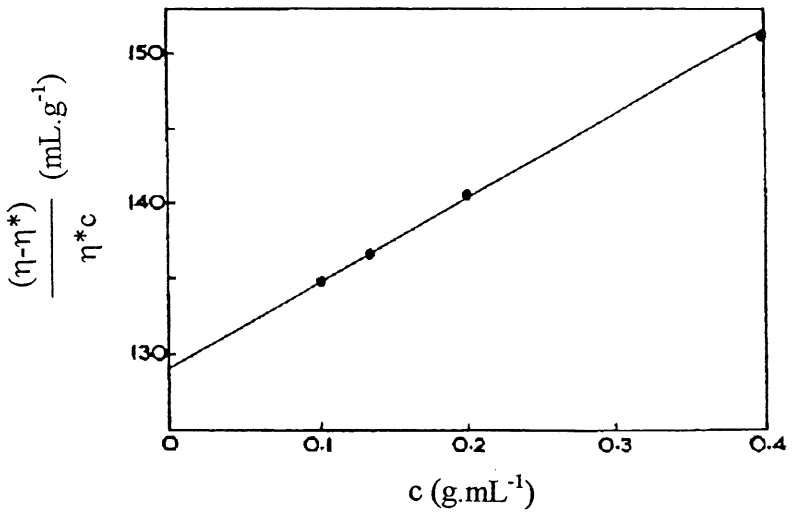

Figure 17. The concentration dependence of the viscosity number for polystyrene in toluene at 30°C (taken from reference 46).

CHAPTER 2

PALLADIUM AND PLATINUM CLUSTERS OF DIARSINE LIGAND

In this research project, two kinds of ligands, i.e. diarsine (dpam=bis(diphenylarsino)methane) and diisocyanide (dmb=1,8-diisocyano-*p*-menthane), have been used to design and synthesize new Pt and Pd clusters. Based upon the different ligands, the results will be reported separately in chapters 2 and 3.

2.1 The tuning of binding properties via the change in cavity size of the unsaturated palladium clusters

The control of host molecule binding properties represents an extremely important aspect of host-guest chemistry and ultimately of molecular recognition. Such a control can only be achieved via structural modification of the host molecule which could be synthetically demanding on most occasions. Over the past few years, P. D. Harvey's group has investigated the host-guest properties of rare kinds of host systems. These systems are the unsaturated trinuclear clusters of type $[M_3(dppm)_3(CO)]^{2+}$ (M = Pd and Pt) (12, 13, 47, 48). X-ray structures revealed that the M_3 metal triangle is located at the bottom of a cavity described by six dppm phenyl groups forming a pocket fence array of *ca.* 2-3 Å opening (10, 11). These systems exhibit a bifunctional binding cavity with the M_3^{2+} center acting as a soft Lewis acid center, and the phenyl groups acting as a hydrophobic pocket. Recently Puddephatt (49) reported a series of related clusters where the dppm ligands were modified in order to reduce the cavity size. They observed a trend in equilibrium constants for phosphine addition on the basis of steric hindrance induced by the substituents on the dppm ligands. In the following work, it will be demonstrated that the cavity structural features and binding properties can, in fact, easily be modified where a larger cavity leads to greater binding constants, *via* a simple substitution of the P atom of the dppm assembling ligands by As atom, and also report an

unprecedented oxidation reaction with I^- anion in presence of O_2, which leads to the oxidative fragmentation of the cluster $[Pd_3(dppm)_3(CO)]^{2+}$ down to $[Pd_2(dppm)_2I_4]$ and to an uncharacterized dark solid.

2.1.1 Synthesis and crystal structure of $[Pd_3(dppm)_3(CO)](PF_6)_2$

$[Pd_3(dppm)_3(CO)](CF_3COO)_2$ has been synthesized in good yield (>80%) by direct reduction of palladium acetate in acetone with CO in the presence of dpam, water and CF_3COOH. The

Table 1. Crystallographic data for $[Pd_3(dpam)_3(CO)](PF_6)_2$

Empirical formula	$(Pd_3As_6P_2F_{12}OC_{76}H_{66})\bullet(CH_2Cl_2)_2$
Formula weight	2223.85
Crystal system	Monoclinic
Space group	P 2_1
Unit cell dimensions	a = 10.835(2) Å
	b = 26.808(4) Å
	c = 14.413(1) Å
	$\alpha = 90^o$
	$\beta = 102.16(2)^o$
	$\gamma = 90^o$
Volume	4092.6(10) $Å^3$
Z	2
Calculated density	1.805 Mg/m^3
Independent reflections	5458
R	0.045
wR	0.052

$R=\Sigma(F_0-F_c)/\Sigma(F_0)$, $wR=[\Sigma(w(F_0-F_c)^2)/\Sigma(wF_0^2)]^{1/2}$, $w=[\sigma^2F_0 + 0.00025F_0^2]$

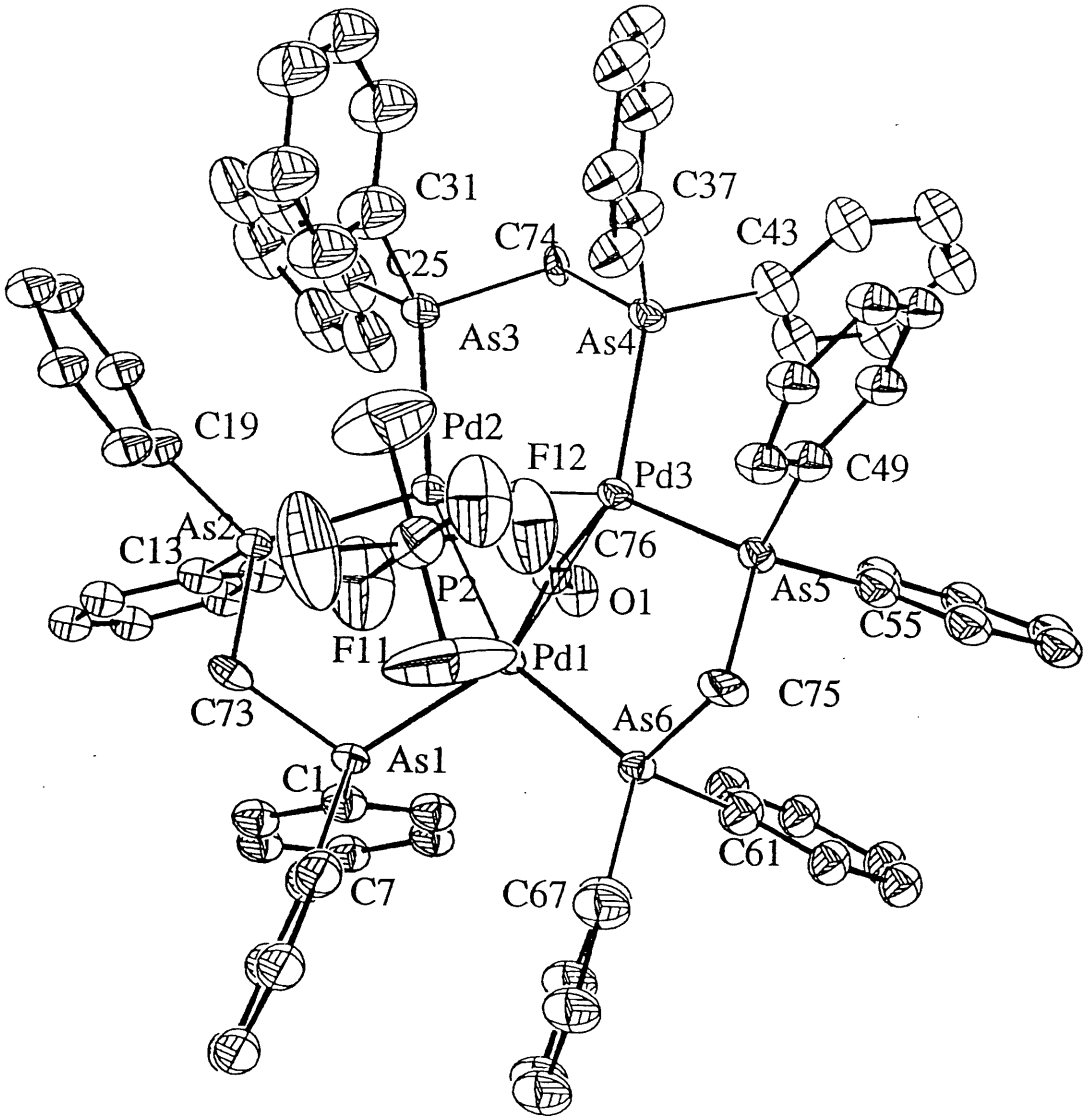

Figure 18. Crystal structure of $[Pd_3(dpam)_3(\mu_3\text{-}CO)](PF_6)_2 \bullet CH_2Cl_2$. Note the PF_6^- anion inside the cavity; H atoms are omitted for clarity.

Table 2. Selected bond distances (Å) and angles (°) for $[Pd_3(dpam)_3(CO)](PF_6)_2$

Pd(1) – Pd(2)	2.6094(12)	Pd(2) – As(3)	2.4298(16)
Pd(1) – Pd(3)	2.5967(11)	Pd(2) – C(76)	2.075(11)
Pd(1) – As(1)	2.4271(13)	Pd(3) – As(4)	2.4130(15)
Pd(1) – As(6)	2.4075(13)	Pd(3) – As(5)	2.4239(14)
Pd(1) – C(76)	2.064(10)	Pd(1) – C(76)	2.070(11)
Pd(2) – Pd(3)	2.5952(12)		
Pd(1) – As(2)	2.4070(14)		

Pd(1) – Pd(2) – Pd(3)	59.86(3)	Pd(1) – Pd(2) – As(2)	96.50(5)
Pd(2) – Pd(1) – Pd(3)	59.80(4)	Pd(3) – Pd(2) – As(3)	97.24(5)
Pd(1) – Pd(3) – Pd(2)	60.34(3)	As(2) – Pd(2) – As(3)	104.43(6)
Pd(1) – C(76) – Pd(2)	78.2(4)	Pd(1) – Pd(3) – As(5)	96.96(5)
Pd(1) – C(76) – Pd(3)	77.8(4)	Pd(2) – Pd(3) – As(4)	96.06(5)
Pd(1) – C(76) – Pd(3)	77.5(3)	As(5) – Pd(3) – As(4)	105.13(5)
Pd(2) – Pd(1) – As(1)	96.30(4)		
Pd(3) – Pd(1) – As(6)	95.19(4)		
As(1) – Pd(1) – As(6)	108.29(5)		

PF_6^- and $B(C_6H_5)_4^-$ salts can be easily obtained from CF_3COO^- salt by metathesis of anions in cold methanol. The peak at 1837 cm^{-1} in IR spectrum, clearly indicates that it comes from μ_3-CO, and the UV-vis spectra are somewhat similar to that of the dppm analogue although the λ_{max} positions are different (12). The dark-red single crystals of PF_6^- salt were grown from the saturated solution in a mixed solvent of dichloromethane and hexane. X-ray structure (Tables 1 and 2) of $[Pd_3(dppm)_3(CO)](PF_6)_2$ is shown in Figure 18. As expected, this cluster is isomorphous with that of the dppm analogue (12). In this structure, two of the dpam phenyl

groups adopt an axial configuration, but also exhibits an important difference: one of PF_6^- counter anions is now located well inside the cavity (d(Pd···F) = 3.10, 3.01Å). Compared to its dppm analogue, the Pd-Pd bond distances (average value: 2.599 Å) are normal. There is, however, one difference, the Pd-As bond lengths. Indeed the Pd-As distance is about 2.42 Å, obviously longer than that of Pd-P (~2.33 Å) due to larger volume of As atom. This difference will significantly affect the cavity size of this host molecule: in $[Pd_3(dppm)_3(CO)]^{2+}$ unit, the cavity H···H distances are of the order of 5.5-6.5 Å (distance between opposite H atoms) (12); in $[Pd_3(dpam)_3(CO)]^{2+}$, these distances increase to 5.9-7.3 Å. This phenomenon is due to a gain in degrees of freedom of the phenyl groups because of longer bond lengths of Pd-As. Compared to the dppm analogue, the size of the cavity is large enough to allow the PF_6^- anion inside the cavity.

2.1.2 Host-guest chemistry

It is possible that the large size of the cavity in the dpam unsaturated clusters will affect their properties as host molecules. This difference made it interesting to examine the binding ability of charged and neutral substrates with these clusters. The λ_{max} of absorption is found to be dependent upon the nature of the substrates, including neutral solvent molecules. The lowest energy absorption band of the $[Pd_3(dpam)_3(CO)](CF_3COO)_2$ system in acetone is located at 502 nm and at 498 nm in methanol. Due to a difference in solubility, and in comparison with the dppm analogue, two salt-solvent systems are investigated (CF_3COO^--MeOH, PF_6^--acetone). The binding constants for the dpam system as both CF_3COO^- and PF_6^- salts, are measured by UV-vis spectroscopy (Chapter 1). In the UV-vis spectra, clear isosbestic points are observed for two systems. The typical spectra are shown in Figure 19. The substrate additions induce blue-shifts of the absorbance bands, especially for strong binding substrates. This is due to the fact that binding substrate molecule interacts with host molecule, and enlarges the energy gap between the HOMO and the LUMO. The data analysis is consistent with a 1:1 stoichiometric complexation from Benesi-Hildebrand, Scott and Scatchard plots

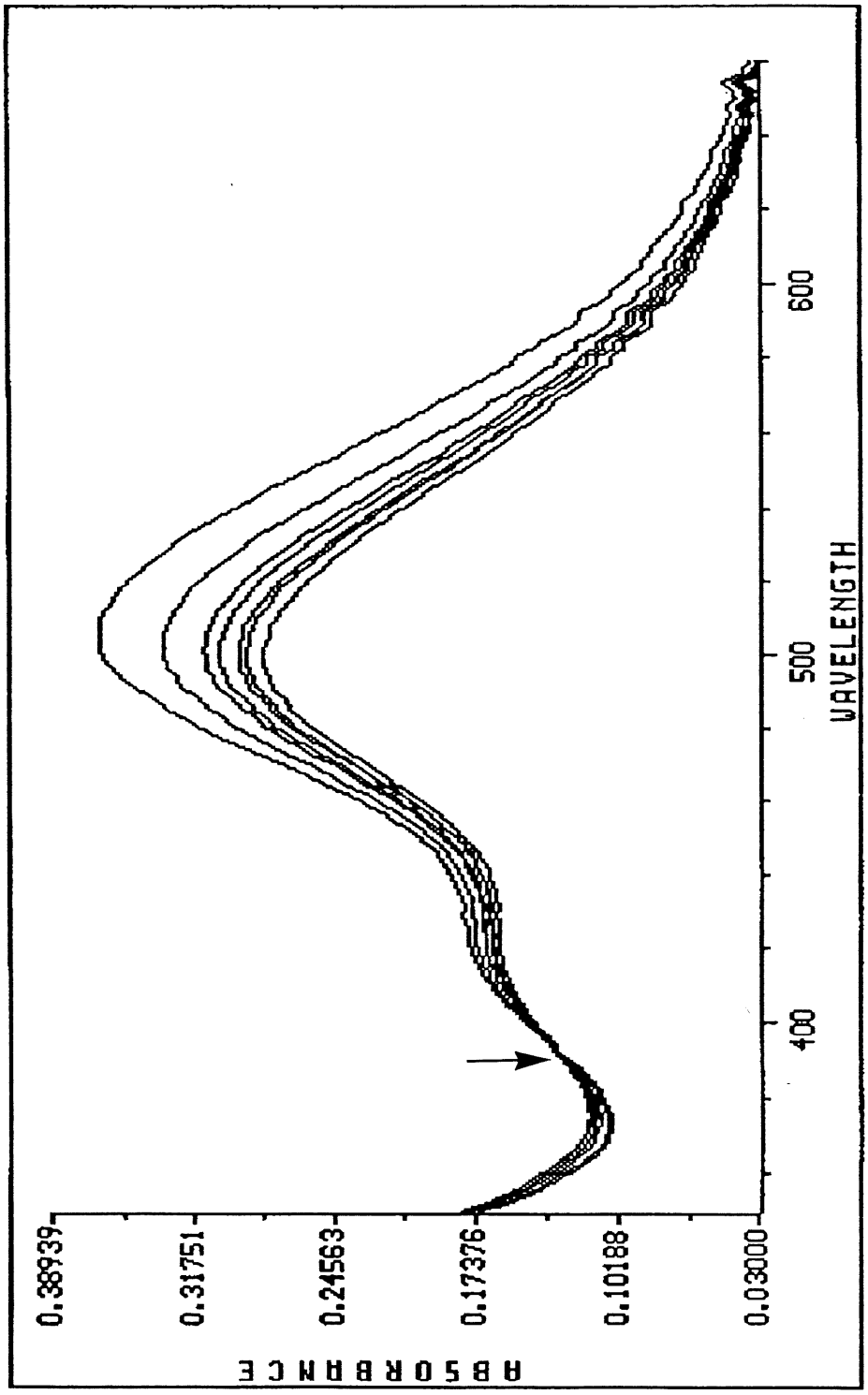

Figure 19. Absorption spectra of $[Pd_3(dpam)_3(\mu_3\text{-}CO)](PF_6)_2$: acetonitrile system in acetone

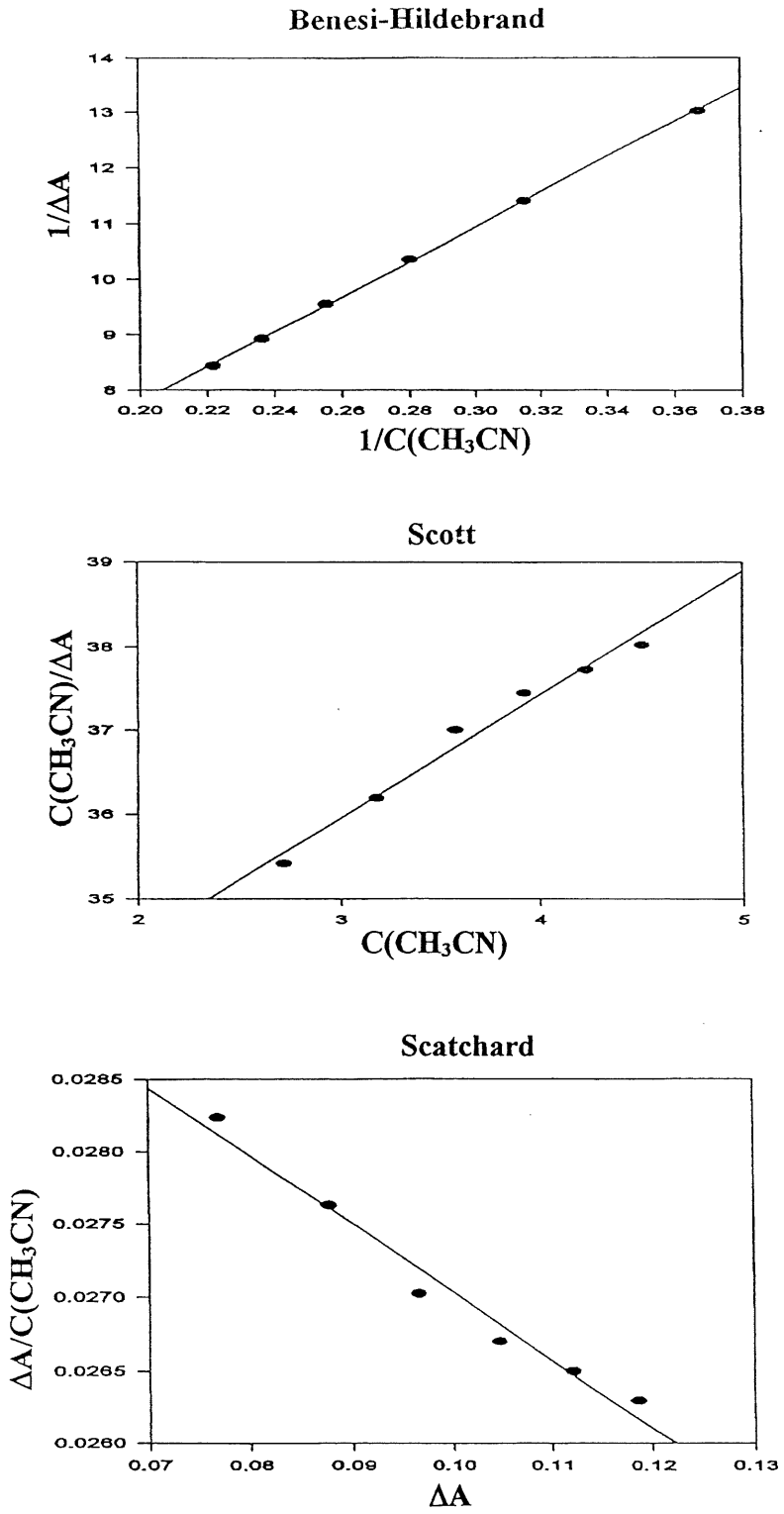

Figure 20. Typical binding constant (K_{11}) measurement experiment (linear plots): Benesi-Hildebrand, Scott, and Scatchard's associated with Figure 19.

Table 3. Comparison of the binding constants for $[Pd_3(dppm)_3(CO)]^{2+}$ and $[Pd_3(dpam)_3(CO)]^{2+}$

Substrates	$[Pd_3(dpam)_3(CO)]^{2+}$/larger cavity		$[Pd_3(dppm)_3(CO)]^{2+}$/smaller cavity	
	PF_6^- salt acetone	$CF_3CO_2^-$ salt methanol	PF_6^- salt acetone	$CF_3CO_2^-$ salt methanol
KI	(> 10000)[a]	(> 10000)[a]	*a*	*a*
Acetate	*b*	3100 ± 100	*b*	730 ± 30
Benzonitrile	0.95 ± 0.01	1.65 ± 0.02	0.28 ± 0.01	1.35 ± 0.20
thf	0.27 ± 0.03	*b*	0.19 ± 0.01	*b*
Pyridine	0.80 ± 0.01	0.56 ± 0.01	0.14 ± 0.01	0.30 ± 0.01
dmf	0.33 ± 0.01	0.13 ± 0.01	< 0.01	0.090 ± 0.005
Methanol	0.21 ± 0.01	—	0.024 ± 0.001	—
Acetonitrile	0.047 ± 0.001	0.085 ± 0.002	< 0.01	0.042 ± 0.005
Water	0.065 ± 0.001	0.15 ± 0.01	0.019 ± 0.001	*c*
NH_4PF_6	< 0.01	< 0.01	*c*	*c*

a The K_{11} values are highly irreproducible for $[Pd_3(dppm)_3(CO)]^{2+}$ even with 10-15 different measurements. For $[Pd_3(dpam)_3(CO)]^{2+}$, the situation is better and an approximated K_{11} value can be provided. This is due to the presence of a quasi-irreversible process in these cases leading to the formation of $[Pd_3(dppm)_3(CO)(X)]^+$ (X = Cl, Br, I), and $[Pd_3(dpam)_3(CO)(X)]^+$. Nonetheless, based upon the amount of X^- necessary to induce a fixed ΔA in the UV-vis spectra, it is found that $[Br^-] > [I^-]$, and that $[X^-]$ is greater for $[Pd_3(dppm)_3(CO)]^{2+}$ than for $[Pd_3(dpam)_3(CO)]^{2+}$. The conclusion can be got that $K_{11}(I^-) > K_{11}(Br^-)$ and that $K_{11}([Pd_3(dpam)_3(CO)]^{2+}) > K_{11}([Pd_3(dppm)_3(CO)]^{2+})$. The value reported is the lowest measured value obtained in a large series of measurements. *b* Not measured. *c* No binding.

(12, 35) (Figure 20, Table 3). All bindings are reversible except for the halide salts for which the bindings are too strong to be accurately measured. It is clear that the binding constants change according to the order: anions, such as I^-, CH_3COO^- > neutral substrates. It is expected that the attraction between the Pd_3^{2+} center and the anion occurs, and for the soft anion, e.g. I^-, the binding constant is larger. Hence for anionic substrates, the binding constants are larger than that for neutral substrates. This order is consistent with the results reported for the dppm system. The main feature is that, in comparison with the constant data for $[Pd_3(dppm)_3(CO)]^{2+}$, for a same salt-solvent system, the binding constants, K_{11}, are always larger for compound $[Pd_3(dpam)_3(CO)]^{2+}$ (Table 3). In this new host system, even PF_6^- anion and water can also bind weakly to $[Pd_3(dpam)_3(CO)]^{2+}$, and the isosbestic points are clearly observed in the spectra. For the $[Pd_3(dppm)_3(CO)]^{2+}$ cluster, substrates, such as PF_6^- and water showed no or very weak binding. The crystal structure of $[Pd_3(dpam)_3(CO)](PF_6)_2$ reveals that one of PF_6^- anions is located inside the cavity constituted by six of the phenyl groups (Figure 18). For the dppm analogue, the two PF_6^- anions are outside (12). The results of binding constant measurements and crystal structures clearly show a direct consequence of the increase in cavity size: large cavity can accommondate large guests. Recently, in a parallel study, Harvey and Braustein reported the binding constants and X-ray structures of a related families of clusters of the type "$M_2M'(dppm)_3(CO)_2$" where a terminal CO ligand was located inside the cavity. In this case most substrates show no binding, and halide ions exhibited weak bind (50).

2.1.3 Reaction with iodide salt

The strong binding ability of iodide anion to $[Pd_3(dpam)_3(CO)]^{2+}$ complexes indicates that there is a tendency to form electron-saturated cluster. Puddephatt et al. reported the X-ray structures for the Cl^- and I^- adducts of $[Pd_3(dppm)_3(CO)]^{2+}$ (9, 51). Cluster $[Pd_3(dpam)_3(CO)]^{2+}$ also reacts with I^- under inert atmosphere in acetone to produce the expected saturated cluster, $[Pd_3(dpam)_3(\mu_3\text{-}CO)(\mu_3\text{-}I)]^{2+}$. UV-vis spectra indicated that this

reaction was carried out fast, and the peak of absorption at 502 nm moved to 482 nm. In the IR spectrum, the ν(CO) peak appeared at 1845 cm^{-1}, which is higher than that in the cluster $[Pd_3(dpam)_3(CO)]^{2+}$. The peak related to CF_3COO^- anion was located at 1680 cm^{-1}, which showed that, this saturated cluster was formed as a CF_3COO^- salt. The dark crystals were grown by diffusion of pentane to the acetone solution of the cluster. The crystal structure (Table 4) indicates that, three palladium atoms, I and C atoms form a trigonal bipyramid (Figure 21), and one CF_3COO^- is located outside the cavity of the cluster. All the bond lengths

Table 4. Crystal data for $[Pd_3(dpam)_3(CO)(I)](CF_3COO)$ and $[Pd_2(dpam)_2I_4]$

Empirical formula	$(Pd_3As_6OC_{76}H_{66}I)\bullet$ $CF_3CO_2\bullet(CH_3)_2CO$	$(Pd_2As_4OC_{50}H_{44}I_4)$ $\bullet CH_2Cl_2$
Formula weight	2062.08	1749.98
Crystal system	Triclinic	Monoclinic
Space group	P $2_1/c$	C 2/c
Unit cell dimensions	a = 10.902(2) Å	a = 21.3996(12) Å
	b = 18.559(4) Å	b = 10.132(3) Å
	c = 37.243(3) Å	c = 24.553(3) Å
	α = 90°	α = 90°
	β = 96.21(1)°	β = 90.403(7)°
	γ = 90°	γ = 90°
Volume	7491(2) $Å^3$	5307.9(17) $Å^3$
Z	4	4
Calculated density	1.828 Mg/m^3	2.190 Mg/m^3
Independent reflections	5458	4639
R	0.052	0.027
wR	0.055	0.030

$R=\Sigma(F_0-F_c)/\Sigma(F_0)$, $wR=[\Sigma(w(F_0-F_c)^2)/\Sigma(wF_0^2)]^{1/2}$, $w=[\sigma^2F_0 + 0.00025F_0^2]$

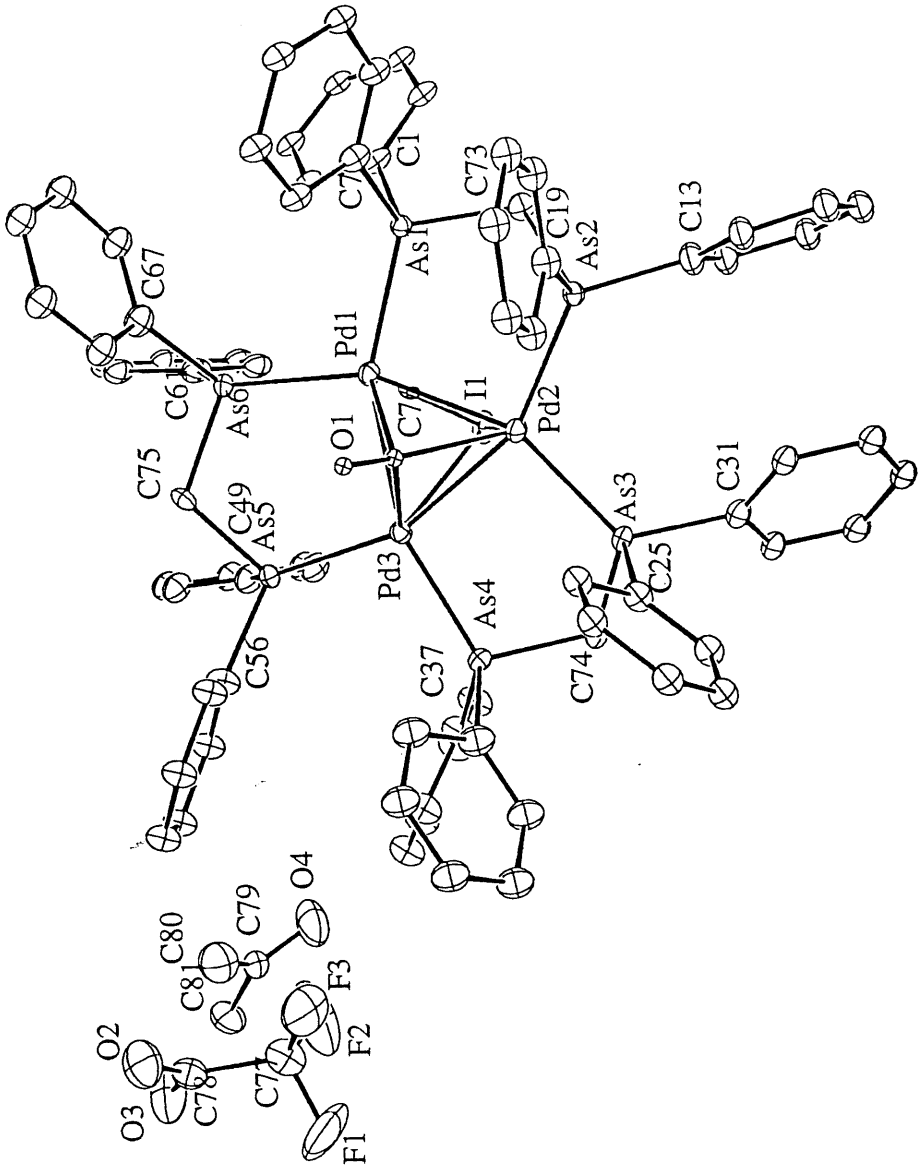

Figure 21. Crystal structure of $[Pd_3(dpam)_3(\mu_3\text{-}CO)(\mu_3\text{-}I)](CF_3COO)$

Table 5. Selected bond distances (Å) and angles (°) for $[Pd_3(dpam)_3(CO)(I)](CF_3CO_2)$

Pd(1) - Pd(2)	2.5973(12)	Pd(1) - C(76)	2.27(2)
Pd(1) - Pd(3)	2.5745(14)	Pd(2) - C(76)	2.39(2)
Pd(2) - Pd(3)	2.5685(14)	Pd(3) - C(76)	2.35(2)
Pd(1) - I(1)	2.9681(18)	Pd(1) - C(76')	2.153(18)
Pd(2) - I(1)	2.881(2)	Pd(2) - C(76')	2.172(19)
Pd(3) - I(1)	2.949(2)	Pd(3) - C(76')	2.133(18)

Pd(2) - Pd(1) - Pd(3)	59.55(4)	Pd(1) - C(76) - Pd(3)	67.6(6)
Pd(1) - Pd(3) - Pd(2)	60.66(4)	Pd(2) - C(76) - Pd(3)	65.6(6)
Pd(1) - Pd(2) - Pd(3)	59.78(4)	Pd(1) - C(76) - Pd(2)	67.6(6)
Pd(1) - I(1) - Pd(2)	52.70(4)		
Pd(1) - I(1) - Pd(3)	51.58(4)		
Pd(2) - I(1) - Pd(3)	52.27(4)		

Table 6 . Selected bond lengths (Å) and angles (°) for $[Pd_2(dpam)_2I_4]$

Pd - I(1)	2.6217(10)	Pd - As(1)	2.3844(10)
Pd - I(2)	2.6395(10)	Pd - As(2)	2.3995(10)
Pd^i- I(2)	3.1562(11)		

I(1) - Pd - I(2)	150.41(2)	$I(2) - Pd - I(2)^i$	109.05(2)
Pd - I(2) - Pd^i	70.95(2)	$I(2) - Pd - As(2)^i$	91.09(2)
As(1) - Pd - As(2)	179.02(3)	$I(2)^i$ - Pd - As(1)	91.63(2)
I(1) - Pd - As(1)	89.16(2)		
I(2) - Pd - As(1)	88.66(2)		

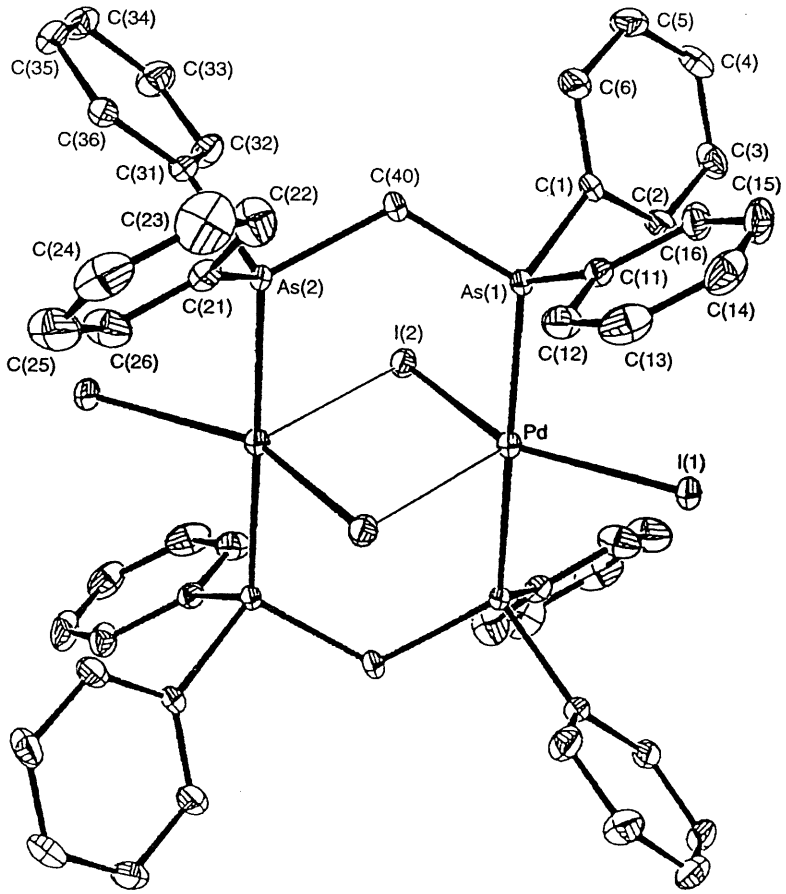

Figure 22. Crystal structure of $[Pd_2(dpam)_2L_4]$

are normal except for the Pd-C bond length which significantly increases by about 0.1-0.2 Å (2.15 and 2.33 Å, Table 5) compared to that for $[Pd_3(dppm)_3(CO)](PF_6)_2$ (2.07 Å). This is consistent with the results of IR measurements, where a higher ν(CO) datum was observed for this cluster (1845 cm^{-1}) (for $[Pd_3(dppm)_3(CO)](PF_6)_2$, this value is 1837 cm^{-1}).

In the presence of O_2, the UV-vis spectra indicated that the intensity of the peak at 484 nm slowly decreased during the reaction. This reaction was carried out faster, using $[Pd_3(dpam)_3(CO)][B(C_6H_5)_4]_2$ as the starting material instead of $[Pd_3(dpam)_3(CO)](CF_3COO)_2$. In four hours, the peak at 484 nm nearly disappeared. Unexpectedly the cluster was oxidized in solution to give $[Pd_2(dpam)_2I_4]$ as identified from X-ray crystallography (Table 6, Figure 22), along with an uncharacterized dark solid. The reasonable explanations for this is that oxygen is involved in this reaction, or cluster fragmentation reaction occurs during the reaction between $[Pd_3(dpam)_3(CO)]^{2+}$ and I^-. This reaction is unprecedented for two reasons. First, the oxidation-fragmentation of these clusters has never been observed for halide substrates before. Secondly, the palladium(II) product reveals a dinuclear structure with bridging dpam, instead of a mononuclear geometry as typically found for the standard $[Pd(dppm)X_2]$ species (X = Cl, Br, I). The larger As atom may be responsible for the lack of chelating ability of the dpam ligand (52). In this new structure, two iodine atoms are semi-bridged, which is different from that of $Pd_2(dmb)_2Cl_4$, where face to face structure is observed (53). The distance between the two palladium atoms is 3.3896(9)Å. Crystallography provides no evidence for weak Pd···Pd interaction (Table 6).

2.2 Properties of a new 58-electron butterfly $[Pt_4(\mu_2\text{-dpam})_3(\mu_2\text{-CO})_3(\eta^1\text{-dpam})]^{2+}$ cluster

In 1969 Dahl et al (54) reported the X-ray structure of a new 58-electron Pt_4 cluster $Pt_4(PPhMe_2)_4(CO)_5$ (**1**; Scheme I). The butterfly structure was uncommon at that time, as well as 58-electron clusters. This structure exhibits two triangular fragments with the same d(Pt-Pt

Scheme I:

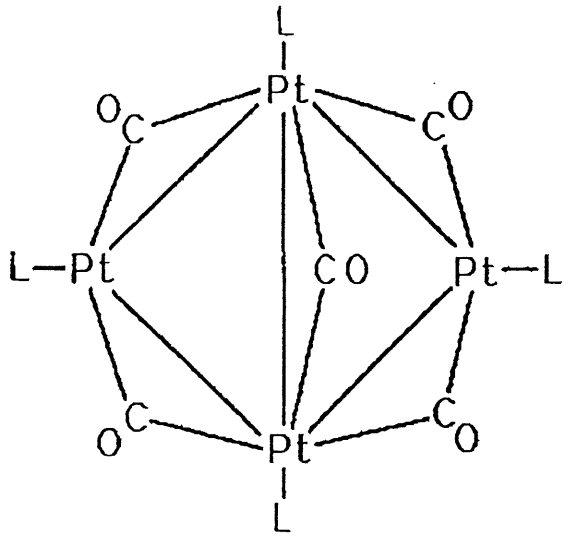

1

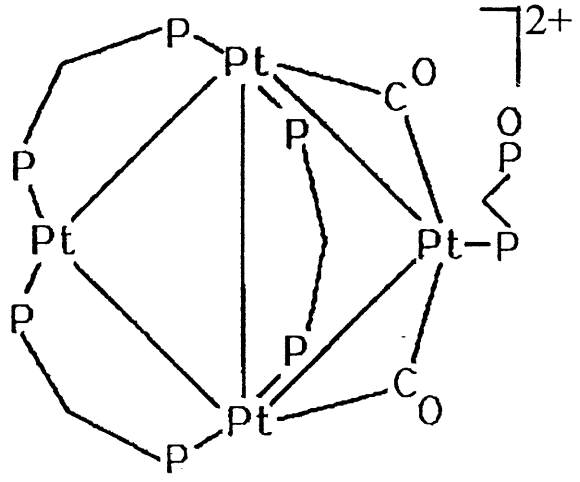

2

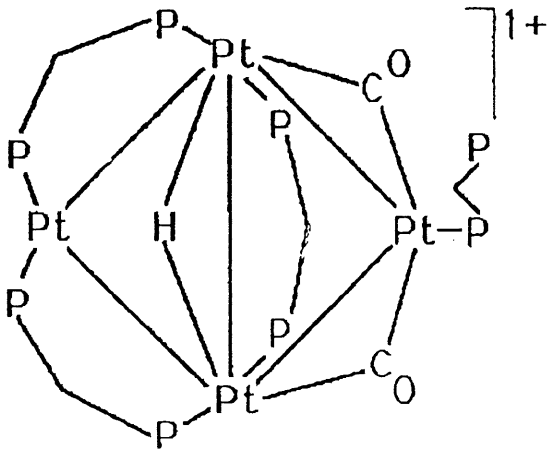

3

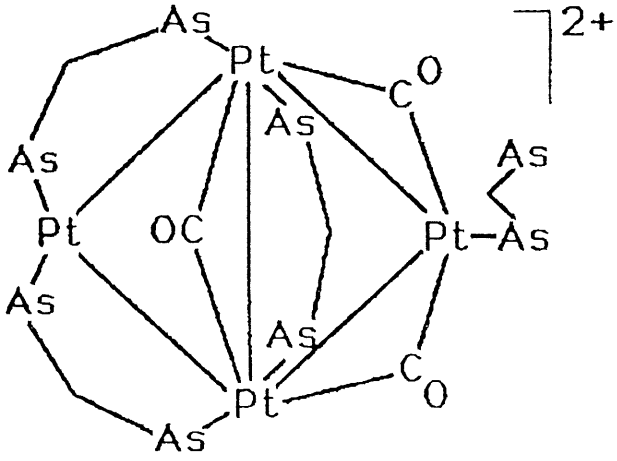

4

) (i.e. 2.750(6) and 2.754(6) Å). The edge shared Pt-Pt bond is longer (2.790(7) Å). Fifteen years later the same cluster was reported again by another group (the different synthetic methods), but the average Pt-Pt distance was significantly shorter (55). In fact, the structure showed two different triangles: a small (d(Pt-Pt) = 2.7280(14) and 2.7064 (15) Å) and a large one (d(Pt-Pt) = 2.7537(13) and 2.7512(15) Å), with a shared Pt-Pt bond (2.7512(15) Å). The non-bonding Pt···Pt distances reduced from 3.543(8) to 3.3347(12) Å. This asymmetry in triangle sizes became more obvious for compounds containing "$Pt_3(\mu_2\text{-dppm})_3$" and CO fragments. Puddephatt et al. (56) reported the structure of $[Pt_4(\mu_2\text{-dppm})_3(\mu_2\text{-CO})_2(\eta^1\text{-dppm=O})]^{2+}$ (**2**). The small triangle shows d(Pt-Pt) of 2.611(2) and 2.617(2) Å, and the large one shows d(Pt-Pt) of 2.739(2) and 2.708(2) Å. The shared Pt-Pt bond length and non-bonding Pt···Pt distances are also shorter (2.700(1) and 3.074(1) Å). The small triangle belongs to the "$Pt_3(\mu_2\text{-dppm})_3$" fragment. Six years later, the same group (57, 58) reported another example of an asymmetric butterfly Pt_4 cluster, $[Pt_4(\mu_2\text{-dppm})_3(\mu_2\text{-CO})_2(\mu_2\text{-H})(\eta^1\text{-dppm})]^+$ (**3**). The charge is induced by the addition of a H^+ to a neutral species, and practically no change is observed in the "$Pt_3(\mu_2\text{-dpam})_3$" small triangle (d(Pt-Pt) = 2.620(1), 2.613(1) and 2.705(1) Å (shared Pt-Pt bond)). The larger triangle exhibits slightly increased d(Pt-Pt) values by ~0.012 Å. The non-bonding Pt···Pt distance is also about the same as in the neutral cluster (although slightly longer: 3.092 (1) Å). The question is why the Pt-Pt distance become shorter when chelating ligand, dppm, replaces the monodentate ligand, $PPhMe_2$. It could be anticipated that the substitution of dppm by dpam (As instead of P) could increase the Pt-Pt bond length as the bite distance is longer. Here it is reported the preparation of and the X-ray diffraction results on a new cluster, $[Pt_4(\mu_2\text{-dpam})_3(\mu_2\text{-CO})_3(\eta^1\text{-dpam})]^{2+}$ (**4**), which shows the opposite. In fact, this cluster exhibits the shortest d(Pt-Pt) values in this series. These results will be complemented with EHMO computations, and ^1H NMR measurement where fluxionality process are observed. During the course of these studies a luminescence behavior has been noted, and has been briefly investigated.

2.2.1 Synthesis and crystal structure of $[Pt_4(\mu_2\text{-dpam})_3(\mu_2\text{-CO})_3(\eta^1\text{-dpam})](PF_6)_2$ (4b)

Reaction of $Pt(dpam)(CF_3COO)_2$ with CO(g) in a methanol/water mixture produces the red-orange product ($[Pt_4(dpam)_4(CO)_3](CF_3COO)_2$, **4a**) in good yield, not $Pt_3(dpam)_3CO^{2+}$. In the IR spectrum, clearly the peak at 1830 cm^{-1} can be assigned to ν(CO). In comparison with the ν(CO) band in $Pt_3(dppm)_3CO^{2+}$ (~1760 cm^{-1}), this value is much higher, but lower than that of terminal CO ligand, indicating that CO bridges the Pt atoms. The CF_3COO^- salt can easily be converted to PF_6^- salt (**4b**) by anion metathesis. The deep orange crystals for **4b** were obtained by diffusion of pentane to acetone solution, which were suitable for X-ray crystallography (Table 7). The structure of **4b** (Figure 23) shows the new typical butterfly geometry generally encountered for 58 valence electron clusters (CVE) (54, 55, 56, 57, 58). Pt_4L_8 (56 CVE) and

Table 7. Crystal data for $[Pt_4(\mu_2\text{-dpam})_3(\mu_2\text{-CO})_3(\eta^1\text{-dpam})](PF_6)_2$ (4b)

Empirical formula	$Pt_4P_2F_{12}As_8C_{103}H_{108}O_3$
Temperature	193 (2) K
Wavelength	0.71073 Å
Crystal system	Orthorhombic
Space group	C c2a
Unit cell dimensions	a = 26.320 (9) Å
	b = 27.613 (6) Å
	c = 28.891 (4) Å
Volume	20998 (9) $Å^3$
Z	4
Density (calculated)	1.925 Mg/m^3
Reflections collected	12041
Independent reflections	9478
R	0.059
wR	0.058

$R=\Sigma(F_0-F_c)/\Sigma(F_0)$, $wR=[\Sigma(w(F_0-F_c)^2)/\Sigma(wF_0^2)]^{1/2}$, $w=[\sigma^2F_0 + 0.00025F_0^2]$

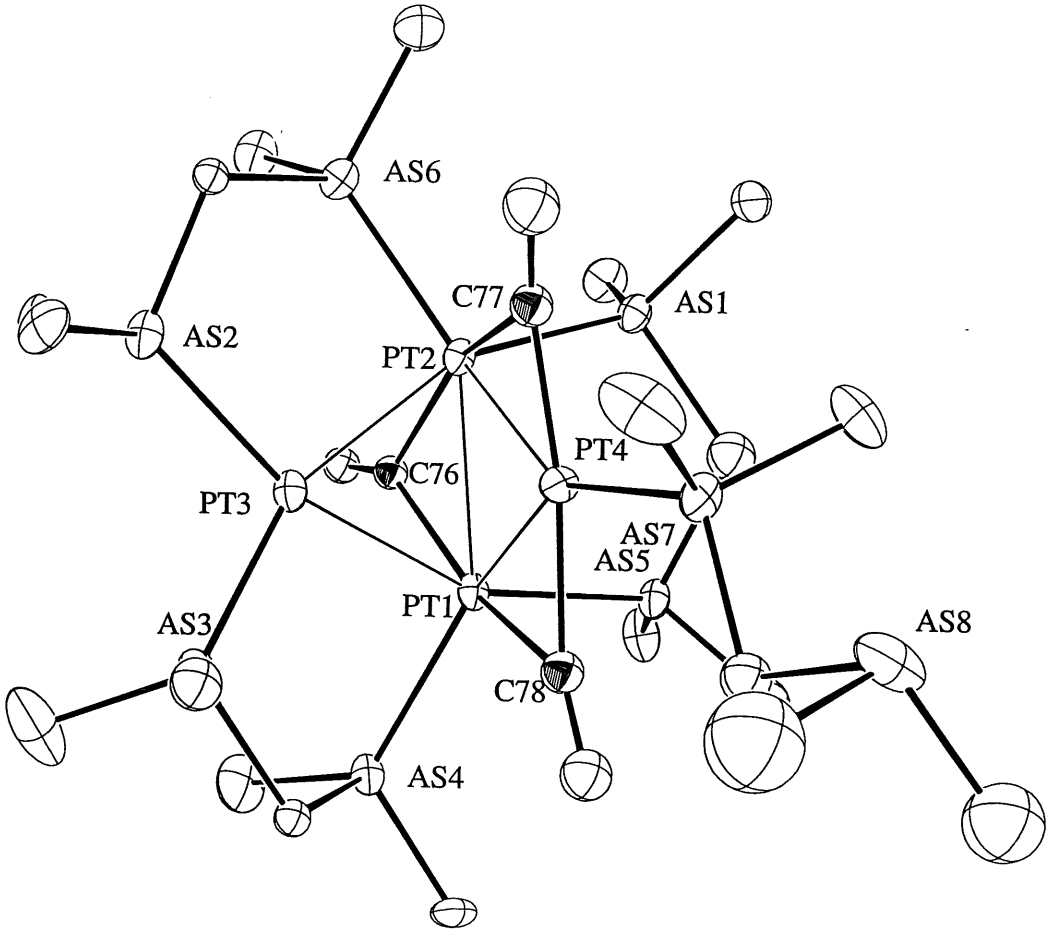

Figure 23. Crystal structure of $[Pt_4(\mu_2\text{-dpam})_3(\mu_2\text{-CO})_3(\eta^1\text{-dpam})](PF_6)_2$ (4b) Black balls: carbon atoms for CO ligands.

Table 8. Selected bond distances (Å) and angles (°) for $[Pt_4(\mu_2\text{-dpam})_3(\mu_2\text{-CO})_3(\eta^1\text{-dpam})](PF_6)_2$ (4b)

Pt1 - Pt2	2.6673(15)	Pt3 - As2	2.362(3)
Pt1 - Pt3	2.6039(12)	Pt3 - As3	2.369(3)
Pt1 - Pt4	2.6892(17)	Pt4 - As7	2.361(3)
Pt2 - Pt3	2.6083(17)	Pt1 - C76	2.058(24)
Pt2 - Pt4	2.7128(16)	Pt1 - C78	2.27(3)
Pt3···Pt4	3.094(1)	Pt2 - C76	2.075(24)
Pt1 - As4	2.420(3)	Pt2 - C77	2.29(3)
Pt1 - As5	2.454(3)	Pt4 - C77	1.93(3)
Pt2 - As1	2.475(3)	Pt4 - C78	2.06(3)
Pt2 - As6	2.397(3)		
Pt2-Pt1-Pt3	59.30(4)	Pt4-Pt1-As4	127.81(8)
Pt2-Pt1-Pt4	60.85(4)	Pt4-Pt1-As5	97.05(7)
Pt3-Pt1-Pt4	71.51(4)	Pt1-Pt2-As1	98.09(8)
Pt1-Pt2-Pt3	59.14(4)	Pt1-Pt2-As6	149.31(9)
Pt1-Pt2-Pt4	59.97(4)	Pt3-Pt2-As1	157.19(9)
Pt3-Pt2-Pt4	71.07(5)	Pt3-Pt2-As6	95.32(9)
Pt1-Pt3-Pt2	61.56(5)	Pt4-Pt2-As1	99.85(9)
Pt1-Pt4-Pt2	59.18(4)	Pt4-Pt2-As6	131.67(9)
Pt1-C76-Pt2	80.4(9)	Pt1-Pt3-As2	157.26(11)
Pt2-C77-Pt4	79.5(9)	Pt1-Pt3-As3	98.21(9)
Pt1-C78-Pt4	76.7(9)	Pt2-Pt3-As2	97.87(10)
Pt2-Pt1-As4	146.98(7)	Pt2-Pt3-As3	158.14(9)
Pt2-Pt1-As5	97.61(9)	Pt1-Pt4-As7	147.25(9)
Pt3-Pt1-As4	91.44(7)	Pt2-Pt4-As7	150.00(10)
Pt3-Pt1-As5	156.88(9)		

$Pt_4L_8^{2+}$ (54 CVE) polynuclear complexes have recently been reported, and their X-ray structures reveal the formation of tetrahedral clusters (59). The bond distances and angles are normal for **4b** (Table 8). The angles between the Pt_3 planes is 95.36 (8)°, and the non-bonding Pt···Pt distance is 3.094(1) Å. At such distance, weak Pt···Pt interactions are anticipated (60, 61). Similarly to the recent literature reports on clusters **1, 2** and **3** (Scheme I), the structure of **4b** also exhibits a small and a large Pt_3 triangles (Table 9). In all cases (except for the X-ray structure of **1** reported by Dahl et al.), the d(Pt-Pt) data for the edge sharing bonds are intermediate values between the small and large triangle d(Pt-Pt) data. For compounds **3** and **4**, one can rationalize this behavior by considering the presence of the +2 charge being localized within the "$Pt_3(dppm)_3$" frames. This observation is consistent with the fact that the average Pt-Pt distances in the $Pt_3(dppm)_3(CO)L^{n+}$ cations, is 2.634 Å (62), where

Table 9. Comparison of Pt-Pt distances (Å) in butterfly clusters

cluster	Small triangle	Edge sharing	Large triangle	Non-bonding Pt-Pt	Reference
1[a]	2.750(6) 2.754(6)	2.790(7)	2.754(6) 2.750(6)	3.543(8)	54
1	2.7064(15) 2.7280(14)	2.7537(14)	2.7512(15) 2.7537(13)	3.3347(12)	55
2	2.617(2) 2.611(2)	2.700(1)	2.708(2) 2.739(2)	3.074(1)	56
3	2.620(1) 2.613(1)	2.705(1)	2.750(1) 2.720(1)	3.082(1)	57, 58
4b	2.6083(17) 2.6039(12)	2.6673(15)	2.7128(16) 2.6892(17)	3.094(1)	this work

a There is no small and large triangle in this cluster.

L = SnF_3, n = 1; L = SCN, n = 1; L = $P(OC_6H_5)_3$, n = 2; L = none, n = 2. The average distance for the small Pt_3 triangle in **3** is 2.646 Å (Table 9). Similarly the average Pd-Pd distance for $Pd_3(dpam)_3CO^{2+}$ and $Pd_3(dpam)_3(CO)I^+$ is 2.580 Å (63), while the average Pt-Pt distance in the small Pt_3 triangle of **4b** is 2.627 Å. In this comparison, it must be remembered that the Pd-Pd and Pt-Pt bond lengths are generally nearly identical for the $M_3(dppm)_3CO^{2+}$ system (M = Pt, Pd). When this +2 charge distribution on the small triangle occurs, then the larger Pt_3 triangle contributes to no charge in **3** and **4.** The Pt-Pt bond length in $Pt_3(\mu_2\text{-}CN(C_4H_9))_3(CN(C_4H_9))_3$ is 2.65 Å (64), and in $[Pt(t\text{-}Bu)_2P(CH_2)_3P(t\text{-}Bu)_2]_2$ is 2.765 Å (65). The average Pt-Pt bond lengths for the large triangle in **3** and **4b** are 2.725 and 2.690 Å, respectively. Such values are indeed appropriate for a zerovalent Pt_3 center. This raises a question what explains the presence of a large and a small triangles in **1** and **2**? In these cases one can easily suspect that the complex charge is not evenly distributed over all the Pt frame. This work does not answer this question specifically, but provides a valuable clue as to what is probably occuring.

2.2.2 FT-Raman spectrum

The FT-Raman of **4a** (as a typical example) in the solid state (50 - 800 cm^{-1}) has been also examined for characterization purposes. Under the approximation of a C_{2v} local symmetry, there should be 5 active ν(M-M) modes: $2a_1 + a_2 + b_1 + b_2$. Below 200 cm^{-1}, four scatterings are indeed evident: 158 (m), 129 (s), 107 (sh) and 85 (s). These are readily assigned to ν(M-M). A comparison with other cyclic Pt clusters (13, 61, 62, 66, 67, 68) is made and presented in Table 10. A trend relating the largest ν(Pt-Pt) values ($\nu(Pt\text{-}Pt)_{sym}$) with the smallest d(Pt-Pt), is readily observed 2.58, 2.60, 2.63, 2.76, 2.96 Å; 170, 158, 149, 122, 112 cm^{-1}. The Raman data are indeed consistent with relatively strong Pt-Pt single bonds. Three other broad peaks (213, 231 and 249) in the low frequency region are also observed, and these are the ν(Pt-As) modes (69). The remainder of the strong peaks in this region are intraligand modes, and are not interpreted further.

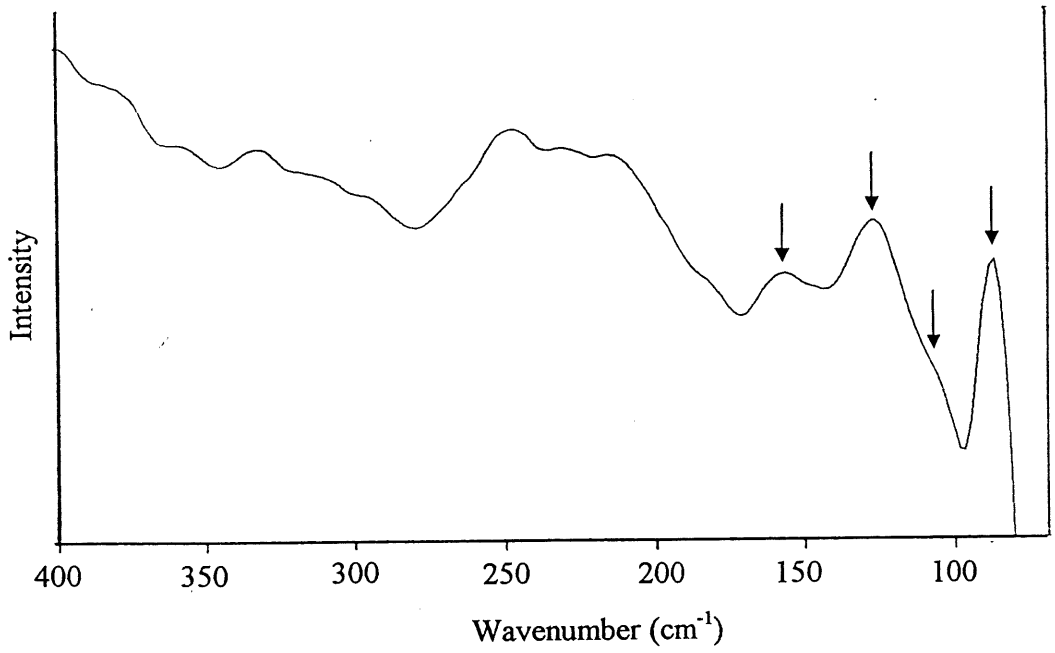

Figure 24. FT-Raman spectrum for $[Pt_4(dpam)_4(CO)_3](CF_3COO)_2$. Experimental conditions: resolution: 4.0 cm^{-1}, no. of scans: 500, laser power: 10 mW at 1064 nm.

Table 10. Comparison of the ν(Pt-Pt) data for cyclic Pt clusters

Compounds	d(Pt-Pt)/Å	ν(Pt-Pt)/cm^{-1}	Approximated local symmetry	Reference
$[Pt_4(dpam)_4(CO)_3]^{2+}$ (**4a**)	2.60- 2.71	158, 129 107, 85	C_{2v}	this work
$[Pt_3(dppm)_3CO]^{2+}$ (PF_6^- salt)	2.634 (average)	149 (a_1), 125 (e)	C_{3v}	13, 62
$[Pt_3(\mu\text{-}PPh_2)_3Ph(PPh_3)_2]$ (close structure)	2.956(3), 2.956(3) 3.074(4)	112 (a_1), 96	D_{3h}	61
$[Pt_3(\mu\text{-}PPh_2)_3Ph(PPh_3)_2]$ (open structure)	2.758(3), 2.758(3) 3.586(4)	122 (sym), 105(asym)	C_{2v}	61
$[Pt_3(C_8H_{12})_3(SnCl_3)_2]$	2.58	170 (a_{1g}), 143 (e_g)	D_{3h}	66, 67
Pt_3^-		225 ± 30, 105 ± 30		68

2.2.3 ^{1}H NMR spectra and fluxionality

4a and **4b** contain three nuclei (S≠0) with significant natural abundance (^{1}H, As, ^{195}Pt). The As nuclei (S = 3/2) has a large quadrupolar moment (Q = 0.3 × 10^{-24} cm^{2}) (70), which induces rapid exchange with the different spin states. For this reason no coupling with other nuclei occurs, which greatly contributes to the simplification of the ^{1}H-spectra in comparison with the ^{31}P-containing dppm ligand. Compounds **4a** and **4b** exhibit three series of -CH_2- signals in

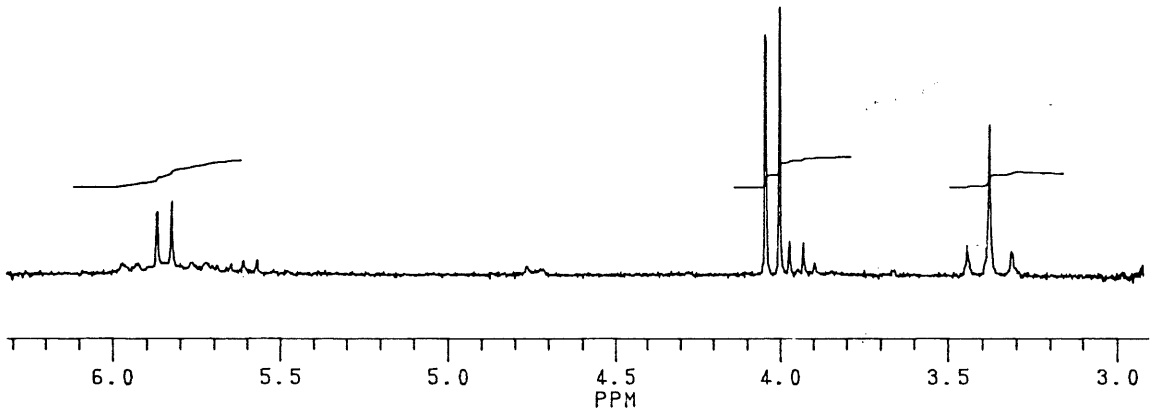

Figure 25. ^{1}H NMR spectrum of $[Pt_4(dpam)_4(CO)_3](PF_6)_2$(4b) in acetone-$d_6$.

Scheme II:

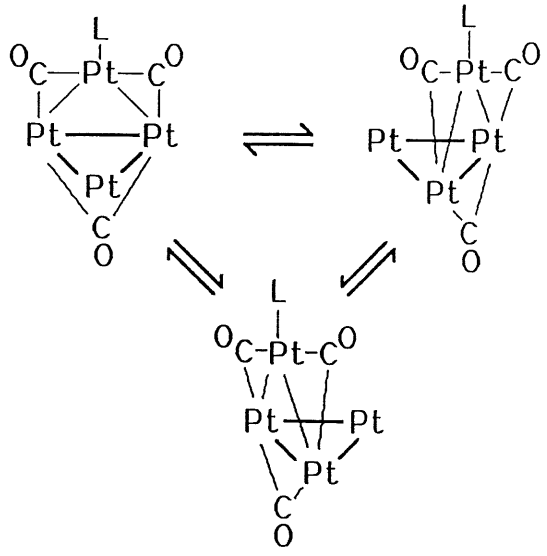

the 5.5-6.0, 3.9-4.1 and 3.4 ppm regions with 3H, 3H and 2H integration intensity, respectively (Figure 25). The simplicity of the spectra and these relative integrations clearly establish a 3-fold symmetry in the molecule, and indicate the presence of fluxionality. Variable-temperature measurements confirm the fluxionality which is greatly slowed at low

Scheme III:

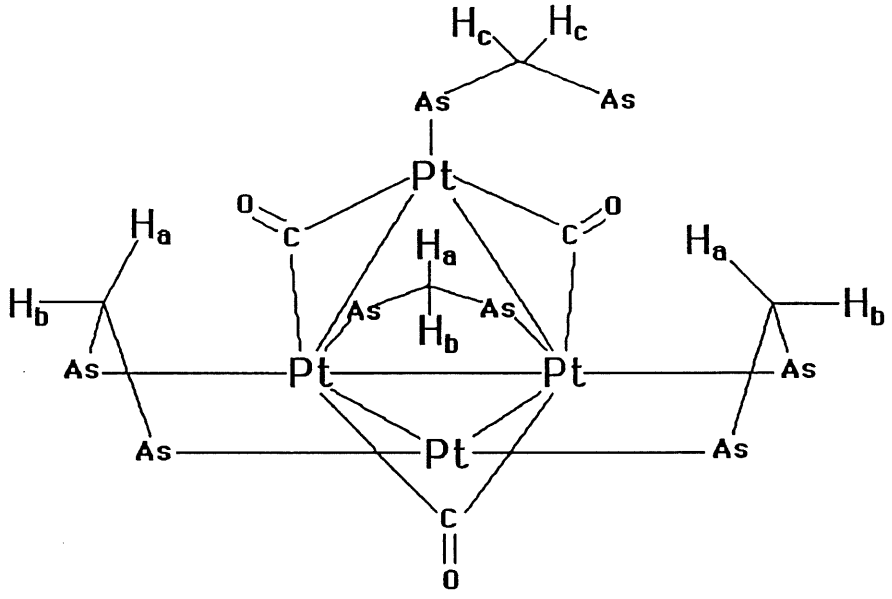

Scheme IV:

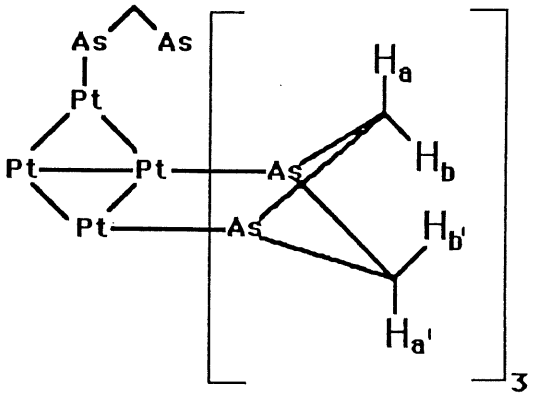

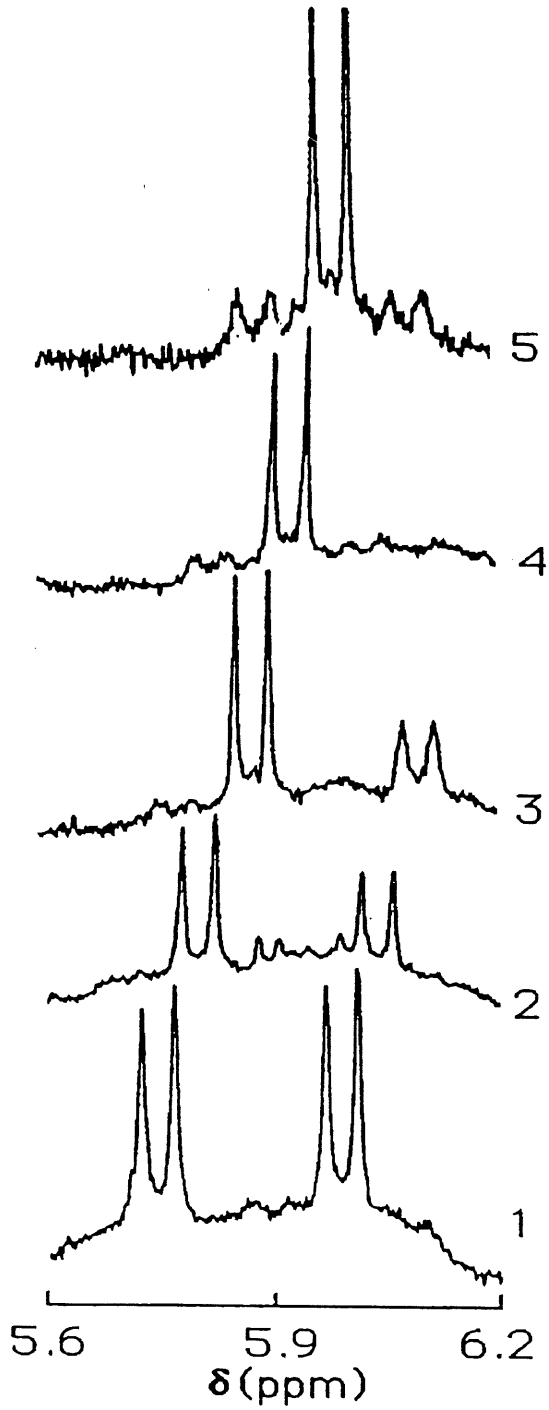

Figure 26. ^{1}H NMR spectra of 4a in DMSO-d_6 in the 5.6-6.2 ppm region (H_b and H_b') as a function of selected temperature: 1-299K; 2-313K; 3-338K; 4-353K and 5-373K.

temperatures (T<193K using acetone-d_6 as solvent). At these temperatures, the spectra become complex readily indicating the loss of the 3-fold symmetry. The results are consistent with a fluxionality process involving a C_3-rotation of the $Pt(\mu_2\text{-}CO)_2(\eta^1\text{-dpam})$ fragment (along with the third bridging CO), over the $Pt_3(dpam)_3$ triangle (Scheme II). This gives rise to three chemically different H nuclei, which are labelled in Scheme III as H_a, H_b, H_c. During the course of the variable-temperature measurements, two conformers have been observed, both having the same signals at different chemical shifts, for both compounds. Conformers 1 and 2 exhibit signals centered at 5.88, 4.03 and 3.48 ppm, and at 5.61, 3.95 and 3.91 ppm, respectively (for the CH_2 region) for **4a** as an example. The $-C_6H_5$ region is far too complex for useful analysis. Upon heating the samples (in DMSO-d_6 for example), conformer 1 is favored while conformer 2 vanishes (Figure 26). The same behaviors are observed for signals

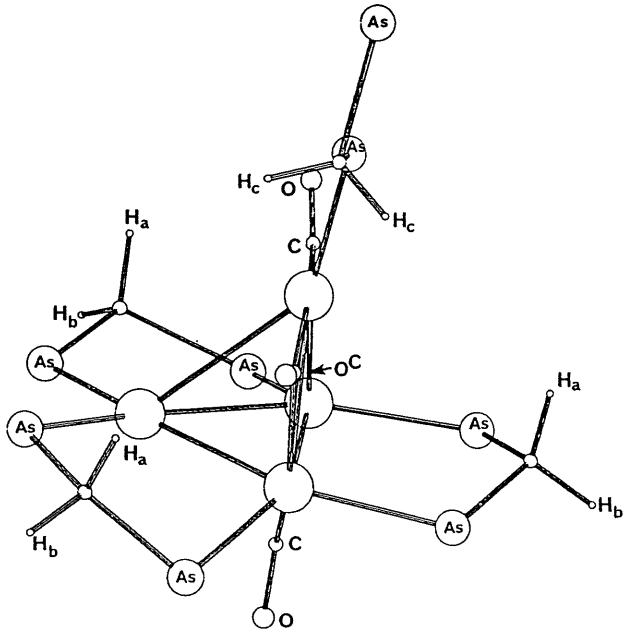

Figure 27. Ball-and-stick drawing based upon the X-ray structure of 4b showing H_a and H_b (conformer 2) with respect to $Pt(\mu_2\text{-}CO)_2(\eta^1\text{-dpam})$ fragment and CO group under the Pt_3As_6 plane. During the C_3-rotation of the fluxional process, H_a lies within the shielding anisotropy cone of the μ_2-CO groups.

centered at ~4 ppm. This process is reversible. These two conformers are related to the three -CH_2- fragments either pointing towards or away from the Pt(η^1-dpam) center (Scheme IV). It is proposed that, e.g. for **4a**, conformer 2 is the stable species where the orientations of three CH_2 groups lead to the least sterically repulsion.

The assignment of the various -CH_2- ^{1}H NMR signals is straightforward. The signal at 3.37 ppm (for conformer 1 for instance) appears as a singlet, and is easily assigned to H_c. The two ^{195}Pt satellites indicated ^{3}J(Pt,H) =39Hz. The signals at 4.03 and 5.88 ppm are the $CH_a'H_b'$ systems, where H_a' points towards the shielding anisotropy cone of the μ_2-CO group under the $Pt_3(dpam)_3$ plane, and appears at 4.03 ppm. In conformer 2, H_a appears at 3.95 ppm and points towards the shielding anisotropy cone of the μ_2-CO group linked to the Pt(η^1-dpam) fragment (Figure 27). In these cases ^{2}J(H_a,H_b) = ^{2}J(H_a',H_b') =13Hz. No coupling with ^{195}Pt occurs (62). The signals for H_b' (conformer 1) and H_b (conformer 2) appear at 5.88 and 5.61

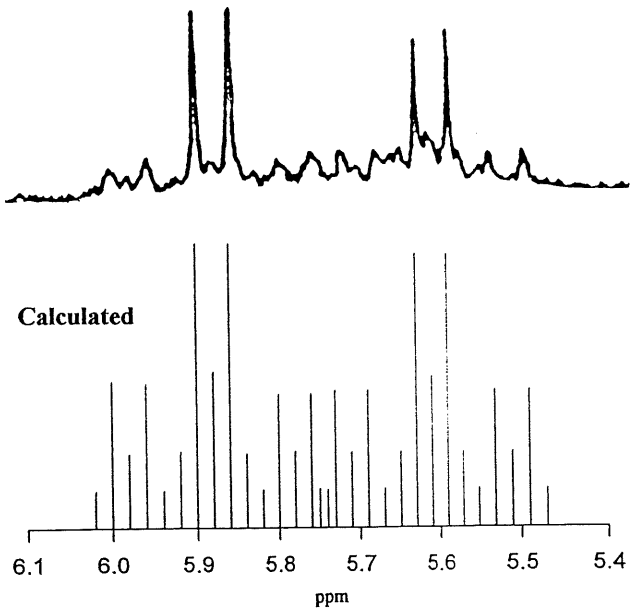

Figure 28. ^{1}H NMR spectra of 4a in the 5.4-6.1 ppm region.

ppm, respectively, where both signals show $^2J(H_a,H_b)= {}^2J(H_a',H_b') = 13$ Hz, as expected. These signals are very complex because of the coupling with the ^{195}Pt and ^1H nucleus. Because of the complexity, the interpretation of the relative intensity must be made taking into account the relative abundance of the isotopomers of the $Pt_3(dpam)_3$ moity (Pt_3=29.4 %, $^{195}PtPt_2$= 44.44 %, $^{195}Pt_2Pt$ = 22.3 %, $^{195}Pt_3$ = 3.73 %). The values of $^3J(Pt,H)$ and $^4J(Pt,H)$ are readily available. $^3J(Pt,H)$ is 60 Hz. Finally the weaker signals near the two strong coupled resonances are assigned to $^4J(Pt,H)$ = 13 Hz (at room temperature, **4a**). Considering the abundance of ^{195}Pt and the above coupling contants, the spectrum in the 5.4-6.1 ppm region can also be calculated (Figure 28) and compared to the experimental spectrum. By taking into account the different bandwith from one NMR peak to another, the comparison is rather good.

The last comment concerns the relative ratio conformer 1/conformer 2 for **4a** and **4b**. This ratio is about 1:1 and 5:1 for **4a** and **4b**, respectively, at room temperature, and conformer 2 in **4b** appears weak at all temperatures. This behavior clearly indicates that CF_3COO^- interacts with the dicationic cluster, in such a way, that conformers favor to exist at room temperature. Part of the answer to this is found in the $Pd_3(dppm)_3(CO)^{2+}$ and $Pd_3(dpam)_3(CO)^{2+}$ cluster host-guest chemistry for which it has been demonstrated that CF_3COO^- interacts more strongly with the unsaturated site of the Pd_3^{2+} center (63, 70). Interaction sites are numerous in **4a** and **4b** and one can not speculate as to how this interaction occurs without a crystal structure.

2.2.4 EHMO computations

Theoretical descriptions of the MO's in cyclic M_3 clusters are numerous (13, 47, 61, 71, 72, 73), but appear to be non existent for M_4 species. Of particular interest for this work, clusters of the type $M_3(\mu\text{-}CO)_3(PR_3)_3$ have been investigated by Evans (72), and by Jaw and Mason (73). For the purposes of this analysis, cluster **4** is considered to be built with two fragments: 1) $Pt_3(\mu\text{-}CO)_3(AsH_3)_5$ and 2) $Pt(AsH_3)_2^{2+}$ bonded to each other via an addition of the

dicationic Pt onto the electron rich Pt-Pt bond (where the two extra AsH_3 groups lie; Scheme V). The first series of computations deal with the model compounds $Pt_3(\mu\text{-}CO)_3(AsH_3)_5$ as fragment A, and $Pt(AsH_3)_2^{2+}$ as fragment B. The interactions occur via the LUMO of fragment B with one of the frontier orbitals (HOMO-1 in this case) of fragment A (Scheme VI). The empty MO for fragment B (-11.06 eV) is composed mainly of Pt d_{xz} and p_x orbitals (

Scheme V:

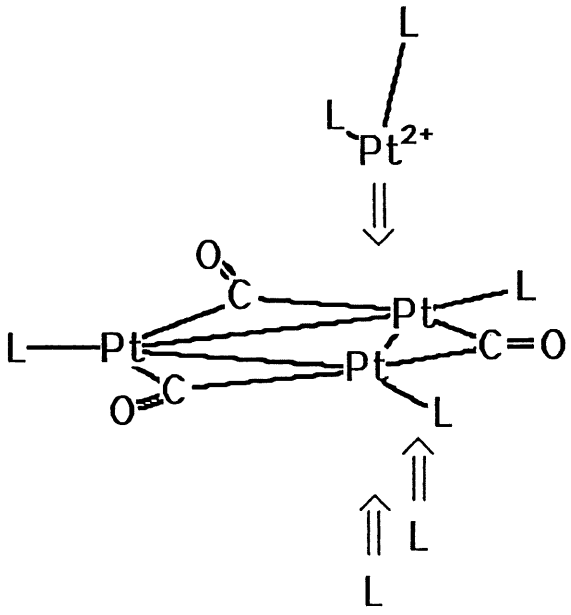

Scheme VI:

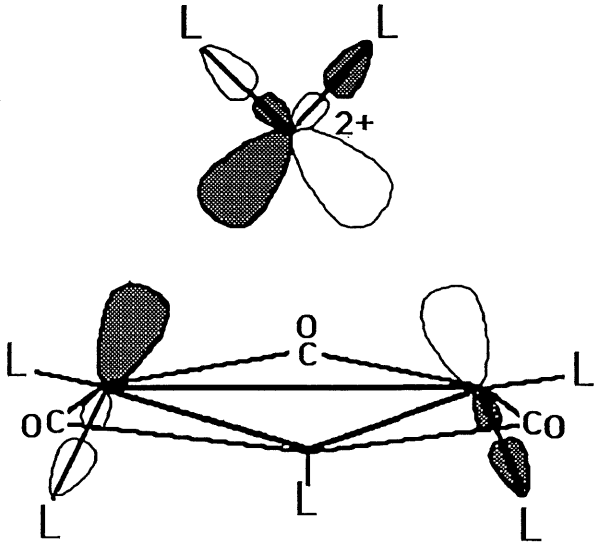

with the z axis being the C_2-rotation axis), and of As p_x, p_z and s MO which form the lone pair orbitals of the AsH_3 groups. The filled MO for fragment A (-10.52 eV) is composed mainly Pt $d_{x^2-y^2}$, d_{xz}, p_z orbitals, and of As p_z orbitals, all located within the interacting Pt-Pt···Pt^{2+} frame. The combination of the $d_{x^2-y^2}$, d_{xz} and p_z Pt orbitals builds a MO with two larger lobes appropriately orientated to favor interactions with fragment A. These interactions generate Pt_2→Pt bonding (HOMO-2; -11.65 eV) and antibonding (LUMO+1; -9.45 eV) MO's (Figure 29), inducing a stablization of 2 electrons by ~0.6 eV. This Pt_2→Pt bonding HOMO-2 exhibits an atomic contribution largely located within the Pt metals also using a minor contribution

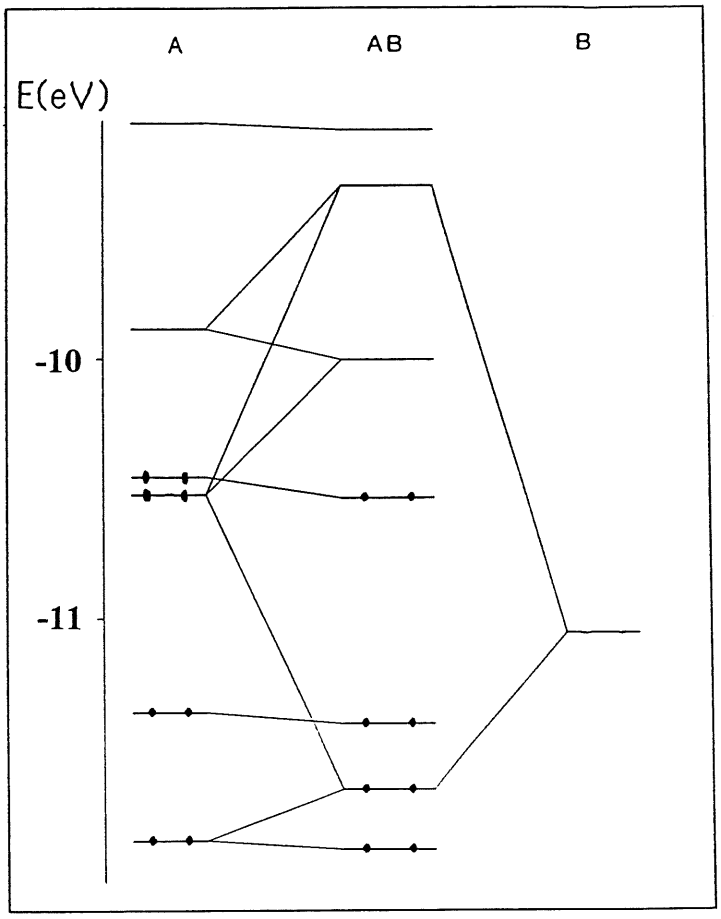

Figure 29. Interaction diagram for $Pt_4(\mu_2\text{-}CO)_3(AsH_3)_7^{2+}$: fragment A = $Pt_3(\mu_2\text{-}CO)_3(AsH_3)_5$; fragment B = $Pt(AsH_3)_2^{2+}$.

from the HOMO-3 of fragment A. As a result the atomic contributions are as follow: edge sharing Pt-Pt bond p_z 8%, d_{x2-y2} 10%, d_{xz} 10%; neutral Pt d_{xz} and d_{xy} 4%; and Pt^{2+} d_{xz} 19%, p_x 10%. Finally ~18% of this MO is formed using the As σ-donor lone pair.

The LUMO and HOMO of $Pt_4(\mu_2\text{-}CO)_3(AsH_3)_7^{2+}$ model compound directly originate from the LUMO and HOMO of fragment A, with very minor perturbation, due to the presence of the Pt^{2+} center (only 2% of the d_{xz}, and 2% s and 4% p_z of the Pt atom contribute to the LUMO and HOMO, respectively). Furthermore, these two MO's appear to be virtually perfectly orthogonal, so the intensity of the lowest energy absorption band is predicted to be weak. The atomic contribution data indicate a large contribution arising from the π*CO system (~55%) in the LUMO. For the HOMO, ~63% of the atomic contributions are located within the Pt_4 frame with very little π*CO, which indicates that the lowest energy electronic transition possesses a great $Pt_4 \rightarrow \pi^*(CO)$ charge transfer character (MLCT). This same conclusion was also reached by Jaw and Mason for $Pt_3(\mu\text{-}CO)_3(PR_3)_3$ species (73).

The last series of computations deal with the variation of the Pt_2-Pt^{2+} bond distances, which were varied from strongly bonded distances of d(Pt-Pt)=2.49 Å, up to weakly interacting distances such as 3.01 Å. The MO energies of the frontier orbitals do not experience dramatic changes with the distance increase. The computed total EHMO energies pass by a minimum somewhere around 2.61 Å. Crystallographically a distance of ~2.60 Å is observed, and compares somewhat favorably with the computations. It is reasonably considered that the relatively small Pt-Pt bond distance in **4b**, in comparison with **1-3**, is due to strong interaction between fragments A and B.

2.2.5 UV-vis and emission spectra

The absorption spectra are characterized by strong bands around 400 nm, a shoulder at ~450 nm, and a long tail extending to ~600 nm (Figure 30). Clearly, there are no strong and allowed

electronic bands in the low energy region, in agreement with the EHMO predictions. Both clusters **4a** and **4b** are not luminescent at 298K, both in the solid states and in solution. However, as an example, **4b** was investigated in ethanol solutions at 77K, and exhibits an emission centered at ~700 nm, with an emission lifetime (τ_e) of 3.2 ± 0.2 μs. Luminescence from bi- or polynuclear Pd and Pt compounds at 77K is not uncommon (28, 74). The large Stoke shift (gap between the lowest energy absorption (~450 nm, shoulder) and the emission maximum, i.e. ~8000 cm^{-1}) and the relatively long lifetime indicate that the emission is a phosphorescence.

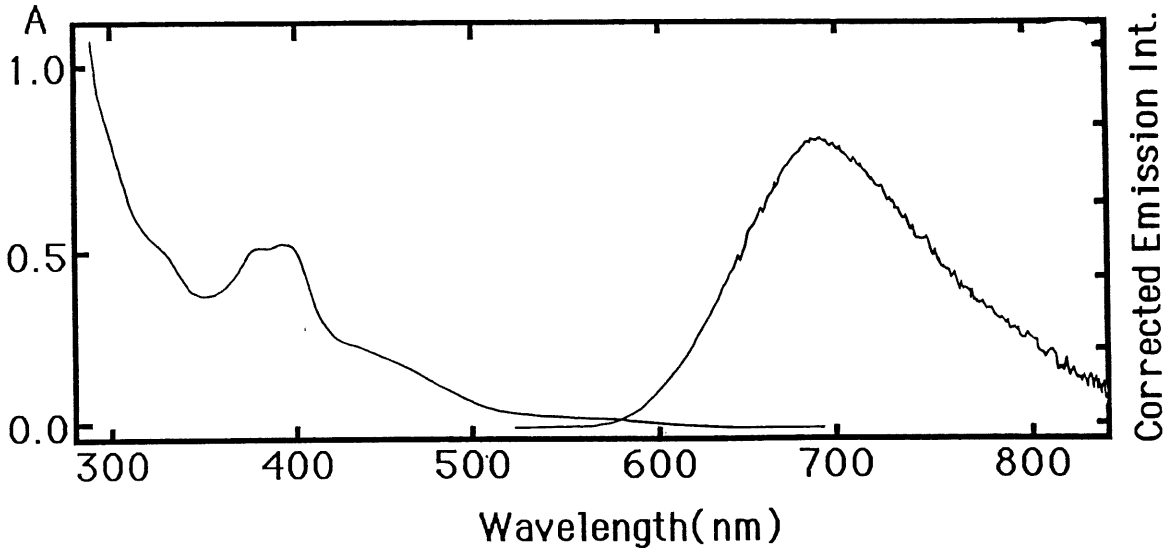

Figure 30. Absorption (left) and emission spectra (right) of 4b in ethanol at 77K

CHAPTER 3

PALLADIUM AND PLATINUM COMPLEXES OF DIISOCYANIDE

3.1 The linear tetranuclear platinum complex $[Pt_4(dmb)_4(PPh_3)_2]^{2+}$ and its diphosphine polymers (dmb=1, 8-diisocyano-*p*-menthane)

Polynuclear complexes containing linear metal-metal chain are currently becoming of considerable interest (14, 15, 16, 17). Incorporation of the units containing metal-metal bonds into the backbone leads to some novel properties of the polymers (75, 76, 77, 78). In linear chain complexes of platinum, the most famous are the conducting polymers, called Krogmann's salts (18). Another family is the so-called "platinum-blue" complexes, where Pt atoms at high oxidation states (≥2) also form linear chains (79). For tetranuclear linear Pt complexes, this chemistry has been dominated by the "platinum-blue" complexes (80, 81-94), where the cluster valence electron count (CVE) is limited to only three counts: 62-, 63- and 64-electrons, with formal Pt oxidation states of 2.00, 2.25 and 2.50, respectively. Recently the chemistry has been expanded to eight atom chain (95) and mixed metal complexes $M_2M'_2$ species (M = Pd, Pt, M' = Cr, Mo) (81, 96). In low oxidation states, platinum atoms also have a strong tendency to form dimers containing metal-metal bond and polyhedral clusters. But a few examples of polynuclear linear chain complexes have been reported, where linear trinuclear platinum chain was prepared by electrochemical reduction of platinum complex in high oxidation state (25), or constructed using tridentate ligand (21, 97). To our knowledge there are no examples of Pt_4 species where the formal oxidation state is lower than 2. Here a new aspect of this chemistry is reported, which led to the preparation and structure of a low valent tetranuclear platinum complex containing a linear chain of metal atoms with a 58-electron CVE, and has been expanded to the preparation of a series of related organometallic polymers containing the units of Pt_4. These species are found to be luminescent at 77K.

3.1.1 Synthesis of $[Pt_4(dmb)_4(PPh_3)_2]Cl_2$

Direct reaction of the d^{10}-d^{10} dimer, $Pt_2(dba)_3 \cdot CHCl_3$ (98) (dba=dibenzylideneacetone), with an excess of diisocyanide, dmb (99), in acetone under inert atmosphere gave an air-sensitive, yellow-orange complex, which was not fully characterized. An addition of triphenylphosphine (PPh_3) to the above complex led to the color change from yellow-orange to red-orange (Scheme VII). This complex was air stable and isolated as a red-orange crystalline solid. The IR spectrum showed that the ν(CN) frequency is 2146 cm^{-1}, which is lower than that of ν(CN) in $Pd_2(dmb)_2Cl_2$ (2170 cm^{-1}) (20), and just higher than that in free dmb (2132 cm^{-1}). This result indicates that the valence for Pt is very low. This compound is readily assigned to the tetramer $[Pt_4(dmb)_4(PPh_3)_2]Cl_2$ using various spectroscopic methods, in particular FAB mass spectrometry (Figure 31). The heaviest fragments clearly arose from $[Pt_4(dmb)_4(PPh_3)_2]Cl$, $[Pt_4(dmb)_4(PPh_3)_2]$, $[Pt_4(dmb)_3(PPh_3)_2]Cl_2$ and $[Pt_4(dmb)_4(PPh_3)]Cl$ (Table 11). In this reaction, two chloride anions are found per Pt_4^{2+} unit, which strongly implies that chlorocarbons react with the Pt(0)-dmb complex in this reaction to give the observed oxidized product.

Scheme VII:

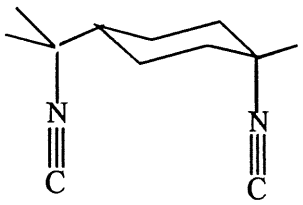

= dmb

$$Pt_2(dba)_3 \cdot CHCl_3 \xrightarrow{+\ dmb} \text{“}Pt_4(dmb)_mCl_n\text{”} \xrightarrow{+PPh_3} [Pt_4(dmb)_4(PPh_3)_2]Cl_2$$

yellow-orange orange

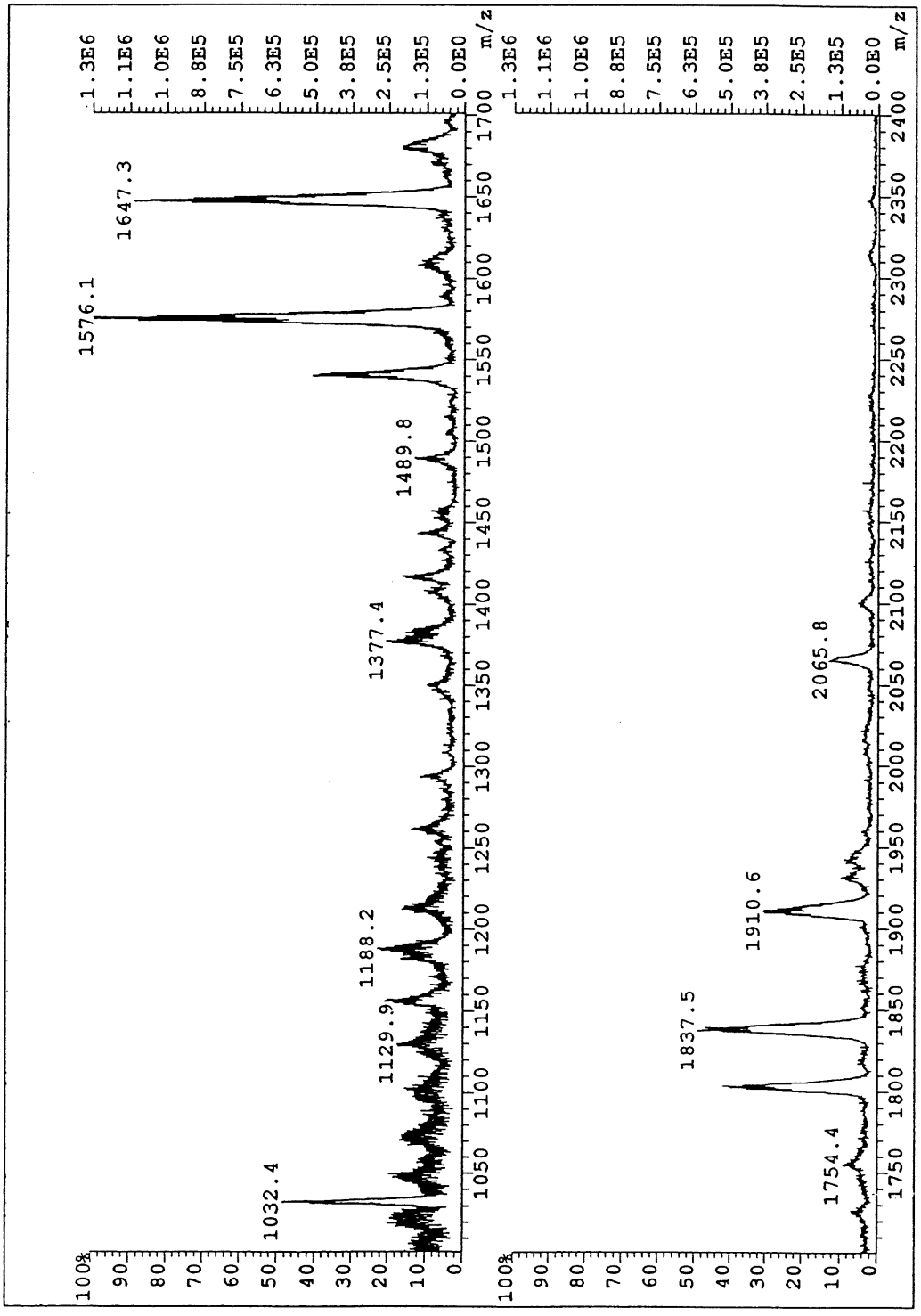

Figure 31. Low resolution mass FAB spectrum of $[Pt_4(dmb)_4(PPh_3)_2]Cl_2$

Table 11. Selected mass FAB data for solid $[Pt_4(dmb)_4(PPh_3)_2]Cl_2$

Peak position	Relative intensity	Assignments	Calc. Mass
1032.4	48	$Pt_2(dmb)_2(PPh_3)$	1033
		$Pt_2(dmb)_3Cl_2$	1031.9
1158	12	$Pt_3(dmb)_3$	1156.1
1188.2	15	$Pt_2(dmb)_4Cl$	1186.8
1294	8	$Pt_2(dmb)_2(PPh_3)_2$	1295.3
		$Pt_2(dmb)_3(PPh_3)Cl_2$	1294.2
1350	7	$Pt_4(dmb)_3$	1351.2
1385	10	$Pt_4(dmb)_3Cl$	1386.6
1418	12	$Pt_3(dmb)_3(PPh_3)_2$	1418.4
		$Pt_3(dmb)_4Cl_2$	1418.3
1489.8	12	$Pt_3(dmb)_2(PPh_3)_2$	1490.4
		$Pt_3(dmb)_3(PPh_3)Cl_2$	1489.3
1542	35	$Pt_4(dmb)_4$	1541.5
1576.1	100	$Pt_4(dmb)_4Cl$	1576.9
1647.3	90	$Pt_4(dmb)_3(PPh_3)Cl$	1648.9
1682	15	$Pt_3(dmb)_3(PPh_3)_2$	1680.7
		$Pt_3(dmb)_4(PPh_3)Cl_2$	1679.6
1754.4	5	$Pt_4(dmb)_2(PPh_3)Cl_2$	1756.4
1804	41	$Pt_4(dmb)_4(PPh_3)$	1803.8
1837.5	50	$Pt_4(dmb)_4(PPh_3)Cl$	1839.2
1910.6	30	$Pt_4(dmb)_4(PPh_3)Cl$	1839.2
1945	8	$Pt_4(dmb)_3(PPh_3)_2Cl_2$	1946.7
2065.8	10	$Pt_4(dmb)_4(PPh_3)_2$	2066.1
2100	3	$Pt_4(dmb)_4(PPh_3)_2Cl$	2101.5

3.1.2 Characterization

3.1.2.1 NMR spectra

^{1}H NMR ^{1}H NMR spectrum of $[Pt_4(dmb)_4(PPh_3)_2]Cl_2$ shows that the ratio between PPh_3 and dmb is 1:2, and exhibits very complex dmb signals spreading over one ppm. This complex ^{1}H NMR behavior does not occur in binuclear compounds of type "$M_2(dmb)_2$" where the dmb ligands are placed trans to each other. It is expected that the orientations of dmb ligands induce the splitting of signals.

^{195}Pt and ^{31}P NMR ^{195}Pt NMR spectrum shows a large peak and a doublet of doublets indicating that there are two kinds of Pt atoms in this complex (Figure 32). Taking into account the intensity and the chemical shift difference between these two doublets, it is easily

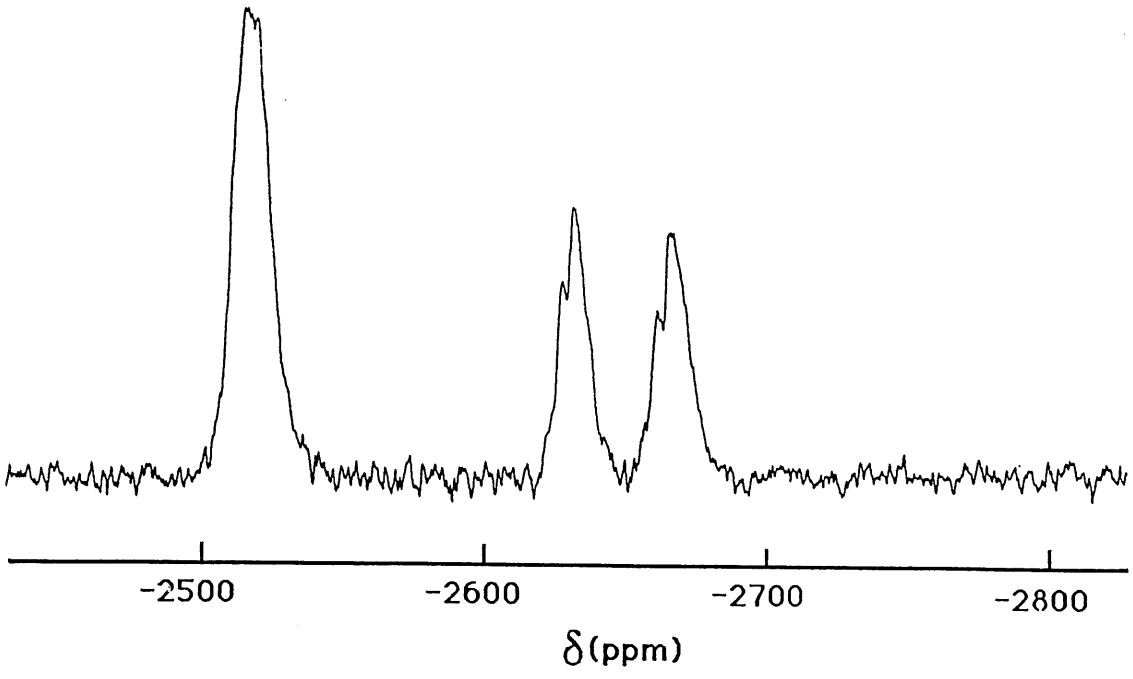

Figure 32. ^{195}Pt-NMR spectrum of $[Pt_4(dmb)_4(PPh_3)_2]Cl_2$ in CD_3CN

deduced that the doublet of doublets at -2700 – -2600 ppm belongs to the Pt nuclei attached by phosphorous atoms, which couple with neigbouring ^{31}P nuclei(^{1}J(Pt-P)), and further couple with the neigbouring ^{195}Pt nuclei (^{1}J(Pt-Pt)). The coupling constants ^{1}J(Pt-P) and ^{1}J(Pt-Pt), are 2250 and 330 Hz, respectively. The greater peak at -2530 ppm comes from the Pt nuclei which are not coordinated by P atoms. Therefore the possible arrangement of four Pt atoms in the complex is linear. The results not only provide information about structural features, but also indicate that, in solutions the linear chain structure remains. In comparison with the ^{195}Pt-NMR spectrum, the ^{31}P-NMR spectrum for $[Pt_4(dmb)_4(PPh_3)_2]^{2+}$ is much complicated. The latter exhibits the expected coupling pattern (Figure 33). Considering the natural abundance of ^{195}Pt nucleus, the ^{31}P NMR is simulated and compared to the experimental data (Table 12). The coupling constants, ^{1}J(Pt-P) and ^{2}J(Pt-P), are 2250 and 448 Hz, respectively, which are the smallest and largest values ever reported for low valent Pt clusters. This comparison includes butterfly and tetrahedral Pt_4, Pt_3 triangle and the $Pt_2(dppm)_3$ dimer, and mainly reflects the difference between cyclic and linear clusters (Table 13).

Table 12. Isotopomer distribution for $[Pt_4(dmb)_4(PPh_3)_2]^{2+}$

Possible Isotopomers		Calculated Abundance
*P-Pt-Pt-Pt-Pt-*P	(a)	19.21%
*P-*Pt-Pt-Pt-Pt-*P	(b)	19.61%
*P-Pt-*Pt-Pt-Pt-*P	(c)	19.61%
*P-*Pt-*Pt-Pt-Pt-*P	(d)	10.01%
*P-*Pt-Pt-*Pt-Pt-*P	(e)	10.01%
*P-*Pt-Pt-Pt-*Pt-*P	(f)	5.01%
*P-Pt-*Pt-*Pt-Pt-*P	(g)	5.01%
*P-*Pt-*Pt-*Pt-Pt-*P	(h)	5.11%
*P-*Pt-*Pt-Pt-*Pt-*P	(i)	5.11%
*P-*Pt-*Pt-*Pt-*Pt-*P	(j)	1.30%

* magnetically active nuclei

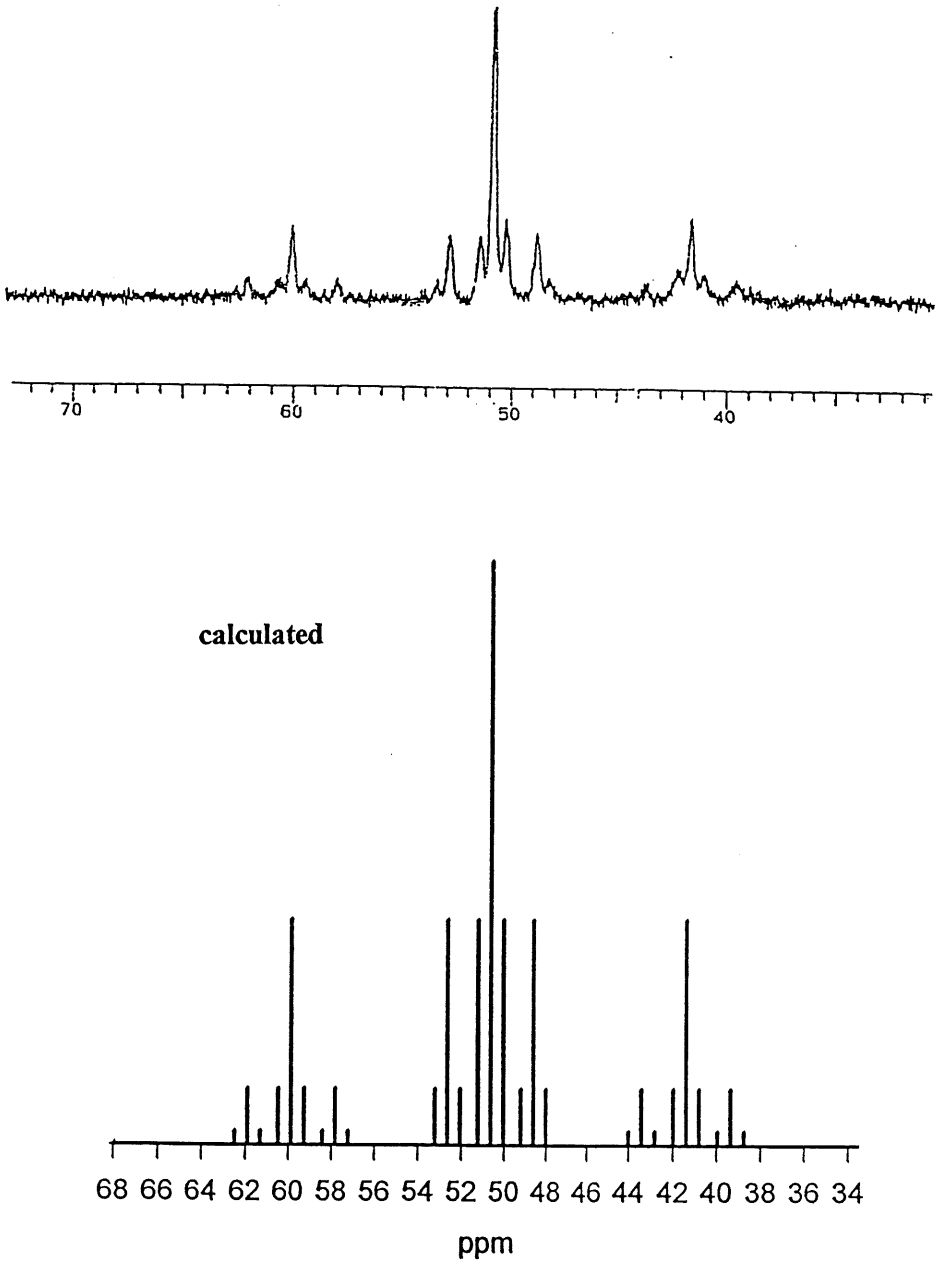

Figure 33. ^{31}**P NMR spectra (experimental and simulated) of** $[Pt_4(dmb)_4(PPh_3)_2]Cl_2$ **in** CD_3CN**. The simulation has been performed using** $^1J(PtP)$**=2200 Hz,** $^2J(PtP)$ **= 490 Hz, and** $^3J(PtP)$ **= 150 Hz.**

Table 13. Comparison of the NMR data(^{31}P, ^{195}Pt) for selected polynuclear Pt complexes

Compounds	δ ^{31}P	$^{1}J(PtP)$	$^{2}J(PtP)$	$^{3}J(PtP)$	δ ^{195}Pt	$^{1}J(PtPt)$	Geo.	Ref.
$[Pt_4(dmb)_4(PPh_3)]^{2+}$	50.5	2250	498	148	-2520	330	linear	this work
$Pt_4(\mu\text{-}CO)_5(PPh_3)_4$	35.5	5118	244	---	-2645	1072	butterfly	55
$Pt_4(\mu\text{-}CO)_5(PPhMe_2)_4$	10.3	5260	260	---	-4180	1110	"	55
$Pt_4(\mu\text{-}CO)_5(PPh_2Me)_4$	25.0	5299	263	---	-4162	1124	"	55
$Pt_4(\mu\text{-}CO)_5(PEt_2)(C(CH_3)_3)_4$	53.6	5074	240	---	-4191	---	"	55
$[Pt_4(\mu\text{-}H)(\mu\text{-}CO)_2(dppm)_3\cdot$	-21.5	3234	---	---	---	---	"	58
$(dppm\text{-}P)]^{+}$	18.8	5400	336	---	-3384	---		
	-31.6	---	---	97	---	---		
$[Pt_4(\mu\text{-}H)(\mu\text{-}CNCH_3)(dppm)_3\cdot$	-22.0	3255	---	---	---	---	"	58
$(dppm\text{-}P)]^{+}$	17.4	5160	342	---	---	---		
	-31.1	---	---	129	---	---		
$[Pt_4(\mu\text{-}H)(\mu\text{-}CO)_2(dppm)_3\cdot$	-21.4	3238	---	---	---	---	"	58
$(dppm{=}O)]^{+}$	15.3	5580	345	---	---	---		
	18.1	---	---	94	---	---		
$Pt_4(\mu\text{-}CO)(CO)_3(PCy_3)_3(H)^{+}$	71.3	3425	230	---	---	---	tetra-	59,100
	49.7	5180	280	---	---	---	hedral	
$Pt_3(\mu\text{-}CO)_3(PCy_3)_3(\mu\text{-}H)^{+}$	38.0	5360	204	---	---	---	triangular	100
$Pt_3(dppm)_3(CO)^{2+}$	-15.1	3720	---	---	-2685	~380	"	11
$Pt_2(dppm)_3$	-36.8	4455	51	--	-47.0	1130	binuclear non-bonded	101

3.1.2.2 Crystal structure

In order to elucidate the structure, red-orange crystals for this complex were grown by diffusing tert-butyl methyl ether into acetonitrile solution of the product. The X-ray diffraction studies confirmed the Pt_4 linear chain structure, and the presence of two Cl^- anions (Table 14,

Table 14. Crystallographic data for $[Pt_4(dmb)_4(PPh_3)_2]Cl_2$

Empirical formula	$\{Pt_4(C_{12}H_{18}N_2)_4[P(C_6H_5)_3]_2\}$ $\bullet(H_2O)_2\bullet(CH_3CN)_2$
Formula sum	$C_{88}H_{112}N_{10}O_2P_2Cl_2Pt_4$
Formula weight	2254.25
Crystal system	Triclinic
Space group	$P\bar{1}$
Unit cell dimensions	a = 12.624 (4) Å b = 14.24 (2) Å c = 27.312(3) Å α = 92.35 (3)° β = 91.655 (15)° γ = 90.28°
Volume	4903(7) $Å^3$
Z	2
Calculated density	1.526 Mg/m^3
Independent reflections	16478
R_1	0.0738
wR_2	0.2097

$R_1=\Sigma(||F_o|-|F_c||)/\Sigma|F_o|$, $wR_2=\{\Sigma[w(F_o^2-F_c^2)^2]/\Sigma w(F_o^2)^2\}^{1/2}$ $[w=1/[\sigma^2(F_o^2)+0.1P)^2$ where $P=(F_o^2+2F_c^2)/3]$.

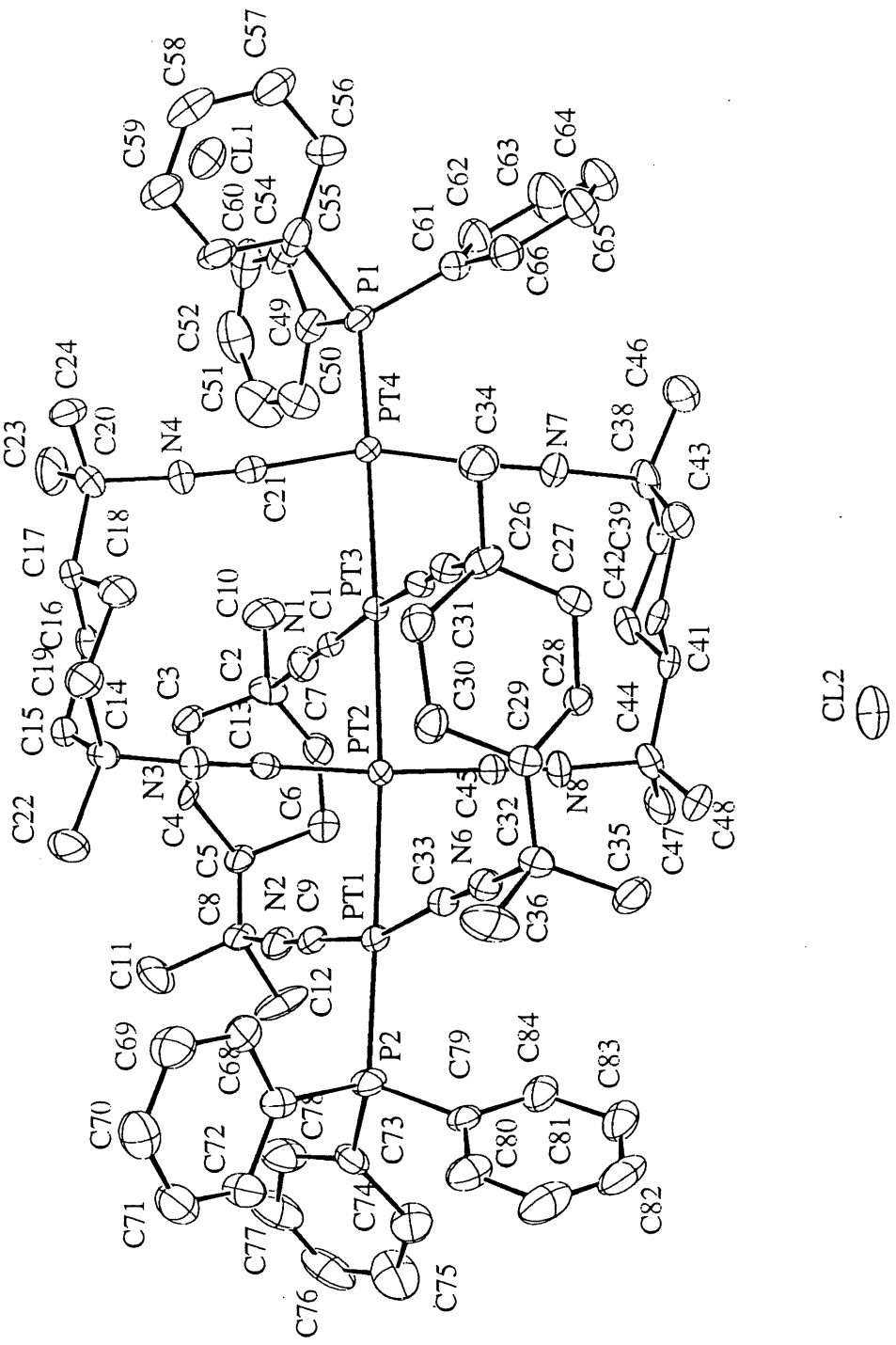

Figure 34. Crystal structure of $[Pt_4(dmb)_4(PPh_3)_2]Cl_2$. The ellipsoids represent 50% probability, and H-atoms and solvent molecules are not shown for clarity.

Table 15. Selected bond distances (Å) and angles (°) for $[Pt_4(dmb)_4(PPh_3)_2]Cl_2$

Pt (1) - P (2)	2.328 (3)	Pt (2) - C (13)	1.914 (9)
Pt (1) - Pt (2)	2.654 (2)	Pt (2) - C (45)	1.916 (9)
Pt (2) - Pt (3)	2.641 (2)	Pt (3) - C (25)	1.934 (10)
Pt (3) - Pt (4)	2.666 (2)	Pt (3) - C (1)	1.935 (10)
Pt (4) - P (1)	2.342 (3)	Pt (4) - C (37)	1.928 (9)
Pt (1) - C (33)	1.926 (9)	Pt (4) - C (21)	1.955 (10)
Pt (1) - C (9)	1.949 (9)		
P (2) - Pt (1) - Pt (2)	171.13 (6)	C (1) - Pt (3) - Pt (2)	84.4 (2)
P (2) - Pt (1) - C (9)	103.3 (3)	C (25) - Pt (3) - Pt (4)	96.5 (2)
P (2) - Pt (1) - C (33)	93.3 (3)	C (1) - Pt (3) - Pt (4)	90.5 (2)
Pt (1) - Pt (2) - Pt (3)	175.775 (18)	P (1) - Pt (4) - Pt (3)	174.84 (7)
C (13) - Pt (2) - C (45)	175.3 (3)	C (37) - Pt (4) - C (21)	160.1 (4)
C (13) - Pt (2) - Pt (3)	88.0 (2)	C (37) - Pt (4) - P (1)	99.6 (3)
C (45) - Pt (2) - Pt (3)	87.5 (3)	C (21) - Pt (4) - P (1)	100.1 (3)
C (13) - Pt (2) - Pt (1)	88.1 (2)	C (37) - Pt (4) - Pt (3)	80.9 (3)
C (45) - Pt (2) - Pt (1)	96.5 (3)	C (21) - Pt (4) - Pt (3)	79.7 (2)
Pt (2) - Pt (3) - Pt (4)	174.825 (19)		
C (25) - Pt (3) - C (1)	172.7 (3)		
C (25) - Pt (3) - Pt (2)	88.6 (2)		

Figure 34). This molecule exhibits an approximate D_2 symmetry. Four platinum atoms are collinear with two phosphorous atoms, forming a six atom quasi-linear chain. Each Pt atom is coordinated by two isocyanide groups and exhibits approximate square-planar geometry. The Pt-Pt distances are 2.666(2), 2.641(2) and 2.655(2) Å (Table 15), which are typical for a Pt-Pt single bond. However these bonds are longer than that of linear triplatinum complex (25) and

Table 16. Comparison of the PtPt distances for various Pt_4 species

Compounds	d(PtPt)/Å		CVE	Formal	References
	outer	inner		oxidation state	
$[Pt_4(dmb)_4(PPh_3)_2]^{2+}$	2.655 (2)	2.641(2)	58	0.50	This work
	2.666(2)				
$[Pt_2(NH_3)_4(C_5H_4ON)_2]_2^{4+}$	2.877	3.129	64	2.00	86
$[Pt_2(en)_4(C_5H_4ON)_2]_2^{4+}$	2.9915(4)	3.2355(5)	64	2.00	87
$[Pt_4(NH_3)_8(C_4O_4)]$	3.162 (2)	3.197(3)	64	2.00	92
$[Pt_2(NH_3)_4(C_5H_6NO)_2]_2^{4+}$	3.022(2)	3.186(2)	64	2.00	80
$[Pt_2(NH_3)_4(C_5H_5N_2O_2)_2]_2^{4+}$	3.131	3.204	64	2.00	93
$[Pt_2(bpy)_2(3,3\text{-}DMGI)_2]_2^{4+}$	2.877	3.129	64	2.00	81
	2.833				
$[Pt_4(NH_3)_8(C_4H_6NO)_4](PF_6)_2(NO_3)_{2.56}$	2.848	2.875		2.14	82
	2.839	2.875			
$[Pt_2(NH_3)_4(C_5H_6ON)_2]_2^{5+}$	2.779	2.885	63	2.25	88
	2.7745(4)	2.8770(5)			
$[Pt_4(en)_4(C_5H_4ON)_4]^{5+}$	2.8296(5)	2.9158(6)	63	2.25	89, 90
$[Pt_2(NH_3)_4(C_5H_5N_2O_2)_2]_2^{5+}$	2.810(2)	2.866(2)	63	2.25	89
	2.793(2)				
$[Pt_4(NH_3)_8(DMGI)]^{5+}$	2.7745 (4)	2.8770(9)	63	2.25	83
$[Pt_4(NH_3)_8(C_4H_6NO)_4](NO_3)_{5.48}$	2.764(8)	2.739(8)		2.37	84
	2.740(8)	2.724(8)			
	2.761(8)				
	2.753(9)				
$[Pt_4(NH_3)_8(C_5H_6ON)_4]_2^{6+}$	2.702	2.709	62	2.50	85
	2.705				

much shorter than those of the so-called "platinum blue" tetranuclear platinum complexes (Table 16). The Pt-P bond lengths are normal (2.328(3) and 2.342(3) Å). The interesting feature is that two dmb ligands bridge two Pt metal atoms forming "$M_2(dmb)_2$" units, 20-membered rings, which are commonly encountered in dinuclear and trinuclear species (20, 26, 28, 30, 102, 103). More interestingly a catenate structure is observed, where two dmb ligands coordinate the first and third Pt atoms, while two others bind the second and fourth. In other words, the two 20-membered rings ($Pt_2(dmb)_2$) are interlocking each other. To our knowledge this is unique in dmb chemistry and rare in inorganic chemistry. The dihedral angle between the $Pt_2(CN)_4$ planes is 75°, not the expected 90°, which is similar to that found in the linear tripalladium complex (23). The dmb bite distances, 5.307(4) and 5.296(4) Å, are very long. The other examples of long dmb bite distances include the encapsulation complex $[Ir_2Ag(dmb)_4]^{3+}$, d(Ir···Ir)=5.284 Å (30, 102), and recently reported polymers $\{[Ag(dmb)_2]Y\}_n$ where Y=PF_6^-, BF_4^-, NO_3^-, ClO_4^-, CH_3COO^- and $TCNQ^-$, 4.9496(1)≤ d(Ag···Ag) ≥ 5.1884(6) (26, 104).

It was reported that metal ion with d^{10} electronic configuration (Ag^+), was encapsulated by dinuclear complex of dmb ($[Ir_2(dmb)_4]^{2+}$) to form trinuclear linear chain complex (102), and Pt(0) species could insert to Pt-Pt bond of dinuclear complex, $[Pt_2(dppm)_2(CNCH_3)_2]^{2+}$, to give "A-frame" complex, $[Pt_3(dppm)_2(CNCH_3)_3]^{2+}$, which was prepared by the reaction of $[Pt_3(CNCH_3)_8]^{2+}$ and the diphosphine ligand, dppm, according to a mechanism proposed by Yamamoto (25). From this viewpoint, this new tetranuclear complex containing linear metal-metal chain, can be considered as the product of encapsulation of one metal atom of one dinuclear complex to another dinuclear complex.

3.1.3 Isomers (head to tail dmb chemistry)

The unsymmetrical dmb ligand, in the complex, can adopt different orientations, which will lead to both geometric and optical isomers. In this molecule, it is expected that this situation

will be complex compared to the dinuclear compounds. Crystallographic studies for $[Pt_4(dmb)_4(PPh_3)_2]Cl_2$ indeed indicate disorder of the dmb within complex. Theoretically the different orientations of four dmb ligands will give five geometric and two optical isomers for $[Pt_4(dmb)_4(PPh_3)_2]Cl_2$ (Figure 35). This head to tail chemistry has previously been reported for "wind mill" $M_2(dmb)_4$ compounds (102), where four geometric isomers are possible. It is

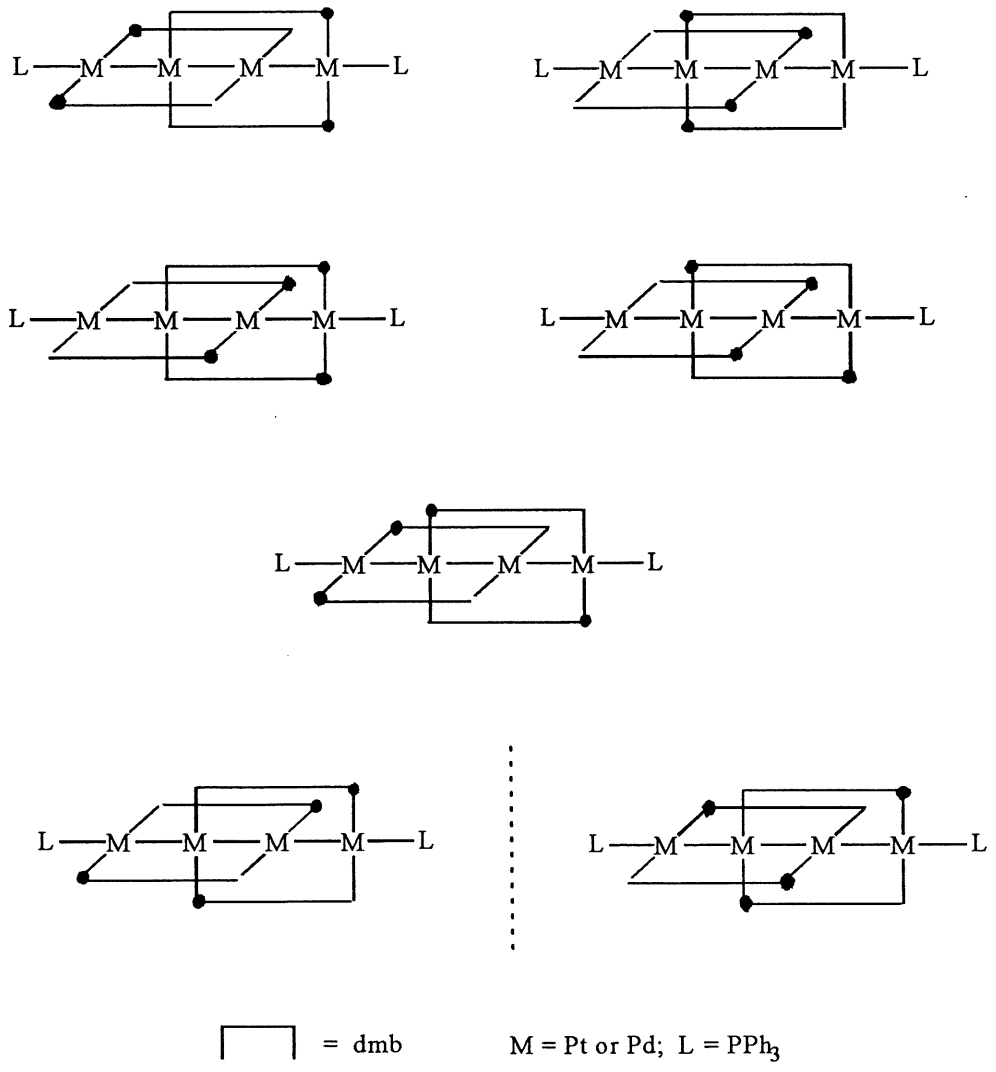

Figure 35. Schematic drawings of the 5 geometric and 2 optical isomers for the $[M_4(dmb)_4(PPh_3)_2]^{2+}$ cluster, showing the head-to-tail chemistry of dmb ligand.

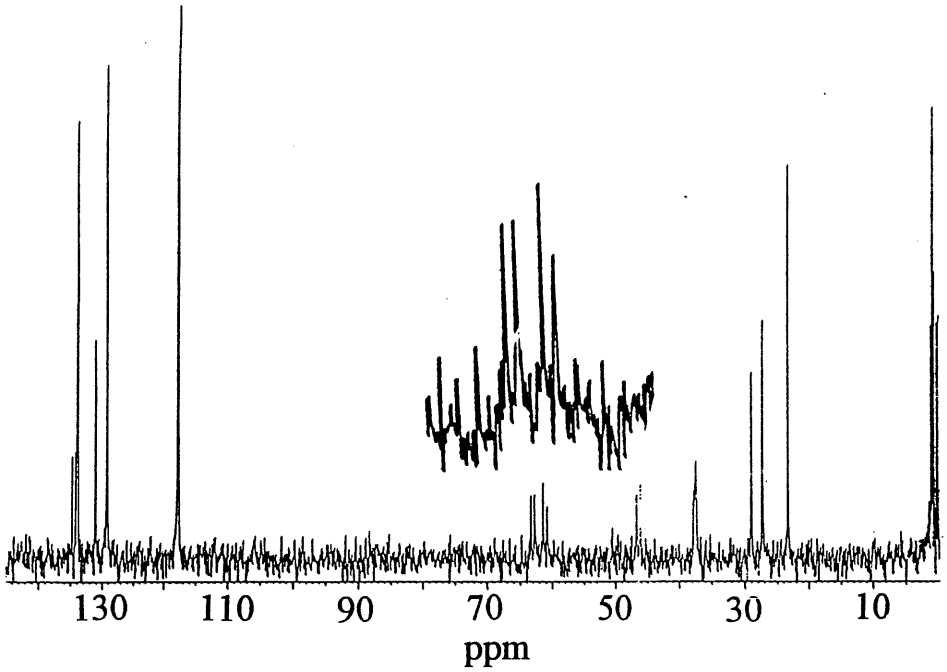

Figure 36. ^{13}C NMR spectrum for $[Pt_4(dmb)_4(PPh_3)_2]Cl_2$
Solvent: Acetonitrile-d_3

expected that in the different isomers of $[Pt_4(dmb)_4(PPh_3)_2]Cl_2$, the different orientations of the unsymmetrical ligands lead to different environments in this molecule, which induce a difference in chemical shifts. These differences are reflected in ^1H and ^{13}C NMR spectra.

For the dinuclear and polymeric complexes, the signals of two quaternary carbon atoms in dmb ligand, generally appear at about 62 and 63 ppm, respectively (26). Because there are two kinds of orientations for dmb ligands, it is believed that there are two kinds of different environments in this complex, which induce the splitting of the peaks. For this tetrameric complex, each of the two signals are indeed split into two peaks (Figure 36). This complexity is clearly associated with the relative proximity of the dmb's placed cis to each other inducing greater chemical shift differences (when compared to a trans geometry), and to the fact that two types of Pt nuclei are present (inner and outer). These phenomena give direct evidences that the geomertric isomers are present in solutions.

3.1.4 Raman spectrum

In order to address the amplitude of the M_2 interactions, the Raman spectrum was measured in the solid state (Figure 37). The strategy of assignment is based on the comparison with literature data for closely related Pt clusters (for which $\nu(M_2)$ has been confirmed by resonance Raman), also taking into account the M_2 bond lengths or separations, and the commonly encountered high intensity of the $\nu(M_2)$ modes (105). Resonance Raman could not be used in this work as the sample proved to be extremely laser sensitive. However the two totally symmetric $\nu(M_2)$ modes are readily observed at 162 and 84 cm^{-1} as only these two

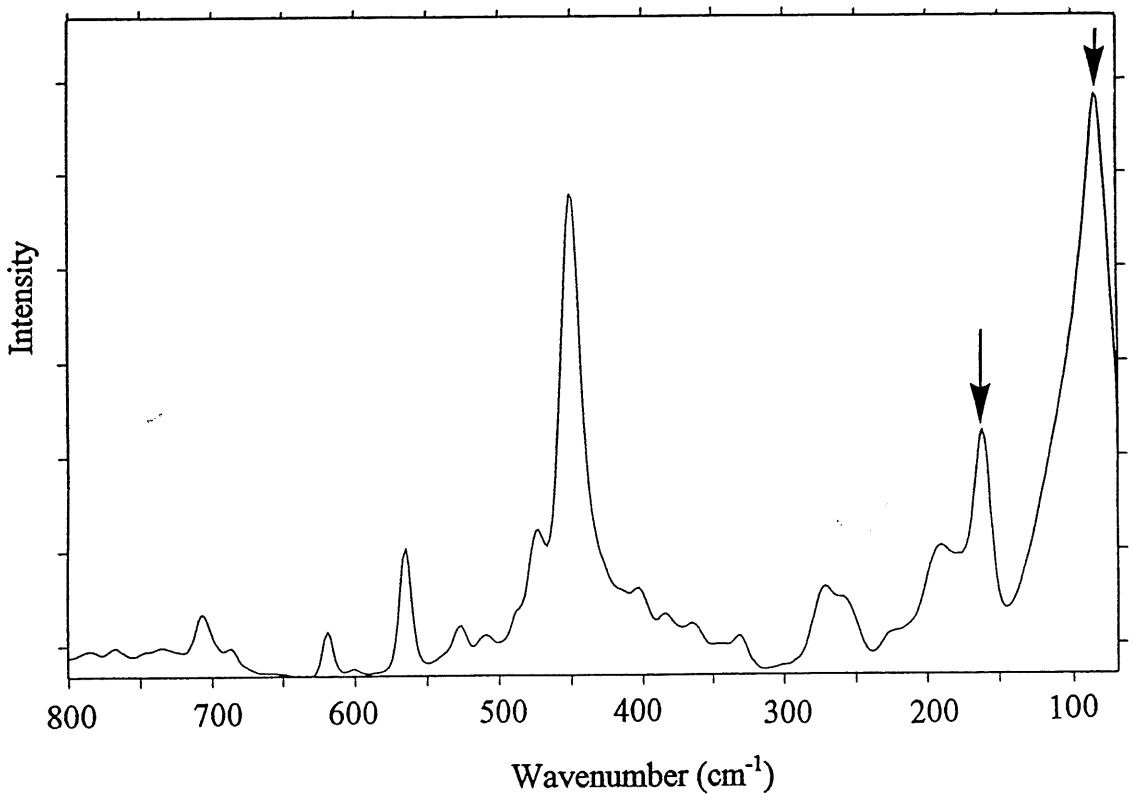

Figuire 37. FT-Raman spectrum for solid $[Pt_4(dmb)_4(PPh_3)_2]Cl_2$. Experimental conditions: resolution: 2.60 cm^{-1}, no. of scans: 100, temperature: 298 K, laser power: 100 mW at 1064 nm.

signals are present in this region. The favorable comparison of these two frequencies with literature for well established compounds indeed supports the assignments (Table 17). Using an empirical equation relating $d(Pt_2)$ with $F(Pt_2)$, the metal-metal force constant (in mdyn·Å^{-1}) (106), and the average $d(Pt_2)$ data (2.66 Å),

$$d(Pt_2) = -0.233\ln F(Pt_2) + 2.86 \qquad [3.1]$$

equation 3.1 gives $F(M_2)$ 2.36 mdyn·Å^{-1}, and is normal for Pt-Pt single bonds.

Table 17. Comparison of the spectroscopic and structural data for linear Pt_3 and Pt_4 complexes.

Compounds	Assignment method	ν(M-M)/cm^{-1}	d(M-M)/Å	Reference
$[Pt_4(dmb)_4(PPh_3)_2]^{2+}$	rel. int. + comp.	162 (a_1) 84 (a_1)	2.655(2), 2.641(2) 2.666 (2)	this work
$[Pt_4(NH_3)_8(C_5H_4NO)_4]^{5+}$	RR	149 (a_{1g}) 69 (a_{1g})	2.774 2.877	88,90,91,107
$[Pt_4(NH_3)_8(C_5H_5N_2O_2)_4]^{5+}$	RR	149 (a_{1g}) 67 (a_{1g})	2.793, 2.865 2.810	89, 107
$[Pt_4(en)_4(C_5H_4NO)_4]^{5+}$	RR	133 (a_{1g}) 67 (a_{1g})	2.830, 2.830 2.906	89,90,107
$[Pt_3(popop)_4]^{6+}$	RR	147 (IR) 85 (R)	2.925	108,109

*RR=Resonance Raman. Rel. int. comp.= assignments based upon the high intensity of the ν(Pt-Pt), and by comparison of data for well established compounds such as these included here.

3.1.5 Preparation and characterization of polymers containing $[Pt_4(dmb)_4]$ units

Organometallic polymers containing metal-metal bonds in the polymer backbone are expected to have some novel photochemical and conductive properties (110). From the structure of $[Pt_4(dmb)_4(PPh_3)_2]Cl_2$, it is clear that the phosphine ligands prefer to coordinate the axial positions. Polymers containing $[Pt_4(dmb)_4]$ units are possible to be prepared using diphospine ligands, instead of the monodentate triphenylphosphine ligand (PPh_3).

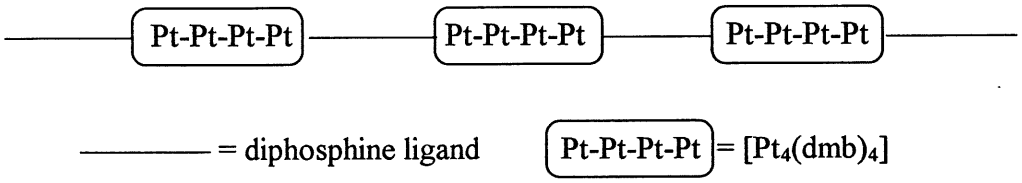

Three diphosphine ligands, $Ph_2P\text{-}(CH_2)_n\text{-}PPh_2$ (n = 4, dppb; n = 5, dppp; n = 6, dpph) have been used to link the $[Pt_4(dmb)_4]$ units. Indeed these Pt_4-diphosphine polymers have been synthesized in good yields. They turn out to be more oxygen sensitive than the corresponding monomer, $[Pt_4(dmb)_4(PPh_3)_2]Cl_2$. The related spectroscopic data are listed and compared in Table 18. The UV-vis and IR spectra are very similar to that of the tetrameric monomer, and the ^1H, ^{13}C and ^{31}P NMR spectra also give the same patterns, suggesting that the units of $[Pt_4(dmb)_4]$ remain in these compounds. The ^{31}P NMR spectra exhibit no evidence of free phosphine ligands, indicating that the concentration of end groups is very low. Furthermore the integration of the ^1H phenyl and dmb signals also suggests that these materials are long polymers.

3.1.6 X-ray powder diffraction

In order to provide further support for the existence of $[Pt_4(dmb)_4]$ units in these polymers, the X-ray powder diffraction studies have been carried out (Figure 38). The diffraction patterns for $[Pt_4(dmb)_4(PPh_3)_2]Cl_2$ and polymers show a fairly good correspondence between

Table 18. Spectroscopic data for $[Pt_4(dmb)_4(PPh_3)_2]Cl_2$ and related polymers

Compounds	^{1}H NMR*	^{31}P NMR*		IR(KBr)	UV(CH_3CN)
	δ ppm	^{1}J(Pt-P) ^{2}J(Pt-P) Hz	δ ppm	ν(CN) cm^{-1}	λ nm
$[Pt_4(dmb)_4(PPh_3)_2]Cl_2$	0.9-2.0(comp. dmb)	2252	51.0	2146	404, 348
	7.3-7.6(comp. Ph)	497			302
$\{[Pt_4(dmb)_4(dppb)]Cl_2\}_n$	0.9-2.1(comp. dmb, CH_2)	2198	54.5	2145	396, 362
	2.76(m, CH_2-P)	486			294
	7.3-7.8(comp. Ph)				
$\{[Pt_4(dmb)_4(dppp)]Cl_2\}_n$	0.9-2.1(comp. dmb, CH_2)	2185	54.8	2144	396, 362
	2.60(m, CH_2-P)	498			296
	7.3-7.8(comp. Ph)				
$\{[Pt_4(dmb)_4(dpph)]Cl_2\}_n$	0.9-2.1(comp. dmb, CH_2)	2212	50.0	2143	394, 364
	2.76(m, CH_2-P)	502			298
	7.3-7.9(comp. Ph)				

* CD_3CN was used as solvent.

comp. = complex; CH_2 = CH_2 group of diphosphine ligand; CH_2-P = -CH_2-PPh_2

their patterns (all the polymers give the same diffraction.). However the important difference is that the polymeric materials are clearly amorphous, while the $[Pt_4(dmb)_4(PPh_3)_2]Cl_2$ is relatively more crystalline. In some way, this result is consistent with the polymeric nature of the material.

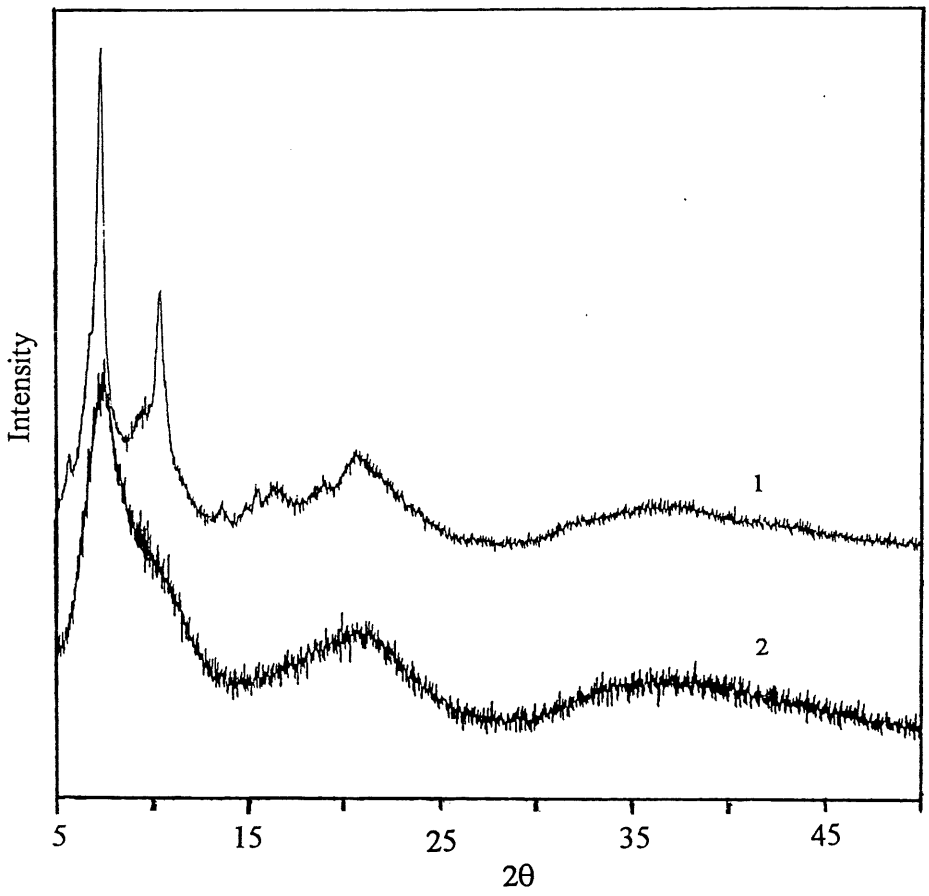

Figure 38. X-ray powder diffraction patterns for $[Pt_4(dmb)_4(PPh_3)_2]Cl_2$ and its polymer. 1-$[Pt_4(dmb)_4(PPh_3)_2]Cl_2$; 2-$\{[Pt_4(dmb)_4(dpph)]Cl_2\}_n$

3.1.7 Viscosity and T_1 measurements

In order to address the polymeric features of these $[Pt_4(dmb)_4]$-diphosphine complexes, these materials are characterized by both T_1 (of the quaternary carbon of dmb ligand) and viscosity measurements. If T_1^{DD} is simply taken as a main variable, it is inversely proportional to τ_C (the correlation time), which is related to the volume of the tumbling molecule (Eq. 1.43). Therefore the smaller is T_1 value, the greater the molecular weight of the materials is (Eqs. 1.40 and 1.41). This approximation is useful in predicting the relative molecular weights of the

polymers $\{[M(dmb)_2Y\}_n$ (26). Compared to the T_1 values of monomer ($[M(CN\text{-}t\text{-}Bu)_4^+$, M=Cu, Ag; ~ 35 s) (111), dimer (~ 7.5 s) (111) and tetramer (3.76 s), T_1 values of these materials are, in fact, very low, which give some evidences that these complexes are of larger sizes.

Table 19. The values of T_1 and intrinsic viscosities of polymers*

Compounds	T_1(s)	$[\eta]$ (cm^3g^{-1})
$\{[Pt_4(dmb)_4(dppb)]Cl_2\}_n$	2.19	3.66
$\{[Pt_4(dmb)_4(dppp)]Cl_2\}_n$	1.69	4.78
$\{[Pt_4(dmb)_4(dpph)]Cl_2\}_n$	2.26	2.06
$\{Cu(dmb)_2BF_4\}_n$*	---	3.08

*Acetonitrile as a solvent; Polymer $\{Cu(dmb)_2BF_4\}_n$ is used as a standard ($\overline{M_n}$ = 133,000 g/mol from osmometry) to determine the magnitude of these polymers.

The viscosity of polymer-containing solutions is known to increase with the concentration. In acetonitrile, the viscosities of these solution are clearly larger than that of the solvent alone, indicating the polymeric character (Figure 39). Due to the novelty of the materials, the known and related $\{[Cu(dmb)_2]BF_4\}_n$ polymer (MW=156,000 from light diffusion (26), MW_n= 133,000 from osmometry (111)) is used to extract the constant K according to Eq. 1.65, and constant a is set to be 0.65 (an average between 0.5 and 0.8, the two extreme limits observed in the literature (46)). In this case, $[\eta]$ = 3.08 cm^3g^{-1} and K is evaluated to be ~1.30×10^{-3}. The results of the viscosity measurements are given in Table 19, clearly indicating polymeric features of these complexes. The estimated molecular weights range from ~84,000 (~ 40 units, $\{[Pt_4(dmb)_4(dpph)]Cl_2\}_n$) to ~307,000 g/mol (~ 150 units, $\{[Pt_4(dmb)_4(dppp)]Cl_2\}_n$). It

is anticipated that the number of CH_2 groups in the diphosphine ligands controls the local conformations and the overall geometry, hence controlling the dimensions of the polymers. Another factor is the quantity of residual phosphine oxides, which end the propagation of the polymeric chain. No attempt was made to vary these polymeric dimensions at this time. It is interesting to note that the results of viscosity measurements are consistent with that of T_1 measurements.

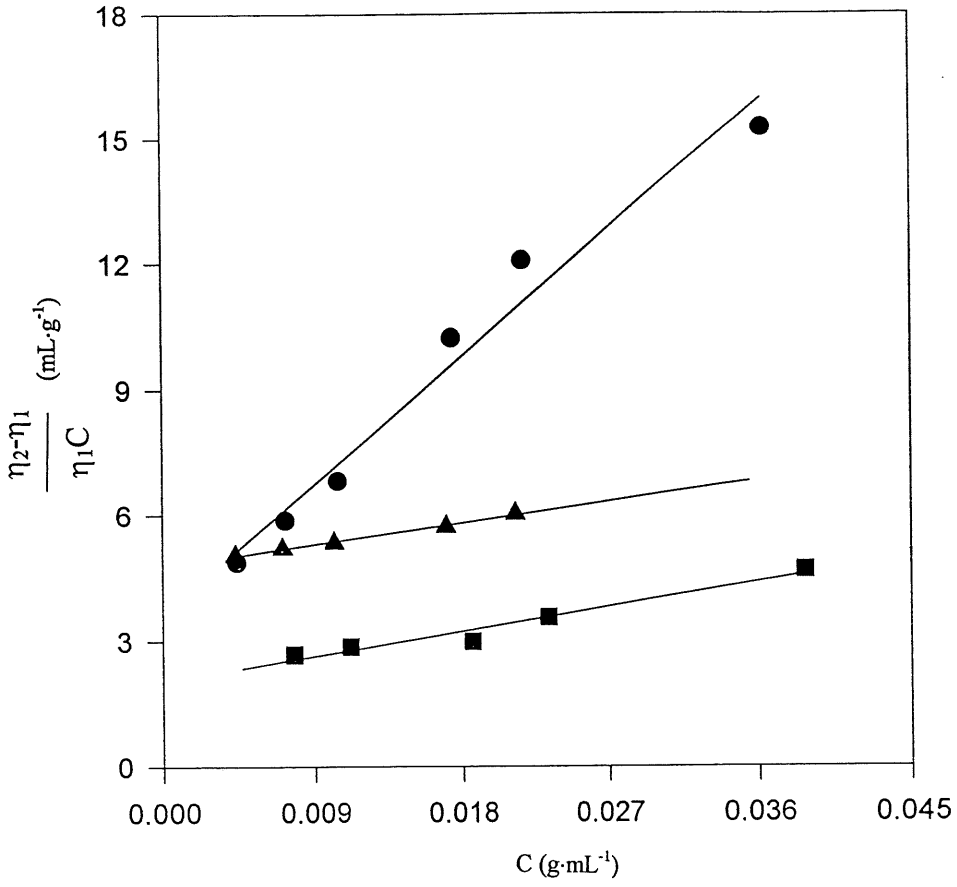

Figure 39. The concentration dependence of the viscosity number at low concentrations. Solvent: acetonitrile. ●—$\{Pt_4(dmb)_4(dppb)Cl_2\}_n$; ▲—$\{Pt_4(dmb)_4(dppp)Cl_2\}_n$; ■— $\{Pt_4(dmb)_4(dpph)Cl_2\}_n$.

3.1.8 EHMO computations

This section addresses the MO picture of the Pt_4 cluster qualitatively since it is the first of this kind, where the intermetallic distances are the shortest and the formal oxidation state of metal is the lowest in the Pt_4 series. Some related works were well described in ref. 112, notably for the description of the related linear chain $Pt(CN)_4^{x-}$ species, the ML_3 fragment, and the singly bonded $Pd_2(dmb)_2X_2$ complexes (X = Cl, Br, I) (28, 113), including the effect of the PdL_3-PdL_3 twist angle on the MO diagram. In the latter cases, the M_2 σ-bonding arises from two square planar $\bullet ML_3$ fragments (i.e. $\bullet Pd(CNR)_2X$) interacting side-by-side (Scheme VIII). These interactions generate the dδ/dδ* and dσ/dσ* MO's. Due to symmetry, these MO's are bound to mix greatly. In addition the HOMO and LUMO exhibit atomic contributions involving the s and p_z orbitals of metal, as well as some orbitals provided by the various ligands. The present computational results are consistent with previous findings which are described below.

Scheme VIII:

For $[Pt_4(dmb)_4(PPh_3)_2]^{2+}$, the model complex $[Pt_4(CNCH_3)_8(PH_3)_2]^{2+}$ is used, and can be best described by the interactions of the fragments $PtL_2(PH_3)^+\cdots PtL_2\cdots PtL_2\cdots PtL_2(PH_3)^+$ (L= $CNCH_3$). The first calculations deal with the geometry where the twist angle is set at 90°. The $\bullet PtL_2(PH_3)^+$ fragment (C_{2v} local symmtry) is isolobal with $AuPR_3$, $Mn(CO)_5$, H and CH_3

which possess a frontier orbital of a_1 symmetry (Scheme IX). This a_1 orbital is essentially a dp hybrid which bulges outside of the planar T-shaped Pt fragment, and its atomic contribution is as follows: 16% d_{z2}, 36% d_{x2-y2}, 12% p_x and 18% s Pt orbitals (the x axis is parallel to the missing vertex of the Pt square-planar coordination). Below this orbital lie the remaining four d M atomic orbitals. The interactions of this fragment with a linear PtL_2 complex (L= $CNCH_3$) generate a new fragment $[(H_3P)L_2Pt\text{-}PtL_2\bullet]^+$, which is also isolobal to that described above (also C_{2v} local symmetry). The MO scheme for this fragment is almost entirely dominated by the Pt-Pt bonding. A qualitative correlation diagram between $\bullet PtL_2(PH_3)^+$ and $\bullet PtL_2\text{-}PtL_2(PH_3)^+$ is provided in Figure 40. The singly occupied a_1 frontier orbital which arises from a $d\sigma^*$ MO of the binuclear fragment, also exhibits this dp hybrid pointing towards the missing vertex of the square-planar Pt coordination. One important difference with literature works (generally using phosphine ligand), is that this frontier orbital is heavily mixed with the π-system of the CNR ligands. For the lower energy MO's, no or very little mixing with the π-system of the CNR ligands occurs.

Scheme IX:

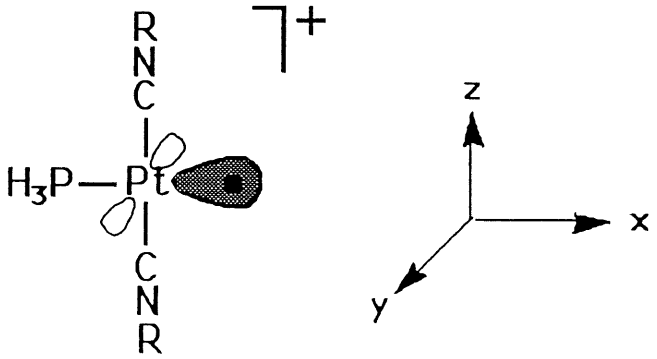

Subsequently, the interactions between two $\bullet PtL_2\text{-}PtL_2(PH_3)^+$ fragments generate the model complex. The overall computational results are presented in Table 20, and the main features are as follows: 1) the HOMO is a filled $d\sigma^*$ involving d_{x2-y2}, d_{z2}, s and p_x M orbitals (x still being the Pt_4 molecular axis) ; 2) as predicted four $d\pi/d\pi^*$, four $d\delta/d\delta^*$, and two $d\sigma/d\sigma^*$

MO's are observed; 3) the HOMO-1 to HOMO-18 (which are all essentially M centered) are closely located (within ~1.6 eV); and 4) numerous dσ, dσ*, dδ and dδ* MO's are greatly mixed in nature. This EHMO model places four quasi-degenerated π*(CNR) MO's as LUMO+1–LUMO+4, and the expected empty dσ* as LUMO. The latter lies just ~ 0.06 eV below the π*(CNR)'s. Since EHMO is a qualitative method, such a small difference is not significant in addressing the correct relative MO energies. In this case, experiments are necessary to address this problem.

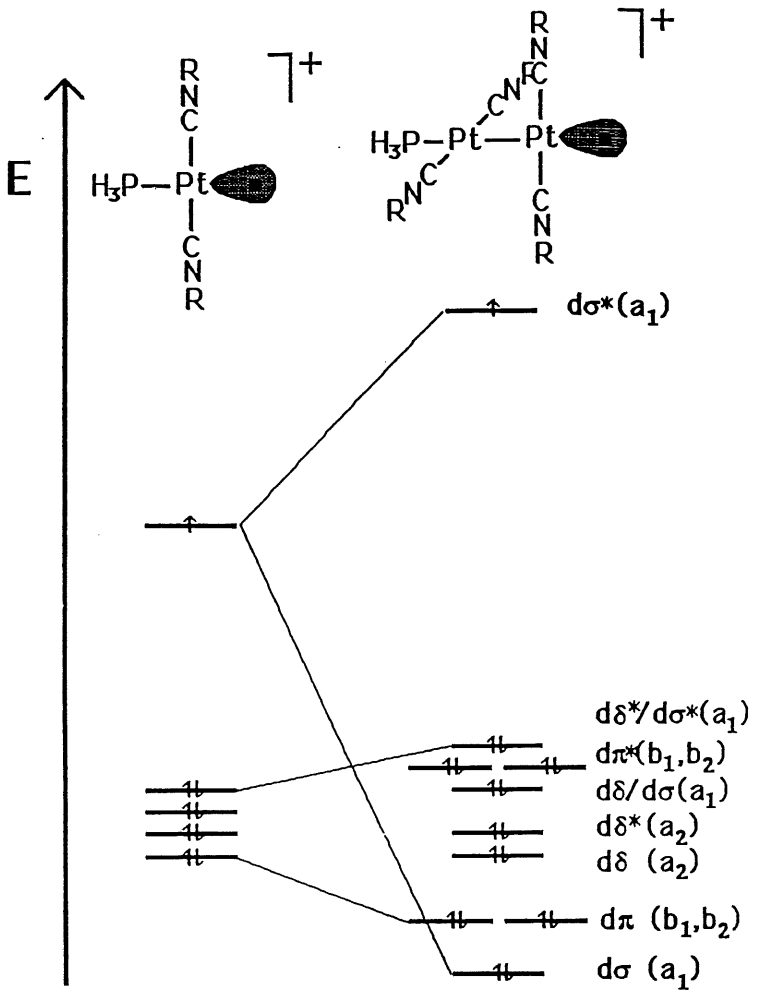

Figure 40. MO correlation diagram between the $[\bullet Pt_2(CNR)_4(PH_3)]^+$ and $[\bullet Pt(CNR)_2(PH_3)]^+$ fragments.

Table 20. EHMO atomic contributions for $[Pt_4(CNMe)_8(PH_3)_2]^{2+}$

MO#	EHMO energy(eV)	Empty or filled	%Pt									%P			%(CNR)C			%(CNR)N			Assignments
			p_z	p_y	p_x	s	d_{z^2}	$d_{x^2-y^2}$	d_{xy}	d_{xz}	d_{yz}	p_x	p_y	p_z	p_y	p_x	p_z	p_y	p_x	p_z	
79	-8.758	empty				4	18	29				4			16			12			dσ*(+CNR(π*)) LUMO
80	-10.295	filled			28	6	9	15				8			8			16			dσ*(+CNR(π*)) HOMO
81	-12.139	filled			14	20	30	21				6									dσ*(+dσ minor contribution)
82	-12.447	"							95												dπ*
83	-12.447	"								95											dπ*
84	-12.674	"				14	58	20													dσ*(+dσ minor contribution)
85	-12.717	"							98												dπ*
86	-12.717	"								98											dπ*
87	-12.739	"				4	52	40													dδ*dσ mixed
88	-12.803	"				6	53	40													dσ*+dδ(mixed)
89	-12.842	"									80							6		6	dδ*
90	-12.876	"									78							6		6	dδ*
91	-12.916	"									78							8		8	dδ
92	-12.946	"									74							8		8	dδ
93	-12.954	"					44	47													dσ
94	-13.028	"							80									10			dπ
95	-13.028	"								82								10			dπ
96	-13.265	"							76									12			dπ
97	-13.265	"								76								14			dπ
98	-13.790	"		4		6	17	52				4						8			dσ+dδ(mixed)

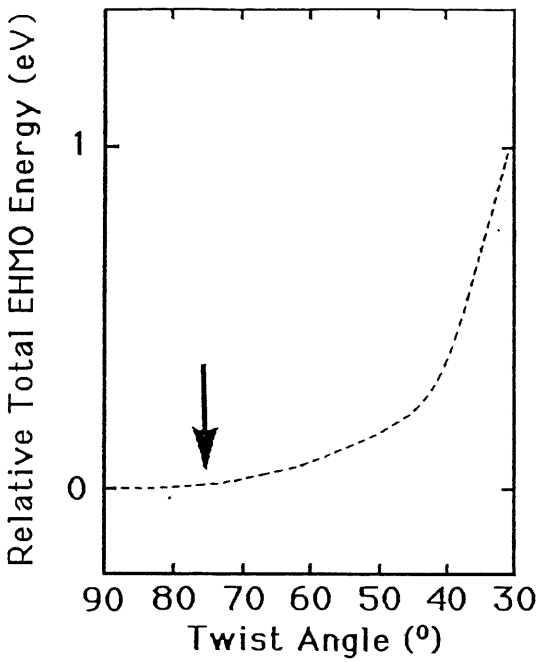

Figure 41. Plot of the total EHMO energy vs the twist angle for $[Pt_4(CNCH_3)_8(PH_3)_2]^{2+}$.

The last series of computations deals with the MO description with the change in twist angle. The total EHMO energy plotted against the dihedral angle between 90° (local symmetry: D_{2d}) and 30° (local symmetry: D_2) for the model complex shows an increase of 0.96 eV in that range (Figure 41). But this total energy is in fact flat (within ~ 0.03 eV) between 90° and 70°. A close examination of the individual MO energies and atomic contributions between these twist angles, shows practically no change in comparison with that presented in Table 20. This is due to the cylindric symmetry of the Pt-Pt single bond. At higher angles, the total energy increases more rapidly with the twist angles, and relates the change in $d\pi$ and $d\delta$ contacts. On the basis of literature, twist angles are generally found between 74° and 81° for linear Pt_n- and Pd_nCNR complexes (23, 25).

3.1.9 Electronic spectra

The electronic spectra are characterized by strong narrow absorptions in the visible region (Figure 42), and have some similarities with the absorption spectra of other M-M bonded

quasi-linear trimers (114). In an attempt to provide a reliable assignment for these low energy electronic bands, the ε data, shapes, and behavior with temperature should be considered. Absorption bands arising from $d\sigma \rightarrow d\sigma^*$ transitions in M_2 σ-bonded compounds, or from $d\sigma^* \rightarrow p\sigma$ transitions in M_2 face-to-face and non-M_2-bonded dimers, generally undergo a significant decrease in fwhm. Numerous examples for this phenomena are available in the literature (see examples for d^7-d^7 and d^9-d^9 σ-bonded M_2 (23, 28, 113, 115), and for non-M_2-bonded dimers such as the d^8-d^8 and d^{10}-d^{10} compounds (116, 117, 118)). This change in fwhm is associated with the presence of low-frequency Franck-Condon active vibrational modes, which upon warming, allows the population of vibrationally excited levels in the ground state to give rise to "hot bands" in the spectra according to a Boltzmann distribution. Upon cooling, these levels are less populated and fwhm decreases. Such modes are generally $\nu(M_2)$, and on some occasions ν(ML) if L is heavy or weakly bonded (ν(ML) is small), which are also active in the Franck-Condon term (119). Higher energy modes could be Franck-Condon active, but there would not be significant change in fwhm. For $[Pt_4(dmb)_4(PPh_3)_2]Cl_2$,

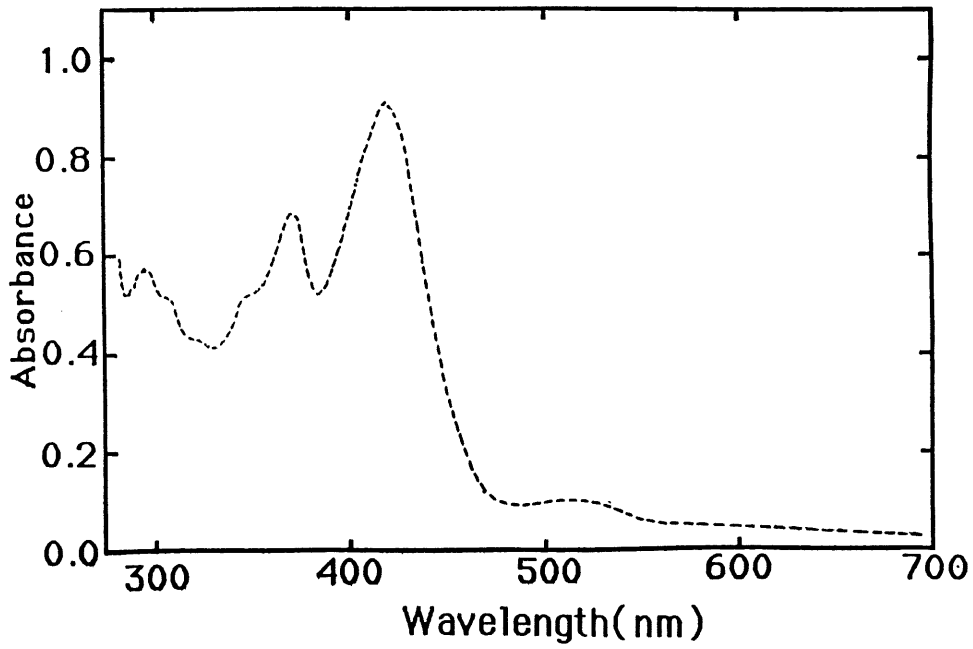

Figure 42. Absorption spectrum of $[Pt_4(dmb)_4(PPh_3)_2]Cl_2$ in ethanol at 77K.

the fwhm data are summerized in Table 21, and indeed indicate a decrease in fwhm for the lowest energy bands. Further the bands are so narrow (1100< fwhm >1820 cm^{-1}) that only a low-frequency Franck-Condon active mode could explain them. These bands are assigned to $d\sigma^* \rightarrow d\sigma^*$ electronic transitions. The EHMO calculation results indicated that the HOMO and LUMO are $d\sigma^*$ orbitals for this complex, which supported the assignment. The low intensity electronic band located at ~520 nm for $[Pt_4(dmb)_4(PPh_3)_2]Cl_2$ is the singlet-triplet absorption ($^3(d\sigma^* \rightarrow d\sigma^*)$). The singlet-triplet splittings measured at λ_{max} of the absorption bands (~4900 at 77K, and ~5600 cm^{-1} at 298K) are comparable to that of other polynuclear Pt compounds ($Pt_2(POP)_4^{4-}$(POP = $HO(O)POP(O)OH^{2-}$), 8800 cm^{-1}(120), $Pt_2(dppm)_3$, 3600 cm^{-1} (117). The ε value for this band (3300 $M^{-1}cm^{-1}$, 298K) also compares favorably to that of $Pt_2(dppm)_3$ (ε for $^3(d\delta^* \rightarrow p\sigma)$=5100, ε for $^3(d\sigma^* \rightarrow p\sigma)$=1200 $M^{-1}cm^{-1}$)(117). The related polymers also exhibit the same spectroscopic characters as for $[Pt_4(dmb)_4(PPh_3)_2]Cl_2$, and assignments remain.

Table 21. Spectroscopic data for $[Pt_4(dmb)_4(PPh_3)_2]Cl_2$

T(K)	λ_{max}(nm)	ν_{max}(cm^{-1})	fwhm(cm^{-1})	ε ($M^{-1}cm^{-1}$)	Assignments
298	405	24700	1820	35800	$^1(d\sigma^* \rightarrow d\sigma^*)$
77	412	24300	1580	---	
298	523	19100	1330	3300	$^3(d\sigma^* \rightarrow d\sigma^*)$
77	515	19400	1100	---	

The tetramer and polymers are not luminescent at room temperature, but are at 77K (Figure 43). In all cases, the structureless emission bands are located around 750 nm and emission lifetimes range from 2.71 to 5.17 ns (Table 22). These relatively long lifetimes and large Stoke shifts (energy difference between the lowest energy allowed electronic absorption and the emission maxima, ~11400 - 12200 cm^{-1}) indicate that these emissions are phosphorescence. However, the calculations predict that at least there are two possibilities for low lying emissive

excited states: 1) M-centered $d\sigma^* \rightarrow d\sigma^*$, and 2) metal-to-ligand-charge-transfer (MLCT). For the mononuclear and polymeric materials $[M(CN\text{-}t\text{-}Bu)_4]BF_4$ and $\{[M(dmb)_2]BF_4\}_n$ (M=Cu, Ag), density functional theory indicated that only low-energy MLCT type absorptions and emissions were possible (26). A comparative compilation of the Stoke shift data in these latter cases (Table 22) shows that these shifts are rather large (26200-28700 cm^{-1}) (26). In the case where only a M-centered emission is possible, i.e. $[Ag_2(dmpm)_2]^{2+}$ (dmpm = $(Me_2P)_2CH_2$), the Stoke shift is much smaller (11800 cm^{-1}) (118). For the comparison purpose, literature and experimental data for a series of luminescing M_2-isocyanide complexes are listed in Table 23, where both M-centered or MLCT emissions have been demonstrated. It is clear that M-centered excited states ($d\sigma \rightarrow d\sigma^*$, $d\sigma \rightarrow p\sigma^*$) provide Stoke shifts that are significantly shorter than that of MLCT. Based on this comparison, the observed emission bands of all the complexes in this work are assigned to the ("spin-forbidden") Pt-centered $d\sigma^* \rightarrow d\sigma^*$ electronic transition.

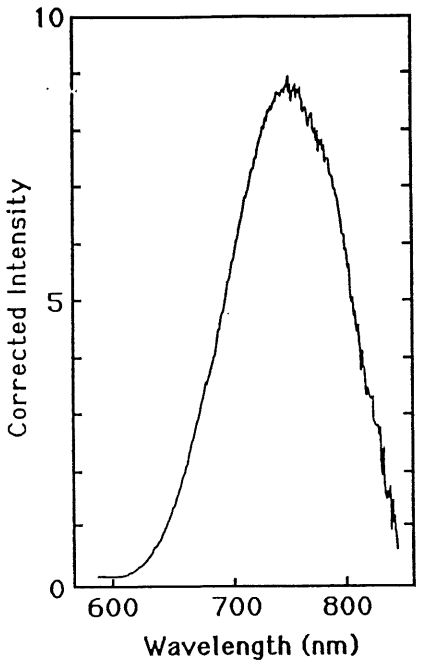

Figure 43. Emission spectrum of $[Pt_4(dmb)_4(PPh_3)_2]Cl_2$ in ethanol at 77K.

Table 22. Comparison of the electronic spectroscopic data for tetramer and polymers*

Compounds	λ_{em}(nm, 77K)	τ_e (ns, 77K)
$[Pt_4(dmb)_4(PPh_3)_2]Cl_2$	750	2.71
$\{[Pt_4(dmb)_4(dppb)]Cl_2\}_n$	736	4.78
$\{[Pt_4(dmb)_4(dppp)]Cl_2\}_n$	750	5.15
$\{[Pt_4(dmb)_4(dpph)]Cl_2\}_n$	755	5.17

*solvent: ethanol

Table 23. Spectroscopic comparison for various low-valent M_n-isocyanide complexes exhibiting either M-centered or MLCT emissions[a]

Compounds	M-centered absorption		Emission		Emission assignment	Stoke shift/cm^{-1}	Refs.
	λ_{max}/nm	ν_{max}/cm^{-1}	λ_{max}/nm	ν_{max}/cm^{-1}			
$Pt_4(dmb)_4(PPh_3)_2^{2+}$	405	24700	750	13300	$d\sigma^*\rightarrow d\sigma^*$	11400	This work
$\{Pt_4(dmb)_4(dppb)\}_n^{+2n}$	394	25400	736	13600	"	11800	"
$\{Pt_4(dmb)_4(dppp)\}_n^{+2n}$	394	25400	750	13300	"	12100	"
$\{Pt_4(dmb)_4(dpph)\}_n^{+2n}$	394	25400	755	13200	"	12200	"
$Pt_2(CNMe)_6^{2+}$	330	30300	542	18500	$d\sigma\rightarrow d\sigma^*$	(11800)	121
$Pd_2(dmb)_2Cl_2$	438	22800	625	16000	$d\sigma\rightarrow d\sigma^*$	6800	28
$Pd_2(dmb)_2Br_2$	422	23700	650	15400	"	8300	28
$\{Au_2(tmb)Cl_2\}_2$	292	34200	450	22200	$d\sigma^*\rightarrow p\sigma$	12000	122
$Ag_2(dmb)_2Cl_2$	232	43100	440	22700	MLCT	20400	118
$Ag_2(dmb)_2Br_2$	241	41500	458	21800	MLCT	19700	118
$Ag_2(dmb)_2I_2$	242	41300	443	22600	MLCT	18700	118

[a] M-centered means either $d\sigma^*\rightarrow d\sigma^*$, $d\sigma^*\rightarrow d\sigma^*$, or $d\sigma\rightarrow p\sigma$. Stoke shifts = ν_{max}(Abs.)-ν_{max}(Emi).

3.2 Preparation, spectroscopic and structural characterization of the $[Pd_4(dmb)_4(PPh_3)_2]^{2+}$ complex and its organometallic polymer $\{[Pd_4(dmb)_5]^{2+}\}_n$. The first 58-electron tetranuclear linear chain Pd clusters

Among all the polynuclear metal-metal chain complexes, the related Pt compounds represent a family that has been explored very well. In comparison with platinum, this chemistry is much poorer for palladium. In fact, in the low oxidation states, the Pd atoms can also form metal-metal bond (7, 22, 23, 24). Only a few of examples containing metal-metal chain have been reported, including a zigzag geometrical $[Pd_4(\mu\text{-}Cl)_3(dppm)_4Cl_2]BF_4$ cluster (123), trinuclear linear chain complexes $[Pd_3(CNCH_3)_8]^{2+}$ and $[Pd_3(CNCH_3)_6(PPh_3)_2]^{2+}$ (23) which were reported over two decades ago, and $[Pd_3(PPh_3)_4]^{2+}$ (24). In this section, an attempt to extend the length of linear chain of related palladium complexes will be made. The preparation, spectroscopic and structural characterization of a low-valent tetranuclear linear chain palladium cluster and its related organometallic polymer will be reported.

3.2.1 Preparation and characterization of $[Pd_4(dmb)_4(PPh_3)_2]Cl_2$

The d^{10}-d^{10} complex, $Pd_2(dba)_3 \cdot CHCl_3$ (124), reacts with an excess of dmb in acetone to give a red solution, which is unstable in air. In solid state, although it is relatively stable, its stability is not enough to fully characterize it. In the UV-vis spectrum, there is a strong peak at 510 nm. To improve the stability of this compound, triphenylphosphine ligand (PPh_3) was added. The color change from red to purple was readily observed, and the peak in UV-vis spectrum moved to 552 nm. The purple product has been isolated as a solid, which is relatively stable in solid state. In solution, this new compound is unstable in the presence of air, and even under inert atmosphere, it also slowly decomposes. This compound has been fully characterized. The ν(CN) frequency is 2154 cm^{-1}, indicating that the oxidation state is low. X-ray fluorescence measurements show that the relative ratio for Pd, P, and Cl is ~2.0, 1.0 and 1.0, respectively.

The FAB spectra exhibit the heaviest peaks at 1746.9, 1711.4 and 1592.0, which are $[Pd_4(dmb)_4(PPh_3)_2]Cl$, $[Pd_4(dmb)_4(PPh_3)_2]$, and $[Pd_4(dmb)_3(PPh_3)_2]Cl_2$ species (Table 24).

The purple crystals of $[Pd_4(dmb)_4(PPh_3)_2]Cl_2$ were grown by diffusion in a nitrogen atmosphere of diethyl ether into a dichloromethane solution containing excess dmb and PPh_3. Although the quality of crystals was poor and prevented further analysis, the X-ray diffraction studies clearly revealed that the structure is similar to that of $[Pd_4(dmb)_4(PPh_3)_2]Cl_2$, which also contain tetranuclear linear Pd-Pd-Pd-Pd chain. It crystallizes in a monoclinic cell (A2), and the related parameters are: a = 18.869 (3), b = 23.234 (3), c = 25.594 (4) Å, β = 108.420 (20)°, V = 10646 (3) $Å^3$, Z = 8 for a formula $Pd_2PN_4C_{32}Cl$ (FW = 719.60), R_1 = 0.148, wR_2 = 0.146. The Pd-Pd bond distance is about 2.53 Å, somewhat typical for Pd-Pd single bond. From the above and result of chemical analysis, this complex was assigned to the tetranuclear cluster $[Pd_4(dmb)_4(PPh_3)_2]Cl_2$. It is reasonable to propose that chlorocarbons are involved in the oxidation reaction (Scheme X). Because of the high reactivity of Pd^0 species (i.e. $Pd_4(dmb)_m^0$), the reaction should occur between the Pd^0 species and chlorocarbon to form the intermediate complex, $Pd_4(dmb)_mCl_2$.

Scheme X:

$$Pd_2(dba)_3{\bullet}CHCl_3 \xrightarrow{+\ dmb} Pd_4(dmb)_mCl_2 \xrightarrow{+PPh_3} [Pd_4(dmb)_4(PPh_3)_2]Cl_2$$

red purple

3.2.2 Reactivity

In order to determine the composition of the red intermediate complex ($Pd_4(dmb)_mCl_2$?), neutral TCNQ (7,7',8,8'-tetracyanoquinodimethane) was added to the solution of this complex, produced by a direct reaction between $Pd_2(dba)_3{\bullet}CHCl_3$ and dmb ligand in acetone.

Table 24. Selected mass FAB data for solid $[Pd_4(dmb)_4(PPh_3)_2]Cl_2$

Peak position	Relative intensity	Assignments	Calc. Mass
808	22	$Pd_3(dmb)(PPh_3)Cl$	807.3
		$Pd_4(dmb)_2$	806.3
890	9	$Pd_3(dmb)_3$	890.1
915	5	$Pd_4(dmb)(PPh_3)Cl$	913.7
924	6	$Pd_3(dmb)_3Cl$	925.6
964	3	$Pd_3(dmb)_2(PPh_3)Cl$	962.1
996	89	$Pd_4(dmb)_3$	996.5
1031	44	$Pd_4(dmb)_3Cl$	1032
1067	9	$Pd_4(dmb)_3Cl_2$	1067.4
		$Pd_4(dmb)_2(PPh_3)$	1068.5
1102	2	$Pd_4(dmb)_2(PPh_3)Cl$	1104.0
1186	70	$Pd_3(dmb)_3(PPh_3)Cl$	1187.9
		$Pd_4(dmb)_4$	1186.8
1222	100	$Pd_4(dmb)_4Cl$	1222.3
1258	5	$Pd_4(dmb)_3(PPh_3)$	1258.9
		$Pd_4(dmb)_4Cl_2$	1257.7
1293	6	$Pd_4(dmb)_3(PPh_3)Cl$	1294.3
1328	6	$Pd_4(dmb)_3(PPh_3)Cl_2$	1329.7
1448	3	$Pd_4(dmb)_4(PPh_3)$	1449.1
1485	8	$Pd_4(dmb)_4(PPh_3)Cl$	1484.6
1590	2	$Pd_4(dmb)_3(PPh_3)_2Cl_2$	1592.0
1712	<1	$Pd_4(dmb)_4(PPh_3)_2$	1711.4
1748	<1	$Pd_4(dmb)_4(PPh_3)_2Cl$	1746.9

Clear change of color from red to blue-green was observed, indicating that the red complex was oxidized and neutral TCNQ became $TCNQ^-$ anion. Over one night, deep blue-purple crystals were directly formed from the original solution at room temperature. The crystal structure is shown in Figure 44. It is confirmed that Pd atoms have been oxidized to Pd(II). In this molecule, the Pd (II) center is coordinated by four isocyanide groups, displaying a square

Table 25. Crystallograghic data for $[Pd_2(dmb)_4(\mu\text{-}Cl)](TCNQ)_4$

Empirical formula	$C_{96}H_{88}N_{24}ClPd_2$
Formula weight	1826.16
Temperature	293 (2) K
Crystal system	Triclinic
Space group	P-1
Unit cell dimensions	a = 13.341 (2) Å
	b = 13.490 (2) Å
	c = 14.645 (2) Å
	α = 108.267 (10)°
	β = 104.834 (10)°
	γ = 101.221 (10)°
Volume	2303.8 (6) $Å^3$
Z	2
Density (calculated)	1.316 Mg/m^3
Theta range for data collected	3.38 to 69.87°
Reflections collected	8739
Independent reflections	8739 [R(int) = 0.0000]
Final R indices [I>2 sigma(I)]	R1 = 0.0757, wR2 = 0.2018
R indices (all data)	R1 = 0.1192, wR2 = 0.2241

$R1=\Sigma(||F_o|-|F_c||)/\Sigma|F_o|$, $wR2=\{\Sigma[w(F_o^2-F_c^2)^2]/\Sigma w(F_o^2)^2\}^{1/2}$ $[w=1/[\sigma^2(F_o^2)+0.1P)^2$ where $P=(F_o^2+2F_c^2)/3]$.

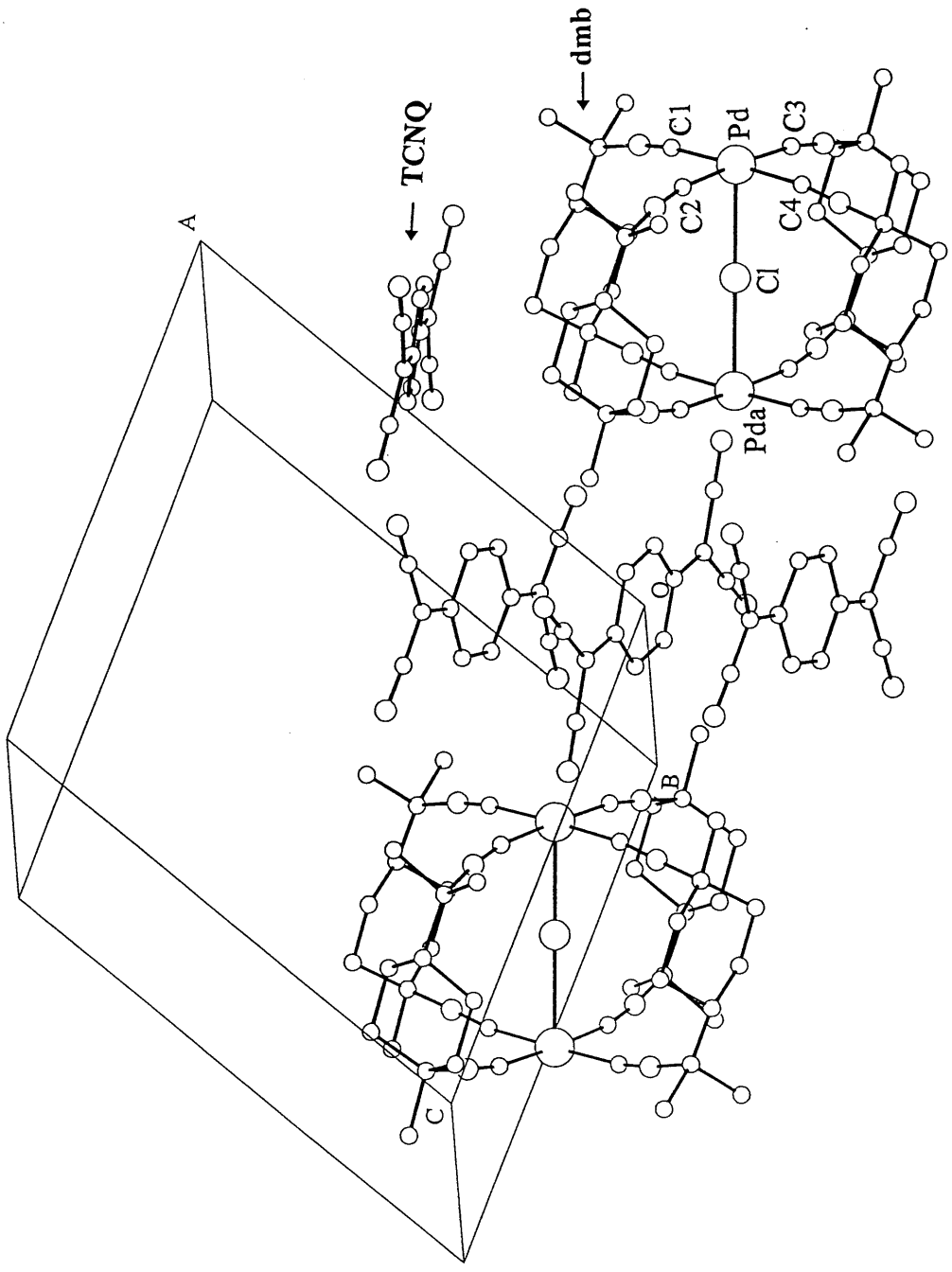

Figure 44. Crystal structure of $[Pd_2(dmb)_4(\mu\text{-}Cl)](TCNQ)_4$

Table 26. Selected bond lengths (Å) and angles (°) for $[Pd_2(dmb)_4(\mu\text{-}Cl)](TCNQ)_4$

Pd-Cl	2.7143 (6)	C(1)-Pd-C(2)	88.9 (3)
Pd-C(1)	1.968 (7)	C(1)-Pd-C(3)	88.8 (3)
Pd-C(2)	1.970 (8)	C(2)-Pd-C(3)	176.5 (2)
Pd-C(3)	1.982 (8)	C(1)-Pd-C(4)	176.7 (3)
Pd-C(4)	1.985 (6)	C(2)-Pd-C(4)	88.8 (3)
		C(3)-Pd-C(4)	93.4 (3)
		Pd-Cl-Pd	180.0

geometry which is typical for transition metal cation with d^8 electronic configuration. In this molecule, the most interesting feature is that one Cl^- anion is symmetrically encapsulated by two Pd atoms. The distance of Pd–Cl is 2.7143 Å, longer than the sum of their ionic radii (~2.61 Å), indicating that the interaction between Pd and Cl atoms arises from an electrostatic attraction. The complexation of small cations by using functional ligands (host system) is well known, but this chemistry is rare for anions. Over ten years ago, H. B. Gray and coworkers reported that binuclear complexes of Ni(II) and Pd(II) with dmb ligands were the effective encapsulating agents for Cl^- and Br^- ions, but no crystal structure was available to prove that (125). In this case, this structure also provides further evidence that chlorocarbon indeed reacts with the Pd^0 species to produce the intermediate complex, in which the ratio for Pd and Cl is 2:1, and hence supports Scheme X.

3.2.3 Preparation and crystal structure of polymer $\{[Pd_4(dmb)_5](O_2CCH_3)_2\}_n$

In the same conditions, a direct reaction of a mixture of $Pd_2(dba)_3 \cdot CHCl_3$ and $Pd(O_2CCH_3)_2$ (molar ratio: 1.5) with an excess of dmb in acetone under inert atmosphere leads to the formation of the organometallic polymer $\{[Pd_4(dmb)_5](O_2CCH_3)_2\}_n$, which is easier to

crystallize than $[Pd_4(dmb)_mCl_2]$. The UV-vis spectra are characterized by a strong absorption peak at 512 nm. In the IR spectra, the ν(CN) band appears at 2152 cm^{-1}. These data are similar to that of $Pd_4(dmb)_mCl_2$. The single crystals suitable for X-ray crystallography were grown by diffusion of pentane into a methyl ethyl ketone solution in the presence of an excess

Table 27. Crystal data for $\{[Pd_4(dmb)_5](CH_3COO)_2(H_2O)_4\}_n$

Empirical formula	$C_{64}H_{104}N_{10}O_8Pd_4$
Formula weight	1567.18
Temperature	293(2) K
Crystal system	Monoclinic
Space group	P $2_1/c$
Unit cell dimensions	a = 19.433 (2) Å
	b = 15.312 (2) Å
	c = 29.156 (2) Å
	α = 90°
	β = 98.841 (10)°
	γ = 90°
Volume	8572.7 (15) $Å^3$
Z	4
Density (calculated)	1.214 Mg/m^3
Theta range for data collection	2.30 to 49.94°
Reflections collected	8796
Independent reflections	8796
Final R indices [I>2sigma(I)]	R1 = 0.0957, wR2 = 0.2932
R indices (all data)	R1 = 0.1655, wR2 = 0.3399

$R1=\Sigma(||F_o|-|F_c||)/\Sigma|F_o|$, $wR2=\{\Sigma[w(F_o^2-F_c^2)^2]/\Sigma w(F_o^2)^2\}^{1/2}$ $[w=1/[\sigma^2(F_o^2)+0.1P)^2$ where $P=(F_o^2+2F_c^2)/3]$.

of dmb ligand. The X-ray structure is shown in Figure 45 (Table 27). In this polymer, a series of $[Pd_4(dmb)_4]$ units are linked by dmb ligands to form a zigzag chain. Within $[Pd_4(dmb)_4]$ unit, four Pd atoms are bonded to each other by metal-metal bonds (Table 28). The Pd-Pd bond distances are 2.5973(18) Å for the inner bond, and 2.6080(18) and 2.6232(19) Å for the outer bonds. These are also typical for Pd-Pd single bonds, but are longer than that found in $[Pd_3(CNCH_3)_6(PPh_3)_2]^{2+}$ and $[Pd_4(dmb)_4(PPh_3)_2]^{2+}$. The four Pd atoms form a quasi-linear chain, where the average ∠Pd-Pd-Pd is 174.5 degree indicating a slight deviation from perfect linearity. In this case, there are two kinds of conformations for dmb ligands. As found in the Pt analogue, four U-shaped dmb ligands bridge Pd atoms to form the Pd_4 fragment. Similarly two 20-membered "$Pd_2(dmb)_2$" rings also interlocked together forming a catenate structure. The dihedral angle between the two "$Pd_2(dmb)_2$" fragments is 82.7°, not 90°, and is larger than the values found in $[Pd_3(CNCH_3)_6(PPh_3)_2]^{2+}$(74.5°) and $[Pt_4(dmb)_4(PPh_3)_2]^{2+}$(75°). The fifth dmb ligand coordinates the axial position, and adopts the rare Z-shaped conformation. In this

Scheme XI:

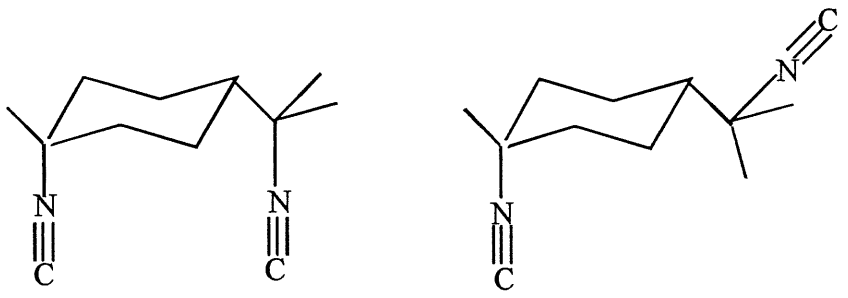

U-shaped Z-shaped

Z-shaped conformation, the $-C(CH_3)_2NC$ group rotates around the C-C single bond (Scheme XI). The latter acts as a bridging ligand to link the $[Pd_4(dmb)_4]$ units to form a polymeric chain (Figure 45). In dmb chemistry, examples of complexes exhibiting this Z-shaped conformer are rare (104, 126). The average Pd-C distances for the axial and equatorial ligands are 2.040(8) and 1.93(6) Å, respectively. This difference is due to weaker back-donation bonding at axial positions than that of the equatorial positions. From Balch's work (23) and

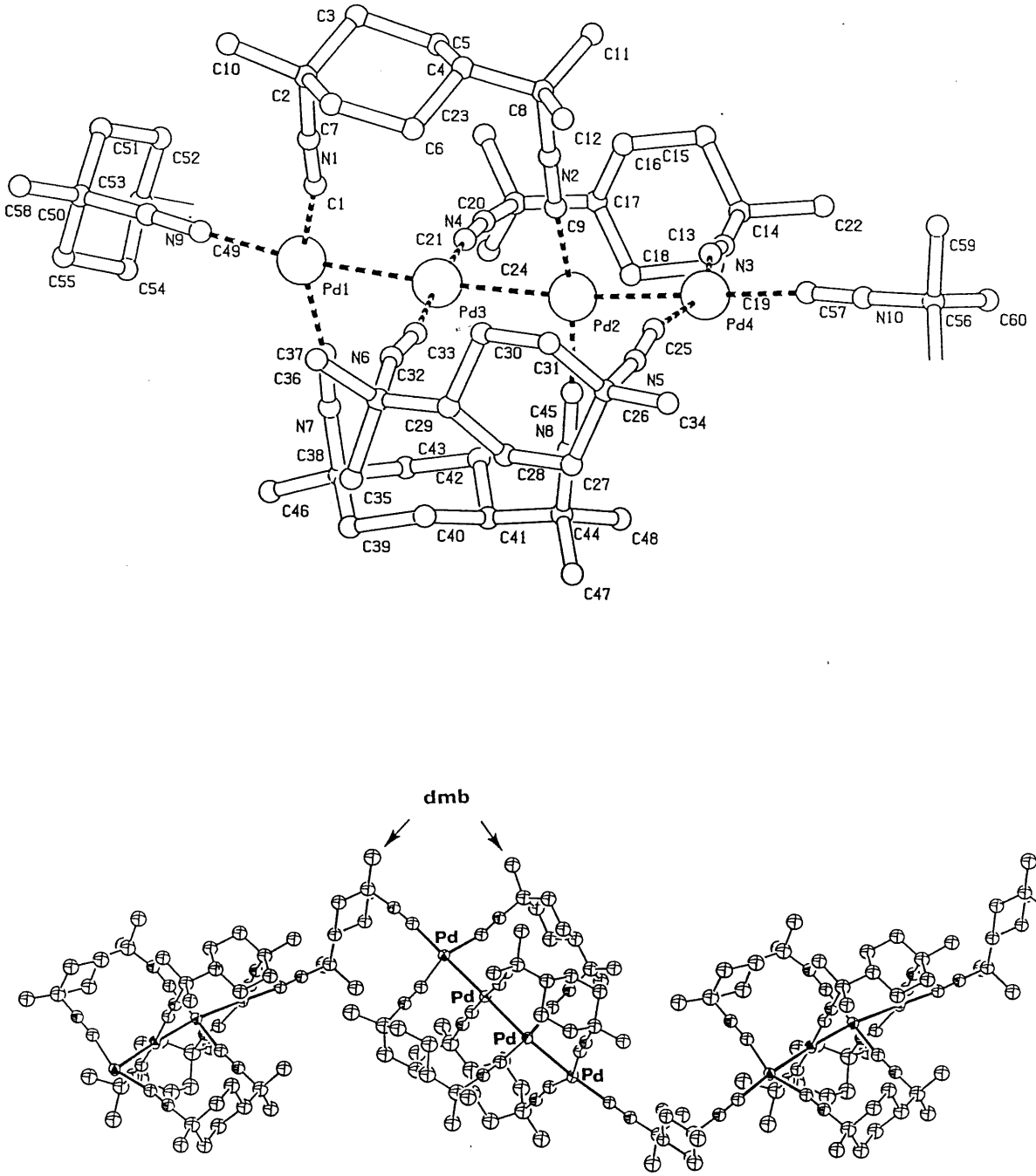

Figure 45. Crystal structure of polymer $\{[Pd_4(dmb)_5](CH_3COO)_2\}_n$

Table 28. Selected bond lengths (Å) and angles (°) for $\{[Pd_4(dmb)_5](CH_3COO)_2\}_n$

Pd(1)-Pd(3)	2.6080(18)	C(1)-N(1)	1.135(16)
Pd(2)-Pd(3)	2.5973(18)	C(9)-N(2)	1.156(16)
Pd(2)-Pd(4)	2.6232(19)	C(13)-N(3)	1.125(19)
Pd(1)-C(1)	1.958(18)	C(21)-N(4)	1.111(18)
Pd(1)-C(37)	1.98(3)	C(25)-N(5)	1.133(18)
Pd(1)-C(49)	2.047(18)	C(33)-N(6)	1.128(18)
Pd(2)-C(45)	1.93(3)	C(37)-N(7)	1.136(19)
Pd(2)-C(9)	1.933(18)	C(45)-N(8)	1.148(19)
Pd(3)-C(21)	1.87(3)	C(49)-N(9)	1.143(16)
Pd(3)-C(33)	1.88(3)	C(57)-N(10)	1.152(15)
Pd(4)-C(25)	1.90(3)		
Pd(4)-C(13)	2.00(3)		
Pd(4)-C(57)	2.032(17)		
Pd(1)-Pd(3)-Pd(2)	175.77(8)	C(45)-Pd(2)-C(9)	168.2(16)
Pd(3)-Pd(2)-Pd(4)	173.28(7)	C(21)-Pd(3)-C(33)	174.8(13)
Pd(3)-Pd(1)-C(1)	77.4(6)	C(25)-Pd(4)-C(13)	152.3(15)
Pd(3)-Pd(1)-C(37)	77.8(12)	C(25)-Pd(4)-C(57)	99.8(12)
Pd(2)-Pd(3)-C(21)	90.5(9)	C(13)-Pd(4)-C(57)	107.4(13)
Pd(2)-Pd(3)-C(33)	86.0(11)	N(1)-C(1)-Pd(1)	166.6(18)
Pd(3)-Pd(2)-C(9)	83.6(6)	N(2)-C(9)-Pd(2)	173.4(18)
Pd(3)-Pd(2)-C(45)	88.8(16)	N(3)-C(13)-Pd(4)	163(3)
Pd(4)-Pd(2)-C(9)	89.8(6)	N(4)-C(21)-Pd(3)	172(3)
Pd(4)-Pd(2)-C(45)	97.9(16)	N(5)-C(25)-Pd(4)	165(3)
Pd(2)-Pd(4)-C(25)	75.7(11)	N(6)-C(33)-Pd(3)	169(3)
Pd(2)-Pd(4)-C(13)	76.8(11)	N(7)-C(37)-Pd(1)	171(4)

C(1)-Pd(1)-C(37)	153.3(13)	N(8)-C(45)-Pd(2)	177(5)
C(1)-Pd(1)-C(49)	99.8(8)	N(9)-C(50)-Pd(1)	172.8(18)
C(37)-Pd(1)-C(49)	105.9(13)		

these studies, the experimental results indeed confirmed that the isocyanide ligands at the axial positions are reactive in comparison with those at the equatorial positions. By adding triphenylphosphine ligand, only the axial isocyanide ligands can be replaced. In this polymer, the dmb bite distances, 5.205 and 5.221 Å are also among the longest ever reported for dmb complexes (Table 29).

Table 29. Comparison of the dmb bite distances (>4.9Å)

Compounds		Bite distances/ Å	References
$[Pd_4(dmb)_4(PPh_3)_2]^{2+}$		5.058 (20)	This work
$\{[Pd_4(dmb)_5](CH_3COO)_2\}_n$		5.205 (3), 5.221 (3)	"
$[Pd_2(dmb)_4(\mu\text{-}Cl)](TCNQ)_3$		5.428 (2)	"
$[Pt_4(dmb)_4(PPh_3)_2]^{2+}$		5.231 (4), 5.307 (4)	"
$[Ir_2Ag(dmb)_4]^{2+}$		5.284 (2)	30
$[Ir_2Ag(dmb)_4(PPh_3)_2]^{2+}$		5.28 (2)	99
$\{[Ag(dmb)_2]Y\}_n$	$Y = NO_3^-$	5.1884 (6)	26
	$TCNQ^-$	5.065 (8)	101
	PF_6^-	4.964 (1)	26
	BF_4^-	4.9557 (9)	"
	ClO_4^-	4.9496(1)	"

The counter anions are acetate groups located outside the polymeric chain. There is no evidence of Cl^- ions within the lattice. It is clear that using $Pd(CH_3COO)_2$ instead of only $Pd_2(dba)_3 \cdot CHCl_3$, the redox reaction occurs between Pd(0) and Pd(II) species, and in this case, chlorocarbon will not be involved in the reaction. Water molecules have been located in the crystals. This hydroscopic behavior is also observed for the organometallic polymer as depicted in the ^1H NMR and IR spectra.

3.2.4 Raman spectrum

The Raman spectra were investigated for $[Pd_4(dmb)_4(PPh_3)_2]Cl_2$ for two reasons. First, the amplitude of the Pd-Pd interactions are addressed via the measurements of ν(Pd-Pd), generally appearing in the low region. Second, the electronic structure for the Pd_4^{2+} species are addressed experimentally using the the first and second moment band analysis described below. For such analysis, the knowlege of all potential candidates as Franck-Condon active modes (usually Raman active) is necessary.

The strategy of assignment for the $\nu(Pd_2)$ bands is based upon the comparison with literature data for closely related Pd complexes (for which $\nu(Pd_2)$ has been confirmed by resonance Raman) (69), also taking into account the M_2 bond lengths or separations (106), and commonly encountered high intensity of the $\nu(Pd_2)$ modes. Resonance Raman could not be used in this work as the samples are sensitive to laser in solutions. In the low frequency region, two strong signals are observed at 165 and 86 cm^{-1} (Figure 46), which are readily assigned to the totally symmetric $\nu(Pd_2)$ modes (ν_1 = ←M-M_2-M→; ν_2 = ←M_2-M_2→) for $[Pd_4(dmb)_4(PPh_3)_2]Cl_2$, respectively. No other candidates for $\nu(Pd_2)$ is available below 250 cm^{-1}. These data compare very favorably with the literature (Table 30), in particular to that of related Pd_3^{2+} species. The empirical equation (Eq. 3.2) gives the force constant, $F(Pd_2)$ = 1.44 mdyn·Å^{-1}. This value for $F(Pd_2)$ compares well with

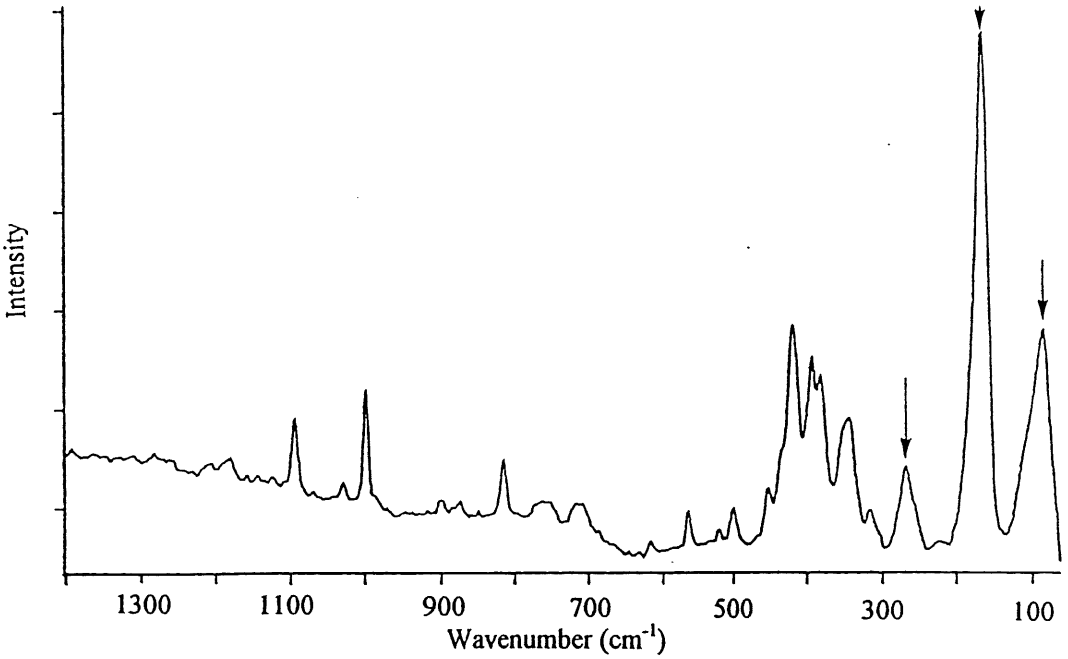

Figure 46. FT-Raman spectrum for $[Pd_4(dmb)_4(PPh_3)_2]Cl_2$. Experimental conditions: resolution: 2.6 cm^{-1}; no. of scans: 100.

Table 30. Comparison of the spectroscopic and structural data for linear and cyclic Pd_n clusters

Compounds	Assignment method	Geometry	ν(Pd-Pd)/cm^{-1}	d (Pd-Pd)/Å	Refs.
$[Pd_4(dmb)_4(PPh_3)_2]Cl_2$	rel. int. + comp.	linear	165 (a_1)	2.524 (10)	this work
			86 (a_1)	2.534 (10)	
$[Pd_3(CNCH_3)_8]^{2+}$	RR	linear	166 (IR)	---	127
			114 (R)	---	
$[Pd_3(CNCH_3)_6(PPh_3)_2]^{2+}$	RR	linear	132 (IR)	2.5921	127
			90 (R)		
$[Pd_3(dppm)_3(CO)]^{2+}$	rel. int. + comp.	cyclic	205 (a_1)	2.600	13
			143 (e)		
$[Pd_4(dppm)_4(H)_2]^{2+}$	rel. int. + comp.	square	183	---	31
			130		

$$d(Pd_2) = -0.387\ \ln F(Pd_2) + 2.67 \qquad [3.2]$$

other binuclear systems with the same $d(Pd_2)$ which also exhibit similar $\nu(Pd_2)$. The related polymer was not investigated since it was too unstable in solutions for the "time consuming" second moment band analysis.

3.2.5 EHMO computations

The nature of the ground and lowest energy excited states are addressed both experimentally and theoretically. Here computational results are described. The EHMO computations were also performed using $[Pd_4(CNMe)_8(PH_3)_2]^{2+}$ as a model, and the procedures were similar to that described for $[Pt_4(dmb)_4(PPh_3)_2]^{2+}$, where the model compound $[Pt_4(CNMe)_8(PH_3)_2]^{2+}$ was used. The main computational results can be described as follows (Table 31): 1) the HOMO is a filled $d\sigma^*$ using mainly the p_x, s, d_{z^2} and $d_{x^2-y^2}$ Pd orbitals, along with some minor p_x contributions from the P and C (isocyanide) atoms; 2) the LUMO is also a $d\sigma^*$ using by the same atomic orbitals with some slight changes in the contributions; 3) the 18 following lower energy levels are located within ~2.5 eV and are all metal centered MO's; 4) the LUMO+1 to 4 are quasi-degenerated and all π^*(CNR) orbitals; 5) mixing between the $d\sigma^*$ and $d\delta^*$, and $d\sigma$ and $d\delta$ orbital does occur. Finally both the HOMO and LUMO are relatively well "isolated" from the other MO's (~1.3 and 0.5 eV, respectively). These large energy separations strongly predict the right order of the frontier orbitals despite the qualitativeness of the computational method. This assignment is supported experimentally below.

The last computation was performed to deal with the model compound $[Pd_4(CNMe)_{10}]^{2+}$ in order to investigate whether any significant differences are present between the two differently axially substituted tetramers. From the crystallographic studies, a small increase in Pd-Pd bond lengths has been observed from $[Pd_4(dmb)_4(PPh_3)_2]^{2+}$ (2.53 Å, average value) to $[Pd_4(dmb)_5]^{2+}$

Table 31. EHMO atomic contributions for $[Pd_4(CNME)_8(PH_3)_2]^{2+}$

MO#	EHMO energy(eV)	Empty or filled	%Pd									%P			%(CNR)C			%(CNR)N			Assignments
			p_z	p_y	p_x	s	d_{z^2}	$d_{x^2-y^2}$	d_{xy}	d_{xz}	d_{yz}	p_x	p_y	p_z	p_y	p_x	p_z	p_y	p_x	p_z	
75	-8.270	empty	11													52				30	π*(CNR)
76	-8.270	"		9											56			32			π*(CNR)
77	-8.316	"	10													4	52			28	π*(CNR)
78	-8.316	"		10											52	4		26			π*(CNR)
79	-9.306	"			4		22	32				4				8					dσ*(+π*(CNR)) LUMO
80	-10.132	filled			14	6	17	21				12			4		4				dσ*(+π*(CNR)) HOMO
81	-11.907	"			6	16	31	24				6									dσ,dδ,mixed
82	-12.613	"				14	56	18													dδ
83	-12.662	"							52	45											dπ*
84	-12.662	"							45	52											dπ*
85	-12.753	"					50	44													dσ*,dδ*,mixed
86	-12.839	"							55	37											dπ*
87	-12.839	"							37	55											dπ*
88	-12.845	"				4	52	40													dσ*,dδ*,mixed
89	-12.952	"									88								8		dδ*
90	-12.980	"									86								8		dδ*
91	-13.006	"					45	47													dσ,dδ,mixed
92	-13.014	"									86								8		dδ
93	-13.040	"									86								8		dδ
94	-13.100	"							42	35										6	dπ
95	-13.100	"							35	42										6	dπ
96	-13.312	"							47	35										10	dπ
97	-13.312	"							35	47										10	dπ
98	-13.592	"				4	22	61				4									dσ

(2.61 Å, average value). Essentially there is no or very little perturbation on the MO energies and the relative atomic contributions, except that the axial ligand is different. More importantly the nature of the frontier orbitals are the same, i.e. π^*(CNR) > $d\sigma^*$(LUMO) > $d\sigma^*$(HOMO) > $d\sigma$, $d\delta$ mixed (HOMO-1).

3.2.6 UV-vis spectra and moment band analysis

The electronic spectra of $[Pd_4(dmb)_4(PPh_3)_2]^{2+}$ and $\{[Pd_4(dmb)_5]^{2+}\}_n$ are characterized by strong narrow absorptions in the visible region (Figure 47). Two spectra are very similar, except that the positions of the lowest energy bands are different. Because the polymer, $\{[Pd_4(dmb)_5]^{2+}\}_n$, is stable only for a limited period in solutions, the following moment band

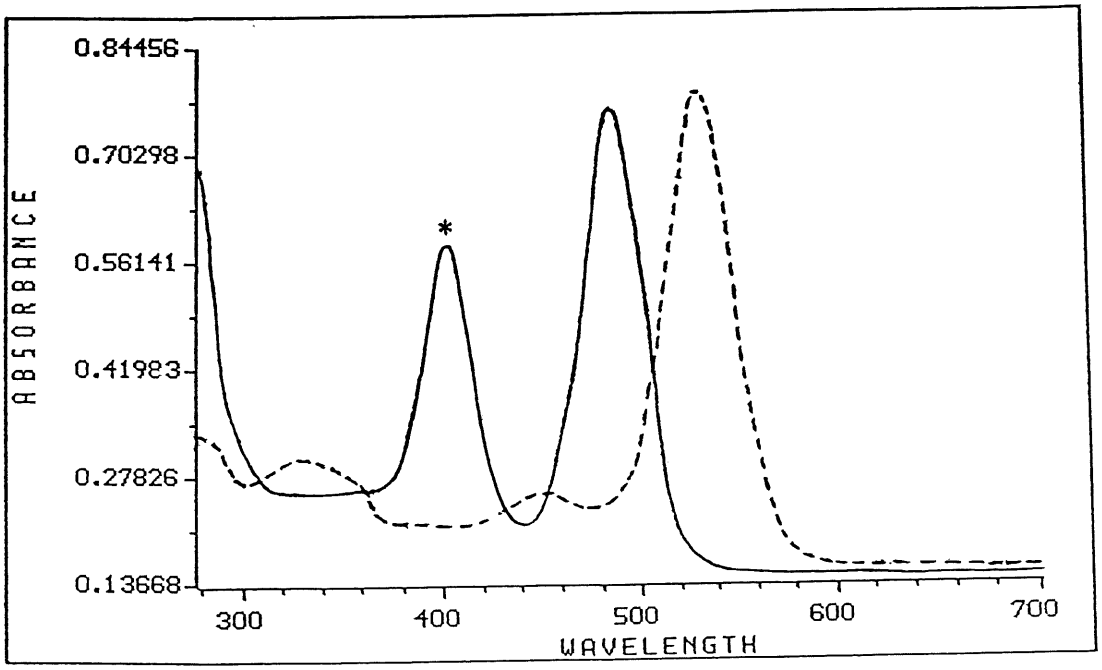

Figure 47. UV-vis spectra of $[Pd_4(dmb)_4(PPh_3)_2]^{2+}$ and polymer $\{[Pd_4(dmb)_5]^{2+}\}_n$ in butyronitrile at 77 K. - - - $[Pd_4(dmb)_4(PPh_3)_2]^{2+}$; — $\{[Pd_4(dmb)_5]^{2+}\}_n$. * polymer sample in solution is partially oxided to d^9-d^9 compounds.

analysis will be performed only for $[Pd_4(dmb)_4(PPh_3)_2]^{2+}$.

It is well known that absorption bands arising from the M-centered $d\sigma \rightarrow d\sigma^*$ transitions in M_2 σ-bonded species, or from $d\sigma^* \rightarrow p\sigma$ transitions in M_2 face-to-face and non-M_2-bonded dimers, generally undergo a significant decrease in fwhm upon lowering temperature (13, 28, 119). This fwhm variation is due to the presence of low-frequency Franck-Condon active vibrational modes, which will affect the bandwidths of the low energy bands. Upon warming the sample, the population of vibrationally excited levels increases; upon cooling, the "excited" levels become less populated and fwhm decreases. For M_2 species, in general, these modes are ν(M-M), and on some occasions ν(M-L) (119). For $[Pd_4(dmb)_4(PPh_3)_2]^{2+}$, the data are as follows: T = 298 K, λ_{max} = 548 nm or 18250 cm^{-1}, fwhm = 2460 cm^{-1}, ε = 53700 M^{-1} cm^{-1}; T = 77 K, λ_{max} = 536 nm or 18660 cm^{-1}, fwhm = 1560 cm^{-1} (in ethanol). This change is remarkable, and these data are clearly consistent with the EHMO calculation results which favor the Pd-centered $d\sigma^* \rightarrow d\sigma^*$ lowest energy electronic transition.

In order to quantify this temperature effect and to provide further support to the above assignment, a moment analysis is performed (128). For a fully allowed electronic transition the oscillation strength is formally temperature independent (i.e. the area under the electronic band is constant with temperature). However assuming that the bands are of Gaussian shape, the normalized first and second moments (ν_{max} in cm^{-1} and $m^2 = (8\ln 2)^{-1}$ $(fwhm)^2$ in cm^{-2}, respectively), follow a temperature dependence of the form:

$$\nu_{max} \text{ and } m^2 = \sum_i A_i \coth\left(\frac{\hbar\omega_i}{2kT}\right) + B \qquad [3.3]$$

where k is Boltzmann constant, T is temperature, and $\hbar\omega_i$ is the ground state vibrational frequency (for an absorption spectrum). The temperature-independent B term in the first-moment equation is related to the electronic transition energy. The B value for the second

moment should be either zero or very small, according to theory (128). For non-zero B values, it has been proposed (119) that nonzero B values are to be attributed to high frequency Franck-Condon active modes which are too energetic to contribute strongly to the temperature dependence.

The UV-vis spectra vs T are shown in Figure 48, where a progressive change both in ν_{max} and $(fwhm)^2$ are clearly observed. Preliminary attempts to describe both parameters and its dependence with T using a single Franck-Condon active mode did not lead to satisfactory fits of the experimental data. This observation is normal since there are more than one potential candidates as Franck-Condon active modes within the $[Pd_4(dmb)_4(PPh_3)_2]^{2+}$ chromophore, and suggests that two or more vibrational modes must be used in the analysis. A recent and similar study on the cyclic trinuclear $[Pd_3(dppm)_3CO]^{2+}$ cluster (dppm = $((C_6H_5)_2P)_2CH_2$) showed that two ν(Pd-Pd) modes were Franck-Condon active in the lowest energy absorption (13). The following attempts involve the use of two modes. Therefore in this situation, Eq. 3.3 becomes:

$$\nu_{max} = A_1 \coth\left(\frac{\hbar\omega_{g1}}{2kT}\right) + A_2 \coth\left(\frac{\hbar\omega_{g2}}{2kT}\right) + B \qquad [3.4]$$

The fit became significantly better and the best fit gave A_1 = -6 cm^{-1}, $\hbar\omega_{g1}$ = 165 cm^{-1}, A_2 = -0.66 cm^{-1}, $\hbar\omega_{g2}$ = 86 cm^{-1}, and $B = 1.93 \times 10^4$ cm^{-1} for the data presented in Figure 48 (Figure 49). Changes in $\hbar\omega_{g1}$ and $\hbar\omega_{g2}$ of more than 20% lead to unacceptable fits. Further when parameters A_1, A_2 and B are modified slightly, the fits become unacceptable again, and the uncertainties obtained for $\hbar\omega_{g1}$ and $\hbar\omega_{g2}$ greatly increase. By using three active modes, the uncertainties decrease only slightly (within 10%). In the Raman spectrum, indeed these two scatterings (86 and 165cm^{-1}) are observed (Figure 46). With these observations, the temperature dependence for ν_{max} can be best explained by a dominating two Franck-Condon

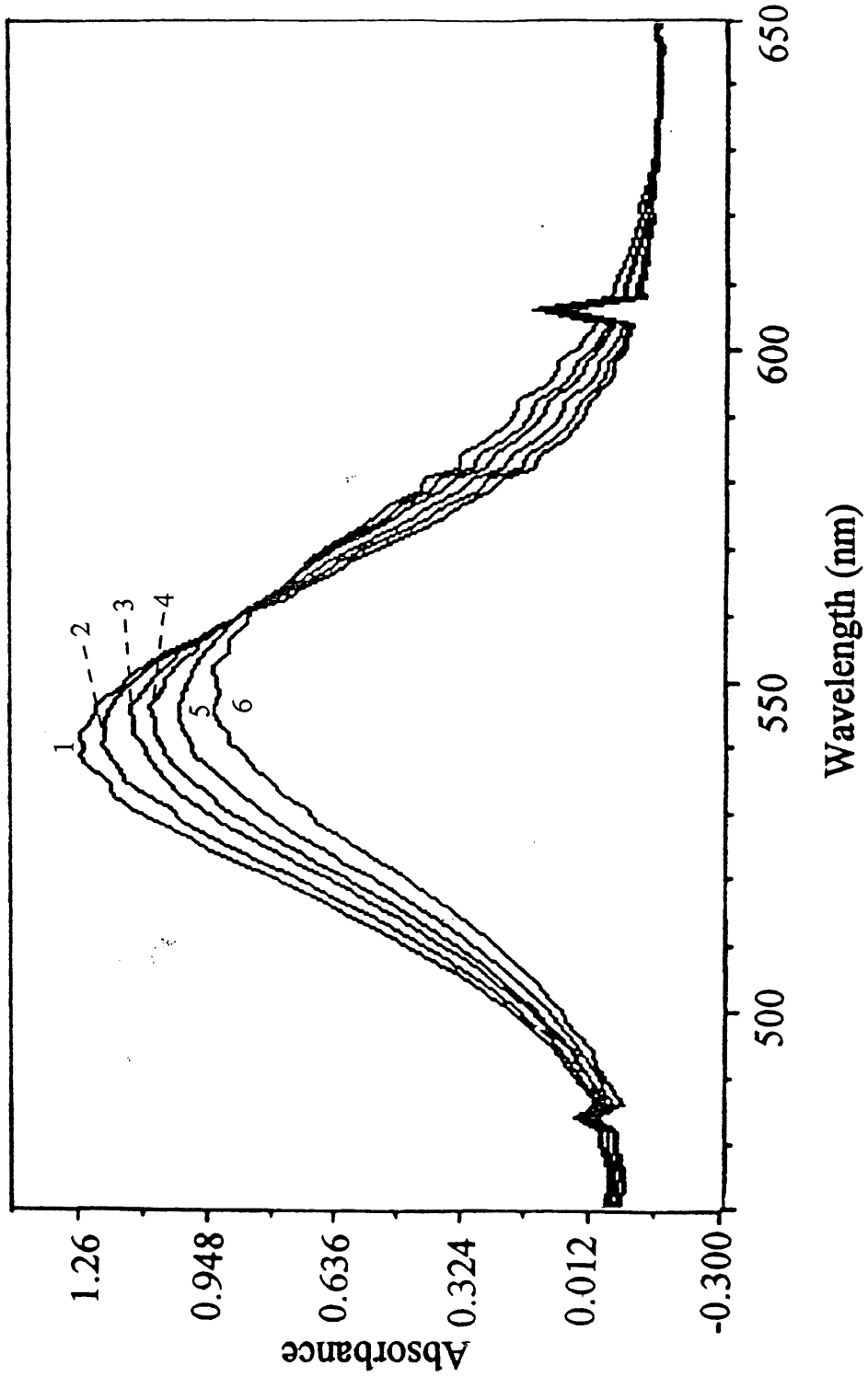

Figure 48. UV-vis spectra of $[Pd_4(dmb)_4(PPh_3)_2]^{2+}$ in butyronitrile vs temperature: (1) 205 K; (2) 217 K; (3) 236 K; (4) 255 K; (5) 272 K; (6) 292 K.

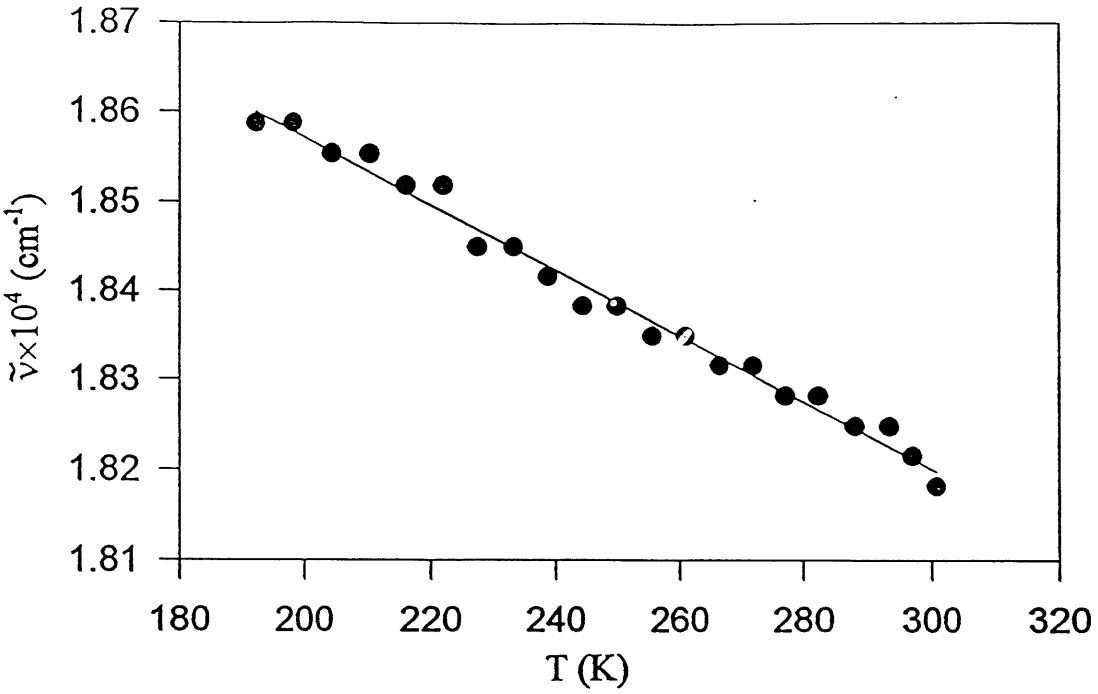

Figure 49. Variation of $\tilde{\nu}_{max}$ of the lowest energy band vs temperature. The black points represent the experimetal data; the line is the best fitted curve.

active mode model. The assignments for these modes are trivial: $\hbar\omega_{g1} = \nu_1$(Pd-Pd) a_1, $\hbar\omega_{g2} = \nu_2$(Pd-Pd) a_1, and hence this strong absorption at ~550 nm arises definitely from a metal centered electronic transition (i.e. $d\sigma^* \rightarrow d\sigma^*$), which is consistent with the EHMO predictions.

For the second moment band analysis, Eq. 3.3 can be written as following form:

$$\frac{(\text{fwhm})^2}{8\ln 2} = A_1 \coth\left(\frac{\hbar\omega_{g1}}{2kT}\right) + A_2 \coth\left(\frac{\hbar\omega_{g2}}{2kT}\right) + B \qquad [3.5]$$

According to theory, $A_i = S\,(\hbar\omega_{ei})^2$, where S is the unitless Huang-Rhys parameter (129), and $\hbar\omega_{ei}$ is the excited state frequency. Since fwhm is measured in cm^{-1} units, then A is in cm^{-2}

units and $\hbar\omega_e$ becomes ν_e in cm^{-1} as well. The parameter S is related to the excited-state distortion, ΔQ, according to following equation (128):

$$S_i = [\frac{\mu_i \omega_e^2}{2\hbar\omega_g}]\Delta Q^2 \qquad [3.6]$$

where μ_i is the reduced mass of the vibrational fragments.

By converting the frequencies ω_i (s^{-1}) into ν_i (cm^{-1}) using $\omega_i = 2\pi c\nu_i$, and assuming that the ratio ν_1/ν_2 is constant (K) for both the ground and excited states, then Eq. 3.5 can be rewritten as:

$$(\text{fwhm})^2 = A\ \{\coth(\frac{0.72\nu_{g1}}{T}) + K^3(\frac{\mu_2}{\mu_1})\coth(\frac{0.72\ \nu_{g2}}{T})\} + B\ (8\ln 2) \qquad [3.7]$$

where

$$A = 16\ \pi^2\ (\ln 2)\ \Delta Q^2\ \nu_{e1}^4(\frac{\mu_1 c}{\hbar\nu_{g1}}) \qquad [3.8]$$

$$K = \nu_{g2}/\nu_{g1} \qquad [3.9]$$

The analysis was performed in two ways. First ν_{g1} and ν_{g2} were assumed to be 165 and 86 cm^{-1}, respectively, in order to extract the slope and intercept for Eq. 3.7. Second, the parameters A, B and ν_{g1} were set as variables, and at the best fit, these parameters are given the following values: $A = 3.79\times10^6$, $B = 4.13\times10^5$, $\nu_{g1} = 165\ cm^{-1}$, and $\nu_{g2} = 86\ cm^{-1}$. The second moment plot of the lowest energy band for $[Pd_4(dmb)_4(PPh_3)_2]^{2+}$ in butyronitrile is shown in Figure 50, and the given parameters are listed and compared in Table 32.

Based upon the comparison in Table 32, some brief comments can be made. The parameter B

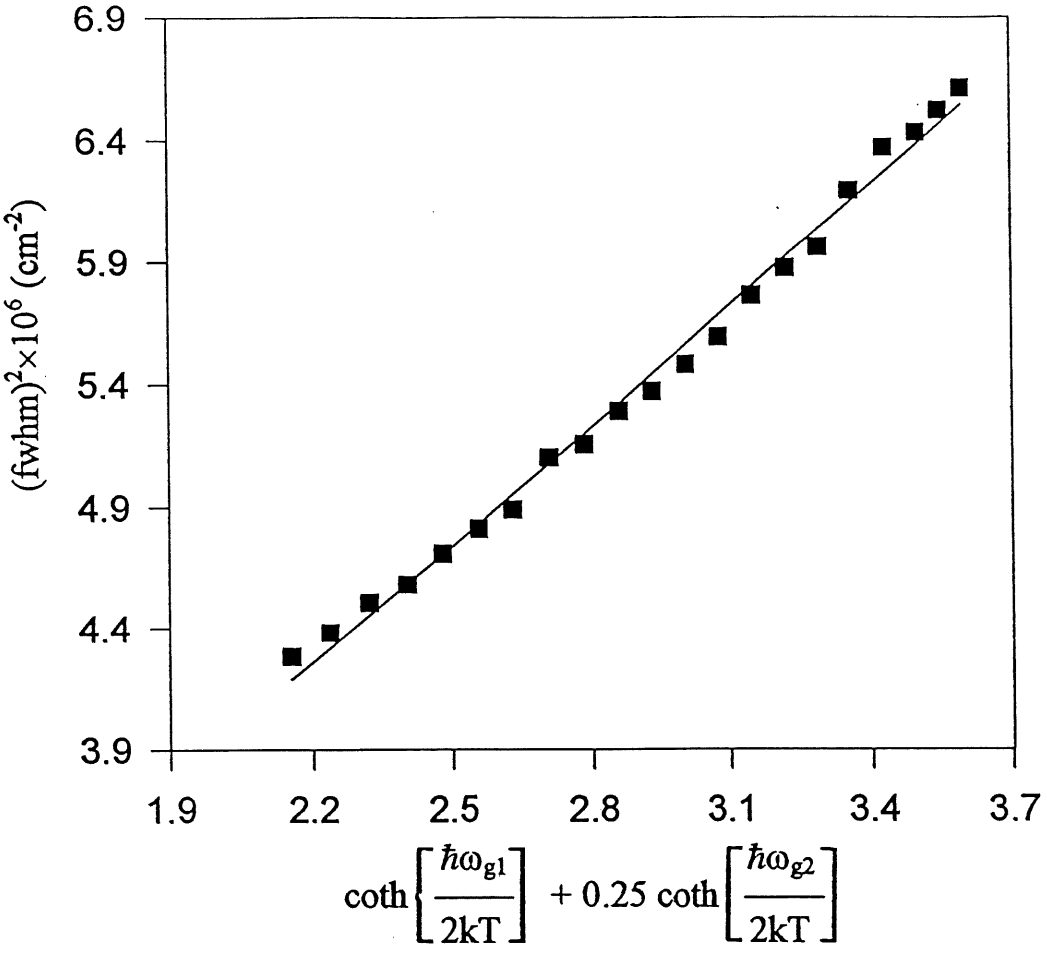

Figure 50. The second moment plot of the lowest energy band for $[Pd_4(dmb)_4(PPh_3)_2]^{2+}$ in butyronitrile. The squares represent the experimental data; the line is the best fit.

(second moment) for the linear complexes appears to be dependent upon the mass of the axially coordinated ligand, i.e. the greater is *A*, the smaller the atomic mass is (P < Cl < Br). This observation is consistent with the literature proposal that *B* is related to higher frequency Franck-Condon active modes which are too energetic to contribute strongly to the temperature dependence (114). In fact, ν(Pd-L) varies according to the following order: ν(Pd-P) (270 cm^{-1}) > ν(Pd-Cl) (240 cm^{-1}) (28) > ν(Pd-Br) (194 cm^{-1}) (28). The parameter *A* in second moment is dependent upon ν_{g1}. The larger ν_{g1} gives larger *A*. This observation with

Eq. 3.8 where $A \propto \nu_{e1}^4$. It is anticipated that, ν_{g1} is large, then ν_{e1} is also large, if ΔQ is comparable for these systems.

Table 32. Comparison of the first and second moment band analysis for various Pd_n^{2+} species

Compounds			First moment			Second moment		Refs.
	$\hbar\omega_{ei}$ (cm^{-1})	$\hbar\omega_{ei}$ (cm^{-1})	A_1 (cm^{-1})	A_2 (cm^{-1})	B (cm^{-1})	A^a (cm^{-2})	B^a (cm^{-2})	
$Pd_4(dmb)_4(PPh_3)_2^{2+}$	165	86	-6.0	-0.66	1.93×10^4	6.84×10^5	4.13×10^5	This work
$Pd_3(dppm)_3CO^{2+}$	190[c]	140[c]	-210	-150	2.27×10^4	9.38×10^5	b	13
$Pd_2(dmb)_2Cl_2$	175[d]	---	-607	---	2.54×10^4	6.45×10^5	1.50×10^5	28
$Pd_2(dmb)_2Br_2$	120[e]	---	-518	---	2.44×10^4	2.71×10^5	0.65×10^5	28

[a] Note that the A and B values are extracted from the graph $(fwhm)^2$ vs coth function, where the slope and the intercept have been divided by 8ln2. [b] This value is very small. [c] The vibrational frequencies obtained by Raman spectroscopy are 205 and 143 cm^{-1}, respectively. [d] Raman datum: 174 cm^{-1}. [e] Raman datum: 131 cm^{-1}.

Eq. 3.8 indicates that ΔQ and ν_{e1} are interdependent. The best fits of the second moment gives $A = 3.79 \times 10^6$, therefore ΔQ can be evaluated if ν_{e1} is known. Unfortunately the ν_{e1} is not known, but it should be lower than ν_{g1} (Table 33). At this point, no further analysis has been performed.

In order to simulate the absorption spectrum of $[Pd_4(dmb)_4(PPh_3)_2]^{2+}$, Heller's time-dependent theory which is equivalent to a traditional Franck-Condon analysis (130), is applied. The time-dependent for formulation of Heller's theory applied to electronic spectroscopy, involved the

Table 33. Selected ΔQ values vs $\hbar\omega_{e1}$ for the excited states of $[Pd_4(dmb)_4(PPh_3)_2]^{2+}$

$\hbar\omega_{e1}/cm^{-1}$	ΔQ/Å	$\hbar\omega_{e1}/cm^{-1}$	ΔQ/Å
160	0.148	140	0.194
155	0.158	135	0.208
150	0.168	130	0.225
145	0.180		

use of wavefunctions which include both the electronic transition moment between two Born-Oppenheimer potential surfaces and the ground-state vibrational wavefunctions. For absorption spectra, the wave functions are displaced in the wave packet and evolve with time according to the time-dependent Schrödinger equation. The overlap between the wave functions at $t = 0$ and $t = t$ is Fourier transformed in order to give the spectrum. By using $\Gamma = 1\times10^{-12}$s, position of the 0-0: 17200 cm^{-1}, and a vibrational bandwidth: 80 cm^{-1}, the simulated spectra exhibit fwhm of ~800-900 cm^{-1} that do not vary with ΔQ. By increasing the vibrational bandwidth to 200 cm^{-1}, the fwhm of the computed bandwidth increases to ~1100 cm^{-1}. Clearly the experimental fwhm (1560 cm^{-1}) is not reached with this simple model, obviously because the temperature-independent contribution (8(ln2)B) is ignored. The most appropriate "high energy" mode is the symmetric ν(Pd-P) (observed at 270 cm^{-1} in Raman spectrum). This mode is selected because the P atoms contribute significantly to the LUMO and HOMO according to the EHMO calculations. By using a three-mode model, for instance, $\nu_1 = 165$, $\nu_1 = 86$ cm^{-1} with $\Delta Q = 0.148$ Å (Table 33), $\nu_1 = 270$ cm^{-1} with $\Delta Q' = \sim0.1$ Å ($\Delta Q'$ is excited distortion along the Pd-P bonds), $\Gamma = 1\times10^{-12}$s and vibrational bandwidth = 80 cm^{-1}, the simulated spectrum gives fwhm ~1400 cm^{-1}. This result represents a drastic improvement of the model. By subsequently changing these values, the experimental value (fwhm = 1560 cm^{-1}) is easily reached. The further work is not necessary since $\Delta Q'$ for this temperature independent

term and the vibrational bandwidth are unknown. But this result indeed demonstrates the contribution of the "high energy" mode of ν_1(Pd-P) to *B* in Eq. 3.5.

3.2.7 Luminescence properties

Both d^8-d^8 and d^{10}-d^{10} complexes of Pd and Pt are known to be relatively strongly luminescent (131, 132), but d^9-d^9 compounds are either nonemissive or weakly luminescent (28). These 58-electron Pd_4^{2+} species are not luminescent at room temperature, but at 77 K, relatively strong emission bands centered at ~ 690 nm have been observed (Figure 51), which are broad and structureless, ranging from 580 nm to over 850 nm. The similar spectra are obtained for $[Pd_4(dmb)_4(PPh_3)_2]^{2+}$ and polymer $\{[Pd_4(dmb)_5]^{2+}\}_n$. The emission lifetimes of these two samples are listed in Table 34, which are in the 0.5-1.2 μs range. The values for $[Pd_4(dmb)_4(PPh_3)_2]^{2+}$ are shorter than that of the polymer regardless of the solvent (butyronitrile or ethanol). The relatively large Stoke shifts (4200-6200 cm^{-1}) and long lifetimes

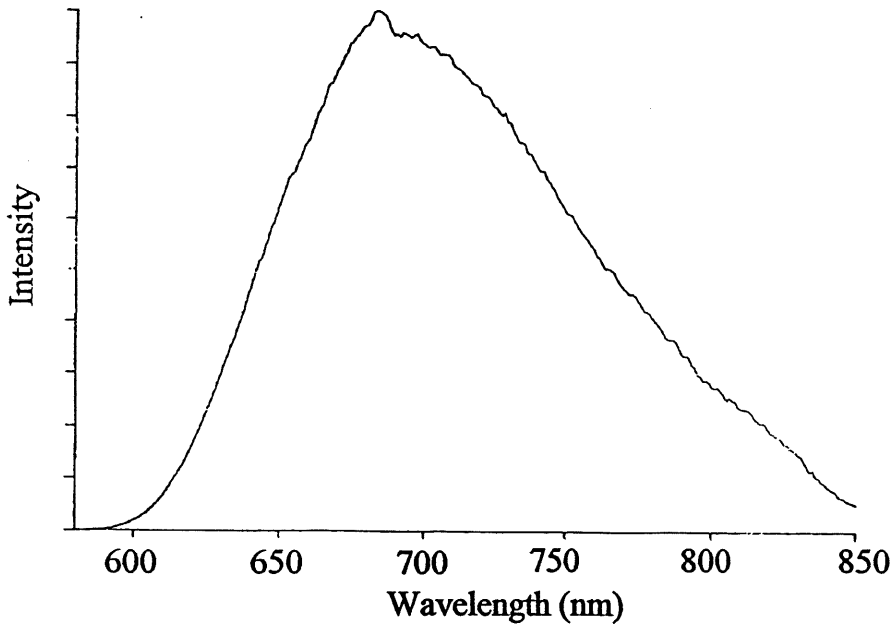

Figure 51. The emission spectrum of $[Pd_4(dmb)_4(PPh_3)_2]^{2+}$ in ethanol at 77 K.

Table 34. Electronic spectroscopic data for $[Pd_4(dmb)_4(PPh_3)_2]Cl_2$ and polymer $\{[Pd_4(dmb)_5](CH_3COO)_2\}_n$

Compounds	λ_{abs}/nm ; 77 K		λ_{em}/nm ; 77 K		τ_e/μs; 77 K	
	BuCN	EtOH	BuCN	EtOH	BuCN	EtOH
$[Pd_4(dmb)_4(PPh_3)_2]Cl_2$	532	534	685	684	0.56 ± 0.01	0.67 ± 0.02
$\{[Pd_4(dmb)_5](CH_3COO)_2\}_n$	490	488	703	698	1.00 ± 0.02	1.14 ± 0.05

indicate that the emissions are phosphorescence, and assigned to $d\sigma^* \rightarrow d\sigma^*$ spin-forbidden transitions. By adding triphenylphosphine (PPh_3) to these solutions, it was discovered that the emissions were significantly quenched for both samples. But an excess of the dmb ligand has no so great influence on the emission maxima and lifetimes. In fact, the lifetimes for the polymer had been measured in the presence of an excess of dmb to stablize the Pd_4^{2+} species. What exactly happened in the solutions when free PPh_3 is present? It is possible that the excess PPh_3 replaces dmb ligand and leads to the breakdown of the cluster.

3.3 Reactivity of low-valent platinum-diisocyanide complex. Synthesis, crystal structure and properties of $[Pt_2Au_2(dmb)_2(PPh_3)_4](PF_6)_2$

Chemistry of phosphine-stablized, platinum-gold complexes has grown enormously over the past two decades and a diversity of compounds have been synthesized (133, 134, 135). In general, two important methods can be used to prepare this kind of clusters. One is oxidative addition of H_2 followed by the substitution of H^+ by Au (I) cations (136). Another pattern is that Au(I) units attack the electron-rich platinum center as an electrophilic group (137). In the latter case, the well-known examples are that, the Au(I), HgX_2 and other metal species with the d^{10} electronic configuration, insert directly into the Pt(I)-Pt(I) bond of $Pt_2(dppm)_2X_2$ to

form the stable trimetallic clusters, so-called "A-frame" complexes (8, 33, 34). These reactions have been intensively studied, and are now well understood. Since the novel, electron-rich and linear Pt_4 chain species, $Pt_4(dmb)_mCl_2$, can be isolated, it is possible to study the chemistry of this species now. Here the reaction between this complex and Au(I) compound is studied.

3.3.1 Synthesis and characterization

Reaction of $Pt_2(dba)_3 \cdot CHCl_3$ with an excess of dmb in acetone gives $Pt_4(dmb)_mCl_2$, which is a yellow-orange solid and characterized by a strong absorption band at 348 nm in UV-vis spectrum. Its structure is proposed to be similar to that of polymer $\{[Pd_4(dmb)_5]^{2+}\}_n$. In a mixture of methanol and acetone (1:3 v/v), an addition of $[Au(PPh_3)_2](PF_6)$ to a $Pt_4(dmb)_mCl_2$-containing solution leads to a color change from yellow-orange to yellow-brown in a few minutes, indicating that new complexes are formed. A yellow-greenish crude product was isolated from precipitation with diethyl ether. Upon dissolving the product in dichloromethane, a deeply colored solution was separated from a pale yellow-greenish insoluble solid by filtration. The insoluble solid in dichloromethane was characterized by UV-vis, IR, ^1H NMR, and mass FAB spectroscopy along with chemical analysis. ν(CN) (IR) is found at 2180 and 2160 cm^{-1} (shoulder), which are lower than that found in the Pt(II)-dmb complex (2221 cm^{-1}). In ^1H NMR spectra, only signals belonging to the dmb ligand were detected for this compound. In the mass FAB spectra, the species $Pt_2(dmb)_2$ (770) and $Pt_2(dmb)Cl$ (615) were readily observed. For comparison, $Pt_2(dmb)_2Cl_2$ complex was prepared by the reaction between $Pt_2(dmb)_2Cl_4$ and $Pt_2(dba)_3$ (molar ratio 1:1) in the presence of an excess of dmb. This method for preparing such a compound has been adapted from a method for synthesizing $Pd_2(dmb)_2Cl_2$ (20). Indeed the UV-vis spectrum and other properties of this pale yellow-greenish solid are very similar to that of $Pt_2(dmb)_2Cl_2$. Based upon the above data and the results of chemical analysis, this complex was assigned to $Pt_2(dmb)_2Cl_2$.

Crystallization of the remaining solution from a mixture of dichloromethane/toluene afforded two kinds of crystals. These are deep-orange and dark-greenish crystals. For the "orange" compound, the ν(CN) peak appears at 2147 cm^{-1}, and the ^1H NMR and UV-vis spectra are identical with that for $[Pt_4(dmb)_4(PPh_3)_2]Cl_2$. The difference is that PF_6^- anion is present in this orange complex (appearing as a strong band at 841 cm^{-1} in the IR spectrum). Further analysis comes from the mass FAB spectrum, which clearly confirmed that this compound is $[Pt_4(dmb)_4(PPh_3)_2](PF_6)_2$ (Table 35). The species $[Pt_4(dmb)_4(PPh_3)_2](PF_6)_2$ and $[Pt_4(dmb)_4(PPh_3)_2](PF_6)$ are readily observed, appearing at 2358 and 2210, respectively.

Table 35. Assignment of the fragments of $[Pt_4(dmb)_4(PPh_3)_2](PF_6)_2$

Peaks	Rel. Int. (%)	Assignments	Calc. Mass
2358	6	$[Pt_4(dmb)_4(PPh_3)_2](PF_6)_2$	2356.05
2210	70	$[Pt_4(dmb)_4(PPh_3)_2](PF_6)$	2211.07
2065	60	$[Pt_4(dmb)_4(PPh_3)_2]$	2066.1
1948	65	$[Pt_4(dmb)_4(PPh_3)](PF_6)$	1948.8
1900	5	$[Pt_3(dmb)_4(PPh_3)](PF_6)_2$	1898.7
1803	100	$[Pt_4(dmb)_4(PPh_3)]$	1803.8
1638	10	$[Pt_3(dmb)_4](PF_6)_2$	1636.4
~ 1618	5	$[Pt_2(dmb)_4(PPh_3)_2](PF_6)$	1620.9

The isolated dark-greenish crystal is possibly a heterobimetallic cluster containing both Pt and Au. The ν(CN) is found at 2164 cm^{-1}, indicating that isocyanide groups do also coordinate the metal centers with relatively high oxidation states. ^1H NMR spectrum clearly shows two kinds of ligands, PPh_3 (δ 7.1-7.6 ppm) and dmb (δ 0.65-1.6 ppm), with a molar ratio PPh_3/dmb of 2 : 1. The two peaks with 1:1 integration ratio around 7.1 - 7.6 ppm belong to two kinds of

PPh_3 ligands, which coordinate two different metal centers. Direct evidence was provided by the mass FAB measurements (Figure 52, Table 36). The heaviest peaks arose from $[Pt_2Au_2(dmb)_2(PPh_3)_4](PF_6)$, $[Pt_2Au_2(dmb)_2(PPh_3)_4]$ and $[Pt_2Au_2(dmb)_2(PPh_3)_3](PF_6)$. Therefore this complex can be assigned to $[Pt_2Au_2(dmb)_2(PPh_3)_4](PF_6)_2$.

Table 36. Assignment of the fragments of $[Pt_2Au_2(dmb)_2(PPh_3)_4](PF_6)_2$

Peaks	Rel. Int.(%)	Assignments	Calc. Mass
2361.9	~3	$[Pt_2Au_2(dmb)_2(PPh_3)_4](PF_6)$	2358.9
2214.9	8	$[Pt_2Au_2(dmb)_2(PPh_3)_4]$	2213.9
2094.7	30	$[Pt_2Au_2(dmb)_2(PPh_3)_3](PF_6)$	2096.6
1951.5	46	$[Pt_2Au_2(dmb)_2(PPh_3)_3]$	1951.6
1688.2	60	$[Pt_2Au_2(dmb)_2(PPh_3)_2]$	1689.3
~1492	20	$[PtAu_2(dmb)_2(PPh_3)_2]$	1494.3
		$[Pt_2Au(dmb)_2(PPh_3)_2]$	1492.3
1427.2	40	$[Pt_2Au_2(dmb)_2(PPh_3)]$	1427.0
1230.4	100	$[PtAu_2(dmb)_2(PPh_3)]$	1232.0
		$[Pt_2Au(dmb)_2(PPh_3)]$	1230.0
1106.4	50	$[PtAu(dmb)(PPh_3)_2]$	1106.9

3.3.2 Crystal structure of $[Pt_2Au_2(dmb)_2(PPh_3)_4](PF_6)_2$

Recrystallization from a mixture of dichloromethane and cyclohexane gave dark-greenish crystals of suitable quality for X-ray crystallography analysis (Table 37, Figure 53). The structure reveals that two gold atoms are located between two platinum atoms to form a doubly bridged cluster Pt_2Au_2 with a rhombic geometry. The dmb ligands still coordinate to Pt

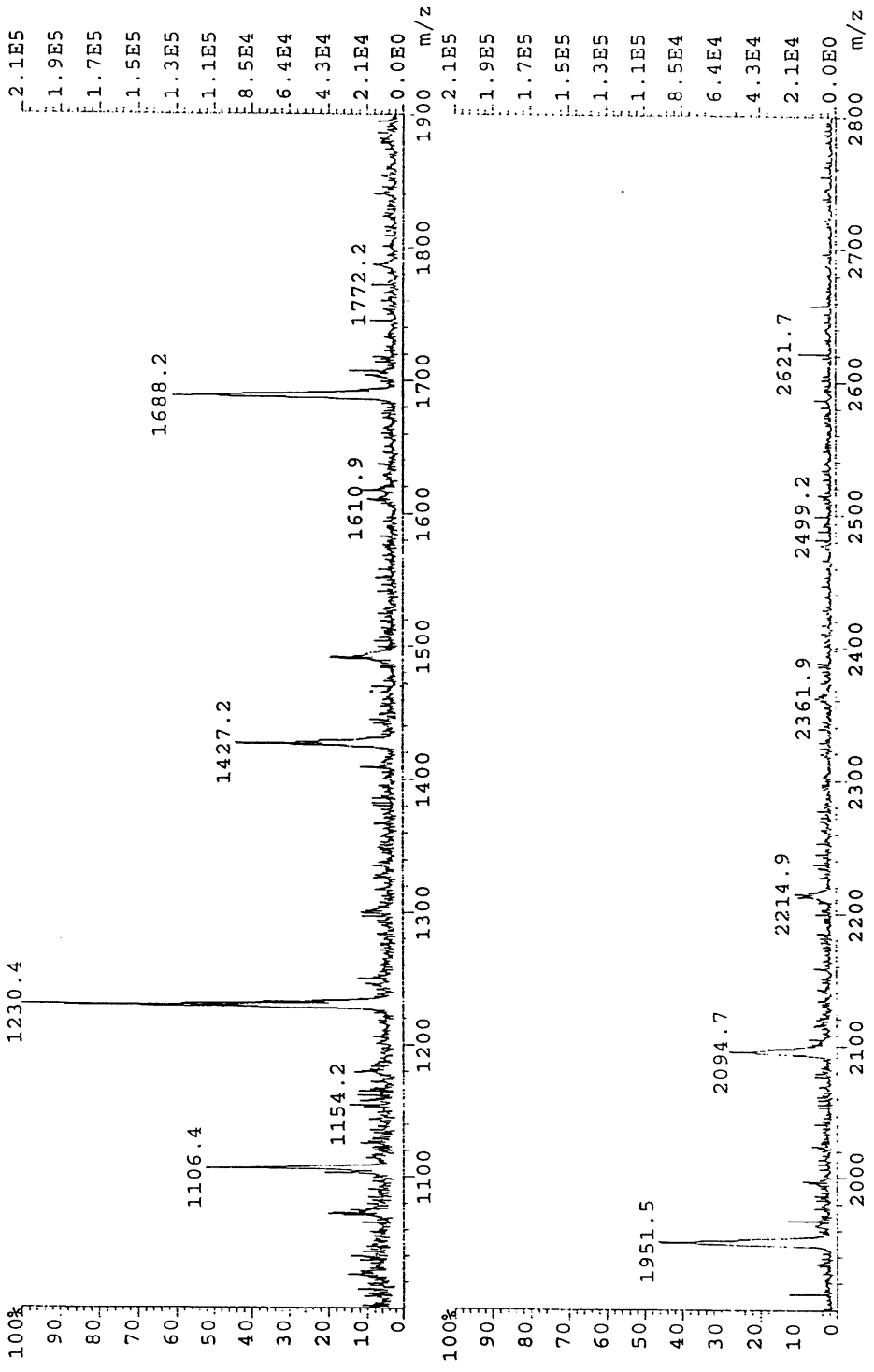

Figure 52. Mass FAB spectrum of $[Pt_2Au_2(dmb)_2(PPh_3)_4](PF_6)_2$.

Table 37. Crystal data for $[Pt_2Au_2(dmb)_2(PPh_3)_4](PF_6)_2$

Empirical formula	$C_{96}H_{96}N_4F_{12}P_6Pt_2Au_2$
Formula weight	2503.98
Wavelength	1.54060 Å
Crystal system, space group	Triclinic, P-1
Unit cell dimensions	a = 12.0371(9) Å, α = 63.790(5)°
	b = 14.0188(9) Å, β = 80.348(7)°
	c = 15.3362(11) Å, γ = 86.711(7)°
Volume	2288.6 (3) $Å^3$
Z	1
Calculated density	2.376 Mg/m^3
Theta ranges	3.25 to 69.86°
Reflections collected/unique	8634 / 8634 [R(int) = 0.0000]
Data/restraints/parameters	8634 / 147 / 499
Final R indices [I>2sigma (I)]	R1 = 0.0447, wR2 = 0.1305
R indices (all data)	R1 = 0.0618, wR2 = 0.1418

$R1=\Sigma(||F_o|-|F_c||)/\Sigma|F_o|$, $wR2=\{\Sigma[w(F_o^2-F_c^2)^2]/\Sigma w(F_o^2)^2\}^{1/2}$, $w=1/[\sigma^2(F_o^2)+0.1P)^2$ where $P=(F_o^2+2F_c^2)/3$.

atoms to form 20-membered ring commonly encountered in the dinuclear complexes. The Pt-Au bond length is 2.83 Å, which is much longer than that found in "A-frame" complexes (i.e. for $(NC)_2Pt_2(\mu\text{-AuCl})(\mu\text{-dppm})_2$, d(Pt-Au)=2.65 Å (34)). In IR spectrum, the band of the isocyanide group (ν(CN)) of dmb ligands appears at 2164 cm^{-1}. In Pt(II)-dmb complexes, the peaks are located around 2230 cm^{-1}, and 2146 cm^{-1} in Pt(0.5)-dmb compound, $[Pt_4(dmb)_4(PPh_3)_2]^{2+}$, in the IR spectra (Table 39). It is clear that some positive charges are located on the Pt centers. If the oxidation state of Pt atom is considered to be +1, then that of Au atom should be zero. As a consequence the bond order(BO) between the Pt and Au atoms

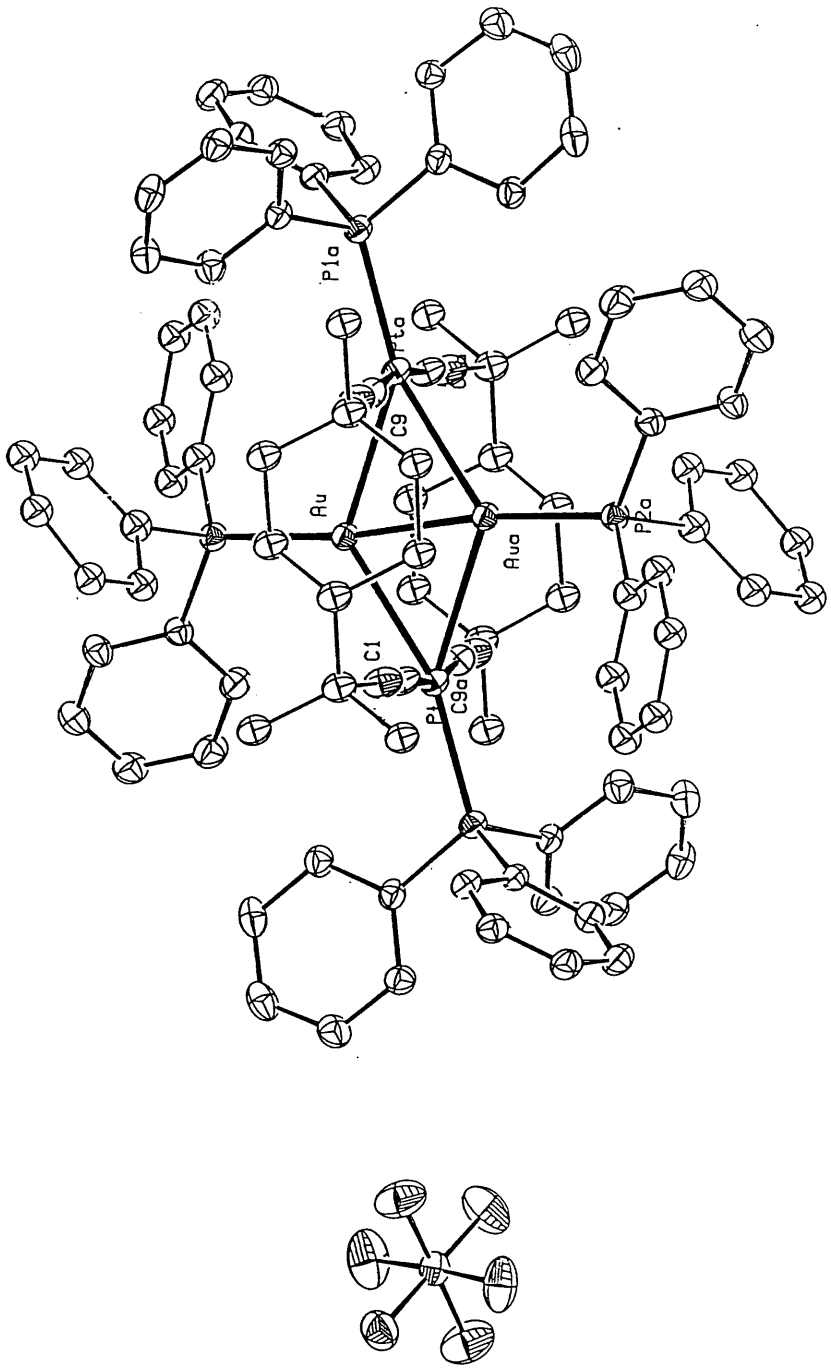

Figure 53. Crystal structure of $[Pt_2Au_2(dmb)_2(PPh_3)_4](PF_6)_2$.

Table 38. Selected bond lengths (Å) and angles (°) for $[Pt_2Au_2(dmb)_2(PPh_3)_4](PF_6)_2$

Pt-C(1)	1.918 (8)	Pt-Aua	2.8422 (5)
Pt-C(9a)	1.928 (9)	Au-Aua	2.5997 (6)
Pt-P(1)	2.3612 (19)	Aua-Pta	2.8082 (5)
Pt-Au	2.8082 (5)	Au-Pta	2.8423 (5)
C(1)-Pt-C(9a)	168.4 (4)	P(1)-Pt-Aua	146.16 (5)
C(1)-Pt-P(1)	98.6 (3)	Au-Pt-Aua	54.738 (13)
C(9a)-Pt-P(1)	92.9 (3)	P(2)-Au-Aua	172.67 (6)
C(1)-Pt-Au	91.2 (3)	P(2)-Au-Pt	123.81 (5)
C(9a)-Pt-Au	77.7 (3)	Aua-Au-Pt	63.297 (15)
P(1)-Pt-Au	157.66 (5)	P(2)-Au-Pta	110.90 (5)
C(1)-Pt-Aua	83.1 (3)	Aua-Au-Pta	61.964(15)
C(9a)-Pt-Aua	87.8 (3)	Pt-Au-Pta	125.261(14)

would be 0.25, lower than that found in the "A-frame" complexes, where the BO is 0.33. This observation is consistent with the comparison of the bond lengths between this complex and the "A-frame" compounds. It is interesting that the Au-Au distance is rather short, 2.598 Å, indicating that this Au-Au bond is very strong. At such a distance, a formal Au-Au bond is expected. The short Au-Au bond length is comparable to that found in the closely related bridged $[Pt_2Au_2(PPh_3)_4(CNC_6H_3Me_2\text{-}2,6)_4]^{2+}$ cluster (2.59 Å), which was prepared from the reaction between $[Au(CNR)_2]^+$ and $[Pt(C_2H_4)(PPh_3)_2]$. A distorted butterfly geometry was observed in this case (138), and it was proposed that the Au-Au bond is due to a large overlap of the outpointing *sp* hybrid orbitals on each Au atom. Except for the different isocyanide ligands, the significant difference between these two structures is the Pt-Au bond lengths. In $[Pt_2Au_2(PPh_3)_4(CNC_6H_3Me_2\text{-}2,6)_4]^{2+}$, there are two kinds of distances, the long one is 2.975

Table 39. IR active ν(CN) data for various Pt-CNR (alkyl) complexes[a]

Compound	Oxidation state	ν(CN) cm^{-1}	Ref.
$Pt_3(CN\text{-}t\text{-}Bu)_6$	0	2150	139
$[Pt_4(dmb)_m]Cl_2$	0.5	2150	This work
$[Pt_4(dmb)_4(PPh_3)_2]^{2+}$	0.5	2146	This work
$[Pt_2Au_2(dmb)_2(PPh_3)_4]^{2+}$	I	2164	This work
$Pt_2(dmb)_2Cl_2$	I	2170[b]	This work
$Pt_2(dmb)_2Cl_4$	II	2221	This work
$[Pt_2(CN\text{-}t\text{-}Bu)_3(Cl)_3(\mu\text{-}CN)]\cdot Pt(CN\text{-}t\text{-}Bu)_2(Cl)_2$	II	2217	60

[a] R = *t*-butyl or dmb; [b] Average value between 2180 (s) and 2160 cm^{-1} (sh).

Å, and the short is 2.715 Å. For this work, all Pt-Au bond lengths are nearly same, ranging from 2.81 to 2.84 Å. According to the concept of isolobal analogy (140) and based upon the structural data for $[Pt_2Au_2(PPh_3)_4(CNC_6H_3Me_2\text{-}2,6)_4]^{2+}$ cluster, Mingos proposed the following mechanism to explain the reaction between $Au(CNR)_2^+$ and $[Pt(C_2H_4)(PPh_3)_2]$(138):

1. Ligand exchange

$$[Au(CNR)_2]^+ + [Pt(C_2H_4)(PPh_3)_2] \rightarrow [Au(CNR)(PPh_3)]^+ + [Pt(CNR)(PPh_3)_2] + C_2H_4$$

2. Oxidative-addition reaction:

$$[Au(CNR)(PPh_3)]^+ + [Pt(CNR)(PPh_3)_2] \rightarrow [(Ph_3P)(CNR)_2Pt\text{-}Au(PPh_3)]^+$$

Then the dimerization of $[(Ph_3P)(CNR)_2Pt\text{-}Au(PPh_3)]^+$ leads to the final product.

In this work, the electrophilic group, $Au(PPh_3)^+$, does not attack the outer Pt atoms in the $Pt_4(dmb)_m]Cl_2$ species in the primary step. Further it does not attack the Pt-Pt bonds either, due to obvious steric reasons. In addition, the molar ratio between $[Au(PPh_3)_2]PF_6$ and $Pt_4(dmb)_mCl_2$ (m was set to be 5) was kept 1:1. One possible explanation for this reaction is as follows: First, $[Pt_4(dmb)_m]Cl_2$ partially dissociates to become d^{10}-d^{10} and d^9-d^9 dimers, and $Au(PPh_3)_2^+$ also dissociates to produce the electrophilic group $Au(PPh_3)^+$. Then the Au species attacks the most electron-rich Pt(0) or $Pt_2(0)$ center in the d^{10} - d^{10} dimer to form PtAu

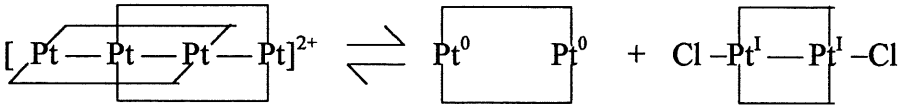

$$Au(PPh_3)_2^+ \rightarrow Au(PPh_3)^+ + PPh_3$$

or Pt_2Au species through an oxidation-addition reaction, where Au(I) is reduced to become Au(0). The latter should have a strong tendency to form Au-Au bonds with other $Au(PPh_3)^+$ species, which leads to the final product.

3.3.3 ^{31}P NMR spectrum

The ^{31}P NMR spectrum of $[Pt_2Au_2(dmb)_2(PPh_3)_4](PF_6)_2$ shows two signals centered at 44.7 and 59.0 ppm with a 1:1 ratio (Figure 54). The peak at 44.7 ppm shows two satellites which are associated with a coupling with ^{195}Pt nucleus (^{1}J(Pt-P) = 2253 Hz), and hence can be easily assigned to the phosphorous atoms coordinating the platinum. The other resonance belongs to the phosphorous atoms attached to gold at 59.0 ppm. Taking into account the distribution of the isotopomers, the ^{31}P spectrum can be satisfactorily simulated (Figure 54b), using the coupling constants derived from the experimental data (Table 40) and based upon

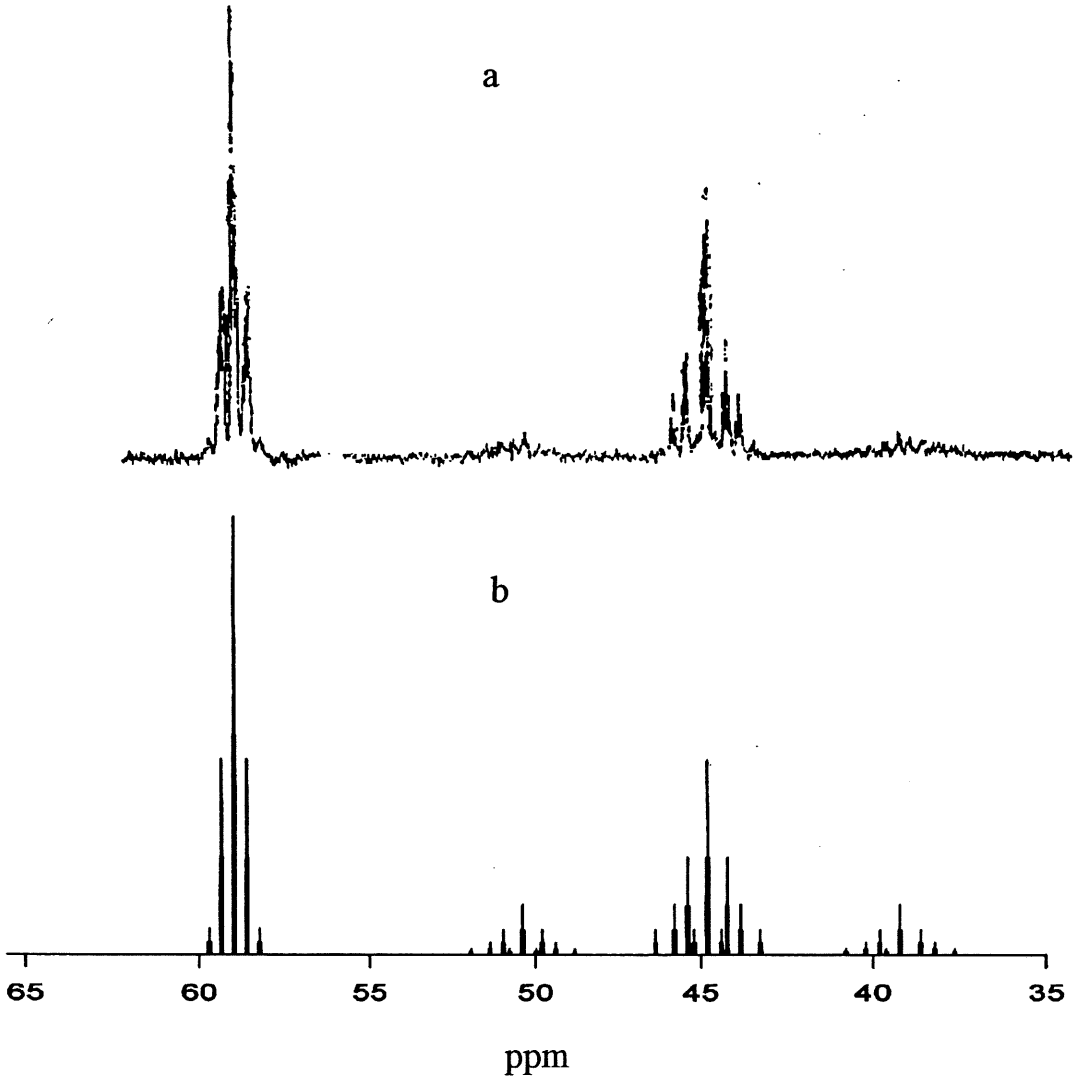

Figure 54. ^{31}P NMR spectra of $[Pt_2Au_2(dmb)_2(PPh_3)_4](PF_6)_2$ in CD_2Cl_2

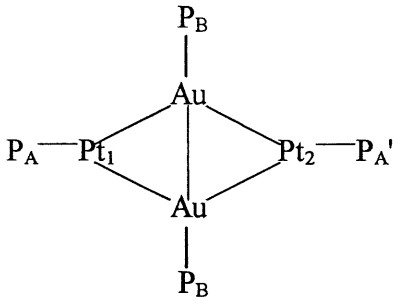

Table 40. Coupling constants for $[Pt_2Au_2(dmb)_2(PPh_3)_4](PF_6)_2$

J/Hz	Pt_1	Pt_2	P_B	P_A'
P_A	2253	395	17	234
P_A'	395	2253	17	
P_B	147	147		17

the D_{2h} local symmetry of the cluster. In comparison with the data reported for $[Pt_2Au_2(PPh_3)_4(CNC_6H_3Me_2\text{-}2,6)_4]^{2+}$ (138), it is observed that the coupling constants between the atoms in the P_A-Pt---Pt-P_A' direction, are always larger for $[Pt_2Au_2(dmb)_2(PPh_3)_4](PF_6)_2$. This result is consistent with the difference in bond lengths and angles between the two structures. The 234-Hz P-P coupling constant is very high for a four-bond coupling. This is likely due to the high symmetry of the cluster and relatively short distance. In the linear complexes, some large ^4J(P-P) values are also reported (141).

3.3.4 FT-Raman spectrum of $[Pt_2Au_2(dmb)_2(PPh_3)_4](PF_6)_2$

To address the amplitude of the short Au-Au bond, the Raman spectrum was measured (Figure 55). In comparison with the literature data (142) and based upon the commonly encountered high intensity of the metal-metal bond, the peak located at 121.2 cm^{-1} was readily assigned to ν(Au-Au), which gave the force constant, $F(Au_2)$ = 0.99 mdyn·Å^{-1}, comparable with those of ν(Au-Au) arising from the singly bonded Au_2 species ($r(Au_2)$<2.6 Å) (142). The comparison between this value and the calculated $F(Au_2)$ one obtained from the following equation:

$$r(Au_2) = -0.290 \ln F(Au_2) + 2.68 \qquad [3.10]$$

(1.32 mdyn·Å^{-1}) is not satisfactory. The difference is very likely due to the model which is used for dinuclear system, and not for this complex. This cluster exhibits two bridging Pt atoms, and their presence should affect the ν(Au-Au).

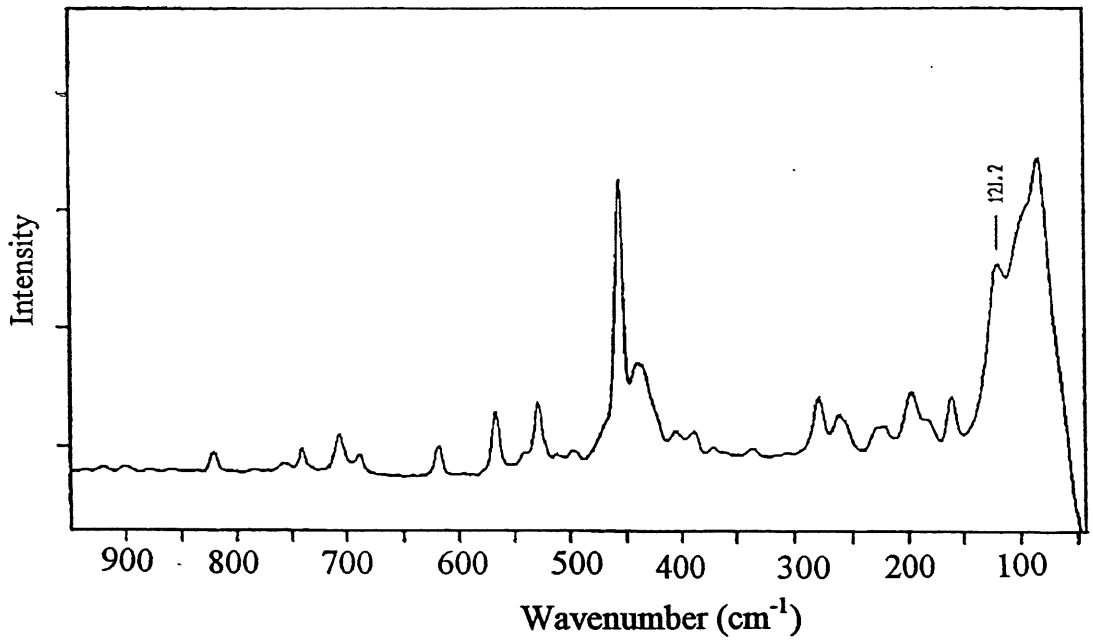

Figure 55. FT-Raman spectrum of $[Pt_2Au_2(dmb)_2(PPh_3)_4](PF_6)_2$

3.3.5 Electronic spectra

The UV-vis spectra of the green $[Pt_2Au_2(dmb)_2(PPh_3)_4]^{2+}$ cluster in solution are characterized by three series of absorptions in the visible region: a weak absorption between 600 and 700 nm, a well "isolated" narrow band at around 500 nm, and another band around 400 nm located on the red side of a series of stronger absorptions between 280 and 400 nm. In an attempt to provide a reliable assignment for these low energy electronic bands, the ε data, shapes, and behaviors with temperature should be considered (119). Upon cooling the samples from room temperature to 77 K, some absorption bands significantly sharpen, but others do not. This is the case for the peak located at 514 nm and those below 400 nm, but much less for the 640 nm band (Figure 56). The data are presented in Table 41, and are as follows for the two lowest energy absorption bands (bands 1 ~ 640 nm, and 2 ~ 515 nm): band 1, fwhm = 2360 and 2100 cm^{-1}; band 2, fwhm = 2400 and 1400 cm^{-1}, for T = 298 and 77 K, respectively.

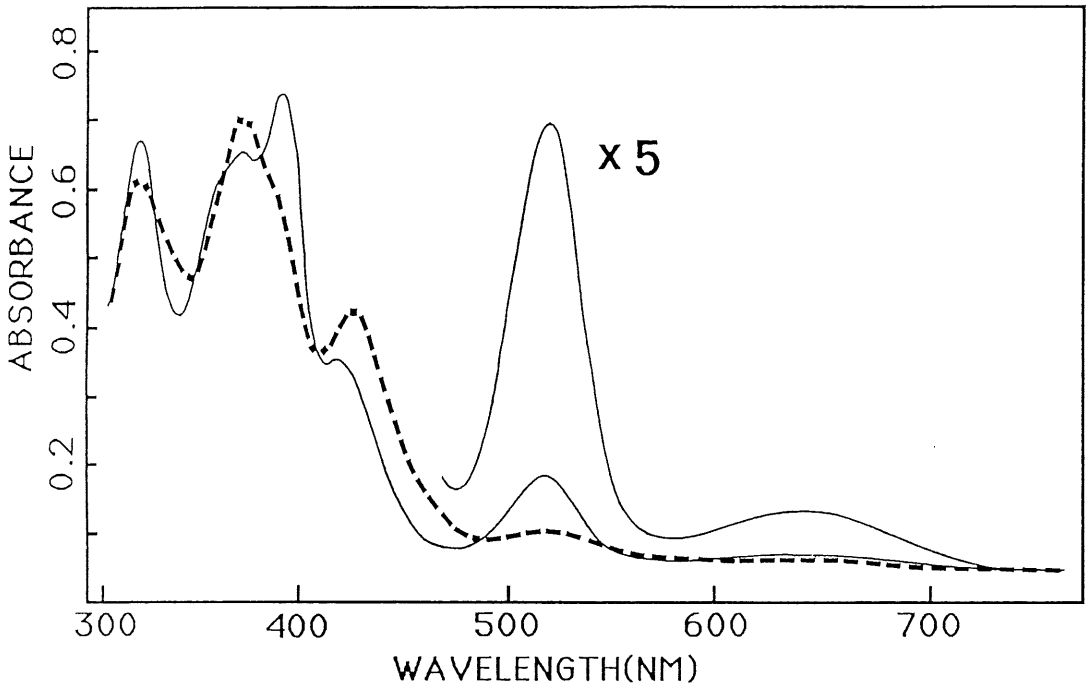

Figure 56. Absorption spectra of $[Pt_2Au_2(dmb)_2(PPh_3)_4]^{2+}$ (as a PF_6^- salt) in butyronitrile at 298 (- - -) and 77K (—).

Table 41. UV-vis spectroscopic data[a]

Band #	298 K				77 K		
	λ_{max} (± 2 nm)	ν_{max} (cm^{-1})	fwhm (± 100 cm^{-1})	ε ($M^{-1}cm^{-1}$ ±5%)	λ_{max} (± 2 nm)	ν_{max} (cm^{-1})	fwhm (± 100 cm^{-1})
1	655	15270 ±50	2360	8.34×10^2	639	15650 ±50	2100
2	526	19380 ±50	2400	2.86×10^3	514	19460 ±80	1400
3	418	23920 ±110	—	2.15×10^4	410	24390 ±110	—
4	366	27320 ±150	—	3.78×10^5	382	26180 ±140	—
					362	27620 ±150	—
5	316	31650 ±200	—	3.23×10^5	314	31850 ±200	—

[a] Solvent: butyronitrile

The data clearly indicate that band 2 (~ 515 nm) must be arise from a M_n-localized electronic transition. The relatively small decrease in fwhm for band 1 (~ 640 nm) indicates that the frequencies of some of the Franck-Condon active modes must be large, and the presence of an MLCT. Literature data show that the fwhm for MLCT bands for the $M_2(dba)_3$ complexes (M

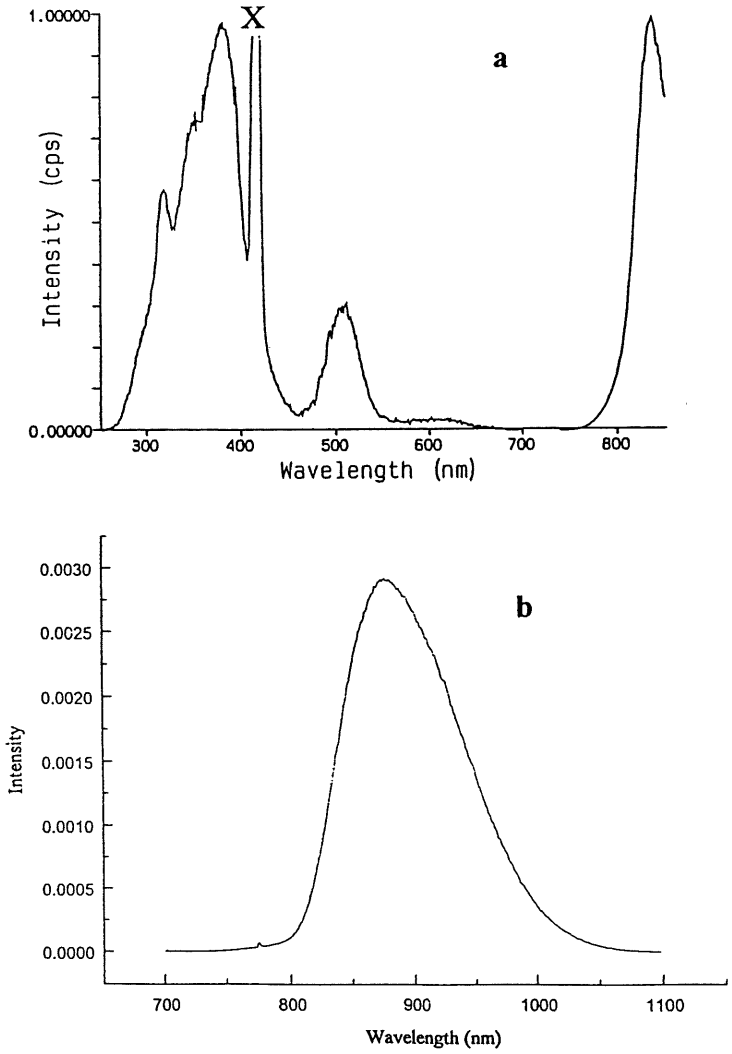

Figure 57. The excitation and emission spectra of $[Pt_2Au_2(dmb)_2(PPh_3)_4](PF_6)_2$.
a. Excitation (left) and emission (right) spectra in butyronitrile at 77K.
b. Emission spectrum at 12 K.

= Pd, Pt) do not change very much from 285 to 77 K, although the λ_{max} may change slightly (131). For the remainder of the spectra, the ε data and the significant decrease in fwhm with the lowering of the temperature, indicate that the bands must arise from M_n-centered transitions.

The cluster ($[Pt_2Au_2(dmb)_2(PPh_3)_4](PF_6)_2$) is not luminescent in solutions at room temperature, but a luminescence is readily detected in the red region of the spectra in the solid state (298 and 12 K), and in frozen solutions (77 K). The excitation and emission spectra measured at 298 K for solid $[Pt_2Au_2(dmb)_2(PPh_3)_4](PF_6)_2$ in NaCl matrices exhibit structureless broad bands at ~ 500 - 600 nm, and ~ 830 nm, respectively. The 77 K solution spectrum presented in Figure 57a also exhibits the same features (λ_{max} = 836 nm). The 77 K emission lifetime in this case is 4.42 ± 0.02 ns. The large Stoke shifts (~ 4200 cm^{-1}) and emission lifetime indicate that this emission is a phosphorescence. Further decrease of the solid sample temperature down to 12 K did not yield to improvement in spectral resolution (Figure 57b). In fact a small red shift is observed (from 830 (298 K) → 870 nm (12 K)), and the use of a different instrument (Université de Montréal) allowed to measure a complete spectrum. In this case, the emission band is weakly asymmetric, not a Gaussian shape.

CONCLUSION

In this project, the synthesis and properties of a series of new low-valent palladium and platinum complexes of diarsine and diisocyanide ligands have been investigated. The diarsine ligand, dpam, led to the preparation of polyhedral clusters (triangle and butterfly), while the diisocyanide ligand, dmb, gave the first 58-electron tetranuclear complexes containing the quasi-linear metal-metal chain. The low-valent Pd and Pt complexes of dpam have been synthesized and structurally characterized as trinuclear $[Pd_3(dpam)_3(\mu_3\text{-}CO)]^{2+}$, and tetranuclear $[Pt_4(dpam)_3(\mu_2\text{-}CO)_3(\eta^1\text{-}dpam)]^{2+}$ clusters. For $[Pd_3(dpam)_3(\mu_3\text{-}CO)]^{2+}$ cluster, the substitution of P by As atom in the bridging ligand, leads to a change in properties of the cluster. First, although the crystal structure is isomorphous with that of the dppm analogue, the cavity size formed by the six phenyl groups adopting the axial configuration, is larger, and one PF_6^- anion is now well located inside it. The binding constants of this larger host system are found to be larger than that of the dppm analogue, which clearly is a direct consequence of the cavity size increase induced by a longer Pd-As bond distance. Secondly, the oxidation-fragmentation reaction of this cluster was also observed. The reaction of the cluster, $[Pd_3(dpam)_3(\mu_3\text{-}CO)]^{2+}$, with I^- under inert atmosphere gave the expected cluster, $[Pd_3(dpam)_3(\mu_3\text{-}CO)(\mu_3\text{-}I)]^+$. Subsequently in the presence of oxygen, the same reaction leads to the breakdown of the cluster to produce the dinuclear complex, $[Pd_2(dpam)_2I_4]$. In this complex, the ligands, dpam, coordinate the Pd(II) centers in bridging fashion, not chelating mode. The related tetranuclear Pt cluster, $[Pt_4(dpam)_3(\mu_2\text{-}CO)_3(\eta^1\text{-}dpam)]^{2+}$, adopts a butterfly geometry containing two edge sharing Pt_3 triangles, in which one is large and one is small, as characterized by X-ray crystallography. It is proposed that this phenomenon is due to the uneven distribution of the positive charges over all the Pt frame. In solutions, a fluxional process occurs, which was investigated by ^1H NMR spectroscopy in some details. The Pt-Pt bonding properties along with the electronic spectroscopic behavior were rationalized using EHMO calculations.

The preparation of low-valent linear chain platinum and palladium complexes were achieved by direct reactions between $M_2(dba)_3 \cdot CHCl_3$ dimers (M = Pd, Pt), and an excess of diisocyanide ligands, dmb. Crystallographic studies for $[Pt_4(dmb)_4(PPh_3)_2]Cl_2$, demonstrated that the four platinum atoms are connected to each other through short Pt-Pt bonds (2.654, 2.641 and 2.666 Å), and form a quasi-linear chain ($\angle PtPtPt = 175.3°$). A catenate structure was observed where two 20-membered rings ($Pt_2(dmb)_2$ units) interlock each other to form this unique structure in dmb chemistry. The organometallic polymers containing $[Pt_4(dmb)_4]$ units, are easily prepared, by using diphosphine ligands of the type $Ph_2P(CH_2)_xPPh_2$ instead of PPh_3. The polymeric features of these diphosphine complexes have been addressed by X-ray powder diffraction, T_1 and viscosity measurements. The intermediate species, $[Pt_4(dmb)_m]^{2+}$, is reactive, and does indeed react with $[Au(PPh_3)_2]PF_6$ to provide a new doubly bridged heterobimetallic cluster, $[Pt_2Au_2(dmb)_2(PPh_3)_4](PF_6)_2$. This cluster exhibits a rhombic structure, where two gold atoms are located between two platinum centers, with a short Au-Au bond (2.598 Å). The tetranuclear linear palladium complex has been prepared in the same way. In this work, chlorocarbon is demonstrated to be involved in the reaction between $M_2(dba)_3 \cdot CHCl_3$ and dmb. The intermediate complex produced by the reaction between $M_2(dba)_3 \cdot CHCl_3$ dimers and dmb, "$Pd_4(dmb)_mCl_2$", reacted with neutral TCNQ to give $[Pd_2(dmb)_4(\mu_2\text{-}Cl)](TCNQ)_4$. In this case, the X-ray structure revealed that a chloride anion is symmetrically encapsulated inside the $Pd_2(dmb)_4^{2+}$ cage. In particular, one organometallic polymer relative to the intermediate state, $\{[Pd_4(dmb)_5](CH_3COO)_2\}_n$, was successfully isolated and its crystal structure was also obtained from X-ray crystallography. In solid state, the repetitive unit, $[Pd_4(dmb)_4]^{2+}$, is linked by a dmb ligand to form a zig-zig chain. EHMO computations for linear tetranuclear complexes predicted that the lowest energy absorption bands arise from $d\sigma^* \rightarrow d\sigma^*$ transitions. For $[Pd_4(dmb)_4(PPh_3)_2]Cl_2$ complex, this prediction has been confirmed by the first and second moment band analysis. These novel linear chain complexes and related organometallic polymers are not luminescent at room temperature, but relatively strong emissions are observed at 77K, which have been determined to be phosphorescence.

The experimental results in this project indicated that these 58-electron, linear chain species, $[M_4(dmb)_m]^{2+}$ (M = Pd, Pt), are very reactive. For instance, $[Pt_4(dmb)_m]^{2+}$ can react with $HGePh_3$ to break H-Ge bond, and also react with other organometallic species to give new heterometallic clusters. The chemistry and applications remain to be explored.

EXPERIMENTAL SECTION

1 Materials

1.1 Clusters $[Pd_3(dpam)_3CO]Y_2$ (Y = CF_3COO^-, PF_6^- and $[B(C_6H_5)_4]^-$) and $[Pt_4(dpam)_4(CO)_3]Y_2$ (CF_3COO^- and PF_6^-)

$Pd(CH_3COO)_2$ (Aldrich), dpam (Pfaltz & Bauer Inc.), CO (Praxair), AgO_2CCH_3 (Aldrich), CF_3COOH (Aldrich), $Na[B(C_6H_5)_4]$ (Aldrich) and NH_4PF_6 (Aldrich) were used without further purification. $Pt(COD)Cl_2$ (COD = cyclooctadiene) (143) was synthesized according to literature procedure.

1.2 Linear clusters, $[M_4(dmb)_4(PPh_3)_2]^{2+}$(M = Pt, Pd) and polymer $\{[Pd_4(dmb)_5]^{2+}\}_n$

K_2PtCl_4 (Pressure Chem.), $PdCl_2$ (Pressure Chem.), $H[AuCl_4]$ (Aldrich), PPh_3 (Aldrich), $Ph_2P(CH_2)_nPPh_2$ (n = 4, dppb; 5, dppp; 6, dpph) (Aldrich) were used without further purification. DBA (144), dmb (99), $Pt_2(dba)_3{\cdot}CHCl_3$ (98), $Pd_2(dba)_3{\cdot}CHCl_3$ (124), $[Au(PPh_3)_2]PF_6$ (145) and TCNQ (146), were prepared according to literature procedures.

2 Instruments

The UV-vis spectra were recorded on a Hewlett Packard 8452A diode array spectrometer. The FT-IR (4000-600 cm^{-1}) spectra were obtained on a Bomem (MB-102) spectrometer. The Raman spectra at 298 K in the solid state were acquired using a Bruker IFS 66/CS FT-IR spectrometer coupled with an FRA 106 FT-Raman module using a ND:YAG laser (1064 nm excitation) and a Notch filter (cut off ~ 50 cm^{-1}). The NMR spectra were measured on Bruker AC-F 300 NMR spectrometer. The X-ray powder diffraction patterns were measured using

the Rigaku/USA instrument using a Cu irradiation tube operating at 40 kV and 30 mA. The luminescent spectra (excitation and emission) were acquired on a steady-state LS-100 spectrofluorometer from Photo Technology Inc., or on a Fluorolog II instrument from Spex. The emission lifetimes were measured using a single photo counting apparatus equipped with a N_2 flash lamp pulsing at 10 KHz. The mass spectra were acquired using a Kratos MS-50 TCTA spectrometer using an Iontech Saddle Field Source Model FAB 11NF operating at 70 kV with 2 mA current. The samples were in thiolglycerol or NBA matrices. The viscosity measurements were performed using the Ubbelohde viscometer.

The chemical analysis measurements (C, H, N) were performed at Université de Montréal (Montréal, Québec). ^{31}P and ^{195}Pt NMR spectra were measured at McGill University (Montréal, Québec).

T_1's were measured by the inversion recovery pulse technique. The measurements were performed on a Bruker AC-F 300 NMR spectrometer operating at 75.47 MHz for carbon-13. The temperature was ~21 °C. The solutions of the polymers were saturated in all cases in order to improve the signal-to-noise ratio.

The measurements of the UV-vis spectra vs temperature were performed using a home-made assembly. The sample temperature, which was controlled by a cooled $N_2(g)$ flow from the bottom to the top of a cylindrical quartz Dewar cell, was monitored using a calibrated gold-chromel thermocouple.

All of the MO calculations were of the extended Hückel type (EHMO) (147, 148) using a modified version of the Wolfsberg-Helmohlz formula (149). The detailed description of the graphic programs used in this work can be found in ref. 150.

3 X-ray crystallography

$[Pd_3(dpam)_3CO](PF_6)_2$: Intensity data were collected at 180 K on an Enraf-Nonius CAD-4 automatic diffractometer using graphite monochromated MoKα radiation. The NRCCAD (151) programs were used for centering, indexing and data collection. The unit cell dimensions were obtained by least square fit of 24 centered reflections in the range of $20° \leq 2\theta \geq 35°$. During data collection, the intensities of two standard reflections were monitored every 60 min. No significant decay was observed. An absorption correction was applied on the data based on PSI-scan measurments on 9 azimutal reflections. The structure was solved by the application of direct methods using the SOLVER program and refined by least-squares using LSTSQ program, both from NRCVAX (152). The atomic scattering factors stored in NRCVAX are from Cromer & Waber (*International Tables for X-ray Crystallography, Vol. IV)*. At convergence the final discrepancy indices were R = 0.045, wR = 0.052, S = 1.27. The residual positive and negative electron densities in the final maps were 0.05 and -0.75e/Å and were located in the vicinity of the PF_6 anions. The ORTEP diagram was generated from NRCVAX. Two solvent CH_2Cl_2 molecules were located in the asymmetric unit by difference Fourier Map. All non-H atoms were refined anisotropically. The H atoms were geometrically placed but not refined. Restrain refinement was used on U_{ij} to be identical for all carbons in each phenyl groups.

$[Pd_3(dpam)_3(CO)(I)](CF_3COO)$: The experimental procedure is identical to that of complex, $[Pd_3(dpam)_3CO](PF_6)_2$. At convergence the final discrepancy indices were R = 0.052, wR = 0.055, S = 1.32. The residual positive and negative electron densities in the final maps were 0.95 and -0.92 e/Å^3 and were located in the vicinity of the Pd atoms. The ORTEP diagram was generated from NRCVAX. One solvent acetone molecule was located in the asymmetric unit by difference Fourier Map. All non-H atoms were refined anisotropically. The H atoms were geometrically placed but not refined. Restrain refinement was used on U_{ij} to be identical for all carbons in each phenyl group. The μ-CO and μ-I atoms are disordered. The occupancy refinement shows a 55:45 ratio for the two orientations.

$[Pd_2(dpam)_2I_4]$: The experimental procedure is identical to that of complex, $[Pd_3(dpam)_3CO](PF_6)_2$. At convergence the final discrepancy indices were R = 0.027, wR = 0.030, S = 1.17. The residual positive and negative electron densities in the final maps were 0.59 and -0.72 e/Å^3 and were located in the vicinity of the I atoms. The ORTEP diagram was generated from NRCVAX. Half solvent CH_2Cl_2 molecule was located in the asymmetric unit by difference Fourier Map. All non-H atoms were refined anisotropically. The H atoms were geometrically placed but not refined.

$[Pt_4(dpam)_4(CO)_3](PF_6)_2$: A dark red crystal was mounted on a quartz capillary and cooled down to 193 K. The profiles of reflections show good quality crystalline material belonging to an orthorhombic system C centered. Intensity data were collected at 193 K on an Enraf-Nonius CAD-4 automatic diffractometer. The NRCCAD programs were used for centering, indexing and data collection. The unit cell dimensions were obtained by least squares fit of 16 centered reflections in the range of $20^\circ \leq 2\theta \geq 25^\circ$. During data collection, the intensities of two standard reflections were monitored every 60 min. A 25% decay was observed and a correction was applied to the data. The structure was solved by the application of direct methods using the NRCVAX program and refined by least squares using LSTSQ also from NRCVAX. An isotropic extinction coefficient was included in the refinement to account for secondary extinction effects; its value was 0.135 (10)μ. The atomic scattering factors stored in NRCVAX are from International Tables Vol IV. Hydrogen atoms were geometrically placed at idealized positions and not refined. At convergence the final discrepancy indices were R = 0.059, wR = 0.058 and S = 1.20. The residual positive and negative electron densities in the final maps were 1.82 and -1.46 e/Å^3 and were located in the vicinity of the Pt atoms. The monodentate dpam moiety is disordered over two sets of sites and occupancy refinement shows a 0.5:0.5 ratio (large thermal motion are observed). The phenyl groups on the disordered As8 (As8') atom were very difficult to locate. An ideal model was generated using the SYBYL program to fit the observed densities into real atomic position of overlapping phenyl rings.

$[Pt_4(dmb)_4(PPh_3)_2]Cl_2$: Intensity data were collected at 293 K on an Enraf-Nonius CAD-4 automatic diffractometer using graphite monochromated CuKα radiation. The NRCCAD program were used for centering, indexing, and data collection. The unit cell dimensions were obtained by least squares fit of 24 centered reflections in the range of $20° \leq 2\theta \geq 35°$. During data collection, the intensities of 3 standard reflections were monitored every 60 min. No significant decay was observed. An absorption correction was applied on the data based on PSI-scan measurements on 9 azimutal reflections. The structure was solved by the application of direct methods using the SOLVER program from NRCVAX and refined by least-squares using SHELXL-97 program (153). The scattering factors are from the International Tables for X-ray Crystallography, (1992) Vol. C, Tables 4.2.6.8 & 6.1.1.4. At convergence the final discrepancy indices were R = 0.0738, wR = 0.2097, S = 1.018. The residual positive and negative electron densities in the final maps were 4.923 and -2.544 e/Å^3 and were located in the vicinity of the Pt atoms. The ORTEP (154) diagram was generated from Xtal-GX. The refinement was carried out using several constraints. The SAME/DELU options were used for the disordered dmb atoms, and the FLAT/DELU options were applied for the phenyl rings. The final occupancies for the disordered dmb are: 0.475(11)/0.525(11), 0.674(14)/0.326(14), 0.690(12)/0.310(12) and 0.646(12)/0.354(12). Two molecules of acetonitrile and two water molecules were located by ΔF map in the asymmetric unit.

$[Pd_2(dmb)_4(\mu\text{-}Cl)](TCNQ)_4$: Intensity data were collected at 293 K on an Enraf-Nonious CAD-4 automatic diffractometer using graphite monochromated CuKα radiation. The DIFFRAC program was used for centering, indexing, and data collection. The unit cell dimensions were obtained by least squares fit of 10 centered reflections in the range of $20° \leq 2\theta \geq 30°$. During data collection, the intensities of two standard reflections were monitored every 60 min. No significant decay was observed. An absorption correction was applied on the data based on PSI-scan measurements on 9 azimutal reflections. The structure was solved by the application of direct methods using the SOLVER program from NRCVAX and refined by least-squares using SHELXL-97 program. At convergence the final discrepancy indices

were R = 0.0757, wR = 0.2018, S = 1.029. The residual positive and negative electron densities in the final maps were located in the vicinity of the Pd atoms. All non-H atoms were refined anisotropically. The H atoms were geometrically placed. The quality of the crystal prevented better refinement.

$\{[Pd_4(dmb)_5](CH_3COO)_2 \cdot 4H_2O\}_n$: Intensity data were collected at 180 K on an Enraf-Nonious CAD-4 automatic diffractometer using graphite monochromated CuKα radiation. The DIFFRAC program was used for centering, indexing, and data collection. The unit cell dimensions were obtained by least squares fit of 10 centered reflections in the range of $20° \leq 2\theta \geq 30°$. During data collection, the intensities of two standard reflections were monitored every 60 min. No significant decay was observed. An absorption correction was applied on the data based on PSI-scan measurements on 9 azimutal reflections. The structure was solved by the application of direct methods using the SOLVER program from NRCVAX and refined by least-squares using SHELXL-97 program. In the asymmetric unit, there are 4 water molecules. At convergence the final discrepancy indices were R = 0.0957, wR = 0.2931, S = 1.232. The residual positive and negative electron densities in the final maps were located in the vicinity of the Pd atoms. All non-H atoms were refined isotropically except for the Pd atoms. The dmb ligands are disordered. The occupancy refinement converged to a 0.598(12)/0.402(12), 0.704(12)/0.296(12), 0.732(12)/0.268(12) and 0.620(13)/0.380(13) ratio. The quality of the crystal combined to the disorder prevented better refinement.

$[Pt_2Au_2(dmb)_2(PPh_3)_4](PF_6)_2$: Intensity data were collected at 293 K on an Enraf-Nonious CAD-4 automatic diffractometer using graphite monochromated CuKα radiation. The DIFFRAC program was used for centering, indexing, and data collection. The unit cell dimensions were obtained by least squares fit of 10 centered reflections in the range of $20° \leq 2\theta \geq 30°$. During data collection, the intensities of two standard reflections were monitored every 60 min. No significant decay was observed. An absorption correction was applied on the data based on PSI-scan measurements on 9 azimutal reflections. The minimum and

maximum transmission factors were 0.0118 and 0.1129. The structure was solved by the application of direct methods using the SOLVER program from NRCVAX and refined by least-squares using SHELXL-97 program. At convergence the final discrepancy indices were R = 0.0447, wR = 0.1305, S = 1.093. The residual positive and negative electron densities in the final maps were located in the vicinity of the Pt and Au atoms. All non-H were refined anisotropically. The H atoms were geometrically placed. The dmb ligands are disordered. The occupancy refinement converged to 0.459(8)/0.541(8). There are two phenyl rings which show disorder. The respective occupancies for C32-C36 and C37-C42 are 0.311(11) /0.689(11) and 0.699(9)/0.301(9).

4 Synthesis

4.1 Synthesis of $[Pd_3(dpam)_3(CO)](CF_3COO)_2$

A mixture of solid $Pd(CH_3COO)_2$ (0.33 g, 1.47 mmol) and dpam (0.74 g, 1.57 mmol) was dissolved in 25 mL acetone. To this solution was added 2 mL of water and 2.5 mL of CF_3COOH. The flask was put in bomb and shaked under CO atmosphere (300 - 500 psi) for 24 hours. The solution was filtered and dried by a rotary evaporator to give a dark red oil, which was washed with n-hexane and diethyl ether to get a black-red solid. The further purification was not carried out because this solid was easy to stick on the beaker and was difficult to collect. Yield: >80%. IR: ν(CO) =1837 cm^{-1}, $\nu(CF_3COO^-)$ =1679 cm^{-1}; ^1H NMR: $\delta(CH^aH^bAs_2)$ 4.56, 4.62 ppm, $^2J(H^aH^b)$ ($(CD_3)_2CO$)=12 Hz; UV-vis: $\lambda_{max}(CH_3OH)$= 498 nm, ε (CH_3OH) =1.95 $\times$ 10^4 $l{\cdot}mol^{-1}{\cdot}cm^{-1}$, λ_{max} ($(CH_3)_2CO$) =502 nm, ε ($(CH_3)_2CO$) =2.02 $\times$ 10^4 $l{\cdot}mol^{-1}{\cdot}cm^{-1}$.

4.2. Preparation of $[Pd_3(dpam)_3(CO)](PF_6)_2$

0.40 g of solid $[Pd_3(dpam)_3(CO)](CF_3COO)_2$ (0.20 mmol) was dissolved in 10 mL of cooled methanol (0 °C). To this solution, an excess of solid NH_4PF_6 was added. Dark-purple solid was obtained by filtration and washing with cold methanol and diethyl ether (0.30 g, 0.146 mmol). Yield: 73%. IR: ν(CO) =1837 cm^{-1}; ^1H NMR: $\delta(CH_2)$ 5.03 ppm(s), FWHM 15 Hz ($(CD_3)_2CO$); UV-vis: λ_{max} ($(CH_3)_2CO$) = 510 nm, ε ($(CH_3)_2CO$) = 2.02×10^4 $l \cdot mol^{-1} \cdot cm^{-1}$. The dark-red crystals suitable for X-ray diffraction were grown by slow evaporation of solvent from saturated solution of this complex in a mixture of dichloromethane and n-hexane.

4.3 Preparation of $[Pd_3(dpam)_3(CO)](BPh_4)_2$

The procedure is similar to the above, just using an excess of $NaBPh_4$, instead of NH_4PF_6. Yield: 86%. IR: ν(CO)=1837 cm^{-1}; UV-vis: λ_{max} (CH_2Cl_2)= 496 nm, λ_{max} (CH_3OH)=492 nm.

4.4 Synthesis of $[Pd_3(dpam)_3(I)(CO)](CF_3COO)$

Solid $[Pd_3(dpam)_3(CO)](CF_3COO)_2$ (0.040 g, 0.02 mmol) was dissolved in 10 mL acetone. To this solution, 5 mL methanolic solution of KI (0.012 g, 0.072 mmol) was added. This solution was stirred under nitrogen atmosphere for two hours, then filtered and evaporated to dryness. The product was extracted with dichloromethane. The diffusion of n-pentane to the acetone solution gave the crystals of $[Pd_3(dpam)_3(I)(CO)](CF_3COO)$. IR: ν(CO) =1845 cm^{-1}, $\nu(CF_3COO^-)$ = 1680 cm^{-1}; ^1H NMR: $\delta(CH_2)$ = 4.61 ppm(s), FWHM = 5 Hz ($(CD_3)_2CO$); UV-Vis: λ_{max} (CH_3OH) = 484 nm.

4.5 Synthesis of $Pd_2(dpam)_2I_4$

$[Pd_3(dpam)_3(CO)](BPh_4)_2$ was used as starting material. The reaction was carried out in air until the peak at 484 nm disappeared. The reaction was detected by UV-vis spectroscopy. Then the solution was evaporated to dryness. The product was extracted by dichloromethane.

The remaining was an uncharacterized black solid. Red crystals suitable for X-ray crystallography were obtained by diffusion of methanol into a dichloromethane solution.

4.6 Synthesis of $[Pt_4(dpam)_4(CO)_3](CF_3COO)_2$

4.6.1 Preparation of $Pt(dpam)Cl_2$

$Pt(COD)Cl_2$ (0.7335g, 1.960 mmol) and dpam (0.9234g, 1.956 mmol) were mixed together in 25 mL of CH_2Cl_2. The suspension was stirred for 5 min at room temperature under $N_2(g)$, then was gently heated to generate a yellow solution. The reaction was carried out for 24 hrs, and $N_2(g)$ was bubbled through the solution to evaporate the solvent. A yellow oil was obtained which was washed with acetone to obtain a pale-yellow powder. Yield: 89%. ^1H NMR($CDCl_3$): δ 4.70(CH_2As_2; s, 2 satellites, $^3J(Pt,H)$=25 Hz; 7.44-7.84(($C_6H_5)_2As$, m).

4.6.2 Preparation of $Pt(dpam)(O_2CCF_3)_2$

Solid $Pt(dpam)Cl_2$ (1.3521g, 1.832 mmol) and AgO_2CCH_3 (0.6115g, 3.663 mmol) were mixed in acetone (20 mL) in the presence of CF_3COOH (5 mL) under a $N_2(g)$ atmosphere. The suspension was stirred for 20 min, then was heated to 60°C for several minutes, and then slowly cooled down to room temperature. The solution was filtered and evaporated to obtain an oily material. This yellow oil was redissolved in acetone (5 mL) and precipitated with n-pentane to give a yellow solid (1.1000g, 1.232 mmol). Yield: 77%. IR (solid): 1680 cm^{-1} ($\nu(CF_3COO^-)$); ^1H NMR (($CD_3)_2CO$): δ 5.10 (CH_2As_2; s, 2 satellites, $^3J(Pt,H)$ = 35 Hz; 7.50-7.90 (($C_6H_5)_2As$, m).

4.6.3 Synthesis of $[Pt_4(dpam)_4(CO)_3](CF_3COO)_2$

$Pt(dpam)(O_2CCF_3)_2$ (0.1036g, 0.116 mmol) was dissolved in a mixture of methanol (10 mL) and water (1 mL). The yellow solution was degassed with N_2(g) for 10 min. Then the solution was heated to near 50°C while CO(g) was bubbled through the solution for 6 hours. The solution color changed from yellow to blue, finally to red-orange. Then CO(g) was continued to be used in order to cool the solution. The solution was then filtered, evaporated to dryness, washed with n-hexane, and dried in *vacuo* to give the crude product, a brown-orange solid. The crude product was purified by dissolving it in acetone and precipitating it with n-pentane (0.075g, 0.108 mmol). Yield: 87%. UV(methanol): λ_{max}=398 nm; IR(solid): 1830 cm^{-1} (ν(CO)); ^{1}H NMR ($(CD_3)_2CO$): δ 6.7-7.6 (m, $(C_6H_5)_2As$), isomer **1**: 5.75 (3H, d, $AsCH_aH_bAs$, $^2J(H_a,H_b)$=13 Hz, $^3J(Pt,H)$ =60 Hz, $^4J(Pt,H)$ =13 Hz), 4.03 (3H, d, $AsCH_aH_bAs$), 3.48 (2H, s, $PtAsCH_2As$, $^3J(Pt,H)$=39 Hz); isomer **2**: idem except δ=5.59,3.95 and 3.90 ppm, respectively.

4.7 Preparation of $[Pt_4(dpam)_4(CO)_3](PF_6)_2$

To methanolic solution (20 mL) of $[Pt_4(dpam)_4(CO)_3](CF_3COO)_2$ (0.1012g, 0.035 mmol), an excess of solid NH_4PF_6 was added. A brown precipitate appeared, which was filtered, washed with cold methanol, and dried in *vacuo*. Yield: 58%. UV-vis (methanol): λ_{max} = 400 nm; IR(solid): 1830 cm^{-1} (ν(CO)), 840 cm^{-1} ($\nu(PF_6^-)$); ^{1}H NMR ($(CD_3)_2CO$): δ 6.7-7.6 (m, $(C_6H_5)_2As$), isomer **1**: 5.88 (3H, d, $AsCH_aH_bAs$, $^2J(H_a,H_b)$ = 13 Hz, $^3J(Pt,H)$ = 60 Hz, $^4J(Pt,H)$ = 13 Hz), 4.03 (3H, d, $AsCH_aH_bAs$), 3.37 (2H, s, $PtAsCH_2As$, $^3J(Pt,H)$ = 39 Hz); isomer **2**: idem except δ = 5.61, 3.95 and 3.91 ppm, respectively. Single crystals suitable for X-ray structure determination were grown by diffusing pentane into an acetone solution.

4.8 Synthesis of $[Pt_4(dmb)_4(PPh_3)_2]Cl_2$

To a slurry solution containing 32.0 mg (0.0264 mmol) of $Pt_2(dba)_3 \cdot CHCl_3$ in 10 mL of acetone, was added 5 mL of a dichloromethane solution containing 34.0 mg (0.1789 mmol) of dmb. One hour later, 23.6 mg (0.0899 mmol) of solid triphenylphosphine (PPh_3) was added,

and the solution was stirred for 2 hours under nitrogen atmospere, during which the color changed to orange. The solution was then filtered and the volume of the solution was reduced to about 2 mL in *vacuo*. Diethyl ether was added to precipite the product as an orange polycrystalline solid. The product was collected by filtration and washed with diethyl ether. Yield: 16.3 mg (0.0076 mmol) 58%. The compound was identified by X-ray crystallography. ^{1}H NMR (CD_3CN): δ 1.0 - 2.1 ppm (complex, 72H, dmb); 7.2 - 7.6 ppm (complex, 30H, PPh_3). ^{13}C NMR (CD_3CN): δ 23.8, 27.6, 27.7, 29.4, 37.8, 38.0, 46.5, 46.6, 61.2, 61.9, 63.1, and 63.7 ppm (dmb); 129.7, 131.6, 134.4 and 134.5 ppm (PPh_3); 134.8 and 135.1 ppm (C≡N). ^{31}P NMR (C_6D_6): δ 50.5 ppm (^{1}J(Pt-P) = 2252 Hz; ^{2}J(Pt-P) = 498 Hz; ^{3}J(Pt-P) = 148 Hz). ^{195}Pt NMR (CD_2Cl_2): δ -2520 (inner ^{195}Pt, fwhm ~ 20 ppm), -2650 ppm (outer ^{195}Pt, d of t, ^{1}J(Pt-P) = 2280 Hz, ^{1}J(Pt-Pt) = 330 Hz). FT-IR (solid) 2146 cm^{-1} (ν(C≡N)). FT-Raman (solid): 2169, 2197 cm^{-1} (ν(C≡N)); 162, 84 cm^{-1} (ν(Pt-Pt)). Mass FAB: calculated for $Pt_4(dmb)_4(PPh_3)_2Cl$ 2101.5, obs.: 2100 m/e (ret. int. ~ 3%), calculated for $Pt_4(dmb)_4Cl$ 1576.9, obs.: 1576.1 m/e (ret. int. 100%). UV-vis (ethanol): λ_{max} (ε) 405 (35800), 358 (31900), 296 nm (22400 $M^{-1}cm^{-1}$) at room temperature. X-ray fluorescence confirmed the presence of Pt, P and Cl in a 2:1:1 ratio. Dark orange crystals suitable for X-ray crystallography were obtained by slow diffusion of *tert*-butyl methyl ether into an acetonitrile solution of the product under nitrogen atmosphere in the presence of an excess of dmb and PPh_3. The presence of acetonitrile and water as solvate molecules was detected by crystallography.

4.9 Synthesis of polymer $\{[Pt_4(dmb)_4(dppb)]Cl_2\}_n$

To a suspension of $Pt_2(dba)_3{\cdot}CHCl_3$ (0.0560g, 0.0542 mmol) in 5 mL of acetone was added solid dmb (0.0713g, 0.375 mmol). This mixture was stirred under nitrogen atmosphere for 4 hours, during which time the black powder ($Pt_2(dba)_3{\cdot}CHCl_3$) slowly dissolved and the solution became yellow-orange. Then 0.0170g of dppb (0.398 mmol) dissolved in 2 mL of dichloromethane, was added to the solution. The color readily became deeper and turned red-

orange. After stirring for two additional hours, the solution was filtered and concentrated to about 4 mL under vacuum. Diethyl ether was used in order to precipitate the product, which was recrystallized in acetonitrile/diethyl ether in the presence of dmb. Yield: 0.0486 g, 91%. Chem. Anal. found: C 43.56, H 5.28, N 5.42%; Theor. for $\{[Pt_4(dmb)_4(dppb)]Cl_2 \cdot 3H_2O\}_n$: C 43.53, H 5.29, N 5.34%. T_{dec} = 150 °C. IR (solid): 2143 cm^{-1} (ν(C≡N)). ^{31}P NMR (CD_3CN): δ 49.6 ppm (^1J(Pt-P) = 2212, ^2J(Pt-P) = 502 Hz).

4.10 Synthesis of polymer $\{[Pt_4(dmb)_4(dppp)]Cl_2\}_n$

Direct reaction of $Pt_2(dba)_3 \cdot CHCl_3$ (0.0630g, 0.061 mmol) and dmb (0.0813g, 0.427 mmol) in 6 mL of acetone under nitrogen atmosphere gave a yellow-orange solution in 4 hours. After 0.0176g of dppp (0.0399 mmol) which was dissolved in 2 mL of CH_2Cl_2, was added to the solution, the color readily changed to red-orange. The solution was stirred for two hours, then filtered and concentrated to about 4 mL. The product was precipitated by diethyl ether, and recrystallized from acetonitrile/diethyl ether. Yield: 0.0530g, 88%. Chem. Anal. found: C 44.94, H 5.69, N 5.67%. Theor. for $\{[Pt_4(dmb)_4(dppp)]Cl_2 \cdot H_2O \cdot CH_3CN\}_n$: C 44.84, H 5.29, N 5.96%. $T_{dec.}$ = 138 °C. IR (solid): 2144 cm^{-1} (ν(C≡N)). ^{31}P NMR (CD_3CN): δ 54.8 ppm (^1J(Pt-P) = 2185, ^2J(Pt-P) = 498 Hz).

4.11 Synthesis of polymer $\{[Pt_4(dmb)_4(dpph)]Cl_2\}_n$

Direct reaction of $Pt_2(dba)_3 \cdot CHCl_3$ (0.0603g, 0.0583 mmol) and dmb (0.0820g, 0.431 mmol) in 6 mL of acetone under nitrogen atmosphere gave a yellow-orange solution in 4 hours. After 0.0172g of dpph (0.0380 mmol) which was dissolved in 2 mL of CH_2Cl_2, was added to the solution, the color readily changed to red-orange. The solution was stirred for two hours, then filtered and concentrated to about 4 mL. The product was precipitated by diethyl ether, and recrystallized from acetonitrile/diethyl ether. Yield: 0.0537g, 92%. Chem. Anal. found: C 45.02, H 5.52, N 5.59%. Theor. for $\{[Pt_4(dmb)_4(dpph)]Cl_2\}_n$: C 45.22, H 5.26, N 5.41%.

$T_{dec.}$ = 132 °C. IR (solid): 2145 cm^{-1} (ν(C≡N)). ^{31}P NMR (CD_3CN): δ 54.8 ppm (^{1}J(Pt-P) = 2198, ^{2}J(Pt-P) = 486 Hz).

4.12 Synthesis of $[Pd_4(dmb)_4(PPh_3)_2]Cl_2$

60.3 mg (0.0583 mmol) of $Pd_2(dba)_3 \cdot CHCl_3$ was dissolved in 6 mL of acetone, and stirred under nitrogen for 30 min. 62.6 mg (0.3295 mmol) of dmb was dissolved in 4 mL acetone and added to the above solution also under nitrogen atmosphere. The solution readily turned red. After 52.2 mg (0.199 mmol) of PPh_3 was added, the color of the solution immediately changed from red to purple. The solution was allowed to stir for 2 hours. Then the solution was filtered and concentrated to about 3 mL. The purple product was collected by precipitation with diethyl ether, filtration, and washed with diethyl ether. Yield: 46.7 mg (0.0262 mmol), 90%. Chem. Anal. (theor.) for $Pd_4C_{84}H_{102}N_8P_2Cl_2$: C 56.60, H 5.77, N 6.29%; Found: C 56.43, H 5.90, N 6.23%. X-ray fluorescence measurements indicate that the relative ratio for Pd, P, Cl is ~ 2.0, 1.0, and 1.0, respectively. ^{1}H NMR (CD_3CN): δ 1.0-2.0 ppm (complex, 72H, dmb); 6.8-7.8 ppm (complex, 30H, PPh_3). ^{13}C NMR (CD_3CN): δ 23.0, 27.3, 27.5, 28.2, 28.5, 37.3, 37.5, 44.6, 45.2, 60.8, 61.4, 62.9, and 63.4 ppm (dmb); 128.8, 129.3, 130.5, and 133.8 ppm (PPh_3); 135.3, 135.5, 138.6, and 139.0 ppm (C≡N-). FT-IR (solid): 2156 cm^{-1} (ν(C≡N)). FT-Raman (solid): 165, 86 cm^{-1} (ν(PdPd)). Mass FAB: calculated for $[Pd_4(dmb)_4(PPh_3)_2]Cl$, 1746.9, obs.: 1748 m/e (rel. int. < 1%); for $Pd_4(dmb)_4Cl$ 1222.3, obs.: 1222 m/e (rel. int. = 100%). UV-vis (ethanol): λ_{max} (ε) 538 nm (53700 $M^{-1}cm^{-1}$. Purple crystals were obtained by diffusion of diethyl ether to a dichloromethane solution under nitrogen atmosphere in the presence of a slight excess of dmb and PPh_3. Single crystals were obtained but were not of sufficient quality for a complete X-ray structure determination. However it is was possible to demonstrate the structure of this complex.

4.13 Synthesis of $[Pd_2(dmb)_4(\mu\text{-}Cl)](TCNQ)_4$

To a suspension of $Pd_2(dba)_3 \cdot CHCl_3$(0.0425g, 0.041 mmol) in 6 mL of acetone was added an excess of solid dmb (0.0406g, 0.214 mmol), which was stirred under nitrogen atmosphere for 2 hours. During the reaction, solid $Pd_2(dba)_3 \cdot CHCl_3$ was dissolved to get a red solution. The solution was filtered and moved to a long tube, then 0.0350g (0.171 mmol) of neutral TCNQ dissolved in 6 mL of acetone was added, and N_2 was induced into the tube. The resulting green solution was left aside at room temperature. Over night, purple crystals formed. Crystals were collected by filtration and washed with acetone and diethyl ether. Yield: 0.0292g (0.018 mmol), 44% (based on Pd). Chem. Anal. (theor.) for $C_{96}H_{88}N_{24}ClPd_2 \cdot H_2O$: C 62.52, H 4.92, N 18.23; Found: C 62.72, H 5.26, N 18.17. IR(solid): 2175 (ν(C≡N) (br. vs.), 2245 (m) cm^{-1}. UV-vis (CH_3CN): λ_{max}: 394, 680, 744, 760 nm. ^1H NMR(CD_3CN): δ 1.45-1.75 ppm (br., dmb); 2.0-2.3 ppm (complex, TCNQ).

4.14 Synthesis of polymer $\{[Pd_4(dmb)_5](CH_3COO)_2\}_n$

A mixture of $Pd(CH_3COO)_2$ (0.0092g, 0.041 mmol) and $Pd_2(dba)_3 \cdot CHCl_3$(0.0652g, 0.063 mmol) was dissolved in 10 mL of acetone. Then to this suspension was added an excess of dmb (0.0632g, 0.332 mmol). The solution was stirred under nitrogen atmosphere for 4 hours. The red solution was then filtered and concentrated to about 4 mL by a rotary evaporator. A mixture of n-pentane and diethyl ether (about 4:1 in v/v) was used to precipitate the product. The bright orange solid was collected by filtration and washed with n-pentane. Yield: 0.0586g, 95%. IR (solid): 2152 cm^{-1} (ν(C≡N); 1572, 1400 cm^{-1} (ν(COO^-). UV-vis (acetone, excess of dmb): λ_{max} = 512 nm. The dark-red crystals suitable for crystallograghy were grown at ~ 0 °C, by diffusion of n-pentane into a methyl ethyl ketone solution in the presence of an excess of dmb.

4.15 Synthesis of $[Pt_2Au_2(dmb)_2(PPh_3)_4](PF_6)_2$

To a suspension of $Pt_2(dba)_3 \cdot CHCl_3$(0.0545g, 0.045 mmol) in 6 mL of acetone was added 0.0740g (0.039 mmol) of dmb which was stirred under a nitrogen atmosphere for 3 hours. The black solid was slowly dissolved to give a yellow-orange solution. The solution was filtered. Then diethyl ether was added to precipitate the starting material, $Pt_4(dmb)_mCl_2$, which was collected by filtration and washed with diethyl ether (0.0366g, 0.020 mmol). This red-orange solid was inserted in a 50 mL of flask, which was purged with N_2(g) to remove O_2(g) for 30 min. A mixture of methanol (1 mL) and acetone (3 mL) was then added by a syringe to dissolve the solid to give a yellow-orange solution, to which 1 mL of acetone solution of $[Au(PPh_3)_2]PF_6$ (0.0183 g, 0.021 mmol) was added. The color of solution changed to brown in a few minutes, which subsequently turned yellow-brown in 2 hours. The solution was filtered, and evaporated to about 2 mL. The yellow-green crude product was collected by precipitation with diethyl ether and filtration (0.0420g). This crude product was then redissolved in dichloromethane to give a deep color solution, and an insoluble solid ($Pt_2(dmb)_2Cl_2$) (~ 0.0250g). The crystallization of the deep color solution provided orange crystals ($[Pt_4(dmb)_4(PPh_3)_2](PF_6)_2$) and dark green crystals ($[Pt_2Au_2(dmb)_2(PPh_3)_4](PF_6)_2$). $[Pt_2Au_2(dmb)_2(PPh_3)_4](PF_6)_2$: Mass FAB: calculated for $[Pt_2Au_2(dmb)_2(PPh_3)_4]PF_6$ 2358.9, obs.: 2361.9 m/e (rel. int. ~ 3%); calculated for $[Pt_2Au_2(dmb)_2(PPh_3)_4]$ 2213.9, obs.: 2214.9 m/e (rel. int. 8%); calculated for $[Pt_2Au_2(dmb)_2(PPh_3)_3]$ 1951.5, obs.: 1951.6 m/e (rel. int. 46%). IR (solid): 2164 cm^{-1} (ν(C≡N). ^{1}H NMR (CD_2Cl_2): δ 0.6-1.6 ppm (complex, 36H, dmb), 7.1-7.6 ppm (complex, 60H, PPh_3). ^{31}P NMR (CD_2Cl_2): δ 44.80 ppm (^{1}J(Pt-P) = 2253 Hz, ^{3}J(Pt-P) = 395 Hz), 59.0 ppm (^{2}J(Pt-P) = 147 Hz, ^{3}J(PP) = 17 Hz). UV-vis (CH_2Cl_2): λ_{max}: 316, 366, 420, 518 nm. The dark-green crystals suitable for crystallography were grown from a solution in a mixture of CH_2Cl_2 and cyclohexane. $[Pt_4(dmb)_4(PPh_3)_2](PF_6)_2$: Mass FAB: calculated for $[Pt_4(dmb)_4(PPh_3)_2](PF_6)_2$ 2356.1, obs.: 2358 m/e (rel. int. 5%); calculated for $[Pt_4(dmb)_4(PPh_3)_2](PF_6)$ 2210, obs.: 2211.1 (ret. int. 75%). IR(solid): 2146 cm^{-1} (ν(C≡N), 841 cm^{-1} ($\nu(PF_6^-)$). ^{1}H NMR (acetone-d_6): δ 1.0 - 2.1 ppm (complex, dmb); 7.2 - 7.6 ppm (complex, PPh_3). UV-vis (CH_3CN): λ_{max}: 298, 358, 406, 518 nm. $Pt_2(dmb)_2Cl_2$: Chem. Anal. (theor.) for $C_{24}H_{36}N_4Cl_2Pt_2 \cdot (C_2H_5)_2O$: C 36.72, H 4.31, N 6.12; Found: C 36.60, H

4.78, N 6.58. Mass FAB: calculated for $Pt_2(dmb)_2$ 770.8, obs.: 770 (rel. int. ~3%); calculated for $Pt_2(dmb)Cl$ 615.9, obs.: 615(rel. int. ~ 5%). IR (solid): 2180, 2160 cm^{-1} (ν(C≡N). UV-vis (CH_3CN): λ_{max}: 292 (s), 320 (s), 404 (shoulder) nm. ^1H NMR (CD_3CN): δ 1.0-2.1 (complex, dmb).

4.16 Synthesis of $Pt_2(dmb)_2Cl_2$

4.16.1 Synthesis of $Pt_2(dmb)_2Cl_4$

0.50g (1.205 mmol) of solid K_2PtCl_4 was dissolved in 10 mL of distilled water. To this solution was added 0.33g (1.740 mmol) of solid dmb. This mixture was magnetically stirred for 5 hours. Then a yellow product was collected by filtration and washed with distilled water and diethyl ether. Yield: 0.18g, 33%. Chem. Anal. (theor.) for $C_{24}H_{36}N_4Cl_4Pd_2 \cdot 2CH_3CN \cdot 2H_2O \cdot 0.5((C_2H_5)_2O)$: C 33.75, H 4.81, N 7.87%. Found C 33.94, H 4.52, N 7.87%. IR(solid): 2221 cm^{-1} (ν(C≡N). UV-vis (CH_3CN): λ_{max}: 196 (s), 258 (m), 352 (w), 464 (m) nm. ^1H NMR (CD_3CN): δ 1.2-1.8 (complex, dmb). FAB mass: calculated for $Pt_2(dmb)(dmb\text{-}CN)Cl_3$ 851.1, obs.: 849.2 (ret. int. <1%); calculated for $Pt_2(dmb\text{-}CN)Cl_3$ 825.1, obs.: 824.0 (ret. int. <1%).; calculated for $Pt_2(dmb)_2Cl$ 806.2, obs.: 805.0 m/e (ret. int. <1%). dmb-CN is dmb that has lost a CN group.

4.16.2 Synthesis of $Pt_2(dmb)_2Cl_2$

Solid $Pt_2(dba)_3 \cdot CHCl_3$ (0.0301g, 0.025 mmol) was dissolved in 10 mL of benzene, to which was added 0.0260g (0.028 mmol) of $Pt_2(dmb)_2Cl_4$ dissolved in 10 mL of acetonitrile in the presence of an excess of dmb (0.031g, 0.163 mmol). The color of the solution changed from purple to brown. Then the solution was evaporated to dryness, and washed with diethyl ether. This solid was redissolved in 5 mL of acetonitrile, then filtered to remove the insoluble species. The product was precipitated with diethyl ether, and collected by filtration and

washed with diethyl ether. Yield: 0.0299g, 64.6%. Chem. Anal. (theor.) for $C_{24}H_{36}N_4Cl_2Pd_2 \cdot 2CH_3CN \cdot ((C_2H_5)_2O)$: C 38.51, H 5.25, N 8.42%. Found C 38.37, H 5.15, N 8.11%. IR(solid): 2180, 2155 cm^{-1} (ν(C≡N). UV-vis (CH_3CN): λ_{max}: 304 (s), 316 (s, shoulder), 406 (shoulder) nm. ^1H NMR (CD_3CN): δ 1.0-1.8 (complex, dmb). Mass FAB: calculated for $Pt_2(dmb)_2Cl_2$ 841.7, obs.: 841 (very weak); calculated for $Pt_2(dmb)_2(CN)$ 796.8, obs.: 798 (ret. int. <1%); calculated for $Pt_2(dmb)_2$ 770.8, obs.: 771 m/e (ret. int. <1%).

BIBLIOGRAPHY

1. D. M. P. MINGOS. Contemporary Physics, 35, 181 (1994).

2. G. LONGONI and P. CHINI. J. Am. Chem. Soc., 98, 7226 (1976).

3. M. KAWANO, J. W. BACON, C. F. CAMPANA and L. F. DAHL. J. Am. Chem. Soc., 118, 7869 (1996).

4. E. L. MUTTERTIES. Science, 196, 839 (1977).

5. D. IMHOF and L. M. VENAZI. Chem. Soc. Rev., 185 (1994).

6. C. L. LEE, C. T. HUNT and A. L. BALCH. Inorg. Chem., 20, 2498 (1981).

7. R. J. PUDDEPHATT. Chem. Soc. Rev., 99 (1982).

8. D. M. HOFFMAN and R. HOFFMANN. Inorg. Chem., 20, 3543 (1981).

9. R. J. PUDDEPHATT, L. MANOJLOVIC-MUIR and K. W. MUIR. Polyhedron, 9, 2767 (1990).

10. L. MANOJLOVIC-MUIR, K. W. MUIR, B. R. LLOYD and R. J. PUDDEPHATT. J. Chem. Soc., Chem. Commun., 1336 (1983).

11. G. FERGUSON, B. R. LLOYD and R. J. PUDDEPHATT. Organometallics, 5, 344 (1986).

12. R. PROVENCHER, K. T. AYE, M. DROUIN, J. GAGNON, N. BOUDREAULT and P. D. HARVEY. Inorg. Chem., 33, 3689 (1994).

13. P. D. HARVEY, S. HUBIG and T. ZIEGLER. Inorg. Chem. 33, 3700 (1994).

14. a) E. C. YANG, M. C. CHENG, M. S. TSAI and S. M. PENG. J. Chem. Soc. Chem. Commun., 2377 (1994); b) F. A. COTTON, L. M. DANIELS and G. T. JORDAN IV. Chem. Commun., 421 (1997).

15. S. J. SHIEH, C. C. CHOU, G. H. LEE, C. C. WANG and S. M. PENG. Angew. Chem. Int. Ed. Engl., 36, 56 (1997).

16. a) K. R. MANN, M. J. DIPIERRO and T. P. GILL. J. Am. Chem. Soc., 102, 3965 (1980); b) A. L. BALCH and M. M. OLMSTEAD. J. Am. Chem. Soc., 101, 3128 (1979); c) K. R.MANN, J. G. GORDON II and H. B. GRAY. J. Am. Chem. Soc., 97, 3553 (1975); d) K. R. MANN, N. W. LEWIS, R. M. WILLIAMS and H. B. GRAY. Inorg. Chem., 17, 828 (1978).

17. G. M. FINNISS, E. CAMPANA and K. R. DUNBAR. Angew. Chem. Int. Ed. Engl., 35, 2772 (1996).

18. a) K. KROGMANN. Angew. Chem. Int. Ed. Engl., 8, 35 (1969); b) T. W. THOMAS and A. E. UNDERHILL. Chem. Soc. Rev., 1, 99 (1972).

19. R. PALMANS, D. B. MACQUEEN, C. G. PIERPONT and A. J. FRANK. J. Am. Chem. Soc., 118, 12647 (1996).

20. D. PERREAULT, M. DROUIN, A. MICHEL and P. D. HARVEY. Inorg. Chem., 31, 2740 (1992).

21. Y. YAMAMOTO, T. TANASE, H. UKAJI, M. HASEGAWA, T. IGOSHI and K. YOSHIMURA. J. Organomet. Chem., 498, C23 (1995).

22. a) N. M. RUTHERFORD, M. M. OLMSTEAD and A. L. BALCH, Inorg. Chem., 23, 2833 (1984); b) Y. YAMAMOTO and H. YAMAZAKI. Bull. Chem. Soc. Jpn., 58, 1843 (1985). c) J. R. BOEHM, D. J. DOONAN and A. L. BALCH. J. Am. Chem. Soc., 98, 4845 (1976). d) S. Z. GOLDBERG and R. EISENBERG. Inorg. Chem., 15, 535 (1976).

23. A. L. BALCH, J. R. BOEHM, H. HOPE and M. M. OLMSTEAD. J. Am. Chem. Soc., 98, 7431 (1976).

24. S. KANAN, A. J. JAMES and P. R. SHARP. J. Am. Chem. Soc., 120, 215 (1998).

25. Y. YAMAMOTO, K. TAKAHASHI and H. YAMAZAKI. J. Am. Chem. Soc., 108, 2458 (1986).

26. D. FORTIN, M. DROUIN, M. TURCOTTE and P. D. HARVEY. J. Am. Chem. Soc., 119, 531 (1997).

27. K. R. MANN. Cryst. Struct. Commun., 20, 1921 (1981).

28. P. D. HARVEY and Z. MURTAZA. Inorg. Chem., 32, 4721 (1993).

29. C. L. EXSTROM, D. BRITTON, K.R. MANN, M. G. HILL, V. M. MISKOWSKI, W. P. SCHAEFER, H. B. GRAY and W. M. LAMANNA. Inorg. Chem., 35, 549 (1996).

30. A. SYKES and K. R. MANN. J. Am. Chem. Soc., 110, 8252 (1988).

31. I. GAUTHRON, J. GAGNON, T. ZHANG, D. RIVARD, D. LUCAS, Y. MUGNIER and P. D. HARVEY. Inorg. Chem., 37, 1112 (1998).

32. a) Y. L. PAN, J. T. MAGUE and M. J. FINK. J. Am. Chem. Soc., 115, 3842 (1993); b) A. L. BALCH, C. T. HUNT, C. L. LEE, M. M. OLMSTEAD and J. P. FARR. J. Am. Chem. Soc., 103, 3764 (1981).

33. a) R. J. PUDDEPHATT and G. J. ARSENAULT. Can. J. Chem., 67, 1800 (1989); b) P. R. SHARP. Inorg. Chem., 25, 4185 (1986).

34. D. V. TORONTO and A. L. BALCH. Inorg. Chem., 33, 6132 (1994).

35. K. A. CONNORS. Binding Constants, John Wiley & Sons, Inc., New York, 1987.

36. P. ATKINS. Physical Chemistry, 4th Ed., W. H. Freeman and Company, New York, 1990.

37. M. K. KEMP. Physical Chemistry, Marcel Dekker Inc., 1979.

38. R. S. DRAGO. Physical Methods in Chemistry, W. B. Saunders Company, 1977.

39. M. KAKUDO and N. KASAI. X-ray Diffraction by Polymers, Kodansha Ltd., 1972.

40. R. J. ABRAHAM and P. LOFTUS. Proton and Carbon-13 NMR Spectroscopy, Heyden & Son Ltd., 1979.

41. E. BREITMAIER and W. VOELTER. ^{13}C NMR Spectroscopy, Verlag Chemie, 1874.

42. J. K. M. SANDERS and B. K. HUNTER. Modern NMR Spectroscopy, 2nd Ed., Orford University Press, 1993.

43. E. D. BECKER. High Resolution NMR, 2nd Ed., Academic Press, 1980.

44. D. O. COWAN and R. L. DRISKO. Elements of Organic Photochemistry, Plenum Press, New York, 1976.

45. N. J. TURRO. Molecular Photochemistry, W. A. Benjamin, Inc., New York, 1967.

46. D. MARGERISON and G. C. EAST. Introduction to Polymer Chemistry, 1st Ed., Pergamon Press Ltd., 1967.

47. P. D. HARVEY, M. CROZET and K. T. AYE. Can. J. Chem., 73, 123 (1995).

48. R. PROVENCHER and P. D. HARVEY. Inorg. Chem., 32, 61 (1993).

49. L. HAO, I. R. JOBE, J. J. VITTAL and R. J. PUDDEPHATT. Organometallics, 14, 2781 (1995).

50. P. D. HARVEY, K. HIERSO, P. BRAUNSTEIN and X. MORSE. Inorg. Chim. Acta, 250, 337 (1996).

51. L. MANOJLOVIC-MUIR, B. R. LLOYD and R. J. PUDDEPHATT. J. Chem. Soc., Chem. Commun., 536 (1985).

52. F. A. COTTON, G. WILKINSON and P. L. GAUS. Basic Inorganic Chemistry, 3rd Ed., Wiley, New York, p.61, 1995.

53. D. PERREAULT, M. DROUIN, A. MICHEL and P. D. HARVEY. Inorg. Chem., 31, 2740 (1992).

54. R. G. VRABKA, L. F. DAHL, P. CHINI and J. CHATT. J. Am. Chem. Soc., 91, 1547(1969).

55. A. MOOR, P. S. PREGOSIN, L. M. VENAZI and A . J. WELCH. Inorg. Chim. Acta, 85, 103 (1984).

56. A. A. FREW, R. HILL, L. MANOJLOVIC-MUIR, K. W. MUIR and R. J. PUDDEPHATT. J. Chem. Soc., Chem. Commun., 198 (1982).

57. G. DOUGLAS, L. MANOJLOVIC-MUIR, K. W. MUIR, M. C. JENNINGS, B. R. LLOYD, M. RASHIDI and R. J. PUDDEPHATT. J. Chem. Soc., Chem. Commun., 149 (1988).

58. G. DOUGLAS, L. MANOJLOVIC-MUIR, K. W. MUIR, M. C. JENNINGS, B. R. LLOYD, M. RASHIDI, G. SCHETTEL and R. J. PUDDEPHATT. Organometallics, 10, 3927 (1991).

59. L. HAO, J. J. VITTAL, R. J. PUDDEPHATT, L. MANOJLOVIC-MUIR and K. W. MUIR. J. Chem. Soc., Chem. Commun., 2381 (1995).

60. P. D. HARVEY, K. D. TRUONG, K. T. AYE, M. DROUIN and A. D. BANDRAUK. Inorg. Chem., 33, 2347 (1994).

61. R. BENDER, P. BRAUNSTEIN, A. DEDIEU, P. D. ELLIS, B. HUGGINS, P. D. HARVEY, E. SAPPA and A. TIRIPICCHIO. Inorg. Chem. 35, 1223 (1996).

62. A. M. BRADFORD, G. DOUGLAS, L. MANOJLOVIC-MUIR and K. W. MUIR and R. J. PUDDEPHATT. Organometallics, 9, 409 (1990).

63. T. ZHANG, M. DROUIN and P. D. HARVEY. Chem. Commun., 877 (1996).

64. M. GREEN, J. A. HOWARD, J. L. SPENCER and G. A. STONE. J. Chem. Soc., Chem. Commun., 3 (1975).

65. T. YOSIDA, T. YAMAGATA, T. H. TULIP, J. A. IBERS and S. OTSUKA. J. Am. Chem. Soc. 100, 2063 (1978).

66. A. TERZIS, T. C. STREKAS and G. T. SPIRO. Inorg. Chem., 10, 2617 (1971).

67. J. A. IBERS and R. G. SNYDER. J. Am. Chem. Soc., 84, 495 (1962).

68. K. M. ERWIN, J. HO and W. C. LINEBERGER. J. Chem. Phys., 89, 4514 (1988).

69. K. NAKAMOTO. Infrared and Raman Spectra of Inorganic and Coordination Compounds, 4th Ed., Wiley, New York, 1986, p.341.

70. R. S. DRAGO. Physical Methods for Chemists, 2nd Ed., Saunders, New York, 1992.

71. C. MEALLI. J. Am. Chem. Soc., 107, 2245 (1985).

72. D. G. EVANS. J. Organomet. Chem., 352, 397 (1988).

73. H. R. JAW and W. R. MASON. Inorg. Chem., 33, 3452 (1990).

74. P. D. HARVEY. J.Clust. Scien., 4, 377 (1993).

75. a) J. L. MALE, B. E. LINDFORS, K. J. COVERT and D. R. TYLER. Macromolecules, 30, 6404 (1997); b) S. C. TENHAEFF and D. R. TYLER. Organometallics, 11, 1466 (1992).

76. M. MORAN, M. C. PASCUAL, I. CUADRADO and J. LOSADA. Organometallics, 12, 811 (1993).

77. R. H. CAYTON, M. H. CHISHOLM, J. C. HUFFMAN and E. B. LOBKOVSKY. J. Am. Chem. Soc., 113, 8709 (1991).

78. M. R. JORDAN, P. S. WHITE, C. K. SCHAUER and M. A. MOSLEY, III. J. Am. Chem. Soc., 117, 5403 (1995).

79. S. J. LIPPARD. Science, 218, 1075 (1982).

80. K. MATSUMOTO, H. MIYAMAE and H. MORIYAMA. Inorg. Chem., 28, 2959 (1989).

81. K. MATSUMOTO and H. URATA. Chem. Lett., 1061 (1993).

82. a) K. MATSUMOTO. Bull. Chem. Soc. Jpn., 58, 651 (1985); b) K. MATSUMOTO and K. FUWA. Chem. Lett., 569 (1984).

83. K. MATSUMOTO, J. MATSUNAMI and H. URATA. Chem. Lett., 597 (1993).

84. K. MATSUMOTO, H.TAKAHASHI and K. FUWA. J. Am. Chem. Soc., 106, 2049 (1984).

85. K. MATSUMOTO and K. FUWA. J. Am. Chem. Soc., 104, 898 (1982).

86. a) L. S. HOLLIS and S. J. LIPPARD. J. Am. Chem. Soc., 105, 3494 (1983); b) L. S. HOLLIS and S. J. LIPPARD. J. Am. Chem. Soc., 103, 1232 (1981).

87. L. S. HOLLIS and S. J. LIPPARD. Inorg. Chem., 22, 2600 (1983).

88. a) J. K. BARTON, D. J. SZALDA, H. N. RABINOWITZ, J. V. WASZCZAK and S. J. LIPPARD. J. Am. Chem. Soc., 101, 1434 (1979); b) J. K. BARTON, H. N.RABINOWITZ, D. J. SZALDA and S. J. LIPPARD. J. Am. Chem. Soc., 99, 2827 (1977).

89. T. V. O'HALLORAN, P. K. MASCHARAK, I. D. WILLIAMS, M. M. ROBERTS and S. J. LIPPARD. Inorg. Chem., 26, 1261 (1987).

90. T. V. O'HALLORAN, M. M. ROBERTS and S. J. LIPPARD. J. Am. Chem. Soc., 106, 6427 (1984).

91. a) J. K. BARTON, C. CARAVANA and S. J. LIPPARD. J. Am. Chem. Soc., 101, 7269 (1979); b) P. K. MASCHARAK, I. D. WILLIAMS and S. J. LIPPARD. J. Am. Chem. Soc., 106, 6428 (1986).

92. G. BERNARDINELLI, P. CASTAN and R. SOULES. Inorg. Chim. Acta, 120, 205 (1986).

93. J. P. LAURENT, P. LEPAGE and F. DAHAN. J. Am. Chem. Soc., 104, 7335 (1982).

94. K. MATSUMOTO, H. TAKAHASHI and K. FUWA. Inorg. Chem., 22, 4086 (1983).

95. a) K. MATSUMOTO, K. SAKAI, K. NISHIO, Y. TOKISUE, R. ITO, T. NISHIDE and Y. SHICHI. J. Am. Chem. Soc., 114, 8110 (1992); b) K. SAKAI, K. KATSUMOTO and K. NISHIO. Chem. Lett., 1081 (1989); c) K. SAKAI and K. KATSUMOTO. J. Am. Chem. Soc., 111, 3074 (1989).

96. a) K. MASHIMA, M.TANAKA and K.TANI. J. Am. Chem. Soc., 119, 4307 (1997); b) K. MASHIMA, H. NAKANO and A. NAKAMURA. J. Am. Chem. Soc., 118, 9083 (1996); c) K. MASHIMA, H. NAKANO and A. NAKAMURA. J. Am. Chem. Soc., 115, 11632 (1993).

97. T. TANASE, H. UKAJI, T. IGOSHI and Y. YAMAMOTO. Inorg. Chem., 35, 4114 (1996).

98. P. M. MAITLIS and K. MOSELEY. J. Chem. Soc., Chem. Commun., 982 (1971).

99. W. P. WEBER, G. W. GOKEL and I. K. UGI. Angew. Chem., Int. Ed. Engl., 11, 530 (1972).

100. K. H. DAHMEN, D. IMHOF and L. M. VENANZI. Helv. Chim. Acta, 77, 1029 (1994).

101. L. MANOJLOVIC-MUIR, K. M. MUIR, M. C. GROSSEL, M. P. BROWN, C. D. NELSON, A. YAVARI, E. KALLAS, R. P. MOULDING and K. R. SEDDON. J. Chem. Soc. Dalton Trans., 1955 (1986).

102. A. G. SYKES and K. R. MANN. Inorg. Chem., 29, 4449 (1990).

103. a) D. PERREAULT, M. DROUIN, A. MICHEL and P. D. HARVEY. Inorg. Chem., 31, 3668 (1992); b) M. RHODES and K. R. MANN. Inorg. Chem., 23, 2053 (1984); c) V. M. MISKOWSKI, S. F. RICE, H. B. GRAY, R. F. DALLINGER, S. J. MILDER, M. G. HILL, C. L. EXSTROM and K. R. MANN. Inorg. Chem., 33, 2799 (1994); d) C. M. CHE, W. T. WONG, T. F. LAI and H. L. KWONG. J. Chem. Soc., Chem. Commun., 243 (1989); e) P. D. HARVEY, M. DROUIN, A. MICHEL and D. PERREAULT. J. Chem. Soc., Dalton Trans., 243 (1989); f) D. C. BOYD, P. A. MATSCH, M. M. MIXA and K. R. MANN. Inorg. Chem., 19, 3331 (1986); g) D. PERREAULT, M. DROUIN, A. MICHEL and P. D. HARVEY. Inorg. Chem., 32, 1903 (1993).

104. D. FORTIN, M. DROUIN and P. D. HARVEY. J. Am. Chem. Soc., 120, 5351 (1998).

105. K. NAKAMOTO. Infred and Raman Spectra of Inorganic and Coordination Compounds, 4th Ed., Wiley, New York, 1986.

106. P. D. HARVEY. Coord. Chem. Rev., 153, 175 (1996).

107. P. STEIN and H. K. MAHTANI. J. Am. Chem. Soc., 111, 3491 (1991).

108. a) M. K. DICKSON, W. A. FORDYCE, D. M. APPEL, K. ALEXANDER, P. STEIN and D. M. ROUNDHILL. Inorg. Chem., 21, 3858 (1982); b) R. E. MARSH and F. H. HERBSTEIN. Acta Crystallogr. Sect. B, 39, 280 (1983).

109. P. STEIN, M. K. DICKSON and D. M. ROUNDHILL. J. Am. Chem. Soc., 105, 3489 (1983).

110. I. MANNERS. Angew. Chem. Int. Ed. Engl., 35, 1603 (1996).

111. M.TURCOTTE and P. D. HARVEY. Unpublished results.

112. T. A. ALBRIGHT, J.K. BURDETT and M. H. WHANGBO. Orbital Interactions in Chemistry, Wiley, New York, 1985.

113. B. I. GILMOUR and D. M. P. MINGOS. J. Organomet. Chem., 302, 127 (1986).

114. A. L. BALCH, V. J. CATALANO, M. A. CHATFIELD, J. K. NAGLE, M. M. OLMSTEAD and JR. P. E. REEDY. J. Am. Chem. Soc., 113, 1252 (1991).

115. a) P. D. HARVEY, P. JOHNSTON and N. J. COVILLE. Can J. Chem., 72, 2176 (1994); b) P. D. HARVEY, I. S. BUTLER, M. C. BARRETO, N. J. COVILLE and G. H. HARRIS. Inorg. Chem., 27, 639 (1988).

116. D. M. SMITH. Ph.D Dissertation, California Institute of Technology, 1989.

117. P. D. HARVEY and H. B. GRAY. J. Am. Chem. Soc., 110, 2145 (1988).

118. D. PICHÉ and P. D. HARVEY. Can. J. Chem., 72, 705 (1994).

119. V. M. MISKOWSKI, T. P. SMITH, T. M. LOEHR and H. B. GRAY. J. Am. Chem. Soc., 107, 7925 (1985).

120. A. E. STIEGMAN, S. F. RICE, H. B. GRAY and V. M. MISKOWSKI. Inorg. Chem., 26, 1112 (1987).

121. M. HEINRICH-ZIETLOW. Ph.D Dissertation, California Institute of Technology, 1988.

122. D. PERREAULT, M.DROUIN, A. MICHEL and P.D. HARVEY. Inorg.Chem., 30, 2 (1991).

123. P. BRAUNSTEIN, M. A. LUKE, A. TIRIPICCHIO and M. TIRIPICCHIO-CAMELLINI. New J. Chem., 12, 429 (1988).

124. Y. TAKAHASHI, T. ITO and Y. ISHII. J. Chem. Soc., Chem. Commun., 1065 (1970).

125. a) C. M. CHE, F. H. HERBSTEIN, W. P. SCHAEFER, R. E. MARSH and H. B. GRAY. Inorg. Chem., 23, 2572 (1984); b) W. L. GLADFELTER and H. B. GRAY. J. Am. Chem. Soc., 102, 5909 (1980).

126. H. XIAO, K. K. CHEUNG and C. M. CHE. J. Chem. Soc., Dalton Trans., 3699 (1996).

127. R. J. H. CLARK and C. SOURISSEAU. Nouv. J. Chim., 4, 287 (1988).

128. a) J. J. MARKHAM. Rev. Mod. Phys., 31, 956 (1959); b) C. J. BALLHAUSEN. Molecular Electronic Structures of Transition Metal Complexes, McGraw-Hill, New York, 1979, p132.

129. K. HUANG and A. RHYS. Proc. R. Soc. (London), A204, 406 (1958).

130. E. J. HELLER. Acc. Chem. Res., 14, 368 (1981).

131. a) P. D. HARVEY, F. ADAR and H. B. GRAY. J. Am. Chem. Soc., 111, 1312 (1989); b) P. D. HARVEY and H. B. GRAY. Polyhedron, 9, 1949 (1990).

132. W. A. FORDYCE, J. G. BRUMMER and G. A. CROSBY. J. Am. Chem. Soc., 103, 7061 (1981).

133. L.H. PIGNOLET, M. A. AUBART, K. L.CRAIGHEAD, R.A.T. GOULD, D. A. KOGSTAD and J. S. WILEY. Coord. Chem. Rew., 143, 219 (1995).

134. D. M. P. MINGOS and M. J. WATSON. Adv. Inorg. Chem., 39, 327 (1992).

135. J. J. STEGGERDA. Comments Inorg. Chem., 11, 113 (1991).

136. a) T. KAPPEN, P. SCHLEBOS, J. BOUR, W. BOSMAN, G. BEURSKENS, J. SMITS, P. BEURSKENS and J. STEGGERDA. Inorg. Chem., 34, 2121 (1995); b) P. BRAUNSTEIN, H. LEHNER, D. MATT, A. TIRIPICCHIO and M. TIRIPICCHIO-CAMELLINI. Agew. Chem. Int. Ed. Engl., 23, 304 (1985).

137. D. M. P. MINGOS and R. W. M. WARDLE. J. Chem. Soc., Dalton Trans., 73 (1986).

138. a) C. E. BRIANT, D. I. GILMOUR and D. M. P. MINGOS. J. Chem. Soc., Dalton Trans., 835 (1986); b) C. E. BRIANT, D. I. GILMOUR and D. M. P. MINGOS. J. Organomet.Chem., 267, C52 (1984).

139. M. GREEN, J. A. HOWARD, J. L. SPENCER and F. G. A. STONE. J. Chem. Soc., Chem. Commun., 3 (1975).

140.a) R. HOFFMANN. Angew. Chem. Int. Ed. Engl., 21, 711 (1982); b) D. G. EVANS and D. M. P. MINGOS. J. Organomet. Chem., 232, 171 (1982).

141. T. TANASE, Y. YAMAMOTO and R. J. PUDDEPHATT. Organometallics, 15, 1502 (1996).

142. D. PERREAULT, M. DROUIN, A. MICHEL, V. M. MISKOWSKI, W. P. SCHAEFER and P. D. HARVEY. Inorg. Chem., 31, 695 (1992).

143. C. H. CLARK and L. E. MANZER. J. Organomet. Chem., 59, 411 (1973).

144. C. R. CONRAD and M. A. DOLLIVER. Organic Syntheses, Wiley, New York, 1943, Collect. Vol. II. p167.

145. A. G. SYKES and K. R. MANN. J. Am. Chem. Soc., 112, 7247(1990).

146. D. S. ACKER and W. R. HERTLER. J. Am.Chem. Soc., 84, 3370 (1962).

147. R. HOFFMANN and W. N. LIPSCOMB. J. Chem. Phys. 36, 2179 (1962).

148. a)R. HOFFMANN and W. N. LIPSCOMB. J. Chem. Phys. 36, 2872 (1962); b) R. HOFFMANN. J. Chem. Phys. 39, 1397 (1963).

149. J. H. AMMETER, H. B. BURGI, J. C. THIBEAULT and R. HOFFMANN. J. Am. Chem. Soc., 100, 3686 (1978).

150. C. MEALLI and D. M. PROSERPIO. J. Chem. Edu., 67, 399 (1990).

151. Y. LE PAGE, P. S. WHITE and E. J. GABE. NRCCAD, An Enhanced CAD-4 Control Program, Proc. Am. Crystallogr., Hamilton Meeting, 1986, Abstract PA23.

152. E. J. GABE, Y, LE PAGE, J. P. CHARLAND, F. L. LEE and P. S. WHITE. J. Appl. Cryst., 22, 384 (1989).

153. G. SHELDRICK. SHELX-97, Institut Anorg. Chemie, Tammannstr. 4, D37077, Göttingen, Germany, 1997.

154. C. K. JOHNSON. ORTEP in Xtal GX. Edotors. Hall & Du-Boulay, U. of Western Australia, 1995.